UNIVERSITY OF Southampton

University of Southampton

Faculty of Engineering & Physical Sciences

Institute for Life Sciences

School of Chemistry

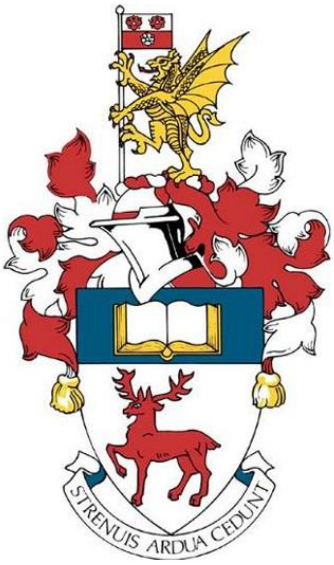

Development of Multiphoton Label-Free Super-Resolution Microscopy Techniques for Biomedical Imaging

by

Peter Benjamin Johnson

Thesis for the degree of Doctor of Philosophy

[January 2021]

University of Southampton

Abstract

Faculty of Engineering & Physical Sciences

School of Chemistry

Thesis for the degree of Doctor of Philosophy

Development of Multiphoton Label-Free Super-Resolution Microscopy Techniques for Biomedical Imaging

by

Peter Benjamin Johnson

Biology exists across a range of spatial scales from whole organisms (up to ~25 m) down to individual molecules (<1 nm). Optical microscopy has allowed the study of many biological processes at scales that are not resolvable by the human eye (~< 100 µm). However, due to diffraction, the resolution of an optical microscope at visible wavelengths is ~200 nm, prohibiting the study of biological processes below this limit. A group of techniques developed to overcome this limit called super-resolution techniques, have improved the resolution to ~1-10 nm. However, these super-resolution techniques require fluorescent labelling of biological samples limiting their applicability especially to live cell or long term imaging. Multiphoton label-free imaging techniques do not require labelling of the sample but are still limited by diffraction.

In this work two methods of label-free super-resolution with multiphoton imaging are established and explored. A physical method employing the photonic nanojet (PNJ) phenomenon is used to improve the resolution of second harmonic generation (SHG) microscopy. Optimal imaging parameters are established alongside developments in sample preparation and imaging workflow to maximise imaging performance. The limit of resolution is established and found to be 125 nm a 2.7 x improvement over the diffraction limit for SHG excited at 800 nm. The method is used to detect ultrastructural changes in fibrillar collagen in lung disease unobservable under diffraction-limited imaging. The method is used further to characterise other extracellular matrix proteins such as elastin, revealing new biophysical insight.

A computational method based on signal fluctuations is also developed for application to cellular autofluorescence signals. Resolution improvement was demonstrated for widefield fluorescence and point-scanning imaging systems. A 3D model sample was refined and lightsheet imaging employed to facilitate multiphoton imaging. The method is used to image mitochondria using the autofluorescence from the metabolic co-enzymes nicotinamide adenine dinucleotide (NADH) and flavin adenine dinucleotide (FAD).

This thesis successfully implements label-free super-resolution using multiple methods and imaging modalities. These tools have led to new biological understanding; moreover, they are simple to implement allowing for widespread use and application to disease research.

UNIVERSITY OF Southampton

Table of Contents

Table of Tables

Table of Figures

Declaration Of Authorship

I, Peter Benjamin Johnson]

declare that this thesis and the work presented in it are my own and has been generated by me as the result of my own original research.

Development of Multiphoton Label-free Super-resolution Microscopy techniques for Biomedical Imaging

I confirm that:

1. This work was done wholly or mainly while in candidature for a research degree at this University;
2. Where any part of this thesis has previously been submitted for a degree or any other qualification at this University or any other institution, this has been clearly stated;
3. Where I have consulted the published work of others, this is always clearly attributed;
4. Where I have quoted from the work of others, the source is always given. With the exception of such quotations, this thesis is entirely my own work;
5. I have acknowledged all main sources of help;
6. Where the thesis is based on work done by myself jointly with others, I have made clear exactly what was done by others and what I have contributed myself;
7. Parts of this work have been published as:
   Jones, M. G. et al. (2018) 'Nanoscale dysregulation of collagen structure-function disrupts mechano-homeostasis and mediates pulmonary fibrosis', eLife, 7, pp. 1–24. doi: 10.7554/eLife.36354.
   Johnson, P.B. et al. (2021) 'Superresolved polarization-enhanced second-harmonic generation for direct imaging of nanoscale changes in collagen architecture', Optica, 8(5), pp. 647-685. doi: 10.1364/OPTICA.411325.

Signed:

Date: 22/04/2022

Acknowledgements

I would like to extend my thanks to the following people without whom completion of this PhD would not have been possible. First and foremost thank you to Prof Sumeet Mahajan for taking a risk by letting a student with minimal microscopy experience and a background in Biomedical Science take on a PhD in microscopy development, requiring a broader skill set than I would have considered possible. Also, thank you for your constant support both academically and beyond, your enthusiasm, hard work and good nature are what I believe have made this research journey enjoyable and the research group so inviting. This brings me to my next thanks, to the Molecular Biophotonics and Imaging Group. Being part of such a diverse group has meant that I always felt like there was someone who could help me solve a problem I had. In particular, I would like to thank Kostas for his tireless upkeep of the imaging systems and teaching me the optical physics needed to understand what I was doing. To Simon, for many fruitful discussions on how to make, mend or modify something to get it to work and for being my first port of call for all thing's biology. To Niall, Jack, Josh, and Adam, for starting out on this with me and providing the peer group nonsense that has kept me motivated in the most daunting parts. To the wider research community at the Institute for Life Sciences and the University of Southampton, the approachable nature of all I have met has led to more support and unexpected collaborations than I could have ever expected. Thank you to all those outside of the research circle, to teammates at Stoneham RFC, old friends and to my family who I'm pretty sure still don't understand what I do but are proud and supportive regardless. Finally thank you to Chelsea, I'm sure you didn't know what you were signing up for when you joined me on this journey but you have taken the good and the bad in your stride, making sure I am always in the best place to do what is needed.

Abbreviations

3B	Bayesian Bleaching and Blinking
AFM	Atomic Force Microscopy
ATP	Adenosine Triphosphate
BAPN	Beta Aminopropionitrile
BG	Background
BTG	Barium Titanate Glass
CARS	Coherent anti-Stokes Raman Scattering
DMD	Deformable Micromirror Device
DMEM	Dulbecco's Modified Eagle Medium
ESI	Entropy based Super-resolution Imaging
ETC	Electron Transport Chain
FAD	Flavin Adenine Dinucleotide
FBS	Foetal Bovine Serum
FLIM	Fluorescence Lifetime Imaging
FOV	Field of View
FSRM	Fluctuations Based Super Resolution Microscopy
FWHM	Full Width Half Maximum
IPF	Idiopathic Pulmonary Fibrosis
LS	Light Sheet
MPAC	Multi Plane Autocorrelation
MUSICAL	Multiple Signal Classification Algorithm
NA	Numerical aperture
NADH	Nicotinamide Adenine Dinucleotide
OPEF	One-photon Excited Fluorescence
PALM	Photoactivation localisation microscopy
PBS	Phosphate Buffered Saline
PDMS	Polydimethylsiloxane
PNJ	Photonic Nanojet
PR	Phenol Red
PS	Polystyrene
RESOLFT	REversible Saturable OpticaL Fluorescence Transitions
ROI	Region of Interest
SACD	Super-Resolution Auto-Correlation Two-Step Deconvolution
SHG	Second Harmonic Generation
SLM	Spatial Light Modulator
SNR	Signal to Noise Ratio
SOFI	Super-Resolution Optical Fluctuation Imaging
SOL	Superoscillatory Lens
SR	Super-resolution
SRRF	Super-resolution Radial Fluctuations
STED	Stimulated Emission Depletion
STORM	Stochastic Optical Reconstruction Microscopy
TIRF	Total Internal Reflection Fluorescence
TPEF	Two-photon Excited Fluorescence

Chapter 1 Background and Motivation

The development of new optical microscopy techniques has been intrinsically linked to the advancement of biomedical research since its inception. The desire to see and understand the living world at a microscopic scale has driven imaging technologies towards their theoretical limits. However, despite the large interest in optical microscopy from both academic and industrial sectors, some established limitations still exist particularly for biological imaging.

1.1 Contrast and Label-Free Imaging

A key issue in biological microscopy is the requirement to label samples to generate specific, meaningful contrast. The simplest form of microscopy is transmitted light absorption microscopy, often called brightfield microscopy. In this technique, light is transmitted through a sample and differences in absorption at different parts of the sample create differences in intensity, thereby generating contrast. Brightfield microscopy has the advantages of being simple and minimally invasive. Unfortunately, most biological samples, especially cells, absorb minimally within the visible spectrum. As such, the contrast is often poor, necessitating the use of either chromatic staining or optical techniques such as phase contrast and differential interference contrast (DIC). Phase and DIC improve contrast and provide morphological information for biological samples. These methods can effectively highlight cells and organelles but give limited information as to their molecular structure or chemical nature. As such, contrast mechanisms that provide more specific information are required.

Fluorescent labelling is one of the most popular methods of overcoming many of the limitations of the morphological techniques mentioned above, providing specificity and sensitivity. Specificity of fluorescent labelling can be achieved in a number of ways including, but not limited to, the use of fluorescently-labelled (primary or secondary) antibodies, DNA probes, fluorescent proteins and structurally or chemically selective fluorescent dyes. Two of the most common ways of achieving specific fluorescent labelling, are immunofluorescence and genetic expression of a fluorescent protein. In immunofluorescence, antibodies raised against the protein of interest are incubated with the sample, unbound antibodies are then washed away prior to incubation with a second antibody that is reactive against the . The second antibody is conjugated with a fluorescent dye, such that the dye now labels the protein of interest. Fluorescent proteins such as Green Fluorescent Protein (GFP) can also be genetically expressed attached to the protein of interest, such that the protein is directly labelled (Pawley, 2006). This method has the advantage of being applicable to live cells, whereas immunolabelling of internal targets requires permeabilization of

the cell membrane, prohibiting live cell imaging. The dyes and fluorescent proteins used in these techniques are often bright enough to allow detection of single molecules (Hu *et al.*, 2014).

Despite the advantages and widespread use of fluorescence there are several limitations. Fluorescent labelling runs the risk that the results observed may contain artefacts of the labelling process. In live systems, there is also the possibility of perturbing the underlying biological system in uncharacterised ways due to the addition of a non-native molecule to a living system. Small molecules such as lipids, some small-molecule hormones, and many signalling molecules are not conductive to labelling due to loss of function on being labelled. Fluorophores also suffer from photobleaching, a term used to describe the irreversible, light-induced destruction of the fluorophore (Dittrich and Schwille, 2001). The precise mechanisms of photobleaching for all fluorophores are not fully understood. The currently accepted theory is that reactions between the excited fluorophore and molecular oxygen in the triplet ground state convert the fluorophore to a non-fluorescent moiety (Dittrich and Schwille, 2001; Pawley, 2006). Other reactions with the excited fluorophore lead to the generation of oxygen radicals and reactive oxygen species (ROS). Although cells have pathways to mitigate the harmful effects of small amounts of ROS, these pathways can become overwhelmed leading to oxidative stress and will ultimately trigger apoptosis (cell death). This process is known as phototoxicity (Dixit and Cyr, 2003; Kolega, 2004; Wagner *et al.*, 2010; Schneckenburger *et al.*, 2012) and poses a particular limitation to long term, live cell imaging. Thus, whilst florescence labelling represents one of the most popular biological imaging modalities, it has many shortcomings that should be addressed.

To overcome some of these limitations, it is possible to exploit nonlinear interactions of light with matter to extract structural and chemical information about the sample in question, without the addition of labels. Two-photon-excited fluorescence (TPEF), and second harmonic generation (SHG) are two of the most widely used multiphoton microscopy techniques. TPEF can excite endogenous biological fluorophores, and SHG can give structurally-specific contrast from endogenous biomolecules such as fibrillar collagen (Zipfel *et al.*, 2003). Crucially these optical effects can provide chemically- and structurally-selective contrast without the addition of fluorescent labels. Beyond the intensity of these signals, additional information is encoded in properties such as the phase, polarisation and emission directionality. Detection of changes in these properties can be highly informative of chemical and structural changes and has been exploited for label-free biomedical imaging and diagnostics (Campagnola, 2011; Mazumder *et al.*, 2017). These techniques do not represent an immediate replacement to microscopy methods using fluorescent labels, but provide another set of imaging modalities that may be more useful in situations where the high specificity and sensitivity can be exchanged for simplified sample preparation or where fluorescent labels cannot be used.

1.2 Optical Resolution

Another key limitation in optical microscopy is spatial resolution. Due to the diffraction of light when passed through an aperture, the resolution of optical microscopy is limited to ~ λ/2 where λ is the imaging wavelength. This is known as the diffraction limit. Generally, this places resolution in the region of 200 nm, when using blue light (~400 nm). Unfortunately, a wealth of biological structures and molecules exist on a spatial scale smaller than this. To investigate these biological species, researchers have historically been forced to use higher-resolution microscopy techniques such as electron microscopy (EM) or atomic force microscopy (AFM). By using electrons rather than photons, EM reduces the imaging wavelength to the de Broglie wavelength of the electrons, which is of the order of nm. By doing this, atomic resolution can be achieved (Robertson and Warner, 2013). However, to achieve this resolution many of the advantages of optical microscopy must be sacrificed. Samples must undergo a complex set of fixation and staining steps and/or flash freezing. This often involves toxic heavy metals; these stains also lack the specificity of antibody markers used in immunofluorescence microscopy, unless other EM compatible immunolabelling techniques such as immuno-Gold labelling are employed. As such, EM lacks the simplicity and potential specificity of optical microscopy. Perhaps more importantly, EM cannot be used for the study of dynamic processes in live cells. More recently, optical super-resolution techniques have been developed to overcome the limit of resolution. For certain techniques, the resolution of optical microscopy has been brought into the range of tens of nanometres (Betzig *et al.*, 2006), facilitating the study of single molecules. Despite the widespread success of these techniques, the vast majority rely on manipulating emission of fluorescent labels and are therefore subject to the same limitations as traditional, labelled imaging methods.

Thus, there is a need for super-resolution, label-free imaging methods. Such methods will allow the study of biological structures and molecules below the diffraction limit in an un-labelled and unperturbed fashion. This holds the potential to elucidate new biological phenomena in both health and disease.

The work in this thesis aims to develop label-free super-resolution methods building on the established multiphoton label-free techniques of SHG and TPEF. In Chapter 2, the underlying theory of label-free imaging and super-resolution are introduced, and the state of the art is presented. Chapter 3 details experimental techniques and methodologies.

Chapter 4 reports the development of a methodology for correlative imaging of tissue using traditional H&E staining and SHG imaging such that images can be placed within a known context and subsequent super-resolution imaging can be performed in a targeted fashion. In Chapter 5 a physical method of super-resolution SHG using photonic nanojets is developed, the polarisation

properties are explored and characterised, then used to further enhance resolution before being applied to the study of lung fibrosis. In Chapter 6 the polarisation enhanced photonic nanojet method is used to further analyse changes in the extracellular matrix, comprising elastin as well as collagen, during lung disease. In Chapter 7, a computational method for achieving label-free super-resolution is explored and used to image mitochondria in a live, unlabelled 3D cell spheroid sample on a lightsheet microscope. Finally, Chapter 8 summarises the conclusions of the presented work, highlighting the relative strengths and weaknesses of the approaches used. Directions for future research are also suggested and the research project is discussed in the context of the COVID-19 pandemic which occurred over the final year of this PhD.

Chapter 2 Theoretical Considerations

2.1 Light-Matter Interactions

The interplay between light and matter forms the basis of all optical imaging techniques. All matter can be described in terms of quantised energy states of its constituents. The interaction between electromagnetic radiation and the energy states of an atom, molecule, or material can result in energetic transitions between such energy states within that species. These energy states can further be described in terms of discrete electronic, vibrational, rotational, and other levels in order of decreasing energetic quanta.

Electronic states with the lowest energy are most stable (electronic ground – S_0) while excited states (S_1,S_2…) have higher energy than the ground state (Figure 1). At each electronic state energetic sublevels may exists due the vibrational state of a chemical bond, these are again quantised states and increase in energy (V_0,V_1,V_2 …). The absorption and subsequent emission of energy can be explained in terms of quantum transitions between these states and manipulation of these transitions is the fundamental basis of many imaging and spectroscopic techniques, including those used in this thesis.

2.1.1 Fluorescence

One such light-matter interaction is fluorescence. A fluorescent molecule (fluorophore) can absorb one (or multiple) photons. Provided the energy of the incident photon(s) matches the energy of an electronic transition within that molecule, an electron is excited from the ground state to one of multiple possible excited electronic states (Figure 1). The probability that a photon will be absorbed is governed by the absorption cross-section (Lakowicz, 1999). From this state the electron relaxes through vibrational energy levels, a process called non-radiative relaxation. The fluorophore may then return to S_0 via one of two pathways. During either process a photon of lower energy and longer wavelength (Stokes shifted), relative to the incident photon is emitted (Figure 1). Fluorescence emission occurs when the S_1 to S_0 transition happens directly, occurring on a nanosecond timescale (Masters and So, 2008). It is also possible for the fluorophore to undergo intersystem crossing into an excited triplet state (T_1, Figure 1) before relaxation, this process is called phosphorescence. The transition from the excited triplet state to the singlet ground state is spin forbidden. This means that return to the ground state is only facilitated by spin orbit coupling, where the spin of the excited electron flips to become complimentary to a

pair electron in the ground state. This process is slow compared to the transitions involved in fluorescence, therefore phosphorescence is slow compared to fluorescence and occurs on the order of 10^{-3}-10^{2} seconds. The increased time spent in the excited triplet state compared to the singlet state is one of the origins of fluorescence intermittency or "blinking", where the fluorophore enters a (comparatively) long lived dark state (Nahidiazar *et al.*, 2016). Whilst in the excited triplet state the molecule is more reactive than when in the ground state and this can lead to reactions that convert the molecule to a permanently non-fluorescent state, a process known as bleaching. Other sources of fluorescence blinking include polarisation effects for freely rotating fluorophores, where the excitation efficiency changes due to fluorophore movement, and photo-induced isomerisation. The *cis* and *trans* isomers of a fluorophore may have a different excitation efficiency at a given wavelength and as a result the fluorophore population can be biased towards a certain isomer. Therefore, molecules can become trapped in a dark state due to the low excitation efficiency for a given isomer (Bagshaw and Cherny, 2006). Fluorescence blinking and bleaching events can often be seen as a barrier to optical microscopy however is also possibly to exploit this photochemistry to improve the spatial resolution of the system (Section 2.4.2).

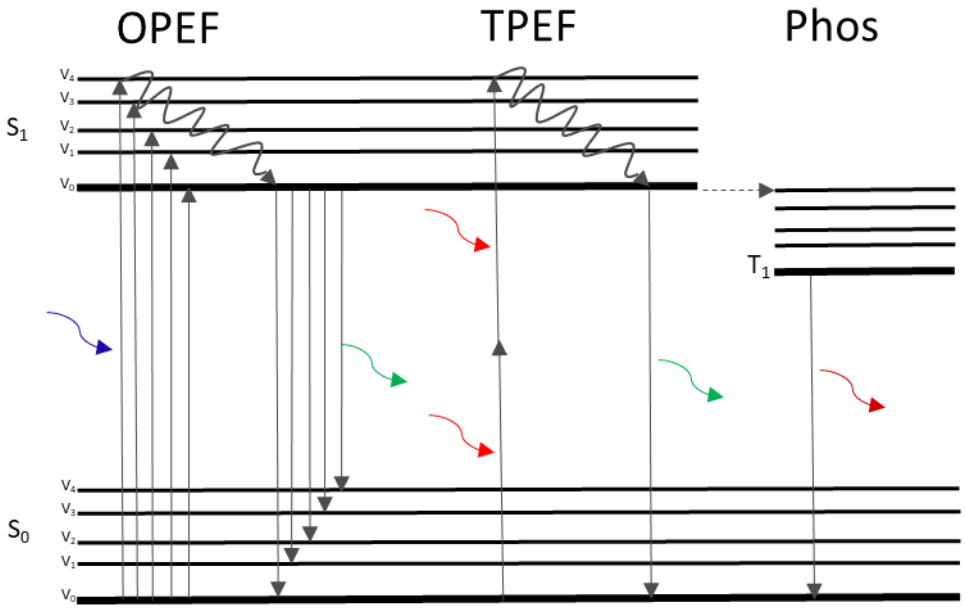

Figure 1: Jablonski diagram depicting the energy transitions of One- (OPEF) or Two-photon-excited fluorescence (TPEF) and phosphorescence.
Absorption of a photon causes the excitation from the singlet ground electronic state (S_0), to any of the vibrational sub-levels of the singlet excited state (S_1). Other higher-energy excited singlet states have not been displayed for clarity. The molecule undergoes non radiative relaxation before returning to S_0. As it returns to S_0 a photon is released of corresponding energy to the transition made. In TPEF excitation occurs due to the simultaneous absorption of 2 photons. If the molecule transitions to an excited triplet state, the emission process is termed phosphorescence.

In her 1931 thesis (Göppert-Mayer, 1931), Maria Göeppert-Mayer theorised that absorption could take place with any number of photons provided the sum of their energies matches the electronic transition of the fluorophore. This was experimentally shown by Kaiser in 1961 (Kaiser and

Garrett, 1961) The incoming photons must arrive simultaneously (within ~0.1 fs) necessitating a high photon flux. Due to the damage threshold of most fluorophores, practical multiphoton excitation uses either two or three photons and simplicity usually dictates that these photons are degenerate (have the same frequency), as only one input laser beam is then required. Multiphoton excitation of fluorescence holds multiple advantages over single photon excitation. The longer wavelengths used are scattered less, allowing greater sample penetration and facilitating better imaging at depth (Theer and Denk, 2006). In addition, multiphoton excitation only occurs at the focal volume, avoiding out of focus excitation and achieving intrinsic optical sectioning without a pinhole as in confocal microscopy (Masters and So, 2008). Finally, it allows the targeting of ultraviolet-excitable fluorophores. These are not usually amenable to imaging due to the phototoxicity incurred at these shorter wavelengths (Kolega, 2004). The interaction of light with a molecule may not result in a transition between the ground state and a 'real' electronic excited state. It may instead only involve virtual energy transitions resulting in no energy transfer to the molecule. Transitions to virtual levels involve scattering processes.

2.1.2 Scattering Interactions

The response of a material to an applied electric field can be described by the induced polarisation of the medium. That is, the dipole moment per unit volume arising from the displacement of charge within the medium.

$$P = \varepsilon_0 \chi^{(1)} E$$

Equation 1 Induced polarisation

Where P is the induced polarisation, ε_0 is the vacuum permittivity, $\chi^{(1)}$ is the first order (linear) susceptibility and E is the applied electric field. For fields of low strength relative to the atomic electric field strength, the response of the medium to the applied field remains linear. At higher field strengths it becomes necessary to consider the nonlinear responses of the material, this can be represented via a Taylor series expansion (Equation 2).

$$P = \varepsilon_0 [\chi^{(1)} E + \chi^{(2)} E^2 + \cdots \chi^{(n)} E^n]$$

Equation 2 Higher order induced polarisation

Different terms in this expansion correspond to higher order phenomena, the first term varies linearly with the electric field and gives rise to processes such as linear absorption, reflection, and Rayleigh scattering. The second term varies with the square of the electric field and encompasses second order processes such as second harmonic generation (SHG), sum frequency generation

(SFG) and hyper-Rayleigh scattering (HRS). The third term ($\chi^{(3)}$) encompasses third order processes such as third harmonic generation (THG), and contains the two-photon absorption cross-section which governs TPEF (Rumi and Perry, 2010) (Figure 2).

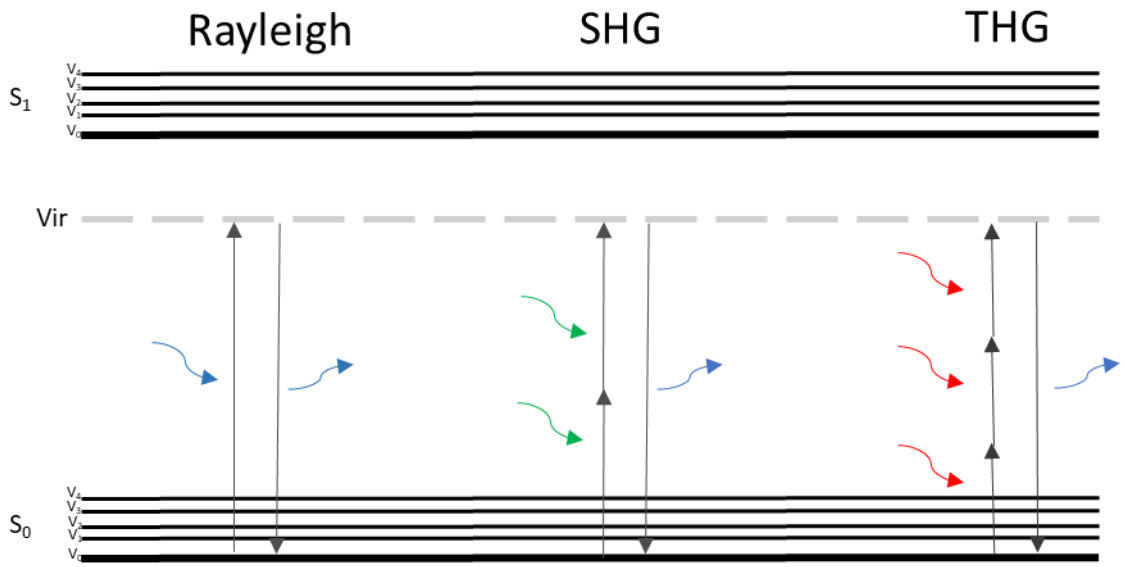

Figure 2: Jablonski diagram depicting the transitions occurring during various linear and non-linear scattering processes.
Excitation of the molecule to a virtual energy state occurs due to absorption of an incoming photon, near simultaneously a scattered photon is emitted. In Rayleigh scattering the energy of the pump and scattered photon are the same, in SHG two simultaneously-absorbed photons are converted to one photon of twice the energy. In Third Harmonic Generation (THG) three incident photons are converted to one photon of three times the energy.

2.1.3 Second Harmonic Generation (Dipole interpretation)

When light of frequency ω is incident on a centrosymmetric molecule the electron cloud of that molecule will be driven to oscillate symmetrically at the same frequency as the incident radiation. As a result of this oscillation, a wave is emitted at frequency ω in a dipole-like emission pattern this is Rayleigh Scattering (Figure 3A). If the light is incident on a non-centrosymmetric molecule (a molecule lacking inversion symmetry), the driven oscillation is asymmetric and waves are generated at 2 additional frequencies, 0 and 2ω (Figure 3B).

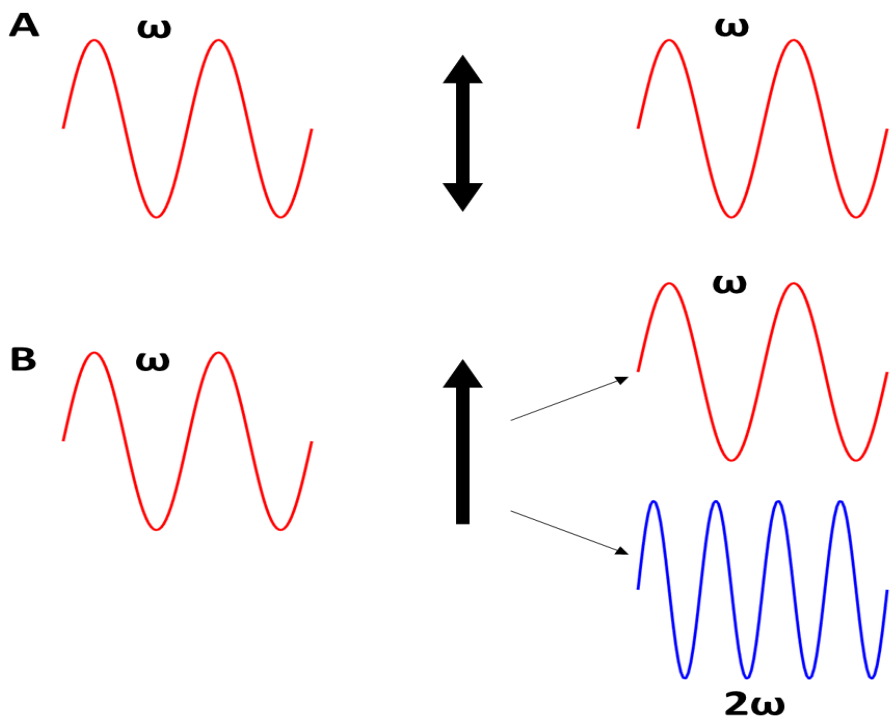

Figure 3: Scattering processes.
A) Scattering of a wave of frequency ω by a centrosymmetric molecule results in a wave generated at ω (Rayleigh scattering). B) Scattering of a wave at ω by a non-centrosymmetric molecule results in additional generation of new frequencies 0 and 2ω.

For a single non-centrosymmetric scatterer, the generation of the wave at 2ω is dipole-like and is called hyper-Rayleigh scattering (HRS). For an arrangement of such scatterers that are ordered within a material, constructive interference of the generated wave occurs leading to summation of signal predominantly in the direction of the incident wave. This is the process of second harmonic generation (SHG) and can be viewed as the macroscopic (material level) equivalent of hyper-Rayleigh scattering. Materials demonstrating this ordered lack of centro-symmetry are most often crystals such as β Barium Borate (BBO), which are routinely used for SHG in the laboratory. Biological sources of SHG include fibrillar collagen, the actin-myosin complex and microtubules (Campagnola, 2011). The fundamental moiety lacking centro-symmetry in proteins is the peptide bond. In the biological structures above, the ordered arrangement of peptide bonds is such that coherent summation of signal to a detectable level is possible (Plotnikov *et al.*, 2006; Deniset-Besseau *et al.*, 2009; Van Steenbergen *et al.*, 2019). Interfaces can also provide the break in symmetry required to generate a second harmonic signal (New, 2011) making SHG a powerful tool for probing the interface between 2 homogenous media (Shen, 1989).

2.1.4 Phase matching

For coherent summation of SHG to occur, the phase matching condition must be satisfied in accordance with conservation of momentum such that

$$2k_f - k_{SHG} = 0$$

Equation 3 Phase matching condition

Where k_f and k_{SHG} are the wave vectors of the fundamental and second harmonic fields respectively (Figure 4**A**).

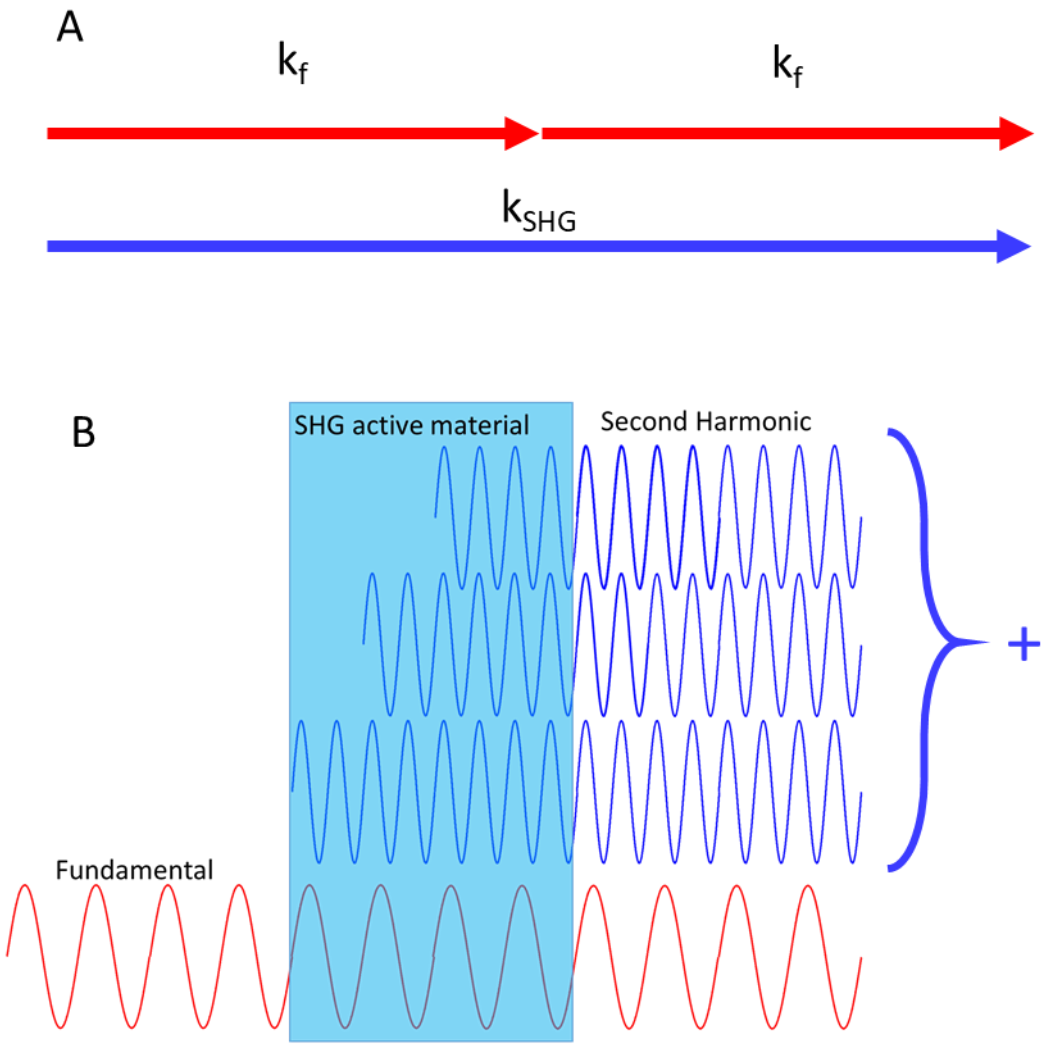

Figure 4: Phase matching of the fundamental (K_f) and Second Harmonic (K_{SHG}) waves dictates primarily forward emission.
(**A**) Momentum conservation under perfect phase matching. (**B**) Under perfect phase matching, the second harmonic signal produced at any point in the material sums coherently with SHG produced at any other point.

Dispersion occurs due to the dependence of the refractive index of a material on wavelength. This results in a phase mismatch between the fundamental and second harmonic fields, as the two fields propagate through the medium a phase-walk is introduced between the two (Pavone and

Campagnola, 2014). After a certain distance propagated within the medium the second harmonic field will be π radians (λ/2) out of phase with the second harmonic field generated at this second point (Figure 5). At this point, energy will begin to be converted from the second harmonic field back to the fundamental due to destructive interference.

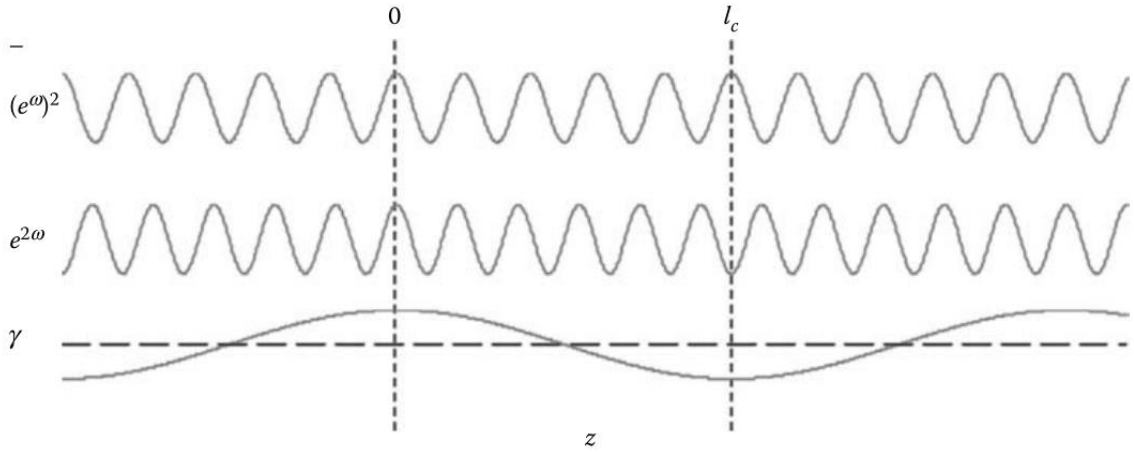

Figure 5: Phase walk in Second Harmonic Generation
Due to the difference in refractive index experienced by the fundamental (ω) and second harmonic (2ω) waves a phase walk occurs between the 2. This results in interference between SHG generated at different points along the propagation axis (z). γ shows the oscillation of interference between the two waves as a function of the distance propagated, l_c = coherence length. Reproduced with permission from (Pavone and Campagnola, 2014).

The distance at which this occurs is known as the coherence length (l_c). In the case of forwards SHG the fundamental and the second harmonic wave are propagating in the same direction and therefore the difference in their speeds (expressed by n) dictates the phase walk. Therefore, the coherence length is proportional to the difference in the refractive indices (Equation 4).

$$l_c^f = \frac{\lambda}{4} \cdot \frac{1}{|n^{2\omega} - n^{\omega}|}$$

Equation 4 Forward coherence length

In the backwards case the fundamental and the second harmonic wave are traveling in opposite directions, thus, the phase walk is proportional to the sum of the refractive indices (Equation 5).

$$l_c^b = \frac{\lambda}{4} \cdot \frac{1}{|n^{2\omega} + n^{\omega}|}$$

Equation 5 Backwards coherence length

As a result of this, the phase walk in the backwards direction is faster than that in the forward direction and as such the backwards coherence length is much shorter than the forward case (Campagnola and Dong, 2011). For example, l_C^f = 13.4 µm and l_C^b = 0.079 µm for a BBO crystal pumped with 1064 nm and SHG at 532 nm.

To avoid phase walk and allow summation of second harmonic light over propagation distances greater than the coherence length it is possible to exploit birefringence of many non-linear crystals. At a given angle, the refractive index for the ordinary wave at ω is the same as that for the extraordinary wave 2ω. This is known as perfect or birefringent phase matching and is the most commonly method of high efficiency phase matching (New, 2011) (Figure 6 PM)

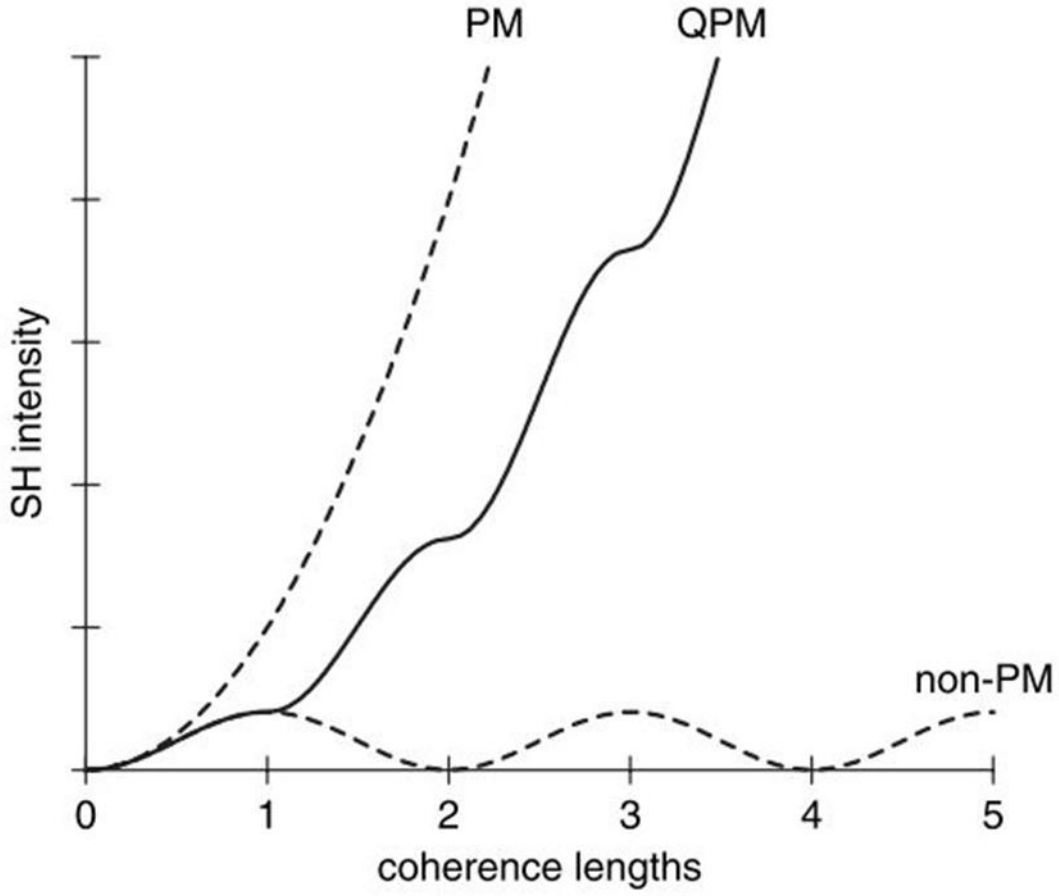

Figure 6: The effect of phase matching on SHG intensity.
The SHG intensity increases indefinitely under perfect phase matched conditions (PM), in non-phase matched conditions (non-PM) the SHG intensity oscillates between a maximum and minimum. The period of this oscillation defines the coherence length, it is determined by the phase mismatch between fundamental and SHG fields. In quasi phase matched conditions (QPM) the sign of the nonlinear susceptibility inverts at the length of the coherence length such that generated SHG signal is always interfering constructively. Reproduced with permission from (New, 2011).

In non-perfectly phase matched conditions it is still possible to achieve significant summation of second harmonic signal. This is achieved by inverting the sign of the non-linear susceptibility after each coherence length such that there is constructive interference between SHG generated at different distances into the material. In crystals this can be achieved by periodically changing the orientation of the crystal lattice via electron bombardment or a pulsed electric field (Houé and Townsend, 1995). This type of phase matching is called quasi-phase matching, it is not as efficient

as birefringent phase matching because there is still a phase walk between the fundamental and second harmonic fields before each inversion of the susceptibility (Figure 6 QPM). Quasi-phase matching is now routinely achieved using periodically poled crystals such as periodically poled lithium neobate (PPLN).

As mentioned above, due to conservation of momentum the SHG emission is generated primarily in the forward direction however, it is possible for SHG to be detected in the backwards direction and this occurs via two main mechanisms. It is possible for SHG to occur in the backwards direction if the scatterers are suitably distributed along the propagation axis, such that they contribute momentum to the SHG process and momentum conservation is satisfied (Mertz and Moreaux, 2001). Because the relative proportion of forward and backwards generated SHG is dependent on the SHG generating domain size and distribution it is possible to extract information about the size and axial distribution of SHG emitters via analysis of the forward/backwards SHG ratio.

A comprehensive exploration of the phase matching conditions in biological media, where birefringent phase matching or controlled periodic poling cannot be achieved, was performed by LaComb *et al.* (LaComb *et al.*, 2008). They showed that the second harmonic signal depends on the SHG generating domain length and the inter domain distance. Here these factors contribute to quasi phase matching allowing for the summation of SHG intensity between anisotropic domains. They showed that the following relaxed phase matching conditions occur

$$\Delta k_f = K_f - (k_{2\omega} - 2k_{\omega})$$

Equation 6

$$\Delta k_b = K_b - (k_{2\omega} + 2k_{\omega})$$

Equation 7

Where Δk_f and Δk_b are the phase mismatches for forward and backwards SHG creation and $K_b$and K_f are the momentum contributions for the media. Forward SHG is dominated by phase matching from smaller Δk_f values, occurring for domains on the order of $l_c = 2\pi/\Delta k_f$ where lc is the coherence length. As a result, forwards SHG is primarily a result of domains close to the size of the coherence length. In opposition to this, backwards SHG is completely reliant on momentum contributions from the media. Therefore, for appreciable backwards SHG to occur compared to forwards SHG the domain size should be smaller than l_c for the forwards field and the domains should be separated by a space on the order of the backwards coherence length. Taking these considerations into account large ratios of forwards SHG to backwards SHG (F_{SHG}/B_{SHG}) occur from

large domains (collagen fibrils) ~the size of the SHG wavelength and also from densely packed fibrils much smaller than λ_{SHG} such that they form a single effective domain. F_{SHG}/B_{SHG} ratios closer to 1 are observed when fibrils are ~ $\lambda_{SHG}/10$ and are spaced ~ l_c for backwards SHG. By understanding these principles, it is possible to extract information about the size and packing of collagen fibrils which can be informative of disease.

Backwards detected SHG also contain contributions from the backwards scattering of forward generated SHG photons. In this case the coherence with the excitation is lost and careful interpretation of the polarisation state should be employed when analysing backwards detected SHG.

Equation 2 also suggests the possibility of 3 photons arriving simultaneously and undergoing a similar process, termed third harmonic generation (THG). Third harmonic generation can occur in isotropic media as the third order susceptibility does not have the same symmetry restrictions as the second harmonic case. The contrast observed when imaging via THG is generated at changes in the third order susceptibility or dispersion such as refractive index mismatches. This occurs because in bulk medium third harmonic signal produced before and after the objective focus interfere destructively producing net zero signal, for constructive interference to occur the aforementioned conditions must be true (Schins *et al.*, 2002). In this way, the structures visualised by THG closely mimic those seen via more traditional contrast mechanisms such as phase contrast or DIC. Examples of this include the imaging of lipid droplets (Débarre *et al.*, 2006), nerve myelination (Lim *et al.*, 2014) or the canaliculi in bone (Genthial *et al.*, 2017).

2.2 Multiphoton Label-Free Microscopy

Both two-photon exited fluorescence (TPEF) and second harmonic generation (SHG) are amongst a wealth of techniques used to produce contrast in microscopy. The next section covers some of the notable applications of these techniques in biomedical imaging.

2.2.1 Biological Application of Second Harmonic Generation

The application of label-free multiphoton microscopy to biomedical imaging has had a widespread research impact. SHG has a broad range of biological applications. SHG dyes arrange in an ordered manner in the plasma membrane of cells. This creates an ordered break in centro-symmetry, which is required for the dye to be SHG active. This order is lost upon membrane depolarisation and has been used to image action potentials in real time (Nuriya *et al.*, 2006). SHG has also been used for label-free imaging of microtubule arrangement (Dombeck *et al.*, 2003) and quantitative analysis of collagen structure and composition under a variety of disease contexts including cancer (Mouras *et al.*, 2010; Nadiarnykh *et al.*, 2010; Campagnola, 2011; Hu *et al.*, 2012; Tilbury and Campagnola, 2015) and fibrotic diseases (Strupler *et al.*, 2007; Martin, Norris and Mcconnell, 2013; Kottmann *et al.*, 2015; Peng *et al.*, 2015; Ranjit *et al.*, 2015). The past 15 years has seen significant advances in the use of SHG imaging, particularly within the above disease areas. This has arisen out of parallel improvements in: a) the imaging technology with respect to resolution and sensitivity *and* b) the increased understanding of the physical principals underpinning SHG in biological tissues. The information that can be extracted using this understanding, such as the polarization anisotropy (Campagnola and Loew, 2003; Williams, Zipfel and Webb, 2005) and signal directionality (LaComb *et al.*, 2008) can give insight beyond morphology alone. SHG has seen great success for imaging collagen as fibrillar collagen is a highly SHG-active structure (Deniset-Besseau *et al.*, 2009) and changes in collagen composition, distribution and morphology underpin many diseases (Kadler *et al.*, 2007).

2.2.1.1 Collagen

Collagen is a key extracellular matrix protein representing ~30% of the protein mass within the body (Ricard-Blum, 2011). Originally understood to provide structural support for many tissues and organs, it is now known that collagens have a diverse set of functions including cell signalling and effects on cellular metabolism (Vogel, 2001). There are, to date, 28 different known isoforms of collagen that can be divided into several families based on their structure and organisation.

These groups are: fibril-forming collagens, fibril-associated collagens, network-forming collagens, anchoring fibrils, transmembrane collagens and basement membrane collagens (Ricard-Blum, 2011). Of these families, by far the most abundant are the fibril forming collagens (types I,II,III,V,XI) constituting ~90% of the total collagen in the human body. Types I and V can be found in: bone, skin, tendons, ligaments, the lung and the cornea. Whilst II and XI predominantly form the collagen structure in cartilage. Type III can be found in the reticular fibres of most tissues (Gelse, Pöschl and Aigner, 2003).

All collagens are characterised by containing a Gly-X-Y tripeptide repeat where X and Y represent other amino acids, most commonly proline and hydroxyproline (Gelse, Pöschl and Aigner, 2003). Extended Gly-X-Y repeats form into a left-handed helix of approximately 1000 residues (300 nm) in length called an α-chain. Three α-chains come together to form a right-handed triple helix held together by hydrogen bonding (Kadler *et al.*, 1996). This triple helix may be homo-trimeric where all α-chains contain the same repeat, or they may be hetero-trimeric where two or more different α-chains form the triple helix. In the case of fibrillar collagens, triple helices further associate to form fibrils. They are stabilised by the formation of covalent cross-links between lysine or hydroxylysine residues in the non-helical ends of the molecule, with hydroxylysine residues of neighbouring collagen molecules (Robins, 2007). Fibrils display a characteristic banding structure under the electron microscope which arises out of a staggered association of individual collagen monomers (Hulmes and Miller, 1981). The periodicity of this banding is approximately 67 nm, but varies depending on multiple factors including collagen type and the tissue preparation steps employed prior to imaging (Jastrzebska *et al.*, 2017) . Collagen fibrils can further associate into fibres which forms the structural scaffold of many tissues.

The hierarchal structure of collagen makes it a very strong second harmonic scatterer with a χ^2 only 10 times less than that of crystalline quartz (Roth and Freund, 1981; Freund, Deutsch and Sprecher, 1986). The non-linear optical response of collagen arises from the peptide bonds in individual α-chains which display a level of intramolecular coherence. Intermolecular coherence between the 3 α-chains within the collagen triple helix occurs due to their relatively ridged structure, ensuring alignment of the harmonophores (Deniset-Besseau *et al.*, 2009). The ordered hierarchical structure of collagen results in the same coherent summation of signal at a molecular and supramolecular scale thus, it exhibits strong SHG signals making it an ideal target for SHG microscopy in biology and medicine.

SHG microscopy has been used to study the reorganisation of collagen structure and morphology during disease. SHG imaging in various collagenous tissues such as: skin (LaComb, Nadiarnykh and Campagnola, 2008), Achilles tendon (Theodossiou *et al.*, 2006), cornea (Latour *et al.*, 2012) and

sclera (Strupler *et al.*, 2007) have been demonstrated. However, SHG microscopy can provide extra information in addition to the observed morphological changes due to the structural requirements of signal generation. Second harmonic generation is a coherent process, and as such, the signal produced is highly directional (LaComb *et al.*, 2008). The direction and intensity of this signal is greatly informative of the structural organisation of the sample in question. It contains information about the size of the SHG emitters (collagen fibres) and their relative packing density. Experiments comparing the ratio of forward to backward SHG signal intensities between healthy and disease tissue have been able to distinguish between the two states using this ratio. LaComb *et al.* (LaComb, Nadiarnykh and Campagnola, 2008), were able to separate normal and osteogenesis imperfecta samples by plotting the forward-backward SHG ratio against imaging depth into the sample. It was determined that the forward to backwards signal ratio increases with imaging depth. The same group were able to perform a similar diagnostic experiment in ovarian cancer (Nadiarnykh *et al.*, 2010). A similar study was undertaken in 2015 by Peng *et al.* (Peng *et al.*, 2015) aiming to improve the diagnosis and prognosis of liver fibrosis at different stages of disease progression. By calculating the F_{SHG}/B_{SHG} ratio and two depths in liver tissue sections from healthy liver and 4 stages of disease progression, it was shown that with disease progression this ratio decreased and this was attributed to the formation of collagenous septa. Collagenous septa are fibrous bands between regions of the tissue such as portal veins; they increase the level of backscattering of second harmonic photons; one of the 2 key mechanisms by which epi-detected SHG signal is produced (Pavone and Campagnola, 2014). . Other methods of obtaining additional information about the collagen structure involve manipulation of the excitation properties such as the wavelength or polarisation, rather than probing the emission properties alone.

Because the SHG intensity is dependent on the phase mismatch (Δk) and this is wavelength dependent, it is possible to use the wavelength dependence of SHG to investigate molecular properties (Freund, Deutsch and Sprecher, 1986; Green *et al.*, 2017). Green *et al.* used ratiometric imaging between excitation wavelengths during the detection of epi-SHG to determine the nature of the emitter. The differential epi-SHG generated at two excitation wavelengths, 860nm and 920nm, was sufficient to differentiate between collagen and myosin (Green *et al.*, 2017).

The strength of the second harmonic signal depends on the relative orientation of the excitation polarisation and of the SHG emitters (Pavone and Campagnola, 2014). When the orientation of the excitation field is parallel to the emitter plane then the signal is maximum and when perpendicular it is minimum (Kim *et al.*, 2000; Yasui, Tohno and Araki, 2004).Thus, it is possible to extract multiple pieces of information about the order and orientation of collagen within tissues

by manipulating polarisation. With suitable model fitting it is possible to calculate the helical pitch angle of collagen within the excitation volume (Tiaho, Recher and Rouède, 2007; Su *et al.*, 2011) and the tilt angle of the helices relative to the fibril axis (Tuer *et al.*, 2011). These measurements are interesting from a biophysical perspective. They allow understanding of the differences between collagen in different tissues (Kumar *et al.*, 2015; Sakaue *et al.*, 2018), the effect of mechanical stretching (Gusachenko *et al.*, 2012) and inform about changes that occur during disease (Han *et al.*, 2008; Hompland *et al.*, 2008; Campbell *et al.*, 2018).

Bancelin *et al.* (Bancelin *et al.*, 2014) used the SHG signal produced by collagen fibrils to determine their absolute size. They determined the number of photons produced by a collagen fibril to have a 4^{th} power relationship with fibril diameter within the focal volume. Using this they were able to use photon counting to accurately measure the diameter of collagen fibrils as narrow as 30 nm. This technique however, cannot be used when imaging dense formations of collagen where fibrils may be closer than the resolution limit. However, the authors believe that in combination with other data detailing collagen density, orientation, and organisation such as that from polarization resolved measurements, their method will still be applicable to measuring the size of collagen fibrils below the limit of resolution. To date, such super-resolution measurements have not been reported in the literature.

2.2.2 Biological Application of Two-photon-excited Autofluorescence

Due to the similar excitation conditions required and the spectrally separated signals, it is possible to simultaneously acquire both second harmonic generation and two-photon-excited fluorescence signals from the same sample. There are a number of biological auto-fluorophores that are excitable in the 700 nm to 1000 nm range including: retinol, flavins (FAD), reduced nicotinamide adenine dinucleotide (NADH), pyroxidine, folic acid, lipofuscin and elastin (Zipfel *et al.*, 2003). Their use as contrast agents spreads across multiple research fields. The use of NADH and FAD imaging can be used to indicate cellular redox status as these two components are key co-enzymes in cell metabolism (Georgakoudi and Quinn, 2012). As a result metabolic imaging by TPEF has seen success in cancer sciences where abnormal cellular metabolism is known to play a key role (Thomas *et al.*, 2014). Cellular autofluorescence in tandem with SHG has also been used in diagnostic procedures for gastric cancer (Yan *et al.*, 2011), and colorectal cancer lesions (Matsui *et al.*, 2017)

As one of the key extracellular fluorophores, elastin imaging has often been used in conjunction with SHG of collagen for investigation of the extracellular matrix in a number of tissues and disease states such as: lung tissue during Idiopathic pulmonary fibrosis (Pena *et al.*, 2007; Tilbury

et al., 2014), cryptogenic organising pneumonia (Kottmann *et al.*, 2015) and cancer (Wang *et al.*, 2009), heart valves and arterial lamellae (K.Konig *et al.*, 2005; Strupler *et al.*, 2007). It has also been used for the investigation of engineered tissues such as blood vessels and ECM scaffolds (Calle *et al.*, 2014), and label-free monitoring of dermal fibroblasts in collagen matrixes (Pena *et al.*, 2010). Using the SHG to TPEF ratio Cicchi *et al.* (Cicchi *et al.*, 2008) were able to distinguish between normal and neoplastic tissue; they further went on to use time-resolved methods such as fluorescence lifetime imaging (FLIM) to highlight a difference in protein composition between healthy, basal cell carcinoma and malignant melanoma tissues. Czekalla *et al.* evaluated the influence of age on the skin ECM using the second harmonic intensity (SHG) to autofluorescence intensity (AF) aging index of dermis (SAAID). Where SAAID = (SHG-AF)/(SHG+AF). In a pilot study they found significant differences between photo-protected regions and those exposed to sunlight (Czekalla *et al.*, 2017).

As can be seen, non-linear optical microscopy is a rich source of information pertaining to both biophysical properties and disease pathology. SHG and TPEF can provide structurally- and chemically-selective contrast without addition of exogenous labels. However, both these label-free optical techniques have limitations in terms of spatial resolution and overcoming this limit is a major challenge in the field of non-linear microscopy.

2.3 Resolution of the Optical Microscope and the Diffraction Limit

In 1873 Ernst Abbe discovered that light focussed by a lens has a minimum spot size due to diffraction, it is determined by both the wavelength of the light and the numerical aperture of the lens used to focus (Abbe, 1873). This is now known as the Abbe and/or diffraction limit and although alone it doesn't define the resolution of an imaging system, it does introduce one of the key factors limiting it. Resolution can be defined as the distance by which 2 objects must be separated for them to be discernible as separate.

Light emanating from a point source in the sample plane will appear as an intensity pattern that has a spread due to the imperfect response of the system when observed at the image plane. This image is referred to as the point spread function (PSF) (Figure 7**B**). The Fourier transform of the PSF is called the Optical Transfer Function (OTF) and is used when exploring resolution in the spatial frequency regime. A sample can be considered as a series of point sources of light and therefore an image can be considered as a series of PSFs thus, resolution is defined as the ability to separate these within an image. A general treatment of this definition of resolution is given by Equation 8

$$d = k\frac{\lambda}{n\sin\theta}$$

Equation 8

Where *d* is the smallest resolvable distance between 2 objects, λ is the wavelength of light in question, *n* is the refractive index of the immersion medium and θ is the half angle of the collection aperture (Figure 7). Collectively *nsin*θ is the numerical aperture (NA), typically this value is in the region of 0.5-1.5 (unless special high refractive index glass is used) The factor *k* represents a value that varies depending on the criterion used for determining two points as resolved. The Abbe, Rayleigh, Houston, and Sparrow criteria are among the most common used to define the spatial resolution of a microscope or imaging system. The Abbe limit states that the factor *k* is equal to 0.5 (Abbe, 1873). The Rayleigh criterion states that 2 objects should be considered resolvable when the centre of one PSF, lies within the first minimum of the second PSF (Rayleigh, 1874, 1903). As 2 point sources may not have equal intensity and the first minimum may be non-zero, a practical figure of a 26.4% intensity drop between the 2 neighbouring peaks is used, or a k of 0.61 (Diaspro, 2002). The Houston criterion measures resolution using the full width half maximum (FWHM) of the PSF and produces a *k* of 0.515 (Houston, 1927). The Sparrow criterion is more commonly used in astronomy and defines two objects as unresolvable when the sum of the

intensities between 2 points no longer produces a saddle when plotted (Sparrow, 1916) (Figure 7C) numerically this gives a value of *k* = 0.47 and is equal to the contrast cut-off distance.

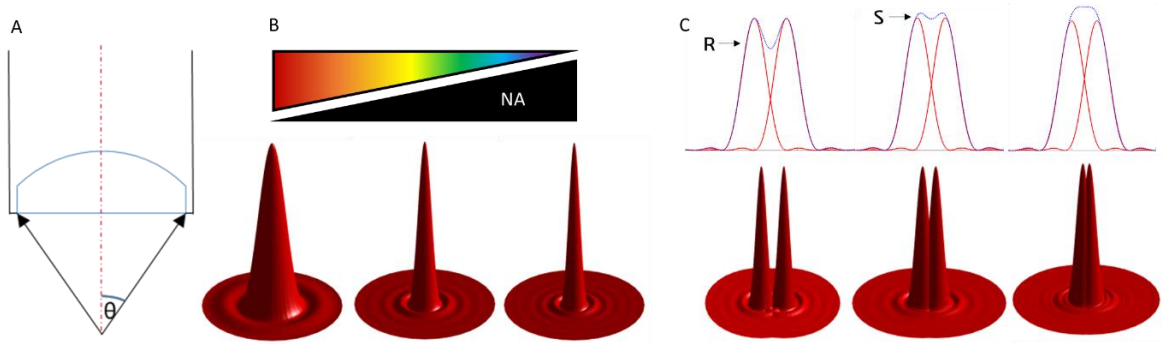

Figure 7: Point spread function and numerical aperture.
(**A**) The numerical aperture of a lens is defined by the refractive index of the immersing medium and the collection half angle θ. (**B**) The point spread function as a function of NA and wavelength (λ), as λ increases the PSF width increases, as NA increases the PSF width decreases.(**C**) PSFs of point sources and decreasing separation. R = Rayleigh criterion, S = Sparrow criterion.

The PSF extends in 3 dimensions therefore it is also necessary to define the axial resolution which is generally worse than the lateral resolution. The equation determining the axial resolution as given by Born and Wolf (Born *et al.*, 1999), defining the distance between the centre and the first minimum of the PSF (therefore satisfying the Rayleigh criterion), is as follows.

$$\mathrm{d_z} = \frac{2\lambda \mathrm{n}}{\mathrm{NA}^2}$$

Equation 9

In multiphoton microscopy it may appear that the resolution would be ~2 times worse than the single photon case due to the wavelengths used being about twice as long. However, this is not strictly the case. In multiphoton microscopy because signal is only generated in the tightly focussed excitation volume it is useful to know the multiphoton PSF which can be calculated as the illumination PSF squared (Zipfel, Williams and Webb, 2003). This can be used to help indicate the resolution. As the volume from which signal is being generated is defined by the excitation volume, the excitation wavelength is used when calculating the PSF.

$$\omega_{xy} = \begin{cases} \dfrac{0.320\lambda}{\sqrt{2}NA} NA \leq 0.7 \\ \dfrac{0.325\lambda}{\sqrt{2}NA^{0.91}} NA \geq 0 \cdot 7 \end{cases} \qquad \omega_z = \frac{0 \cdot 532\lambda}{\sqrt{2}} \left[\frac{1}{n - \sqrt{n^2 - NA^2}}\right]$$

Equations 10/11

The above framework was developed for TPEF which is an incoherent process having isotropic emission whereas coherent processes such as SHG have a directional emission profile (Zipfel *et al.*, 2003). Thus, calculation of the multiphoton excitation volume can only give an approximation to the resolution of a coherent imaging system, which will in general be slightly worse (Pawley, 2006).

2.3.1 The effect of sampling and pixilation

The absolute limit of resolution as stated by Abbe assumes that the PSF is smooth and defined by an infinite number of samples. In reality, this is not achievable and an image in instead captured by a finite number of receivers, be they photoreceptive cells in the human eye or pixels in a digitised image. According to the Nyquist-Shannon sampling theorem, to faithfully reproduce a signal without aliasing, the original signal must be sampled with at least twice the frequency of this highest frequency component (Burger and Burge, 2009). In the case of digitally-recorded microscopy, this means that the effective pixel size should be less than half of the expected resolution. In a camera detector chip, the receiver is of a finite size, with a typical physical pixel size being in the range of ~5-20 µm for a scientific complimentary metal oxide semiconductor (sCMOS) or charge coupled device (CCD). For an example high numerical aperture objective of 63x magnification and 1.2NA imaging at 500 nm the diffraction-limited resolution according to Abbe is 500 nm/2.4 = 208 nm. As can be seen, this is significantly smaller than the pixel size of the camera and therefore to be faithfully recorded the image must be magnified. For a 5 µm pixel size the 63x magnification of the objective makes the effective pixel size ~79 nm, meaning each PSF is sampled by ~2.6 pixels therefore satisfying Nyquist-Shannon sampling. If the magnification afforded by the objective is not sufficient to achieve sufficient sampling additional lenses may be added to the imaging path to reduce the effective pixel size. However, increasing magnification will not increase resolution indefinitely. Once adequate sampling is achieved, i.e. >2 pixels per PSF, additional magnification will be “empty”, creating a larger image without increased resolution.

In the case of point scanning systems, an image is formed not on a camera chip, with all point images simultaneously, but by scanning the laser focus across the sample and allocating the recorded intensity at a given point to a digital (not physical) pixel. The maximum area of the sample that can be imaged is defined by the objective’s field of view, any size area up to and including this area can be imaged by adjusting the range of angles covered by the beam-scanning mirrors. As such, sufficient sampling can be achieved in two ways: For a sample area of a fixed size the distance between each scan-point can be set such that each PSF is sampled by at least 2 scan-points and therefore, pixels. Or for a fixed number of pixels in the final image, e.g. 1024 x 1024, the area of the sample imaged can be set such that there are >2 pixels per PSF.

In techniques that involve labelling, the requirement for sufficient sampling should also be considered during the labelling process. To accurately image a structure at a given resolution, the labels should be spaced at least twice as close as the expected resolution (Long, Robinson and Zhong, 2014). This can become a limiting factor when applying certain super-resolution techniques (see below) that have resolutions of ~20 nm to immuno-labelled samples, as the complex of a primary and secondary antibody has dimensions of a similar size (Sahl, Hell and Jakobs, 2017).

2.3.2 Ideal samples for characterising resolution

When developing new microscopy methods and evaluating their resolution it is necessary to use suitable samples. Ideally, such a sample is of a defined and consistent size such that any variation between images of the sample can be concluded to be due to variations in the imaging system and not the sample. The structure and dimensions of an ideal sample should also be verifiable via other high-resolution imaging techniques to confirm sizes measured using the new technique and/or reported in the literature. When used to evaluate a new super-resolution method, the resolution sample should also have features that are not resolvable under diffraction-limited conditions but are near to the expected limit of resolution of the super-resolution method.

When evaluating the resolution of a microscopy system it is common to image a sub-diffraction-limited size object. This results in an image of the point spread function being recorded, the FWHM of the PSF is often used as an indicator of the resolution of the system. This is readily achieved for fluorescence-based imaging techniques using sub-diffraction-limited fluorescent beads or quantum dots. This method also has the advantage of helping to identify aberrations in the imaging system as these can often be observed as deviations in recorded PSF from the ideal PSF. For imaging modalities based on other contrast mechanisms such as SHG used in this thesis, other sub-diffraction-limited size objects that are SHG-active such as barium titanate nano crystals can be used (Liu *et al.*, 2014). As the resolution is often defined as the minimum distance at which two-objects can be resolved with sufficient contrast, samples that allow this measurement to be made are also very useful. A common example is two slits separated by a distance smaller than the diffraction limit (You, Kuang and Zhang, 2016). However, as slits are not typically fluorescent, samples made of fluorescent strips such as PSF check (https://www.psfcheck.com/psfcheck-slides), have been developed.

“Nano rulers“ made of two fluorescent molecules bound to a DNA-based separator of a defined length have also been developed for the same purpose

(https://www.gattaquant.com/products/nanoruler.html) . However, to date an SHG-active equivalent does not exist. The examples above are useful for characterising the resolution under ideal imaging conditions. However, to evaluate the resolution within a biological sample, where variations in refractive index, sample thickness and other sources of aberration can cause a deterioration in resolution from the ideal case, biological resolution samples are required.

Certain structures have been identified within biological samples that satisfy the requirements of an ideal resolution sample, and these are now regularly used to evaluate the resolution of new microscopy methods, including super-resolution methods. One common example is the nuclear pore complex (NPC) (Sahl, Hell and Jakobs, 2017). The NPC is made of 8 gp120 subunits that arrange in a circle with 8 fold symmetry (Löschberger *et al.*, 2014). The central channel of the NPC has a diameter of ~40 nm. Because the gp210 subunits can be fluorescently labelled, the ability to resolve individual sub-units serves as a good biological standard to evaluate resolution. Unfortunately, due to a lack of SHG active labels this would not work well as a method of evaluating the resolution in an SHG based imaging system.

Other commonly-used biological resolution standards include components of the cytoskeleton, specifically microtubules and fibrillar actin. Both of these components form fibrillar structures with widths below the diffraction limit; individual actin monomers form strands, which in turn form filaments with a width of ~7.7 nm (Fowler and Aebi, 1983), and an individual microtubule has a width of ~25 nm (Moores, 2008). Both values have been determined by transmission electron microscopy and are well below the diffraction limit. As such they can be used in a similar fashion to sub-resolution beads or strips, to determine the resolution via measurement of the PSF. Both proteins also readily form bundles of multiple filaments, introducing variability to the true width of structures, thus, it is useful to find situations where the organisation of these filaments is also well defined. An example of this is the organisation of microtubules within centrioles.

Amongst their roles, centrioles nucleate the formation of cilia and flagella and can be found at the core of the centrosome. They are involved in the organisation and separation of chromosomes during cell division. The microtubules arrange as triplet microtubules with a 9 fold rotational symmetry (Winey and O'Toole, 2014). Alpha and beta tubulin (the building blocks of microtubules) can be fluorescently labelled and the defined microtubule organisation makes centrioles useful for super-resolution fluorescence microscopy (Fu and Zhang, 2019). Microtubules have also been shown to be SHG active and therefore the centriole could serve as a good sample to evaluate the resolution of new super-resolution SHG methods. However, it has been reported that microtubules lose their second harmonic activity upon fixation (Van

Steenbergen *et al.*, 2019), thus, measurements could only be made in live cells. Furthermore, most eukaryotic cells only have one centriole making it difficult to locate within the cell and with the correct orientation. Cells with cilia/flagella may have a greater number of centrioles but will most likely be moving whilst live, as fixation removes SHG activity, this becomes a complex measurement. Due to these difficulties, the development and characterisation of biological samples suitable for super-resolution imaging, particularly for multiphoton modalities, represents an important field that warrants it's own independent research.

2.4 Super-resolution

For much of 20th century, the diffraction limit was perceived to be a hard limit to the resolution of optical microscopy. However, in the last 20 years significant advances have been made in overcoming this limit giving rise to a plethora of “super-resolution” (SR) techniques. The majority of super-resolution techniques are based on fluorescence microscopy, with the 2014 Nobel Prize in Chemistry being awarded “for the development of super-resolved fluorescence microscopy.”(*The Nobel Prize in Chemistry*, 2014). Broadly, SR techniques can be placed into 3 groups: Optical bandwidth expansion, post recovery of optical bandwidth and point spread function engineering, each having their own advantages and disadvantages. Point spread function engineering aims to decrease the size of the effective point spread function below the classical diffraction limit. Optical bandwidth expansion improves resolution by increasing the range of spatial frequencies that are collected, often via structured illumination or very high numerical aperture (NA) lenses (exploiting the proportionality between NA and resolution) . Finally, post recovery techniques use large numbers of images to reconstruct an image of higher spatial resolution.

2.4.1 Optical Bandwidth Expansion

In this section, two methods based on structured illumination and solid immersion lens approaches to achieve super-resolution by optical bandwidth expansion are described.

2.4.1.1 Structured Illumination

The most common optical bandwidth expansion technique is Structured Illumination Microscopy (SIM). To understand SIM a brief introduction to Fourier optics is required. The Fourier transform of a signal represents the information as a series of sine waves and their corresponding coefficients. Thus, the information in a signal (for our case, an image) is represented as information ranging from low to high spatial frequencies. In a Fourier transformed image lower spatial frequencies are found at the centre and increasingly higher spatial frequencies at increasing distance from the centre (Figure 8).

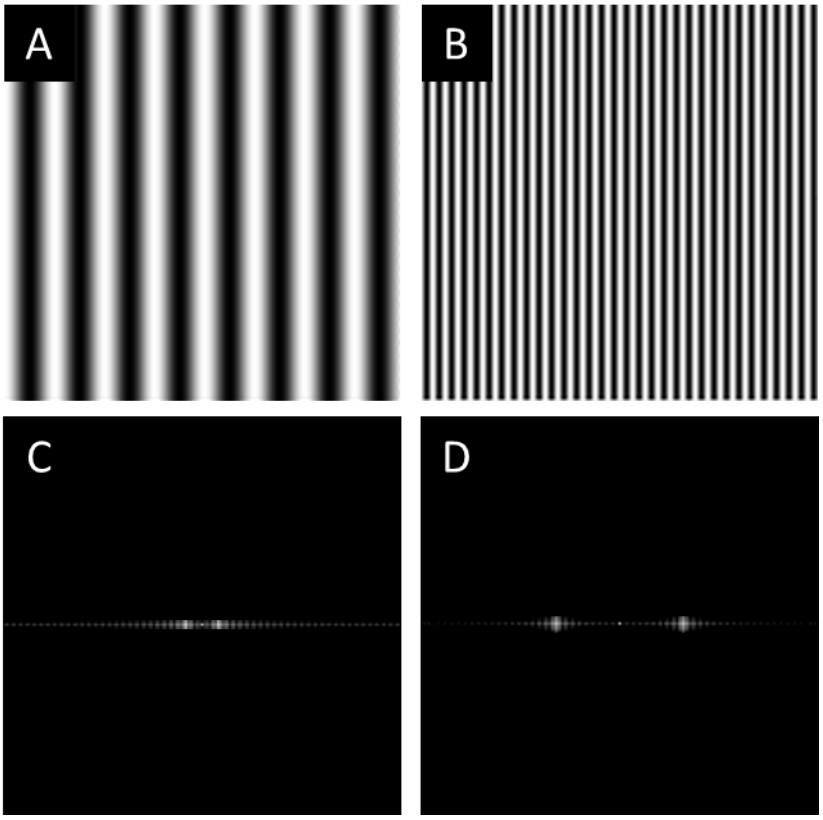

Figure 8: The Fourier transform displays spatial frequencies.
Images of sinusoidally oscillating intensity of low frequency (**A**) and high frequency (**B**). Fourier transforms of these images show that lower frequencies appear closer to the centre (**C**), whilst higher frequencies appear further from the centre (**D**)

This can be attributed to the way an image is captured by a lens; features of low spatial frequency cause light to diffract by small amounts and are focused by the lens near its central axis, therefore

appearing near the centre in Fourier space. Features of higher spatial frequency diffract to wider angles and are focused by the objective to regions distant from the lens central axis. This is reflected by the proportionality between the objective collection angle and resolution. In this way, it can be seen that the resolution of a system i.e. the highest spatial frequencies that can be detected, can also be expressed by how large the observable region in Fourier space is. Features falling outside of this observable region are too small to resolve.

Structured illumination microscopy (SIM) overcomes the diffraction limit by exploiting the concept of Moiré fringes. When two patterns of fine detail are super imposed, a third (beat) pattern becomes observable, this pattern is of lower frequency than the two overlapping patterns and as such is easily resolvable by the imaging system. In SIM the sample (pattern 1) is illuminated with sinusoidally varying intensity (pattern 2) (Figure 9**A**). The observed pattern (pattern 3) is a convolution of pattern one and pattern two, containing high frequency information from both the structured illumination pattern and the sample. By deconvolving the two, it is possible to retrieve high frequency information from the sample that would not otherwise be resolvable. In Fourier space, this can be seen as an effective expansion of the observable region to include regions further from the centre, and therefore containing higher spatial frequencies (Figure 9**C**). By taking multiple images with the illumination pattern shifted both in phase and orientation it is possible to reconstruct a super-resolved image (Figure 9**D/E**). It has also been shown that rather than a sinusoidal illumination pattern unknown speckle patterns may be used for excitation in a method termed blind-SIM (Mudry *et al.*, 2012). Use of speckle pattern illumination removes the requirement of precise knowledge of the illumination pattern. This decreases the sensitivity of SIM imaging to misalignment, at the cost of an increased number of frames needed for SR reconstruction.

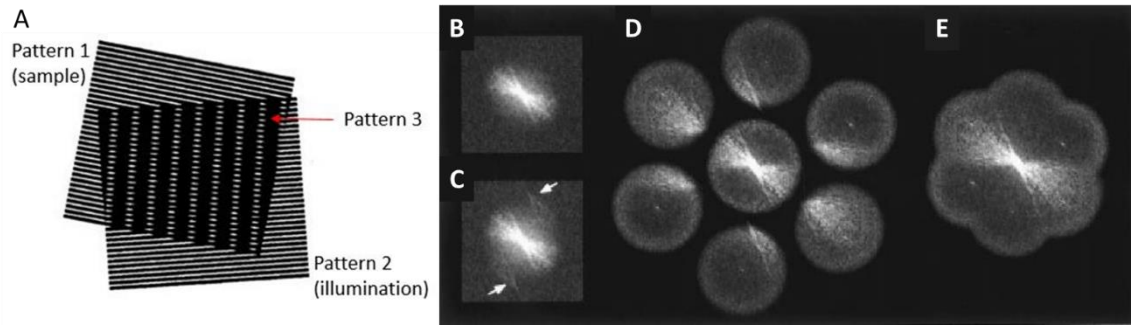

Figure 9: Structured illumination microscopy
A) The superposition to the sample pattern and the illumination pattern create a 3rd beat pattern (Moiré fringes). (B) The Fourier transform of an image taken using conventional illumination and structured illumination (C), The rrows highlight high spatial frequency information that has been shifted into the collection band of the microscope. (D) Information components computationally separated from the interference image, these can be reassigned to their true locations (E) before being inverse transformed to a final image. Adapted with permission from (Gustafsson, 2000).

The resolution improvement in SIM (in general) has a limit of a factor of two; this limit of improvement in resolution has been experimentally achieved in both 2 (xy) (Gustafsson, 2000) and 3 (xyz) (Gustafsson *et al.*, 2008) dimensions. This limit can be overcome by decoupling the pattern generation from the detection objective, instead generating an interference pattern for illumination using a high refractive index waveguide (Helle *et al.*, 2020) or a pair of mirrors (Joseph *et al.*, 2020) and has been employed to achieve super-resolution over a large FOV using a low NA objective. By exploiting a non-linear relationship between the illumination intensity and fluorophore emission it is also possible to improve the resolution by a factor greater than 2, such is the case for saturated SIM (SSIM). The resolution of SSIM is theoretically unlimited however practical constraints such as photobleaching and signal to noise ratio limit improvement. As a pioneer group in SIM, the Gustafsson lab were able to demonstrate a resolution of <50 nm in a fluorescent bead sample using SSIM (Gustafsson, 2005). Although (in general) the improvement in resolution is limited, SIM is fast and gentle enough to easily facilitate live cell imaging (Shao *et al.*, 2011), due to the relatively low number of diffraction-limited frames required to generate a super-resolved image.

2.4.1.2 Solid Immersion Lenses

Solid immersion lenses (SIL) improve the resolution of the system by using a hemispherical or "superhemispherical" (Weierstrass) lens of high refractive index (up to n=3.5) (Mansfield and Kino, 1990) placed on the surface of the sample to in addition to a standard objective. The hemispherical SIL has a height of h = r, where r is the radius of the complete sphere. The superhemispherical SIL has a height of $h = r(1+^{n-}1)$ (Figure 10). Addition of the SIL increases the effective NA of the system. In the case of a hemispherical SIL the collection half angle is now 90° (sin90 = 1) and therefore its NA is defined only by its refractive index. This makes the effective NA of the optical system the product of the coupling objective NA and the refractive index of the SIL. In the case of the Weierstrass lens the maximum achievable NA is the product of the coupling objective NA and the square of the SIL refractive index (Wu, Ghislain and Elings, 2000). Practically it is easier to work using hemispherical SILs as they are easier to fabricate and suffer less longitudinal chromatic aberration (Born *et al.*, 1999). SILs have been combined with fluorescence microscopy to achieve resolutions of ~λ/3.5, this has been taken further and combined with other super-resolution fluorescence modalities to achieve resolutions a small as 34 nm in combination with STED (Kim *et al.*, 2017) and 12 nm in combination with STORM (Wang *et al.*, 2019).

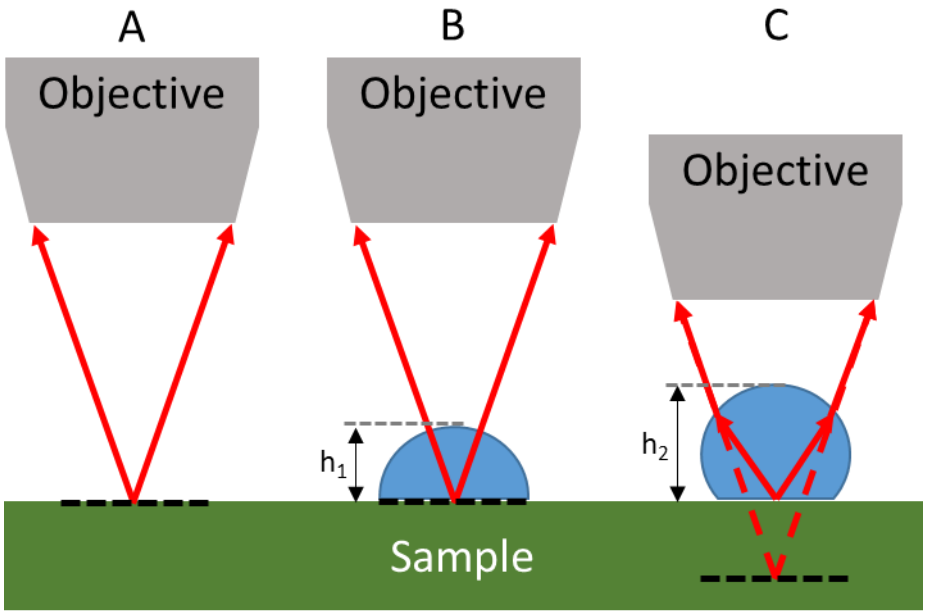

Figure 10: Schematic of solid imaging with solid immersion lenses.
A) Usual imaging configuration without a SIL red lines represent the widest angles of light collected by the objective. Black dashed line indicates the imaging plane. B) Imaging using a hemispherical SIL of height h_1, C) imaging using a superhemispherical SIL of height h_2.

2.4.2 Post Recovery of Optical Bandwidth

This section covers single molecule localisation techniques and fluctuations-based techniques. Both methods use temporally separated signals to mathematically recover optical bandwidth post-acquisition.

2.4.2.1 Single Molecule Localisation

In Single Molecule Localisation Microscopy (SMLM) spatially overlapping PSFs are separated in time by taking a series of images of a sample where each frame contains only a few sparsely activated fluorophores. Mathematical fitting of the centroid of each PSF gives the most likely location of the fluorophore. All fluorophore locations are then used to generate a single super-resolved image (Figure 11).

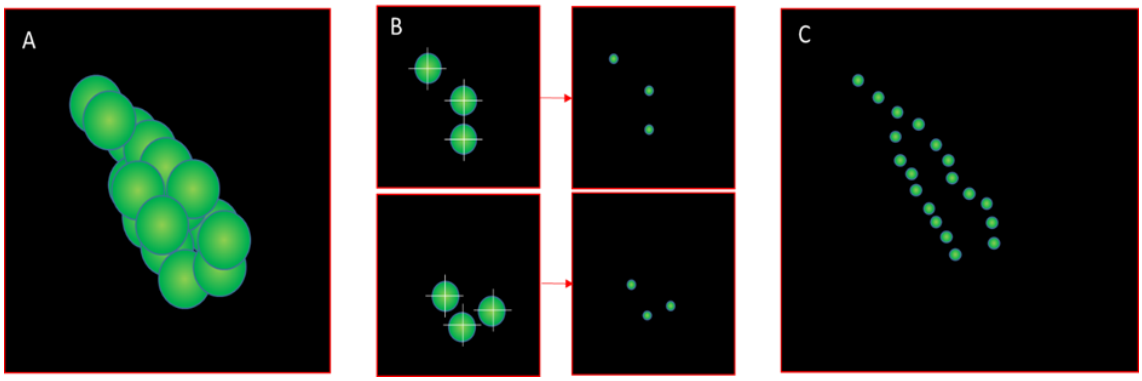

Figure 11: Single Molecule Localisation.
(A) wide field image showing multiple overlapping fluorophores that aren't resolvable. (B): Single frames showing subsets of sparsely activated fluorophores, [Gaussian] fitting of the activated fluorophores improves the resolution. (C): Summation of the fitted frames generates a super-resolved image.

Sparse activation of fluorophores can be achieved using photo switchable dyes (Rust, Bates and Zhuang, 2006) or proteins (Betzig *et al.*, 2006). They can be selectively activated or forced into a dark state using a combination of light pulses of different wavelengths and intensities. Using these methods, resolutions of ~20 nm can be achieved (Van De Linde *et al.*, 2011). The impressive resolutions reported in SMLM come at a cost. Specialist photo-switchable dyes or proteins such as EosFP or Dronpa (Chozinski, Gagnon and Vaughan, 2014), or harsh environments that encourage fluorescence blinking are often required (Van De Linde *et al.*, 2011). Acquisition of thousands of frames is also needed, decreasing temporal resolution and limiting application. This can be improved using multi-emitter fitting algorithms and decreasing the imaged FOV (Huang *et al.*, 2013). Throughput can be improved using waveguide illumination and a low magnification, large FOV detection objective (Diekmann *et al.*, 2017). Despite these improvements SMLM experiments

are limited in their applicability to live cell imaging where movement and phototoxicity become issues.

2.4.2.2 Fluctuations based Super Resolution Microscopy

To overcome the issues of SMLM a new generation of techniques that do not rely on localising isolated emitters but on the statistical independence of fluctuations in fluorescence emission to achieve super-resolution. Each of these techniques differs in the computational method of achieving super-resolution but all require the acquisition of a temporal image stack containing temporally fluctuating signals, like that in traditional SMLM (Figure 12). However, fluctuation-based methods require fewer frames (50-1000), do not need strict on/off emitted states and work with higher emitter density (Opstad *et al.*, 2020). Additionally many of these methods have been demonstrated using conventional fluorophores such as GFP (Cox *et al.*, 2012; Gustafsson *et al.*, 2016), removing the need for specialised labelling protocols. Resolutions as good as 49 nm have been demonstrated using these techniques, bringing them close to the resolution of established SMLM methods without many of the drawbacks.

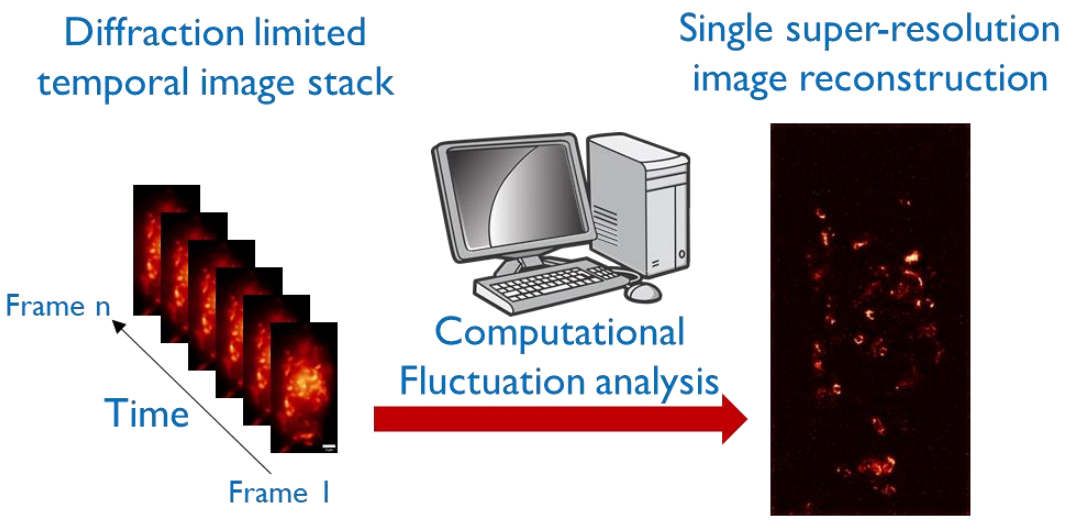

Figure 12: Fluctuations based Super-resolution
These microscopy techniques use computational analysis of statistically independent emissions over time to localise emitters and produce a super-resolution image.

However, care must be taken when using these techniques, as it is possible that the localisation algorithms will lead to the introduction of image artefacts. As the field is in its relative infancy "ground truth" verification of the structures using an established high-resolution technique is often required. The propensity for artefacts has also led to the development of programs such as SQUIRREL (Culley *et al.*, 2018) to identify locations in a super-resolution image reconstruction that are most likely to contain these artefacts.

Key examples of these techniques include: Entropy based super-resolution imaging (ESI), Super-resolution optical fluctuation imaging (SOFI), Super-resolution imaging with autocorrelation two-step deconvolution (SACD), Super-resolution radial fluctuations (SRRF), Bayesian analysis of blinking and bleaching (3B) and Multiple signal classification algorithm (MUSICAL).

Entropy based super-resolution imaging (ESI) (Yahiatene *et al.*, 2015) calculates the entropy at each pixel and uses higher-order moments (which characterise different properties of the temporal intensity distribution of each pixel) to narrow the effective PSF by $\sqrt{n}$ where n is the order of the moment. Resolutions of 130 nm (separation distance) using 5000 original frames, and 136 nm (PSF FWHM) with only 1000 initial frames have been achieved with ESI. ESI has been demonstrated to be able to use bleaching of a fluorophore as the source of entropy for resolution improvement, improving the applicability to a wider range of fluorophores. The resolution improvement is determined by the order of the moment used in ESI, to achieve higher resolutions an iterative process is used. As a result of this to achieve highest resolution image stacks of thousands of frames are required.

Another technique that uses an iterative process to improve resolution is Super-resolution optical fluctuation imaging (SOFI) (Dertinger *et al.*, 2009). SOFI calculates the autocorrelation function for the temporally varying signal at each pixel, that is, the similarity in the signal detected at a given pixel over time. The SOFI intensity value assigned to each SR pixel is given by the integral of the temporally varying signal (the total recorded intensity), over the correlation function. The correlation function can be calculated for increasing orders, for the n^{th} order function, it is proportional to the point spread function (PSF) to the power n and thus the resolution can be improved iteratively by a factor of $\sqrt{n}$ where n is the SOFI order. Using SOFI, a resolution of 55 nm (PSF FWHM) has been achieved using 2000 raw frames calculating the 25^{th} SOFI order. Because SOFI decreases the size of the PSF in all 3 dimensions it is possible to achieve 3D super-resolution. To this end SOFI has been applied to 3D imaging to achieve an axial resolution of ~500 nm (0.8 times the diffraction-limited resolution) (Chen *et al.*, 2016). It has also been shown that resolutions of 85 nm can be achieved with as few as 300 frames. This is done by multiplexing spectrally different dyes and collecting 100 frame image stacks in each colour, the decrease in effective labelling density improves the performance of SOFI (Zeng *et al.*, 2015).

Super-resolution imaging with autocorrelation two-step deconvolution (SACD) (Zhao *et al.*, 2018) operates in a similar manner to SOFI, calculating signal autocorrelation but

implementing a deconvolution step before and after the autocorrelation analysis. This has the advantage that it decreases the number of raw frames required to achieve super-resolution by calculating signal correlations between different combinations of images in the stack. Using this approach as few as 16 frames are required for resolutions of 64 nm. It has been shown that the fluctuations required for ESI and SOFI can be created by the illumination rather than intrinsic fluctuations. Speckle patterns (Kim *et al.*, 2015) and waveguide interference patterns (Diekmann *et al.*, 2017) have both been used effectively to this end for SOFI and ESI respectively

Bayesian analysis of blinking and bleaching (3B) (Cox *et al.*, 2012) models the entire dataset and uses the analysis of bleaching and blinking events to calculate the most probable location of each fluorophore. This technique has demonstrated 50 nm resolutions (peak separation) using 200 frames. 3B is computationally intensive taking prohibitively long times create super-resolution for FOVs > 5μm^2.

Super-resolution radial fluctuations (SRRF) (Gustafsson *et al.*, 2016) uses the radial symmetry of fluorescence emission to calculate local gradient convergence (radiality) on a sub-pixel basis and analyses this over the temporal stack. Single static fluorophores result in a continuous peak with a reduced full width half maximum (FWHM) relative to the diffraction-limited image. This technique has been demonstrated to achieve resolutions of 49 nm with as few as 100 raw frames. This requirement for only a low number of frames, combined with rapid data processing via GPU optimisation of the algorithm have led to high popularity of SRRF. It has been used to image protein localisation in bacterial membranes (Weihs *et al.*, 2018) and cardiomyocytes (Correll *et al.*, 2017). It has even been integrated with Andor's iXon camera to achieve full FOV super resolution at > 10 frames per second (andor.oxinst.com/products/srrf-stream).

Multiple signal classification algorithm (MUSICAL)(Agarwal and Macháň, 2016) uses a sliding soft window to calculate eigen-images and associated singular values of the temporal stack. The eigen-images are the base set of images required to recreate any of the images observed in the stack through their combination. Each eigen-image represents an underlying pattern present in the image stack. By selecting a threshold eigen-images representing signal and noise are separated. Projections of the PSF at test points on a subpixel grid of the eigen-images are then determined and the values returned from these test points are entered into an indicator function which is very large at the location of an emitter and small otherwise. The sliding windows are then stitched together to create a single SR image. Resolutions of 50 nm

(PSF FWHM) have been shown using as few as 49 raw frames making MUSICAL one of the highest performing fluctuations-based methods.

Although not strictly a fluctuations based technique the use of Haar wavelet kernel (HAWK) analysis allows super resolution imaging using high emitted density data sets (Marsh *et al.*, 2018). This is achieved by a pre-processing step that produces a data set of many more frames with a lower emitter density. Common SMLM fitting algorithms such as thunderStorm can then be used to create the super-resolution image. Using this method resolutions of ~70 nm (Fourier ring correlation) were demonstrated for 400 raw frames.

As the pixel intensity of many of the computational super-resolution techniques is the result of an algorithm designed to improve resolution, the intensity often cannot be related to the initial emitter concentration, and therefore the initial target concentration. Thus, when using these methods, one should not make inferences about emitter concentration from pixel intensity. Furthermore, due to the computational processing often involving assumptions about the images being processed there is the possibility of artefacts. Therefore, when interpreting results obtained using one of these methods it is important to consider the effect these might have. Despite these limitations, fluctuations based imaging is an exciting super-resolution field that has shown promising results whilst is still in its relative infancy.

2.4.3 Point Spread Function Engineering

Point spread function (PSF) engineering, sometimes referred to as focus engineering, concentrates on manipulating the excitation volume to be smaller than the diffraction-limited PSF. This is achieved using specialist focussing schemes or beam combinations that reduce the effective excitation volume.

2.4.3.1 Stimulated Emission Depletion Microscopy

STimulated Emission Depletion (STED) microscopy proposed and implemented by Hell and Wichmann (Hell and Wichmann, 1994) uses a combination of two laser beams to achieve resolutions as small as 20 nm (Donnert *et al.*, 2006). A conventional Gaussian beam excites a diffraction-limited PSF then a second doughnut shaped beam, drives stimulated emission from the fluorophores around the edge of the Gaussian PSF. This results in an effective PSF smaller than the diffraction limit (Figure 13). The size of the effective PSF has no theoretical minimum provided there is infinite potential laser power available for driving stimulated emission (Westphal and Hell, 2005). The higher laser powers required in STED microscopy (1-200 MW/cm^2) (Sahl, Hell and Jakobs, 2017) when compared to confocal fluorescence (1-100 kW/cm^2) (Jemielita *et al.*, 2013) can result in a much higher rate of photobleaching, and the chances of cell phototoxicity are increased (Wäldchen *et al.*, 2015). However, STED has been implemented with common labels such as GFP (Katrin I. Willig *et al.*, 2006) and live cell imaging has been successfully accomplished (Valentin Nagerl *et al.*, 2008). In a similar technique called REversible Saturable OpticaL Fluorescence Transitions (RESOLFT) it is now possible to use far lower laser powers ($4.4W/cm^2$) by switching suitable fluorophores into a dark state rather than stimulating emission. (Hofmann *et al.*, 2005). STED has been applied to fields such as cell biology (Eggeling *et al.*, 2009) and neuroscience (Katrin I Willig *et al.*, 2006; Korobova and Svitkina, 2010). STED microscopy has the same key limitation as SMLM techniques. To achieve super-resolution there is a reliance on manipulating fluorescence emission to achieve super-resolution, the stimulated emission process involves driving electrons from a real, excited state to an unexcited state at a wavelength separate to the detection wavelength. During SHG, the electrons are only excited to a virtual excited state and emission is instantaneous, therefore it is not possible to drive stimulated emission. The process of subtractive or dark beam imaging uses a method similar to STED and can be used with SHG, this is covered in chapter2.5.3.

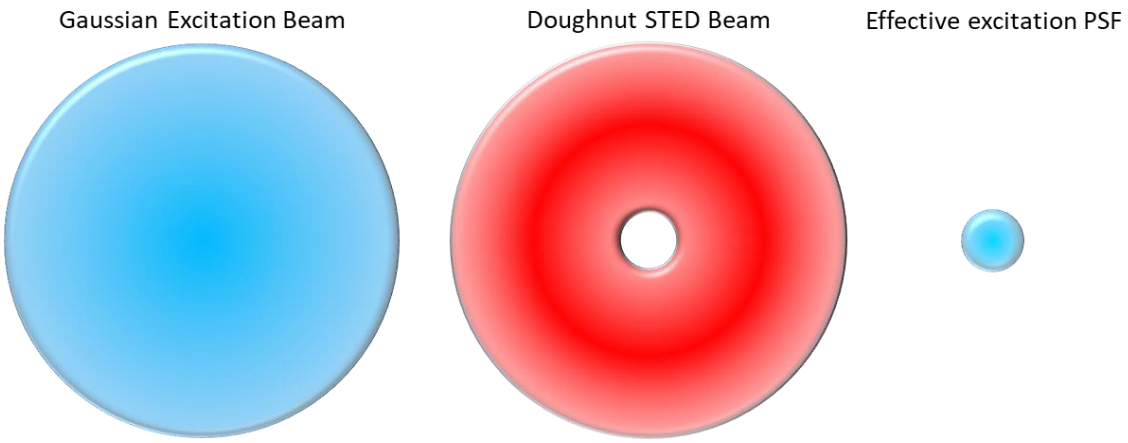

Figure 13: Beam profiles used in STED.
The Gaussian beam excites a diffraction-limited PSF, the hollow STED beam forces stimulated emission from the fluorophores within the volume of the torus. Emission only occurs from the fluorophores at the centre of the excitation PSF which corresponds to a sub-diffraction-limited volume.

2.5 Label-Free Super-Resolution

Of those super-resolution techniques that have been reviewed thus far, the majority and best established rely on fluorescent labels to achieve super resolution. Stochastic techniques require temporal manipulation of fluorophore emission to achieve super-resolution, a phenomenon not yet exploitable for the light emitted in many label-free modalities. STED and RESOLFT also use the properties of fluorophores to create an excitation volume smaller than the diffraction limit. This leaves the question: are there any super-resolution methods that are applicable to nonlinear label-free microscopy?

2.5.1 Structured Illumination Microscopy

As structured illumination microscopy doesn't rely on exploiting properties of fluorescence but instead on patterning the illumination it is amenable to label-free imaging. A common example is differential interference contrast (DIC) SIM (Chen *et al.*, 2013)). Multiphoton label-free SIM imaging has been practically realised by Chia-Hua Yeh *et al.* (Yeh *et al.*, 2018) in a technique called fringe scanning SHG microscopy (FS-SHGM). Here the laser scan pattern is modified such that scanned rows are not adjacent to each other but are instead separated by rows that are not illuminated. This "quasi-comb" scanning creates an intensity modulation of 0 to 1 between the illuminated and non-illuminated rows. The images of all scanned rows are integrated into a single frame of the camera which replaces the traditional point detectors of conventional SHG microscopy. By varying the phase and orientation of the quasi-comb scan and subsequently deconvolving and reassigning the images as in traditional SIM, a lateral resolution improvement of 1.4x, and due to the optional sectioning effect of SIM (Wilson, 2011; Dan, Yao and Lei, 2014) an axial improvement of 1.56x was achieved.

Another SIM based method, first implemented with TPEF by Urban *et al*. (Urban *et al.*, 2015) and subsequently applied to SHG (Urban *et al.*, 2018) uses an electro optic modulator (EOM) to sinusoidally modulate the intensity of the illumination beam. The modulation is synchronised with the scan pattern such that the sample is illuminated with a sinusoidally varied intensity pattern. Similar to the work by Yeh *et al* (Yeh *et al.*, 2018) all scan points for a single illumination pattern are integrated into a single frame of the camera. As with traditional SIM, images are acquired at 3 pattern orientations and 3 pattern phases for a total of 9 diffraction-limited images to form a single super-resolution image. For label-free SHG the authors report a 1.59 fold improvement in lateral resolution when imaging nanowires and demonstrate super-resolution imaging at depths of up to 80 µm.

Huttunen *et al.* (Huttunen *et al.*, 2017) theoretically proposed a label-free SIM implementation in which the phase of the illumination field is modulated rather than the intensity and the emitted signal is measured interferometrically. In the proposed scheme the excitation beam is split into an object and a reference arm. The object arm is projected onto a spatial light modulator (SLM) and the 1st diffraction order imaged onto the sample using a high-NA objective. The SHG signal is collected using a second high-NA objective and imaged onto the camera. The reference arm is passed through a nonlinear crystal to generate second harmonic light, this is passed through a delay line that allows shifting of the phase difference between the object and reference arm before being recombined with the SHG signal and imaged onto the camera chip. The authors calculate an up to 4 fold improvement in resolution due to both the frequency doubling of SHG and the resolution doubling due to the structured illumination. This is improved to 6 fold for third harmonic generation (THG). Some key limitations to this technique are readily apparent. Due to the widefield nature of the illumination, a high powered (amplified) laser system would be needed to achieve suitable power at the sample for SHG. This is further exacerbated by the fact that a significant proportion of the beam power is lost in the 0 order diffraction from the SLM. Secondly, interferometric detection with a frequency doubled beam would be highly sensitive to misalignments that could easily confound imaging data. It is most likely for these reasons that a practical realisation of this coherent SIM imaging is yet to happen, despite the attractive possibility of an increase in resolution.

2.5.2 Image Scanning Microscopy

It is often overlooked that the first technique able to provide resolution better than the diffraction limit was confocal microscopy; it is capable of improving resolution by a factor of $\sqrt{2}$ with an infinitely small pinhole (Sheppard and Wilson, 1978). Unfortunately, this has the effect of excluding most of the signal. Thus, practically, signal to noise limitations often lead researchers to use a pin hole size of one Airy unit (AU), resulting in diffraction-limited resolution. Sheppard proposed a solution to this problem (Sheppard, 1988), in which the pinhole is removed and an image is recorded on a camera for each position of the excitation spot. The images are then processed using a Fourier filter, pixel intensities re-assigned, and the appropriate magnification applied in post processing to generate a single super-resolved image of twice the resolution. This was practically realised by Muller and Enderlein (Muller and Enderlein, 2010) significantly later in a technique called image scanning microscopy (ISM). The major drawback of ISM is the significant number of images required to generate a final SR image, and the relatively long exposure times required by a camera compared to a point detector (ms vs µs). Some of these draw backs can be

overcome by scanning multiple excitation spots using a deformable mirror or spinning disk excitation scheme (York *et al.*, 2012; Schulz *et al.*, 2013).

To further improve imaging speed, an all optical solution was implemented 3 years later by De Luca *et al.* (De Luca *et al.*, 2013), termed re-scan microscopy. The emission light is "re-scanned" onto the camera chip at 2x the excitation scan angle automatically reassigning pixel intensity. A similar solution called optical photon reassignment microscopy (OPRA) was also implemented by Roth *et al*. (Roth *et al.*, 2013). Here, no extra re-scan mirror is needed but instead intermediate beam expansion between de-scanning and subsequent rescanning using the same scanner is used for photon reassignment. This optical setup also has the advantage that a resonant scan mirror can be used as it does not need to be synchronised with a second mirror pair, significantly improving imaging speed. The ability to nearly double the resolution of a laser scanning microscope opens the opportunity to achieve SR with multiphoton label-free modalities. This has recently been achieved by Gregor et al with a lateral resolution of 151 nm (Gregor *et al.*, 2017). Barlow *et al.* (Barlow *et al.*, 2020) demonstrated SHG imaging with a resolution of 149 nm, 1.7x better than diffraction-limited imaging. They used a Zeiss Airy scan detector; a commercially available implementation of ISM, that uses a specially designed PMT array instead of a camera.

2.5.3 Subtractive imaging

Switching Laser Mode (SLAM) microscopy also called 'dark beam imaging' (Dehez, Piché and De Koninck, 2013) is a technique that uses an azimuthally polarised TE_{01} laser beam to improve resolution. In 2013, Dehez *et al.* (Dehez, Piché and De Koninck, 2013) explored this both theoretically and experimentally on three different imaging devices. A confocal reflectance microscope, a confocal fluorescence microscope and a two-photon fluorescence microscope (Zeiss LSM 510).

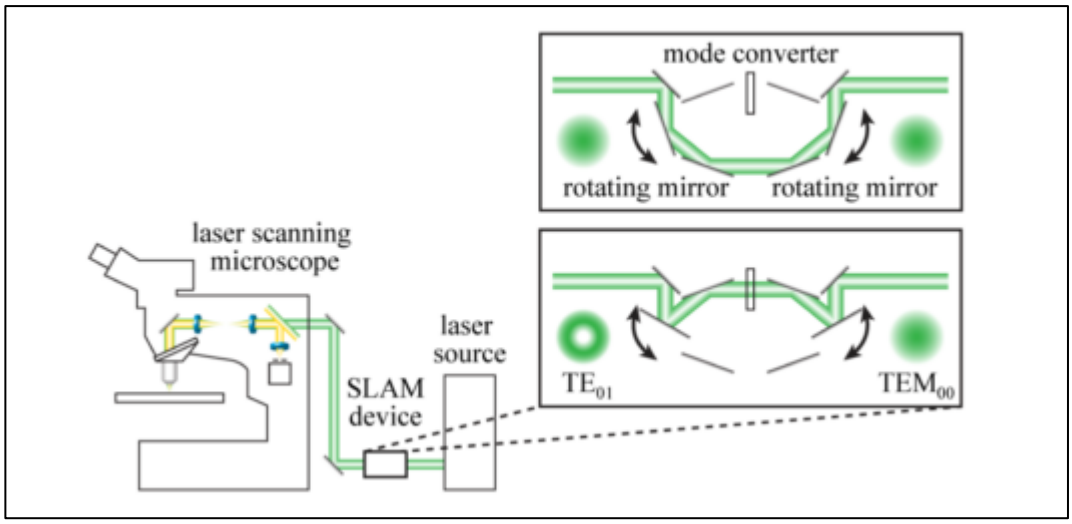

Figure 14:SLAM microscopy.

A schematic diagram of the alterations made to convert a normal microscope to a SLAM scope. A SLAM device (mode converter) that converts the Gaussian (TEM_{00}) beam to a hollow (TE_{01}) beam is added. Rotating mirrors direct the beam either through, or around the mode converter so that sequential images can be acquired with either beam. Adapted with permission from (Dehez, Piché and De Koninck, 2013)

A "SLAM device" was retrofitted between the laser and the microscope stand (Figure 14). The SLAM device consists of rotatable mirrors that are able to direct the beam via a series of low order half-wave plates and a π-phase shift plate, or can be rotated to omit these components. When directed through the wave plates the Gaussian beam is converted to the azimuthally polarised TE_{01} laser beam. This beam contains a dark region at its centre. The dark spot at the centre of this beam (the dark beam) defines the resolution of the system and can be focussed to a size of λ/4 (Haeberlé and Simon, 2009). Images are acquired sequentially, once with a Gaussian beam and once with the dark beam. One image is then subtracted from the other and results in contrast and resolution enhancement. The authors were able to show a resolution of 130 nm for a 1.2NA objective and 810 nm two-photon excitation.

2.5.4 Superoscillations

The principle of superoscillations states that band limited functions are able to oscillate locally faster than their fastest Fourier component (Berry and Popescu, 2006). With respect to imaging, this means it is possible to focus light to a "hot spot", smaller than the diffraction limit. In practice, a precision tailored mask is used to cause calculated interference of the illumination light such that that the focal spot is smaller than the diffraction limit. Superoscillatory lenses (SOLs) also called Toraldo filters (honouring Toraldo di Francia, a pioneer in translating the mathematical concept of superoscillations to optics), bring with them their own challenges and restrictions. Alongside the focal hot spot, a large halo of significantly higher intensity is also generated which

limits the contrast and field of view. However, by introducing an opaque blocking region at the centre of the SOL a shadow region is generated within which the superoscillatory spot forms, separating the illumination spot from the sidebands (Rogers *et al.*, 2013). The limitation of this technique relative to standard SOLs is that the spot is extended axially decreasing axial resolution. The other major difficulty is the practicality of generating a suitable mask. However, in 2012 a SOL was implemented in practice (Rogers *et al.*, 2012). Rogers *et al*., generated a binary mask capable of generating a focal hotspot of 185 nm in diameter projected to 10.3 µm from the surface of the mask. In this experiment, the authors imaged transmitted signal of a 640 nm diode laser, through a series of nano holes and slits, achieving a resolution in the region of 140 nm (~λ/4.6). To further improve the functionality of superoscillatory imaging beam shaping can be performed by a pair of spatial light modulators (SLMs), rather than using a mask (Rogers and Zheludev, 2013). The beam is reflected off the surface of a pair of SLMs, one to control the amplitude of the beam, and one to control the phase (Figure 15). In this way, it is possible to tailor the diffraction of the beam such that it interferes to produce a superoscillatory spot at the focus of the microscope objective. This can be in the order of a few hundred microns from the objective aperture (Rogers and Zheludev, 2013) and therefore represents an opportunity to image deeper into samples or the surface of rougher samples.

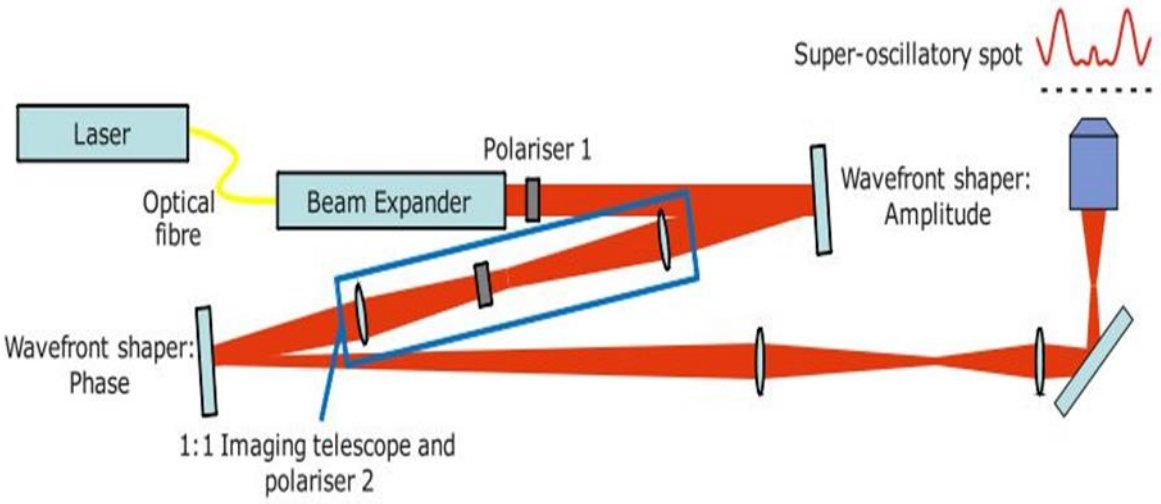

Figure 15: A schematic diagram of a super-oscillatory imaging setup using spatial light modulators.
The wavefront is shaped in both amplitude and phase using a pair of SLMs such that a superoscillatory spot is formed at the microscope focus.Reproduced with permission from (Rogers and Zheludev, 2013).

It has been shown that superoscillations can improve resolution of both fluorescently labelled samples (Kozawa, Matsunaga and Sato, 2018) or without the use of fluorescent labels (Rogers *et*

al., 2020), leaving this technique open to development for multiphoton imaging. However, to date there has been no implementation of superoscillations with TPEF or SHG imaging.

2.5.5 Microsphere Assisted Microscopy and Photonic Nanojet Imaging

Crossing the categories of PSF engineering and optical bandwidth expansion is the field of microsphere assisted microscopy (MAM) (Lai *et al.*, 2016). Also referred to as microsphere-aided optical microscopy (MAOM) (Upputuri and Pramanik, 2017), microsphere optical nanoscopy (MONS) (Lee, Li, Ben-Aryeh, *et al.*, 2013) or photonic nanojet (PNJ) imaging (Upputuri *et al.*, 2014). A PNJ is a localised focus of light with an intensity cross section narrower than the diffraction limit that can propagate over multiple wavelengths (Chen, Taflove and Backman, 2004). Initial demonstrations of the phenomena used high refractive index spheres or cylinders to generate the PNJ and this is still the most common experimental implementation. However, theoretical studies have investigated cuboids (Liu *et al.*, 2018), cones, prism structures (Minin, Minin and Geints, 2015) and spheres with multiple/graded refractive indices (Patel, Kushwaha and Swami, 2018a). Typically, dielectric spheres of sizes between 5 µm-100 µm in diameter are placed on the surface of a sample to focus the light into a PNJ, decreasing the size of the illumination point spread function of the system (Yang *et al.*, 2016). By scanning the illuminating beam over the sphere, the PNJ is scanned over the sample forming a virtual image which is detected in the far-field using the illumination objective (Figure 16). It has been shown that a real image may also be detected, dependent of the refractive index contrast between the sphere and the immersion medium (Lai *et al.*, 2016). Common microsphere materials include Barium titanate glass (BTG) (Darafsheh *et al.*, 2012; Darafsheh, Guardiola, Palovcak, *et al.*, 2015; Yang *et al.*, 2016), fused silica (FS) (Lee, Li, Ben-Aryeh, *et al.*, 2013; Yan *et al.*, 2014) and polystyrene (PS) (Liu and Wang, 2014; Yan *et al.*, 2014, 2015; Cao *et al.*, 2015).

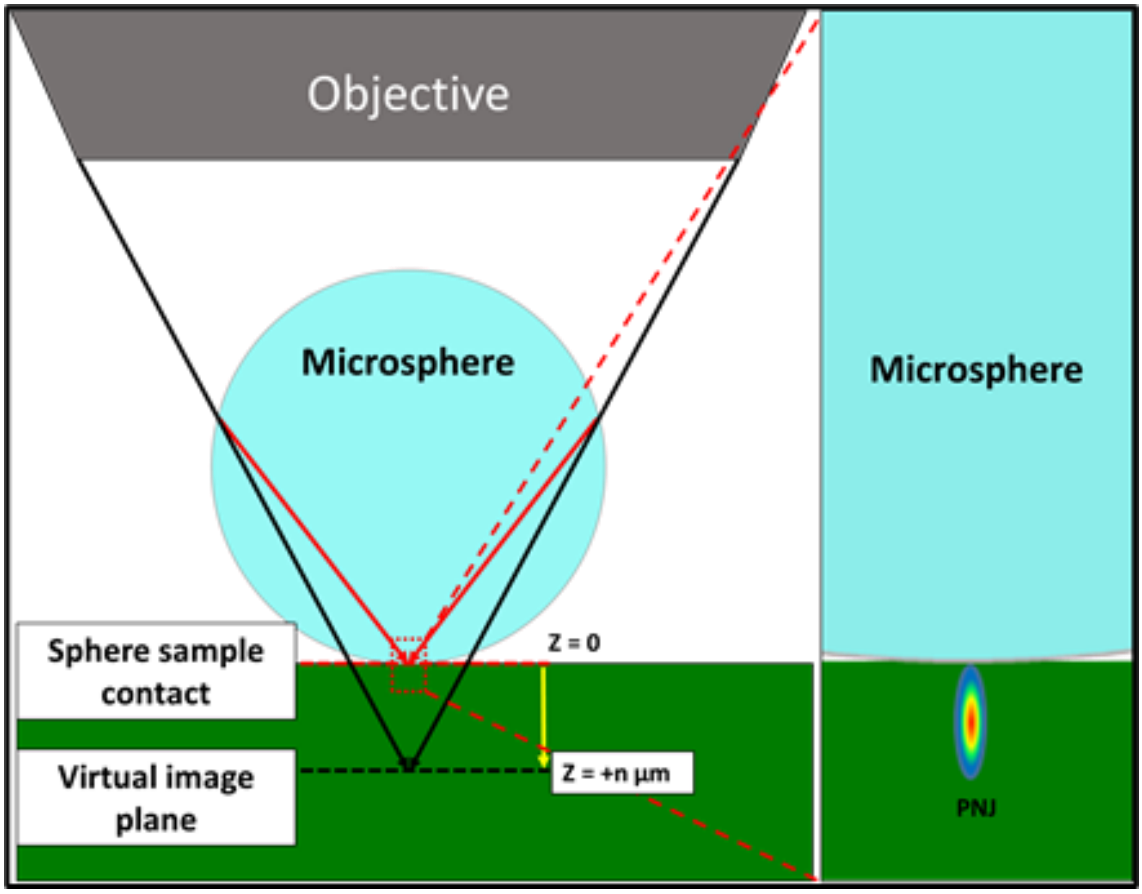

Figure 16: Microsphere Assisted Microscopy principle.
A sphere with a diameter of 5-100 µm is deposited onto the sample surface, light is focussed by the sphere into a photonic nanojet (red arrows) decreasing the PSF size and generating a super-resolved virtual image. The objective is focussed beneath the sample plane at z = n µm (black dashed lines) and used to relay the SR image into the microscope.

The underlying super-resolution mechanism has not been conclusively explained however, it has been suggested that it involves a combination of factors. These include, the collection and conversion of evanescent waves into propagating waves (Hoang *et al.*, 2015), whispering gallery modes (Zhou *et al.*, 2017) and the sub diffraction FWHM of the PNJ (Chen, Taflove and Backman, 2004; Lecler *et al.*, 2007; Liu and Wang, 2014; Sundaram and Wen, 2014; Gu *et al.*, 2017; Luk'yanchuk *et al.*, 2017; Yang *et al.*, 2017).

PNJ focusing and resolution is affected by microsphere diameter and refractive index ratio between the sphere and the immersing medium (Darafsheh *et al.*, 2012; Lee, Li, Wang, *et al.*, 2013). As the relative refractive index between the microsphere and the surrounding medium approaches 2 the position of PNJ formation approaches the sphere surface, and the intensity of the PNJ increases (Figure 17).

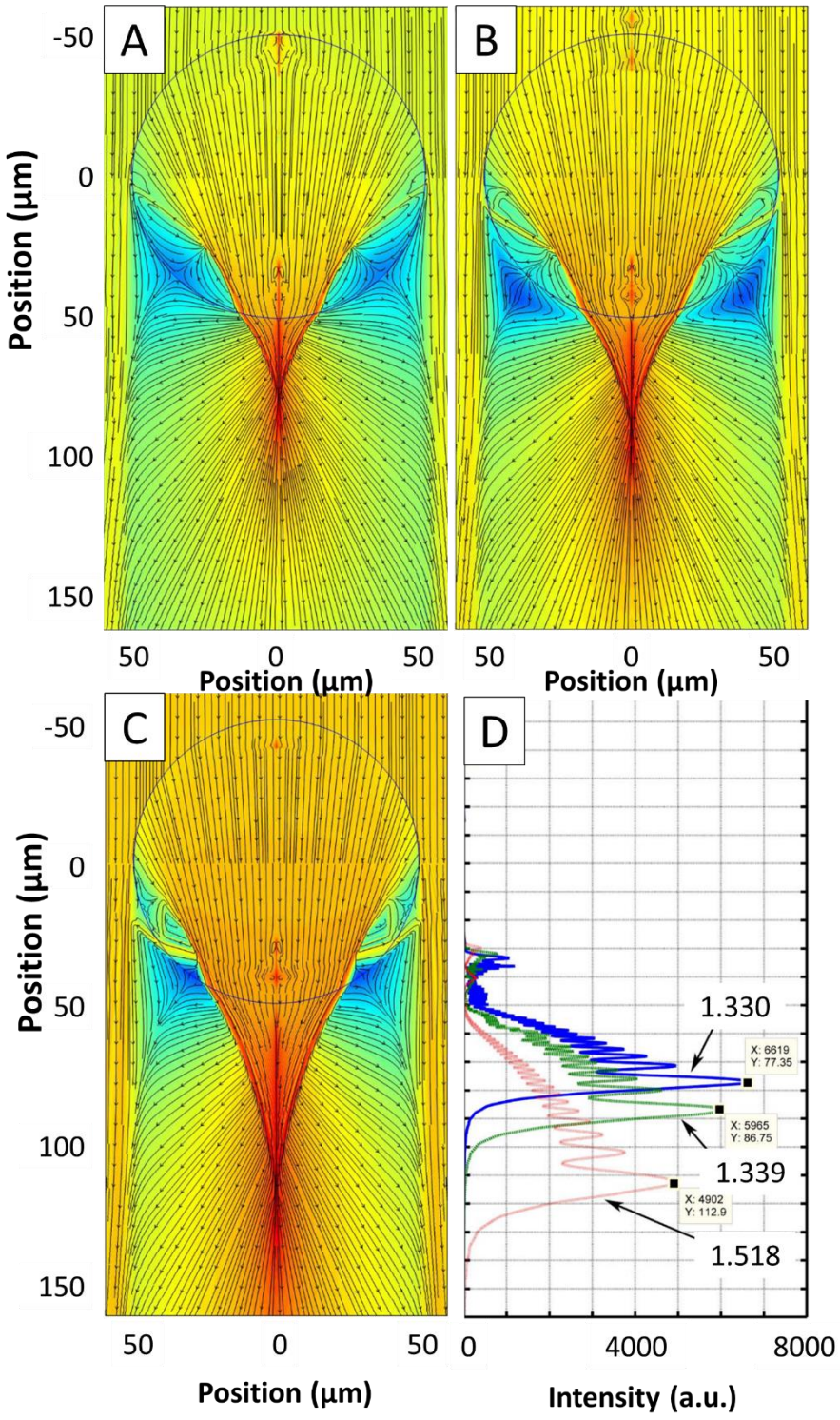

Figure 17:The effect of refractive index contrast on PNJ formation.
BTG - Barium titanate glass (A) A BTG sphere in water (n=1.33), (B) a BTG sphere in 40% sugar solution (n=1.399), (C) a BTG sphere in microscope immersion oil (n=1.518). As the refractive index contrast decreases, position of the photonic nanojet focus moves away from the sphere surface. (D) The intensity distribution plotted along the x-z plane for (A), (B) and (C), which are the blue, green and pink lines respectively. As the relative refractive index decreases the intensity of the PNJ also decreases. Adapted with permission from (Lee, Li, Wang, *et al.*, 2013)

The microsphere diameter affects the location of PNJ formation. For a fixed illumination wavelength decreasing the sphere size moves the PNJ focus closer to the sphere surface (Figure 18) (Lee, Li, Ben-Aryeh, *et al.*, 2013), eventually the PNJ forms within the sphere (Yang *et al.*, 2016). The size of the sphere also affects the waist of the photonic nanojet (Yang *et al.*, 2016) i.e. the FWHM of the area of highest intensity. It was shown that spheres of ~6 μm diameter have the narrowest waist once normalised against illumination wavelength.

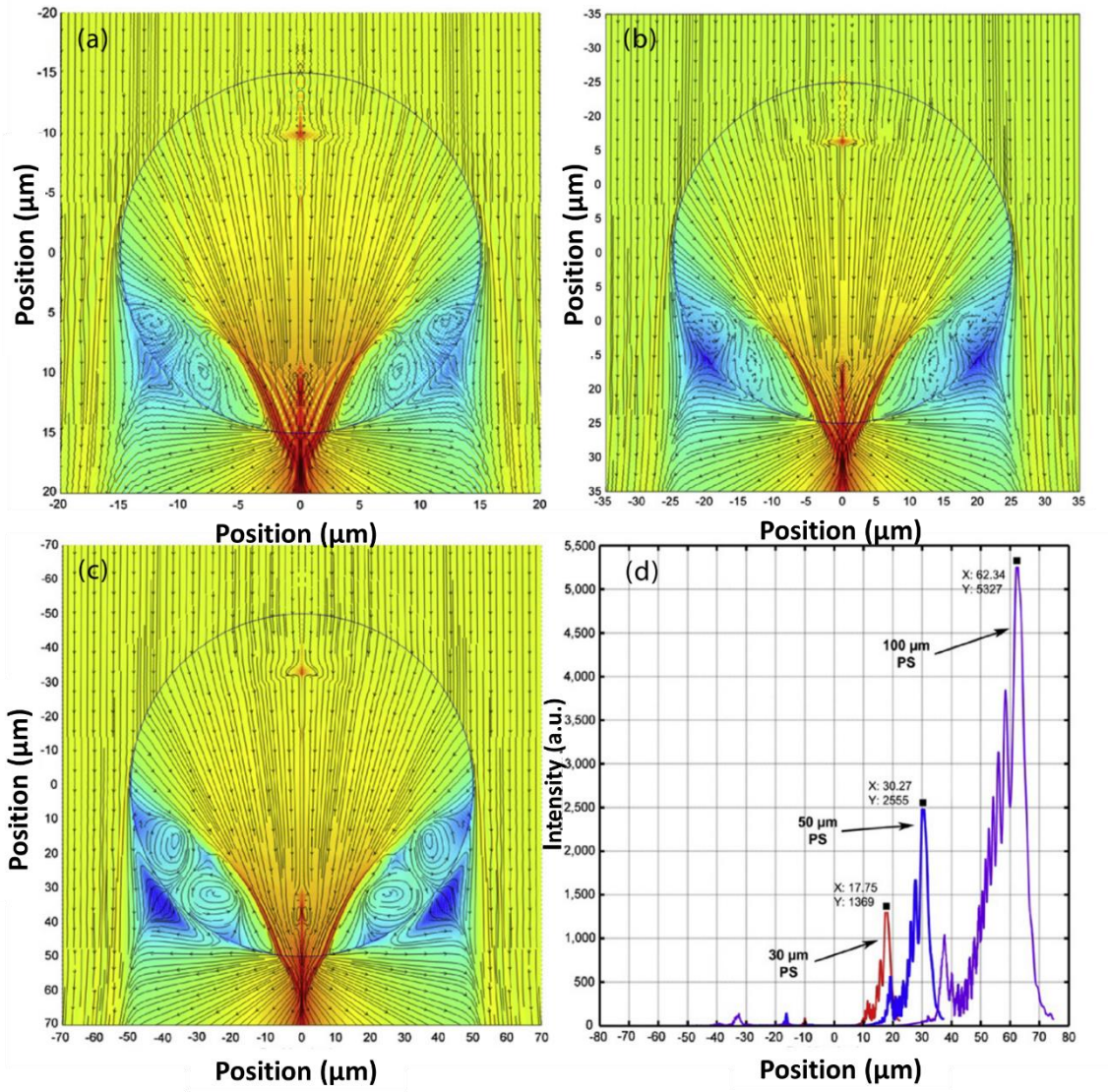

Figure 18: Effect of sphere size on PNJ formation.
Poynting vector simulations of (a) 30 μm sphere, (b) 50 μm sphere,(c) 100 μm sphere under 600 nm plane wave illumination. (d) Intensity plots in the XZ plane running along the PNJ. As the size of the sphere increases the PNJ forms further from the sphere surface and the PNJ intensity increases. Reproduced with permission from (Lee, Li, Ben-Aryeh, *et al.*, 2013).

A third factor affecting the magnification in PNJ imaging is the focal position of the objective relative to the plane at which the sphere and sample meet. Magnification increases with distance from the sphere-sample interface (Upputuri *et al.*, 2014; Lai *et al.*, 2016). i.e. for the virtual image

case focusing the objective further towards the sample will achieve greater magnification and the opposite is true for real imaging. This statement holds true for a limited range of focal positions within which a super-resolved image can be obtained, outside of this range the quality of the image deteriorates rapidly (Yang *et al.*, 2017). The distance of this focal range from the sphere-sample contact increases with sphere size (Lai *et al.*, 2016).

PNJ imaging of biological samples has been demonstrated, including adenoviruses (Li *et al.*, 2013), γ-tubulin, and a cytochrome c oxidase protein (MTCO1) in mouse AML12 cells (Yang *et al.*, 2014). In the latter paper, they report a maximum resolution of ~λ/7. This resolution has been exceeded by Yan *et al.* (Yan *et al.*, 2014), who achieved a 25 nm (λ/17) lateral resolution, combining PNJs with confocal imaging to observe gold nanodots. In 2014 Upputuri *et al.* (Upputuri *et al.*, 2014) showed that this technology could be applied to at least one form of label-free imaging. They were able to image the line features of a blue ray disc using coherent anti-stokes Raman scattering (CARS) microscopy, giving a resolution in the range of 170 nm. In this study, PS spheres were used with diameters ranging from 1 to 6 µm. This paper is of particular interest as it shows that it is possible to achieve multiphoton, label-free super-resolution, opening the door to explore this further for other label-free imaging modalities such as TPEF and SHG.

The major limitations of PNJs are effective localisation of microspheres to a suitable area of the sample, restricted field of view and requirement for the sphere to be in close proximity to the sample. To effectively localise microspheres to the region of interest, they have been attached to the end of a fibre (Aakhte *et al.*, 2017), micropipette (Krivitsky *et al.*, 2013) or AFM cantilever (Duocastella *et al.*, 2017). To increase the field of view, which is limited by the sphere size and therefore, the desired resolution, 2 main approaches have been explored. One method exploits the fact that in 2 dimensions a microfiber and a sphere are the same. Thus, by laying a fibre across the sample an extended field of view can be achieved in one axis (Maconi *et al.*, 2018). The second approach involves creating an array of spheres embedded in a transparent film and imaging multiple super-resolution FOVs in a single objective FOV (Darafsheh, Guardiola, Palovcak, *et al.*, 2015; Xing *et al.*, 2017; Wang *et al.*, 2018). A different approach to combat localisation and FOV at the same time is to employ a scanning technique combined with image stitching. Chen *et al*. (T. Chen *et al.*, 2018) used micro translation of the sphere attached to a probe. The most elegant solution so far is where an adaptor for the microscope objective has been developed that is able to control the sphere/objective distance whilst the sample/sphere distance is controlled by the microscope focusing system. This has been implemented for a single sphere (L.-W. Chen *et al.*, 2018) and for a sphere array (Yan *et al.*, 2017; Huszka and Gijs, 2018). This precise control over the sphere-sample distance also allowed demonstration that contact is not necessary to achieve resolution improvement (Ling *et al.*, 2018). However, it is noted that the SR capability decreases

rapidly with increasing distance, this can be linked to the effective projection distance of the PNJ from the sphere surface and the rapid decay of evanescent fields with distance.

2.6 Conclusions:

In this chapter the key light matter interactions used in the research presented in this thesis were explained in terms of their physical origins and how they have be used to generate label free contrast in microscopy. The concept of spatial resolution was also introduced, and the current methods of super-resolution imaging explained. From the current state of the art, it is clear that whilst significant progress has been made in super-resolution technologies, most advances have been directed towards fluorescent labelled techniques. It is also clear that the field of label-free super-resolution is still in its relative infancy and is an emerging research frontier. Many of the articles referenced relating to multiphoton, label-free imaging have been published within the duration of this research studentship highlighting the relevance of the work that has been undertaken. Of the methods discussed structured illumination methods such as SIM and ISM have seen the greatest success for label-free imaging, however, they are still (generally) limited to a maximum resolution improvement factor of 2 and require complex imaging set-ups to implement. Similarly, although simpler, subtractive imaging offers a limited improvement in resolution. PNJ imaging holds the most promise for development as it neither relies on specific properties of the target species nor involves complex modifications to an existing multiphoton imaging set-up. Also of note are the computational, fluctuation-based methods which have yet to be explored for multiphoton label-free imaging. Super-resolution imaging with label-free techniques has the potential to elucidate new physiological and pathological phenomena by allowing researchers to observe structures noninvasively in the unperturbed state on a nanometre scale.

Chapter 3 Experimental Section

This chapter contains details of experimental methods including imaging systems, sample preparation, data processing and analysis and simulation parameters where these are not explicitly stated in results chapters. This chapter is designed to avoid redundancy between, and aid continuity within results chapters.

3.1 Materials

- 110 nm fluorescent beads (Invitrogen, TetraSpeck, T7279).
- 12 well cell culture plate (Corning, Costar 3513) . 15 mM GTP (R0461, ThermoFisher).
- Agarose, low melting point (A4018, MERCK).
- Acidified water (0.005 % v/v, glacial acetic acid in distilled water)
- BacLight LIVE/DEAD viability kit prepared using manufacturer's instructions (Thermo Fisher Scientific, L7012).
- Barium titanate doped glass (BTG) microspheres, Cospheric LLC, Santa Barbara, CA) were obtained in 2 size ranges 5 µm-22 µm (small) and 55 µm-60 µm (large), the refractive index of the spheres is n=1.9.
- Clearene (3803600, Leica Biosystems),
- Collagen (11179179001, MERCK).
- DI water, milliQ
- Direct red 80 0.7 mM (365548, MERCK),
- Dulbecco's modified Eagle's Medium (DMEM 32430027, Gibco, Fisher Scientific) supplemented with 10 % v/v foetal bovine serum (FBS 1265701, Gibco, ThermoFisher) and 1 % v/v penicillin-streptomycin (Pen-strep15070063, Gibco, ThermoFisher).
- EGTA, Ethylene glycol-bis(2-aminoethylether)-N,N,N',N'-tetraacetic acid (E3889, MERCK).
- Elastic Stain Kit (ab150667, abcam),
- Eosin 1% solution (E4009, MERCK)
- Ethanol (51976, MERCK)
- Fluorinated Ethylene Propylene (FEP) copolymer film (RS-online, FEP FILM 304X200X0.025MM).
- Mayer Haematoxylin (51275, MERCK)
- MitoTracker Orange CMTMRos (M7510, ThermoFisher Scientific).
- Number 1.5 Ø =16 mm coverslips (Agar Scientific, AGL46R16-15) ,
- Paraformaldehyde 16% Solution (methanol-free) - 10x10 ml ampoules (AGR1026, Agar scientific). Elastin (MERCK, E1625).
- Phosphate Buffered Saline, PBS pH7.2 produced in house.
- PIPES, Piperazine-1,4-bis(2-ethanesulfonic acid) (P6757, MERCK).
- poly-L lysine (1 mg/ml) (MERCK, P4707).
- Richard-Allen mounting medium (ThermoScientific 12657746),
- Scott's Tap Water ($MgSO_4$ • 7H2O, 200 g/L + $NaHCO_3$, 20 g/L) (S5134, MERCK). $MgCl_2$ (M1028, MERCK).
- Sylguard 184, (761036,Sigma-Aldrich).
- Taxol (20 µM) (Paclitaxel, T7402, Merck)
- Tris base (T1378, MERCK)
- Tubulin (TL488M-A, Cytoskeleton, Inc) (www.Cytoskeleton.com).
- Tubulin Tracker Green (T34075, ThermoFisher Scientific).
- Ultra-low attachment coated 96 well plates (Corning, 7007).

3.2 Atomic Force Microscopy

AFM images were acquired on a Digital Instruments Multimode IV AFM system, operating in tapping mode in air. Silicon tips with an aluminium coating (<8 nm tip radius) (APEX probes, Nanoworld, NCHR) were used. Probes were autotuned using Nanoscope III 5.12r3 software before use. A resonance frequency of 330 kHz and a force constant of 42N/m was used for all images. A scan rate of 2Hz and 512 samples per line/512 lines per image were used.

3.3 Laser Scanning Multiphoton Imaging

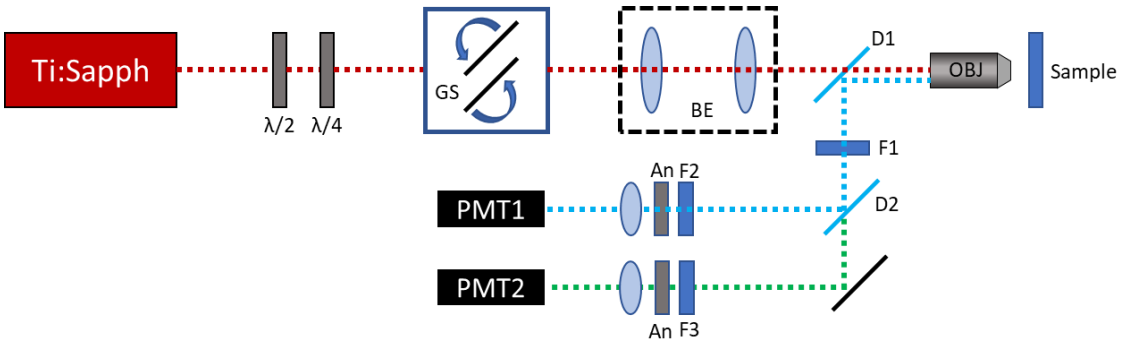

Figure 19:Multiphoton Imaging System
The output of a tuneable (710 nm – 990 nm)femtosecond pulsed laser (Ti:Sapph) is passed through a half (λ/2) and quarter waveplate (λ/4) to control the polarisation at the objective focus. The beam is scanned by a pair of galvanometric mirrors (GS), expanded (BE) and passed through an objective to illuminate the sample. Excitation is separated from emission via a dichroic mirror (D1) and short pass filter (F1). Signals are separated using a dichroic mirror (D2) and filtered (F2) before being focussed onto PMT1. Longer wavelength signals were filtered using F3 and detected on PMT 2 For polarisation sensitive detection an analyser (An) was placed immediately after F2/F3. GS: Galvo scanner, BE: Beam expander.

3.3.1 System specifications

Second harmonic generation imaging was performed on a home-built multiphoton imaging system which consists of a tuneable (710 nm – 990 nm) femtosecond pulsed laser (MaiTai, Spectra physics) that generates 120 fs pulses with a 80 MHz repetition rate, coupled into a Leica DRMB upright microscope stand. Laser scanning is performed using a pair of galvanometric mirrors (Cambridge Instruments). The beam is expanded using a telescope to overfill the objective back aperture and is directed into the objective using a dichroic mirror (Semrock FF685-DI02-25X36). Signal is collected in the backwards direction and separated from the excitation laser by the same dichroic mirror, then cleaned using a short pass filter with 697 nm cut off (Semrock FF697-SDi01-25x36). For observing the second harmonic signal a laser excitation was 800 nm unless otherwise stated. Signals were separated using a dichroic mirror at 458 nm (Semrock,

FF458-Di02). Signals <458 nm were further selected using bandpass filters (typically for SHG measurements a band pass filter centred at 400±20 nm) (Thorlabs, FB400-40) and detected by focussing onto PMT1 (Hamamatsu, H10722-01). See Appendix 3 for full specifications).
Signals >458 nm were selected using another band pass filter (Changed between experiments) focussed onto PMT2 (Hamamatsu, H10722-20). For polarisation-based measurements an analyser (LPVISE 100-A, Thorlabs) can be placed after each bandpass filter.

This system was also equipped with a halogen lamp for bright field transmission imaging and a mercury lamp for reflectance bright field or single photon fluorescence imaging. Bright field images were captured on a Retiga 2000R CCD (Q-Imaging), this has a chip size of 1600 x 1200 pixels and a pixel size of 7.4 µm x 7.4 µm. The camera was controlled using Micromanager software. All image processing was performed in Fiji (Schindelin *et al.*, 2012). A series of different objectives were used dependent on the imaging task being undertaken; the specifications of all objectives used on this system are listed below.

Objective	Magnification	Numerical Aperture	Working Distance (µm)
HC PL APO 63x1,2 W CORR UVIS CS2	63	1.2	0.22
HC APO L 63x/0,90 W U-V-I	63	0.9	2,200
HC PL 20x/0.50	20	0.5	1,270
HI PLAN 5x/0.12	5	0.12	14,000

3.3.2 Acquisition software

Multiphoton image acquisition was controlled using ScanImage 2016b software from Vidrio Technologies. This software was used to synchronise galvanometer scanning and data acquisition from the PMTs with a DAQ card (6110S, National Instruments). Pixel size was adjusted by changing the size of the scan field and number of pixels per imaged to ensure adequate sampling for the wavelength, numerical aperture and field of view used. Images were saved as tiff files.

3.3.3 Tile scanning

Tiled images were acquired using a self-written user function script written in MATLAB to run in ScanImage. The script uses the #acquisitionDone flag to trigger a translation in the x direction before initiating another acquisition, this is looped until the x limit is reached triggering a return

to the original x co-ordinate and a translation in y before restarting movements in x. This process is repeated until the y limit is reached resulting in ending of the acquisition. (Appendix B)

3.4 Deltavision Widefield Imaging system

All widefield fluorescence images were acquired using a DeltaVision Elite system (GE Life Sciences) An SSI 7-band light-emitting diode (LED) was used for illumination and a PCO Edge 4.2 sCMOS camera with a chip size of 2048 x 2048 pixels and 6.5 µm x 6.5 µm physical pixel size was used for acquiring the images on this system. Acquisition was controlled using SoftWoRks software (version 6). The system was maintained at 37°C using an environmental chamber. For MUSICAL image stack acquisitions the camera was run in fast acquisition mode using the rolling shutter.

Objective	Magnification	Numerical Aperture	Effective pixel size (nm)	Working Distance (µm)
PLAPON 60XO (discontinued)	60	1.42	107.5	0.15
U-Plan S-Apo (discontinued)	20	0.75	325	0.65

3.5 Whole slide imaging

Whole slide images were acquired using an Olympus dotslide Virtual slide microscopy system fitted with a Olympus CC12 colour camera, using a 20X, 0.75 NA objective (Olympus UIS-2 UPLANSAPO 0.75). Images were stored as Olympus Virtual Slide images (.vsi) and viewed using Olympus OlyVIA software. Regions of interest were exported at Tiffs for further processing in Fiji.

3.6 Lightsheet imaging system

Lightsheet imaging was performed on an Aurora lightsheet microscope (M Squared Life Ltd) customised to perform multiphoton label-free imaging. The system (Figure 20) consists of illumination lasers either single photon excitation using a series of continuous wave lasers at 405 nm, 488 nm, 561 nm and 660 nm or a femtosecond near IR pulsed laser (MaiTai. Spectra Physics, Detailed above). Excitation is selected using a galvanometric mirror to target the desired laser into the microscope. A cubic phase mask is used to produce an Airy Beam profile at the focus of the objective (section 3.6.1), a resonant scan mirror oscillating at 8KHz forms the digital light sheet.

The system uses two objective arranged orthogonally, the excitation objective was a 20x/0.5 NA water dipping objective: (Olympus UMPLFLN20XW, NA 0.5), and the detection objective was a 40x/0.8 NA water dipping objective (Olympus: LUMPLFLN40XW, NA 0.8). Signals are separated using a filter wheel containing changeable band pass filters and then focussed onto the camera (Hamamatsu Orca Flash V3), with a chip size of 2048 x 2048 pixels and 6.5 µm x 6.5 µm pixels. The full field of view of the detection objective was 302 µm and the effective pixel size was 147 nm, this is due to an additional lens in the detection path (Figure 20 L5). Samples were mounted in a custom sample holder (section 3.6.2) for imaging, 3D stacks were acquired by moving the sample stage perpendicular to the light sheet (along the central axis of the detection objective). The microscope was controlled using home-written python software. All Lightsheet imaging was performed at room temperature.

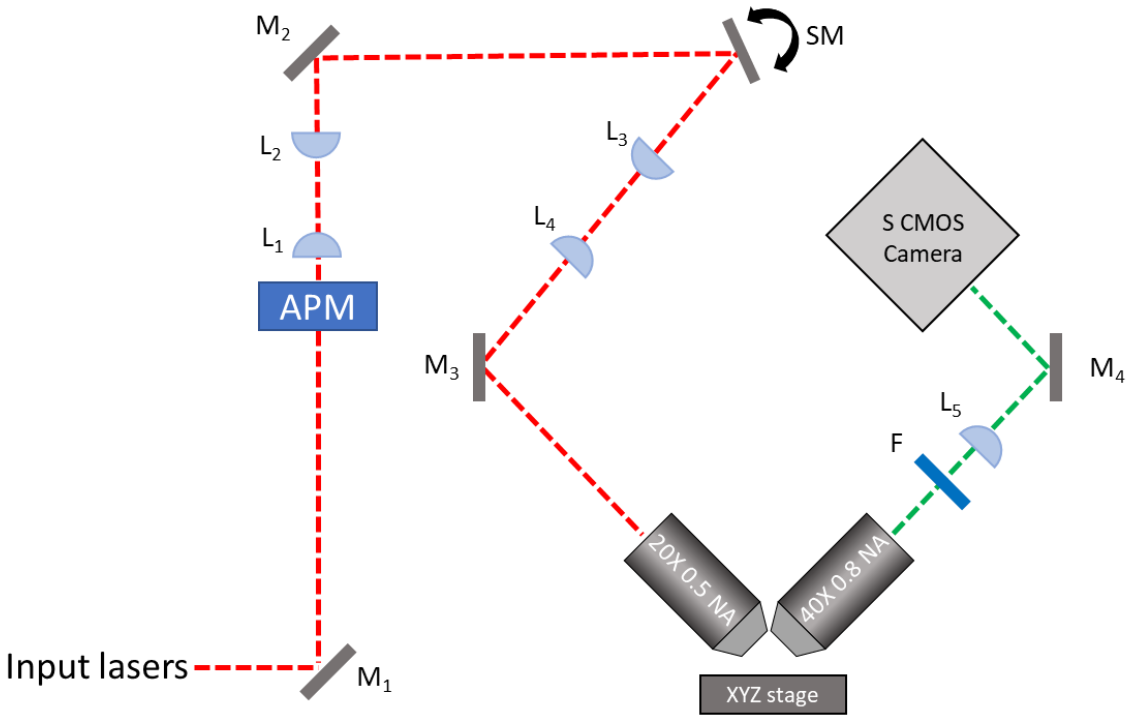

Figure 20: Light Sheet Imaging System
Laser beam passes through a cubic phase mask (APM). This beam is expanded by a lens pair (L1 /L2) onto a resonant scanning mirror (SM) oscillating at 8 kHz. The reflected beam is relayed by a second lens pair(L3/L4) and is incident on the back aperture of the illumination objective (Ob1). The beam is focussed through this objective and illuminates a plane through a sample on the XYZ stage with an Airy beam. Signal from the sample is collected through the perpendicular detection objective, and is filtered by optical filters in the detection path (F). The collimated beam is focussed with a lens (L_5) onto the chip of the sCMOS camera.

3.6.1 Airy lightsheet

The light sheet microscope used in this work uses an Airy Beam as opposed to a Gaussian or Bessel beam illumination. The Airy beam is generated using a cubic phase mask; a transmissive optical component that imparts a cubic phase modulation to the wavefront of the illumination beam in Fourier space / in the back aperture of the objective. The phase modulation imparted is described by the equation: $k(x^3+ y^3)$ were a change to k changes the amplitude of the phase modulation. The equation above assumes normalised coordinates in the back aperture of the objective, and is scaled appropriately for real-world application - i.e. x=-1 to 1 are spread across -2.5 to 2.5 mm in real space. An Airy beam is a propagation invariant beam capable of extending the FOV of a light sheet microscope by 10 times over a Gaussian system (Vettenburg *et al.*, 2014). This allows for the rapid capture of images over a large FOV with uniform high resolution without the need for translation of the illumination sheet. Airy beams also display "self healing" properties helping to minimise shadowing effects due to sample absorption often experienced in lightsheet microscopy. The Airy beam has a non-symmetric multi-lobed profile which can affect the quality of light sheet imaging without use of deconvolution algorithms (Vettenburg *et al.*, 2014). To avoid the need for deconvolution, the cubic phase mask used to generate the light sheet was rotated by 45 ° so that the system operated in a planar Airy light sheet conformation. This has been shown to be advantageous for two-photon microscopy beyond removing the need for deconvolution as it further extends the uniform FOV compared to a conventional Airy beam (Vettenburg *et al.*, 2014). Further details of the lightsheet it's self can be found in section 7.3.12.

3.6.2 Lightsheet Sample Preparation

Samples for light sheet imaging were suspended in a 30 µl gel droplet of filtered 1% solution of low melting point agarose (A4018, MERCK). The droplet was formed on a custom sample holder consisting of a microscope slide, a polydimethylsiloxane (PDMS) pedestal and a sample bath. Once the droplet was formed the sample was inverted to encourage the sample to move to the surface of the droplet. Samples were left to cool for ~10 mins at room temperature to allow the agarose to set into a gel. For biological samples the immersion medium used sterile phosphate buffered saline (PBS), for non-biological samples the immersion medium was DI water. In both cases immersion medium was filtered through a 220 nm pore size filter (Sartorius 10509821, Fischer Scientific).

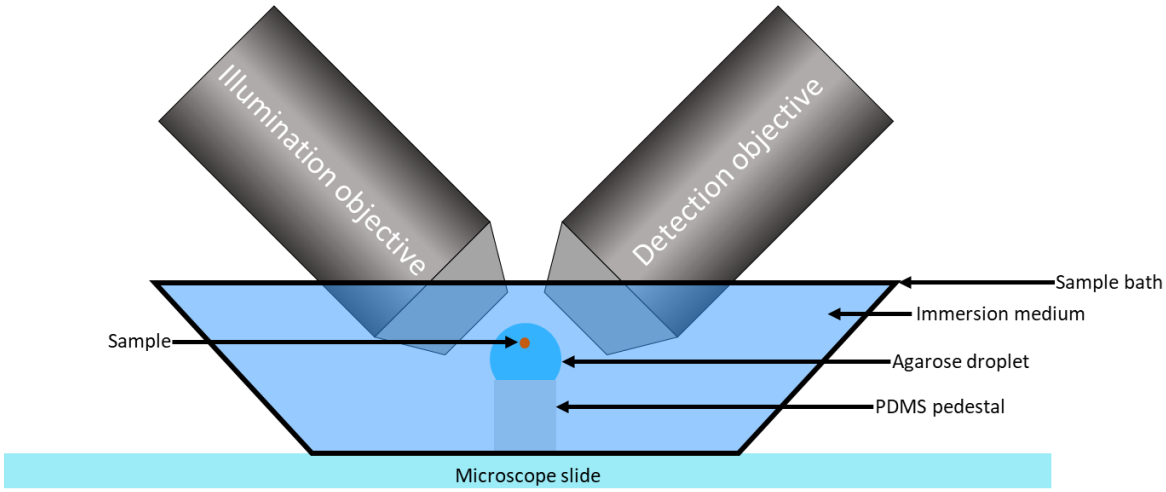

Figure 21: Cross section of the custom sample holder for light-sheet imaging.
Samples were mounted in a droplet of agarose on a PDMS pedestal such that they were within the focal distance of the orthogonal objectives. A boat holds the immersion medium for the dipping objectives.

3.7 Data processing

All image processing was performed in FIJI (Schindelin *et al.*, 2012) unless otherwise stated. All spectra, peak analysis and statistical analysis were performed in Origin (OriginLab 2020).

3.8 Focussed Ion Beam Milling

FIB milling was kindly performed by Artemis Karvounis. FIB was performed on an FEI Helios NanoLab 600 FIB system. Each cut was formed by using an ion beam of Ga+ ions, with an acceleration voltage of 30 keV and beam current of 28 pA. Silicon membranes were commercially sourced (Norcada, Inc.), 200 nm thick polycrystalline silicon membrane 1x1 mm, 200 µm Silicon frame 5x5 mm.

3.9 Absorption Measurements

Spectra were acquired on a home-built absorption setup consisting of an Ocean optics DH-2000 light source fibre coupled to a 1 cm path length cuvette holder, transmitted light was analysed using a fibre coupled visible light spectrometer (Ocean optics USB 2000). Spectra were acquired using Spectrasuite software (OceanInsight, Formerly Ocean optics).

3.10 One-photon Fluorescence Spectra

One-photon fluorescence spectra were acquired using a Cary Eclipse spectrophotometer (Agilent Technologies, Ca). Samples were held in quartz cuvettes (10 x 10 x 45 mm). All spectra were

acquired using 5 nm excitation and emission slit widths. PMT gain was set to high and scan speed set to slow. All presented spectra are an average of 3 repeat measurements unless otherwise stated.

3.11 Multiphoton Excitation Spectra

Multiphoton excitation spectra were acquired using the multiphoton imaging system described above (section 3.3.1). Samples were imaged at 10 nm wavelength intervals. The intensity of a region of interest was plotted against wavelength to generate spectra. All presented spectra are an average of 2 ascending and two descending wavelength scans.

3.12 Nanojet Simulations

Simulations were kindly performed by Johnson Singh. Numerical simulations were carried out using COMSOL Multiphysics 5.4, a FEM (finite element method)-based numerical software to investigate light propagation through the barium titanate-doped, glass microsphere. A full field formalism was adopted with periodic boundary conditions (Floquet) applied on all the four sides of the computational geometry assuming an infinite 2D periodic structure in the x-y plane, solving the wave equation in a three-dimensional model. The incident beam was assumed to be a plane wave, linearly polarised along x axis propagating from the front side of the microsphere, i.e. along the z direction and the excitation wavelength was set at 800 nm. The size of the microsphere was taken to be 14 µm or 60 µm and was positioned at the centre of the computational window. The refractive index of the microsphere was assumed to be n_{ms} =1.9 and also assumed to be embedded in water medium (n = 1.33). The relative permeability was taken to be µr =1. The entire structure was divided into domains and sub-domains, and each domain was meshed using free tetrahedral meshing of maximum element size 6 elements per wavelength outside the microsphere and extremely fine meshing within the sphere. Direct solver method was adopted to solve for the wave equation.

3.13 Unstained Tissue Samples and Histological Staining

Dewaxing - Paraffin embedded wax sections were dewaxed in 2 washes of Clearene for 10 minutes followed by 5 minutes, and hydrated through graded ethanol solutions of 100%, 100%, 70% ,50%, 20%, 0% (Ethanol + DI water, %V/V) for 5 minutes in each solution. At this point

unstained samples were sealed under a coverslip using nail varnish or left uncovered if used for microsphere imaging.

H&E staining - H&E stained samples were stained in Mayer Haematoxylin solution for 5 minutes then run under Scott's tap water for 5 minutes to "blue". Blueing is the process of conversion of the soluble red haematoxylin to the insoluble blue form. They were then stained in eosin solution for 5 minutes before briefly being washed with tap water. They were then dehydrated through graded ethanol's in the reverse order (lowest ethanol concentration first) of the hydration steps. Each dehydration step was performed for 5 minutes before changing to the next alcohol grade., before being mounted in Richard-Allan mounting medium (~10 µl) and covering with a coverslip (No 1.5 22 x 32 mm, AGL462232-15, agar scientific).

Direct Red staining for Collagen - Samples were stained in Direct Red stain solution (1 mg/ml, 0.7 mM) for 1 hour, washed in two changes of acidified water (0.005 % v/v, glacial acetic acid in distilled water) for 1 minute each, and shaken dry. Samples were dehydrated in graded ethanol changes of 50%, 70% 100%, 100% for 5 minutes each. Samples were mounted in Richard-Allan mounting medium (~10 µl) and sealed under a coverslip (No 1.5 22 x 32 mm, AGL462232-15, agar scientific).

Verhoff-Van Gieson Staining - Samples were stained using an Elastic Stain Kit. Dewaxed sections were placed in working Elastic stain kit for 15 minutes, and rinsed under tap water to remove excess stain. Slides were dipped in Differentiating solution ~20 times until desired differentiation was achieved. This was checked under a transmitted light microscope. Slides were then rinsed in tap water and stained using Van Geison's Solution for 5 minutes. They were then rinsed in two changes of 95% ethanol (EtOH + DI H_20 % v/v) and dehydrated in 100 % ethanol. Prior to imaging the sections were rehydrated in DI H_2O and sealed under a coverslip.

3.14 Cell Culture

The neuroblastoma cell line SH-SY5Y was used for all cell-based imaging experiments. Cells were maintained in a regular culture for imaging experiments. Cells were maintained in Dulbecco's modified Eagle's Medium (DMEM, Gibco) supplemented with 10 % v/v foetal bovine serum (FBS, Gibco) and 1 % v/v penicillin-streptomycin (Pen-strep, Gibco). Cells were passaged every 3-4 days, routinely checked for mycoplasma infection and discarded at high passage number (>20). At the point of passage, cells were removed to be used for generation of adherent cell coverslips or cell spheroids.

3.15 Preparation of Adherent Cell Coverslips

Number 1.5 Ø =16 mm coverslips (Agar Scientific, AGL46R16-15) were washed by sonicating in 100% EtOH for 2 minutes prior to use. Once dry, coverslips were placed in a 12 well cell culture plate, incubated with poly-L lysine (1 mg/ml) for 20 minutes, washed 3 times with sterile de-ionised H_20 and left to dry at 37°C overnight. Cell-containing medium was added dropwise to dry coverslips to a final number of ~40,000 cells, the final volume of the well was topped up to 3 ml with warm cell culture medium. Cells were left for 24-48 hours to adhere to the coverslip and reach suitable confluence for imaging.

3.16 *In vitro* Polymerisation of Microtubules

Fluorescently-labelled tubulin was reconstituted at a concentration of 5mg/ml in BRB80 buffer (see below), flash frozen in liquid nitrogen in 2 µl aliquots and stored at -80 °C until required. Microtubule polymerisation was carried out at 37°C with 3mM GTP, this was achieved by addition of 0.5 µl of 15 mM GTP in BRB80. Polymerisation was allowed to proceed for 30 minutes before the addition of 100 µl of 20 µM Taxol, used to stabilise microtubules against temperature-induced depolymerisation. Microtubules were used immediately after stabilisation.

BRB80 Buffer: 80 mM PIPES, 1 mM $MgCl_2$, 1mM EGTA, pH 6.8 using KOH.

3.17 Preparation of PDMS

For preparing microspheres embedded in a film, the widely used polymer, polydimethoxysilane (PDMS) was used. PDMS was made using the 2 part kit (Sylguard 184 Elastomer) that contains a silicone base polymer and a curing agent that causes polymerisation. PDMS was mixed in a 10:1 ratio of silicone to curing agent in a plastic cup and mixed using a plastic pipette. The mixed polymer was placed in a vacuum chamber to degas, Microscope slides were cleaned by sonication in 100% EtOH for 5 minutes before use. Dry BTG glass spheres were randomly dispersed on the surface of a clean, dry microscope slide. A thin layer of PDMS was poured over the spheres and cured overnight in a 60 °C oven. After curing, the PDMS layer with embedded microspheres was carefully peeled from the slide to be used as a flexible, microsphere-embedded coverslip.

3.18 *In Vitro* Collagen Gel

Collagen solution was adjusted to a final concentration of 3 mg/ml with 10X concentration indicator-free DMEM. The solution pH was adjusted to ~7.4 using 1 M NaOH. The solution was then deposited onto glass coverslips (Number 1.5 Ø =16 mm (Agar Scientific, AGL46R16-15), in 100 µl aliquots. Each coverslip was placed in a separate well of a 12 well cell culture plate. Plates were incubated at 37 °C for 1 hour. Before imaging the gel was inverted onto a clean glass slide so that the coverslip was on top.

Chapter 4 Correlative H&E and Second Harmonic Imaging

The work presented in this chapter contributed results published in the peer-reviewed journal eLife: "*Nanoscale dysregulation of collagen structure-function disrupts mechano- homeostasis and mediates pulmonary fibrosis" Mark G Jones, Orestis G Andriotis, James JW Roberts, Kerry Lunn, Victoria J Tear, Lucy Cao, Kjetil Ask, David E Smart, Alessandra Bonfanti, Peter Johnson, Aiman Alzetan, Franco Conforti, Regan Doherty, Chester Y Lai, Benjamin Johnson, Konstantinos N Bourdakos, Sophie V Fletcher, Ben G Marshal , Sanjay Jogai, Christopher J Brereton, Serena J Chee, Christian H Ottensmeier, Patricia Sime, Jack Gauldie, Martin Kolb, Sumeet Mahajan, Aurelie Fabre, Atul Bhaskar ,Wolfgang Jarolimek, Luca Richeldi, Katherine MA O'Reilly, Phillip D Monk, Philipp J Thurner Donna E Davies*

Jones, M. G. et al. (2018) 'Nanoscale dysregulation of collagen structure-function disrupts mechano-homeostasis and mediates pulmonary fibrosis', eLife, 7, pp. 1–24. doi: 10.7554/eLife.36354.

4.1 Abstract

Diagnosis of Idiopathic pulmonary fibrosis (IPF) and other interstitial lung diseases requires the analysis of histologically stained samples for hallmark disease features. The staining process is time consuming and the contrast is non-specific, making identification of pathology difficult. Second harmonic generation (SHG) microscopy provides structurally-specific contrast highlighting fibrillar collagen. It can be used for the identification of disease features without sample staining but is yet to be adopted for routine diagnostic imaging. The microscopes needed for each type of imaging are different and are thus rarely implemented on the same system. Here a workflow is created for correlative imaging between two systems that can place the specific contrast of SHG in the context of H&E staining, familiar to pathologists. This method allows for rapid whole-slide imaging using transmitted light microscopy followed by targeted SHG imaging of regions of interest. This methodology has scope to aid the diagnosis of fibrotic lung disease and other diseases that cause altered collagen morphology. Moreover, the targeting of SHG imaging to regions of interest will facilitate the acquisition of images with limited field of view such as super-resolution methods.

4.2 Background

Idiopathic pulmonary fibrosis (IPF) is one of multiple interstitial pneumonias and a prototypic fibrotic lung disease (Richeldi, Collard and Jones, 2017). Afflicted patients will display dyspnoea (difficulty in breathing), along with other non-specific symptoms associated with lung dysfunction, such as a dry cough. In acute cases, patients may show influenza-like symptoms, and the survival time from diagnosis shows a median of 2-4 years (Ley, Collard and King, 2011). The past 10 years have shown significant progress in understanding the underlying factors contributing to this disease. It is now accepted by IPF researchers that there is a combination of interacting environmental and genetic factors contributing to disease progression, accelerated by repeated micro-injuries to alveolar epithelium (Richeldi, Collard and Jones, 2017). Structurally, there is significant reorganisation of the lung tissue extracellular matrix (ECM) during fibrosis; it is believed that a positive feedback loop between dysfunctional cell behaviour and abnormal ECM contributes significantly to the overall fibrosis (Parker *et al.*, 2014).

Current diagnosis relies on a combination of clinical, radiological, and pathological criteria. Careful assessment of clinical history and lung function in combination with routine chest radiographs are used to indicate if the patient has a form of interstitial pneumonia over other diffuse parenchymal lung diseases (Travis *et al.*, 2002). Diffuse parenchymal lung diseases also called interstitial lung diseases, are a broad group of disorders that affect the lung parenchyma consisting of over 200 separate conditions ('The Diagnosis, Assessment and Treatment of Diffuse Parenchymal Lung Disease in Adults', 1999). If an interstitial pneumonia is suspected, high-resolution computed tomography (CT) data is used to give a more detailed picture. However, IPF diagnosis is made exceedingly difficult by the need to exclude many other causes of observable abnormalities: such as medication, workplace exposures and various other connective tissue diseases. Failing diagnosis via high-resolution CT a lung biopsy may be required. Data from histopathological studies has characterised multiple features indicative of IPF; however, these are more often also features of another interstitial lung disease, thus, diagnosis often comes with a degree of uncertainty. It is therefore desirable to explore other tools for the investigation and diagnosis of IPF. Multiphoton imaging techniques: such as two-photon-excited autofluorescence (TPEAF) and second harmonic generation (SHG) are able to provide label-free, chemically and structurally selective contrast, particularly of ECM components including elastin and collagen (Zipfel *et al.*, 2003); thus they present themselves as attractive alternatives to histological staining.

Histopathological analysis is typically carried out using a transmitted light microscope wherein the sample is stained using a dye mixture of Haematoxylin and Eosin (H&E). This procedure is known as

H&E staining. Samples for H&E staining are first fixed in formalin before being dehydrated and embedded in paraffin wax; this both preserves the tissue and allows for sectioning. The wax blocks are then sectioned into thin sections, typically 5-10 µm thick, and mounted onto microscope slides. Tissue sections must then be de-waxed and rehydrated before staining, re-dehydrating, clearing, and finally embedding in mounting medium. This is an extensive process taking multiple days, by contrast multiphoton imaging requires minimal sample preparation. There is no need for addition of dyes as the contrast sources are intrinsic to the tissue (Zipfel *et al.*, 2003) and due to the increased penetration depth and inherent optical sectioning of multiphoton excitation thin sectioning is not strictly necessary (Masters and So, 2008). Thus, sample preparation can be as minimal as immobilisation of the unprocessed tissue on a static surface (Matsui *et al.*, 2017).

The systems used to capture images are also usually optimised towards either transmitted light microscopy or multiphoton imaging, that is, only one modality, often creating discrepancies between images acquired using each. To generate meaningful combined data with labelled and label-free imaging it is necessary to generate a workflow that allows correlative imaging between both modalities. In this chapter a correlative imaging workflow is developed for whole slide H&E stained images allowing the identification and annotation of regions of interest (ROIs) by disease experts. The ROIs are used to guide targeted, diffraction-limited SHG imaging and the two images are co-registered. Correlative H&E/SHG overlaid images place the structurally-specific contrast generated by fibrillar collagen in the recognisable context of H&E staining thus, aiding future understanding of disease pathology.

4.3 Methods

4.4 Optimising Image Acquisition and Sample Preparation

Due to the heterogeneous nature and morphological changes observed in IPF tissue, it is necessary to image large areas of tissue to ensure detection of hallmark pathological features and give an accurate diagnosis. For acquiring multiphoton images the system described in Section 3.3 was used, all images were acquired using circular polarisation to ensure equal excitation of all collagen fibre orientations. A 20x/0.5NA objective was used for the acquisition of all images shown in this chapter and a 512x512 pixel image was acquired with 8 µs pixel dwell time. The scanned field of view (FOV) was 250 µm X 250 µm. To image a large area of the sample, tiled images were acquired and computationally stitched into a mosaic. This was achieved using a home-written tiling script that allows a user-defined x step and y step which dictates the translation of the stage between successive image acquisitions, moving across the sample in a "reading" fashion (Figure 22**A**). Image stitching was performed using the "Grid/Collection stitching" plugin for Fiji, this plugin uses the correlation between the Fourier transform of each tile within a region of overlap between the two tiles (Preibisch, Saalfeld and Tomancak, 2009). For successful image stitching a certain amount of overlap is required between neighbouring tiles. It was found that 14% overlap was enough for good stitching and an 11x11 grid of tiles was able to image a sufficient area (~2 mm^2) using a 20x/0.5NA objective.

To obtain the best signal to noise ratio (SNR) is it desirable to image at the maximum power possible without damaging the sample; at average powers exceeding 18 KW/cm^2 sample damage increased to significant levels (Figure 22**B** red oval) setting an upper limit for excitation power. Sample damage was identified as regions of intense brightness that increased in size with multiple scans of the same FOV. The same regions would also appear in the longer wavelength imaging channel indicating a broad emission (Figure 22 **C/D**), which is not characteristic of SHG. Avoiding sample damage was particularly important for tiled images; the bright spots observed as a result of sample damage interfered with image stitching, which relies on structure alignment. For an 11x11 grid of images a calculated total imaging time of ~4 minutes is required, practically this rose to ~10 minutes due to time taken for the script to run and stage movement. Longer pixel dwell times (>8 µs) would allow collection of more signal however, this led to longer acquisition times where issues regarding axial stage drift were observed.

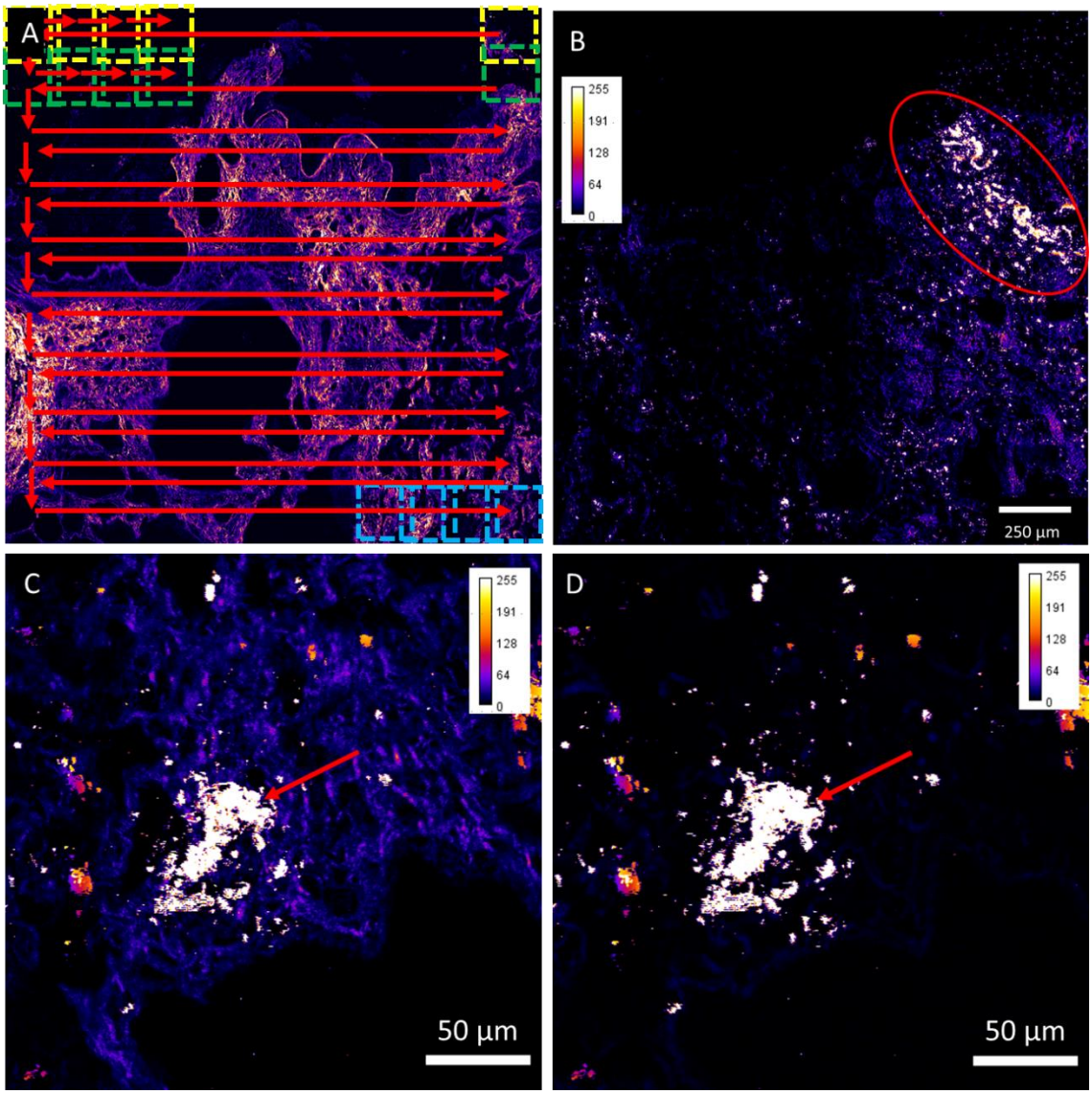

Figure 22: Determining suitable large area imaging parameters
(**A**) Diagram depicting the raster pattern of the tiling script. The FOV is translated by a user-defined step in x to image overlapping FOVs until a limit is reached, it is then returned to the starting x co-ordinate before being translated in y, this is repeated until the y limit is reached. The first 4 tiles and last tiles of the first (yellow squares) and second (green squares) rows have been indicated. The last 4 tiles of the final row have also been indicated.(**B**) Mosaiced SHG image highlighting some areas of sample damage as well that occurs at higher excitation powers (red oval).Sample damage was identified as regions of high intensity that increased in size with multiple scans. The intensity was present both in the 400 nm (SHG) channel (**C**) and in the 520 nm channel (**D**) indicating broad non-specific emission. Damage in C/D is indicated by red arrows.

H&E staining is common practice in tissue pathology however it can pose a limitation to multiphoton imaging. Comparison of images acquired of both stained and unstained sections (Figure 23) showed that under the same excitation powers, H&E stained slices showed an increased likelihood to damage (Figure 23 Red arrows). This appeared to be located near areas of dense collagen and locations of red blood cells, as eosin stains red blood cells and connective tissue it is most likely absorbance of the excitation laser by eosin that increases the propensity for laser induced damage. As a result of this,stained IPF tissue sections showed an increased likelihood to damage compared to stained healthy lung sections as they contain more areas of dense collagen deposition. For future correlative imaging, bright field H&E and SHG imaging should be performed on serial slices rather than on the same slice as the H&E staining increases the susceptibility to damage.

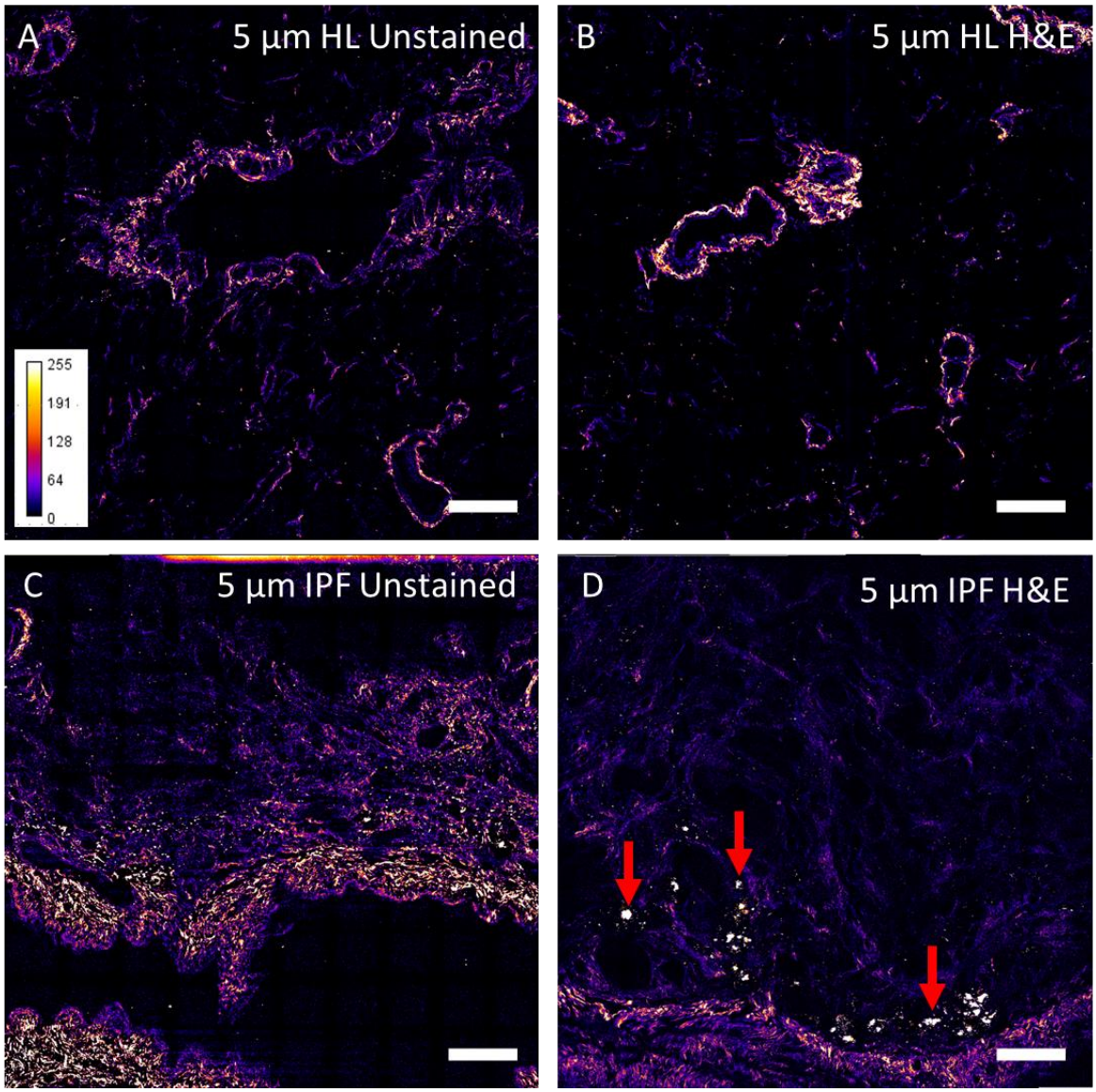

Because correlative imaging was to be performed on serial sections it was important to determine the minimum slice thickness such that the features of two serial section are as similar as possible. Two different section thicknesses were imaged (5 µm and 10 µm) to see the effect on image quality. The overall image quality seen in both 5 µm (Figure 23 **A,B,C,D**) and 10 µm (**E,F,G,H**) tissue sections was comparable. However, 10 µm thick slices showed a slightly increased likelihood for laser-induced sample damage (Figure 23 **B** vs **F, D** vs **H**). Sample damage was assessed visually by inspecting images for amorphous high intensity regions as indicated in Figure 22 **C/D.** It was concluded that subsequent imaging would be performed on 5 µm slices to minimise differences between serial sections and minimise the chance of sample damage when imaging.

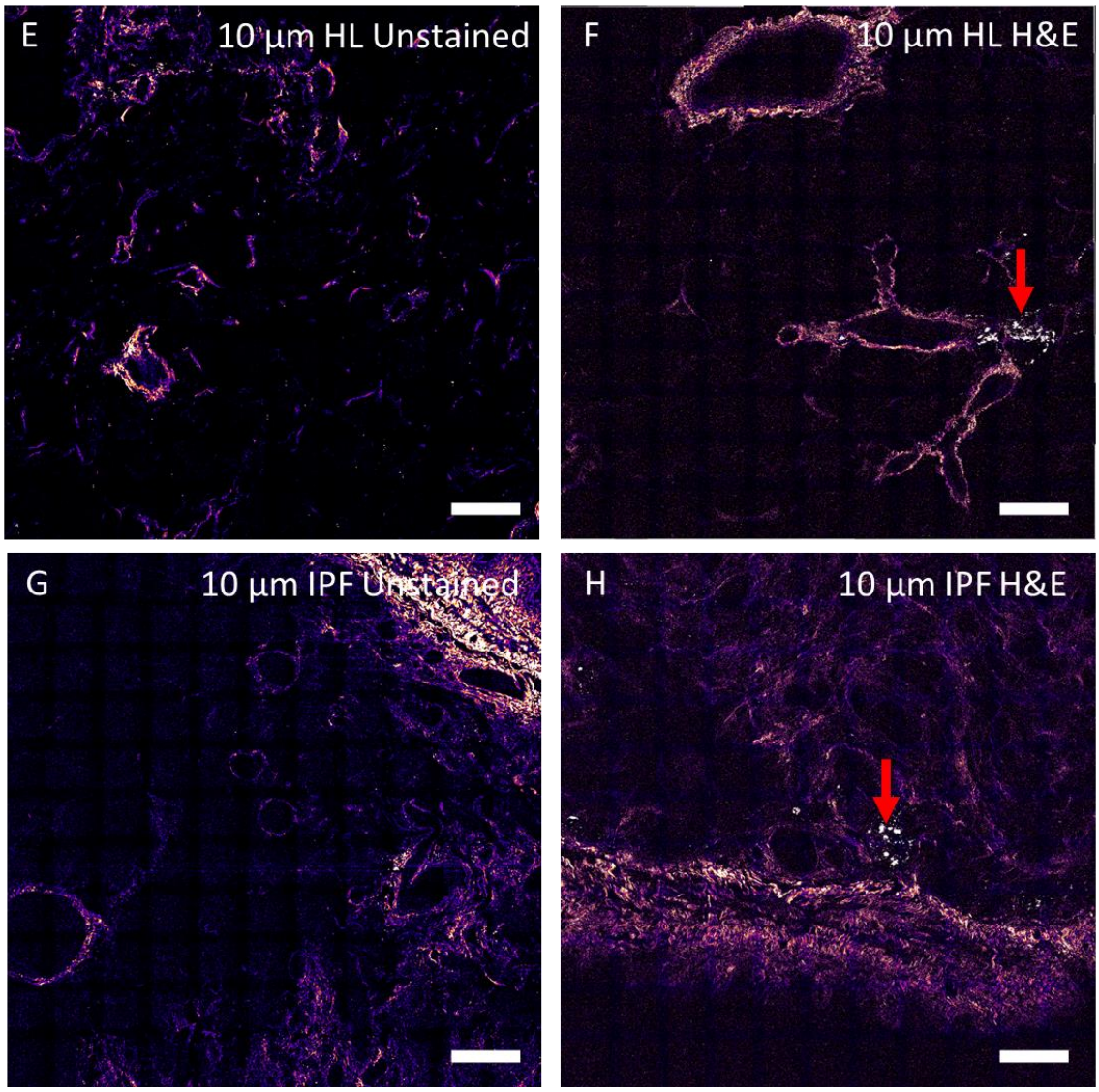

Figure 23: Comparative SHG images of Unstained and H&E stained lung tissue samples. Unstained tissue slices (**A,C,E,G**) were less likely to be damaged by the laser than H&E stained samples (**B,D,F,H**)(red arrows). Damage was most common around dense collagen regions and red blood cells. Stained IPF tissues were more likely to be damaged than stained Healthy lung samples. Changing the sample thickness from 5 µm (**A,B,C,D**) to 10 µm (**E,F,G,H**) didn't appear to affect the likelihood of laser induced sample damage**.** Scale bars 200 µm.

4.5 Image co-registration

The next step in generating a correlative H&E/ SHG imaging protocol is to generate a co-registration methodology to overlay SHG images onto H&E images. This allows the collagen distribution, as shown through SHG, to be placed within the more commonly recognised H&E context. This will also help to identify if SHG imaging shows a higher/lower level of sensitivity than H&E staining.

Many commercial systems can perform both the acquisition and stitching of tiled images quickly and to a high degree of accuracy, often referred to as digital slide imaging. This capability was exploited to perform H&E imaging for co-registration with SHG, an Olympus dotSlide imaging system was used to capture whole slide (~2 cm x 1.5 cm) images of healthy and IPF lung tissue using a 20x/0.75NA objective.

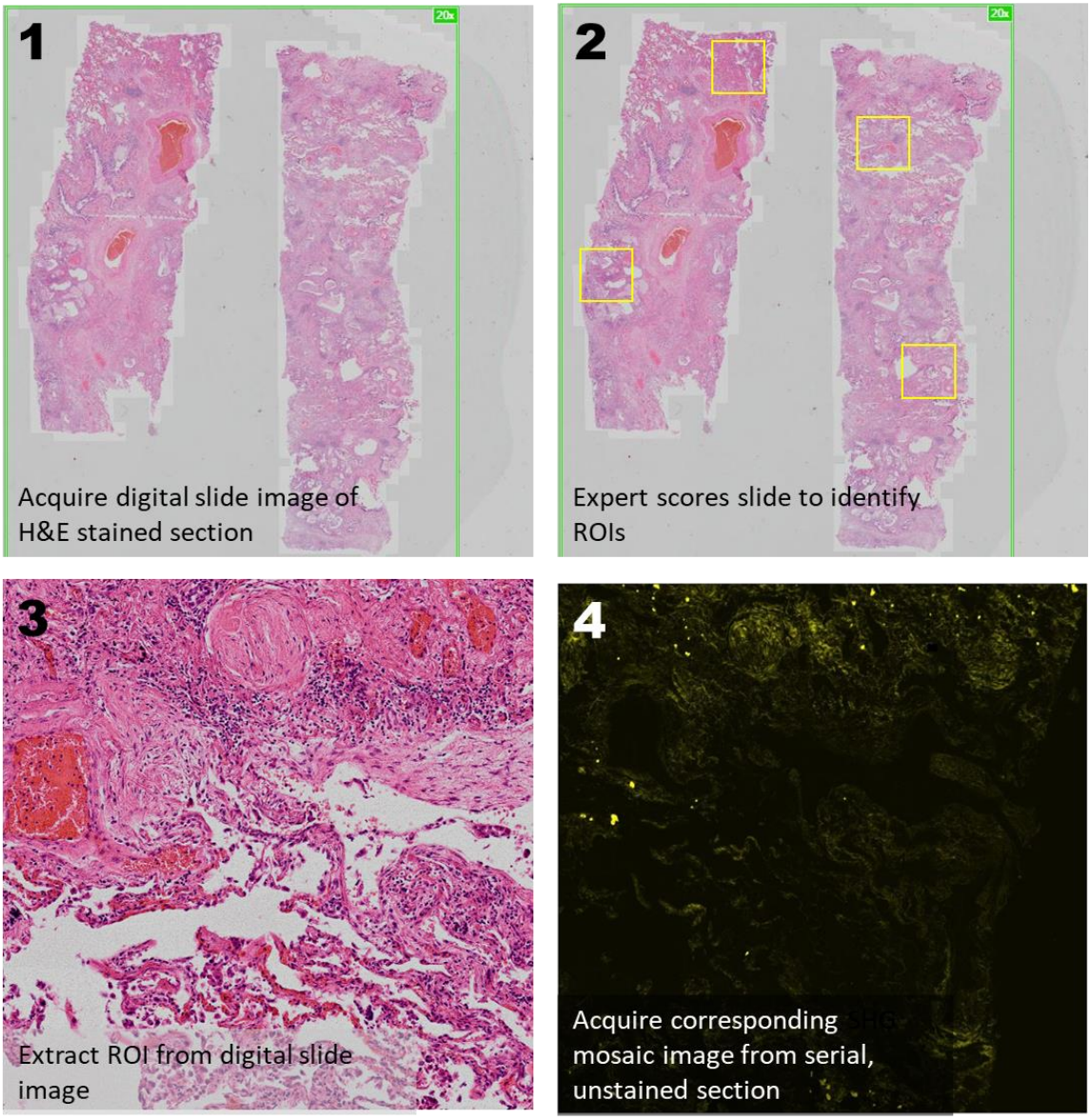

These images were presented to a pathologist for scoring and identification of regions of interest (ROI) (yellow squares Figure 24-**2**). These regions were extracted from the whole slide images and used to guide SHG imaging on a serial section. The SHG mosaic image wasthen co-registered to the extracted ROI from the H&E dotSlide image. Due to the many optical differences between the two imaging systems, a simple overlay does not produce the desired result. To achieve correct co-registration the landmark correspondences plugin within Fiji was used. The H&E image is used as the template image onto which a series of landmarks are placed (Blue triangle Figure 24-**5**); these can be vertices, edges or prominent structures such as blood vessels and alveoli.

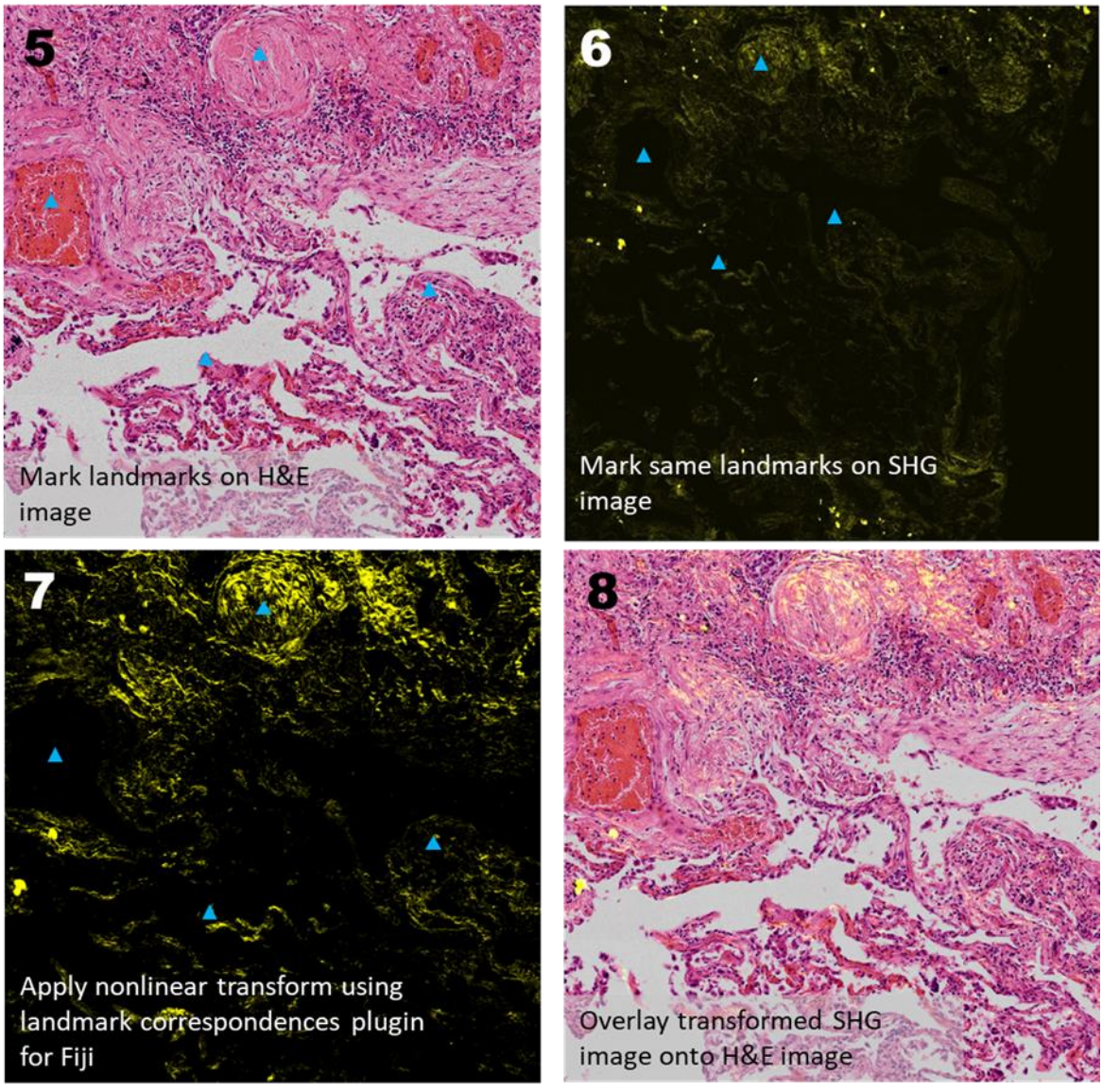

Figure 24: Workflow for creating overlaid H&E and SHG image.
First whole slide H&E images are acquired (**1**), they are then scored by an expert to identify ROIs for SHG imaging (**2**). The ROIs are extracted from the H&E images (**3**) and used to guide SHG image acquisition (**4**). Landmarks are placed on the H&E (**5**) and SHG (**6**) images. The SHG image is transformed (**7**) and overlaid onto the H&E image (**8**).

The accuracy of co-registration increased with the number of landmarks used, an average of ~100 landmarks was used to register each 800 µm x 800 µm FOV. These same landmarks are then identified in the image to be transformed (SHG image) and marked (Figure 24-**6**). The plugin then performs a nonlinear affine transform to the SHG image (Figure 24-**7**). An affine transform may consist of translation, scaling, homothety, similarity, reflection, rotation, shear mapping (Burger and Burge, 2009). The final step is to overlay the two images, SHG images were rendered in yellow to maximise contrast with the H&E staining (Figure 24-**8)**.

To verify the validity of the co-registration, images were taken of both healthy lung tissue and of IPF diseased lung (Figure 25). The images show that the method is able to produce images that place the structurally-specific SHG signal into the more broadly recognised context of H&E stained images. The biological sources of SHG are known to be fibrillar collagen, the actin-myosin complex and microtubules (Campagnola and Dong, 2011). The SHG signal from microtubules is known to be lost upon fixation and the signal observed was extracellular, therefore, the SHG signal was most likely from fibrillar collagen. The distribution of collagen was show to change in IPF (Pena *et al.*, 2007) and this is in agreement with the observed results, suggesting the signal was primarily from fibrillar collagen. The healthy lung SHG image (Figure 25 **C**) shows a concentrated ring of SHG signal. When viewed in the H&E image (Figure 25 **A**) this can be seen to surround a vessel (Figure 25 **A,C** red arrows), which is consistent with usual collagen distribution in lung tissue (Kottmann *et al.*, 2015). The IPF image shows a greater general distribution of collagen and the collagen forms a series of ball like structures (Figure 25**D** red arrows). When viewed on top of the H&E image it can be seen that these collagen structures are found next to masses of fibroblast cells and form the fibrotic foci (Pena *et al.*, 2007) found in IPF tissue (Figure 25**F**). The accurate matching of the collagen distribution in H&E and in SHG for both healthy and IPF lung tissue samples verifies that the correlative imaging protocol can produce meaningful images for correlative visualisation and analysis.

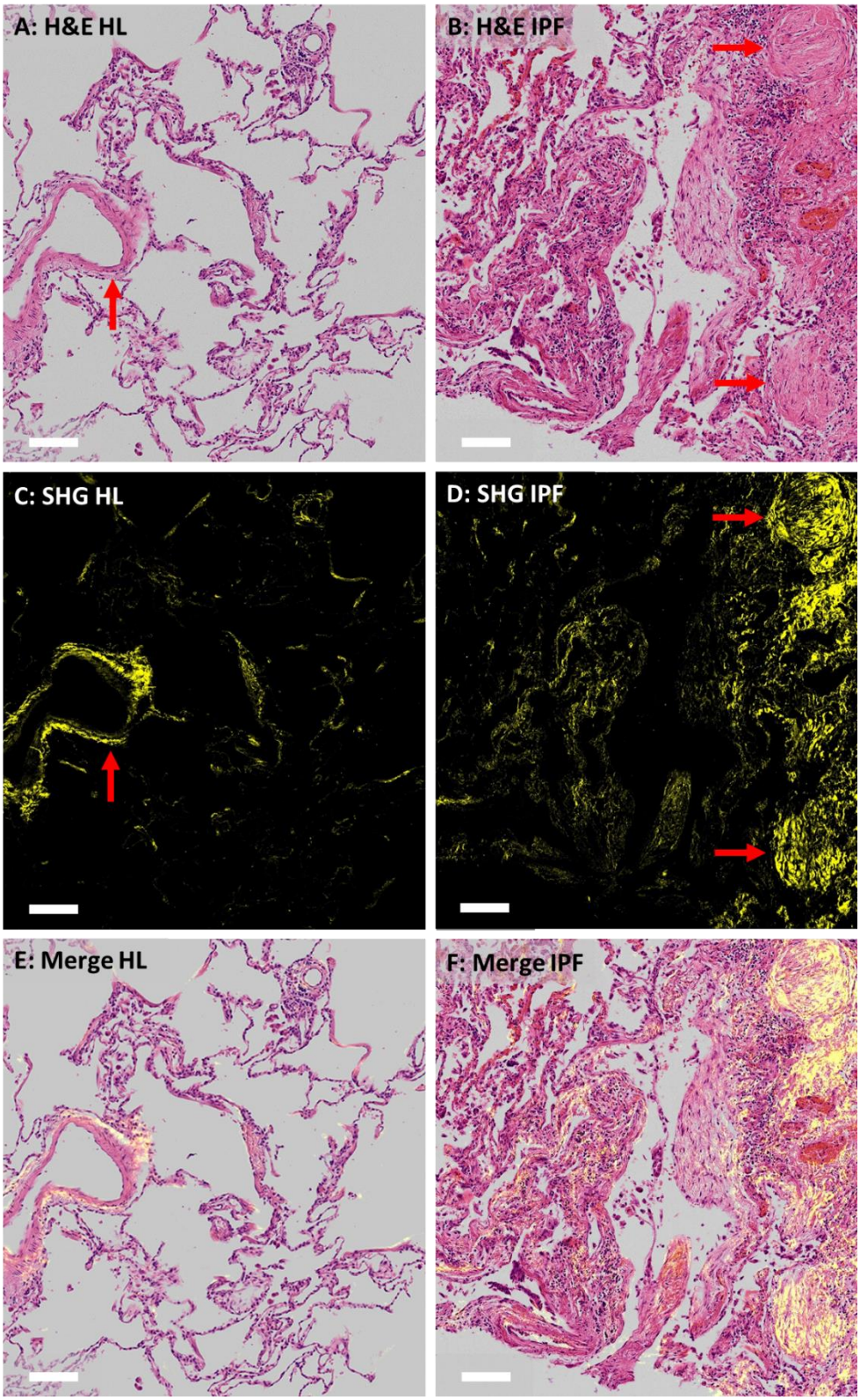

Figure 25: Correlative H&E and SHG images.
Top row: H&E images of healthy lung tissue (**A**) and IPF lung tissue (**B**). Middle row: Corresponding co-registered SHG images highlighting the distribution of collagen. (**C**) The collagen in healthy lung is primarily located around blood vessels (red arrow), whereas in IPF (**D**) the collagen forms dense deposits at fibrotic foci (red arrows). Bottom Row: Overlaid images of SHG on H&E. The collagen architecture highlighted by SHG is faithfully overlaid onto the H&E background. Scale bar 100 µm

4.6 Discussion and Conclusions

The work in this chapter establishes a workflow for the acquisition and co-registration of transmitted light microscopy images of H&E stained sections with label-free Second Harmonic Generation images. SHG images were able to highlight hallmark features of IPF such as fibrotic foci, and these were placed in the context of H&E stained slide images more familiar to pathologists. Ultimately, this workflow may allow for the simplification of IPF diagnosis by replacement of analysis of H&E images with analysis of SHG images; removing multiple sample preparation steps. However, the current protocol still contains the paraffin embedding and sectioning steps to allow correlation with images of H&E-stained sections which is time consuming. To progress further steps would need to be taken to validate imaging of bulk unprocessed biopsy samples. SHG is also able to provide additional information to morphological features that may aid in disease diagnosis.

Second Harmonic Generation imaging has been used previously to provide insight into the disease pathology of IPF. Pena *et al.* showed that SHG microscopy could be used to identify general lung fibrosis by changes in intensity and hallmark fibrotic features such as fibroblastic foci (Pena *et al.*, 2007). Tilbury *et al.* Developed this process further combining SHG intensity imaging with texture analysis to accurately diagnose IPF with >94% accuracy (Tilbury *et al.*, 2014). Kottman *et al*. (Kottmann *et al.*, 2015) used the ratio of forwards-detected SHG, to backwards-detected SHG to probe collagen microstructure highlighting a change for IPF vs healthy lung. They found this change was present between structurally different regions such as fibroblastic foci and honeycombed regions, *and* neighbouring “normal” tissue containing preserved alveolar architecture. Honeycombed regions are regions where usual alveolar architecture is lost and randomly distributed air spaces lined by fibrous tissue form (Ley, Collard and King, 2011). The authors also observed this ratio was only decreased in IPF and not in COP (Cryptogenic Organizing Pneumonia). COP is another common fibrotic lung disease characterised by changes in the collagen architecture, highlighting the diagnostic capability of the technique. More recently, James *et al.* (James *et al.*, 2019) also showed a decrease in F_{SHG}/B_{SHG} ratio between normal and IPF lung tissue. The decrease in this ratio is indicative of smaller and less organised collagen fibrils. They went on further to analyse the samples using SHG circular dichroism (SHG-CD) noting a decrease in chirality in IPF vs healthy lung. They attributed this to an increase in collagen type III (Col III) although this was not consistent with analysis of collagen pitch angle which suggested no change in the Col I/Col III ratio. These analyses were all performed using diffraction-limited SHG measurements, and despite polarisation-resolved methods indicating changes in the collagen ultrastructure, they provide an average signal over the volume of the PSF. As such, subtle changes

in SHG signals due to changes in collagen ultrastructure may become averaged out within the volume of the PSF, prohibiting detection of these subtle changes.

To analyse ultrastructural changes in collagen scientists are still reliant on high resolution techniques such as transmission electron microscopy (TEM) (Friess, 1998; Eyden and Tzaphlidou, 2001; Starborg *et al.*, 2013) and atomic force microscopy (AFM) (Wen and Cynthia Goh, 2006; Strasser *et al.*, 2007; Jones *et al.*, 2018). Despite the significant gain in resolution afforded by both AFM and TEM, each have drawbacks. TEM requires the use of heavy metal stains for contrast, whilst AFM analysis requires isolation of the collagen making native analysis in tissue unrealistic. Due to these limitations there is a clear need for an imaging technique capable of analysing fibrillar collagen in its native state. Thus, a super-resolution label-free SHG imaging method affording the benefits of SHG with improved resolution is highly desirable and will be applicable to the characterisation of many fibrotic diseases. The current protocol provides a step towards this goal however, further validation of SHG signal obtained in completely unprocessed sections is required.

The co-registered images generated by the work flow developed in this chapter can be used to guide such a super-resolution SHG imaging modality and the super-resolution images can be placed in the context of H&E images for interpretation in the context of disease pathology.

Chapter 5 Super-Resolution Second Harmonic Generation Using Photonic Nanojets

This chapter presents work published in the peer-reviewed journal Optica: “Superresolved polarization-enhanced second harmonic generation for direct imaging of nanoscale changes in collagen architecture” *Peter Johnson, Artemis Karvounis, H. Johnson Singh, Christopher J. Brereton, Konstantinos Bourdakos, Kerry Lunn, James JW Roberts, Donna E Davies , Otto L. Muskens, Mark G Jones and Sumeet Mahajan*

Contributions: P.Johnson Developed photonic nanojet imaging and performed all imaging experiments, data processing and analysis, design of resolution standards and participated in design of the study. A.Karvounis produced silicon resolution samples. J Singh performed optical simulations. C J Brereton, K Lunn, J JW Roberts, D Davies and M Jones provided lung tissue model and human lung tissue samples. O Muskens provided guidance on data interpretation. S Mahajan conceptualised, designed, and coordinated the study. P.Johnson and S.Mahajan wrote the manuscript and all other authors gave contribution and approval of the final publication.

5.1 Abstract

Super-resolution (SR) optical microscopy has allowed the investigation of many biological structures below the diffraction limit. However, most of the techniques are hampered by the need for fluorescent labels. Non-linear, label-free techniques such as Second Harmonic Generation (SHG) provide structurally-specific contrast without the addition of exogenous labels, allowing observation of unperturbed biological systems. The photonic nanojet (PNJ) phenomenon was used to achieve super-resolution SHG (SR-SHG). A resolution of ~λ/6 with respect to the fundamental wavelength, a ~2.3-fold improvement over diffraction-limited SHG under the same imaging conditions, was achieved. Crucially, it was shown that the polarisation properties of excitation are maintained in a PNJ. This was observed in experiment and simulations. This allowed resolution to be further enhanced by detection of polarisation-resolved SHG (p-SHG) by observing anisotropy in signals. These new findings allowed us to visualise biological SHG-active structures such as collagen at a scale previously unresolvable by SHG microscopy. Moreover, the use of an array of self-assembled, high-index spheres overcame the issue of a limited field of view for such a method, allowing PNJ-assisted SR-SHG to be used over multiple fields of view simultaneously. Dysregulation of collagen at the nanoscale occurs in many diseases and is an underlying cause in diseases such as lung fibrosis. This study demonstrated that pSR-SHG allows unprecedented observation of changes at the nanoscale that are invisible by conventional diffraction-limited SHG imaging. The ability to non-destructively image SHG-active biological structures without labels at the nanoscale with an optical method heralds the promise of a new tool to understand biological phenomena and drive drug discovery.

5.2 Background

Second Harmonic Generation (SHG) microscopy is a structurally-specific technique that highlights non-centrosymmetric structures without the addition of exogenous and potentially perturbative labels. SHG active materials include certain non-linear crystals such as Barium Titanate ($BaTiO_3$) and biological macromolecules including: myosin (Plotnikov *et al.*, 2006), microtubules (Van Steenbergen *et al.*, 2019), DNA (Zhuo and Ni, 2015) and fibrillar collagen (Williams, Zipfel and Webb, 2005; Strupler *et al.*, 2007; Chen *et al.*, 2012). SHG imaging is widely used to image fibrillar collagen (Pavone and Campagnola, 2014). SHG is highly polarisation sensitive; intensities depend on the relative orientation between the excitation and the second harmonic active structure (Campagnola and Dong, 2011). Thus, polarisation resolved SHG (p-SHG) is used to acquire information about the orientation and degree of organisation of harmonophores, for example, to calculate the helical pitch angle of collagen fibrils (Su *et al.*, 2011) and the tilt angle of the helices relative to the fibril axis (Tuer *et al.*, 2011). It has also been used to understand the differences between collagen types in tissues (Romijn, Finnøy and Lilledahl, 2018), and investigate the effect of mechanical stretching on collagen disorder within tendon tissue (Gusachenko *et al.*, 2012). Collagen and its deposition/accumulation plays a critical role in many diseases especially fibrotic diseases such as liver fibrosis and idiopathic lung fibrosis (Tilbury *et al.*, 2014; Kottmann *et al.*, 2015; Peng *et al.*, 2015). The ability to resolve SHG-active structures at the nanoscale is needed as changes occur at the level of molecular-structures and assemblies such as the actin-myosin complex (Plotnikov *et al.*, 2006), microtubules (Dombeck *et al.*, 2003) and fibrillar collagen (Strupler *et al.*, 2007; Campagnola and Dong, 2011; Lutz *et al.*, 2012), all of which are SHG-active. Despite the growing utility of SHG in collagen imaging there has been limited progress in development of super-resolution (SR) SHG methods (SR-SHG), especially compared to SR fluorescence modalities (Hell *et al.*, 2015).

A handful of implementations of SR-SHG have recently been demonstrated. The concept of dark beam imaging has been used to improve the resolution of an SHG microscope(Tian, Fu and Gu, 2015), reporting a 1.3 fold improvement in lateral resolution. Gregor *et al.* (Gregor *et al.*, 2017) also achieved SR-SHG using an image scanning method, reaching a resolution of 151 nm with additional computational processing, and more recently Barlow *et al.* (Barlow *et al.*, 2020) implemented a similar approach modifying a commercial Zeiss AriyScan system. Two practical implementations of SHG using structured illumination have been practically realised; Yeh *et al*. (Yeh *et al.*, 2018) used a modified quasi-comb scanning to modulate the illumination pattern at

the sample achieving a 1.4 times improvement in lateral resolution, whilst Urban *et al.* (Urban *et al.*, 2018) used a regular scan pattern but instead modified the illumination intensity such that a sinusoidal illumination pattern was achieved, reporting a 1.59 times improvement in lateral resolution. This handful of practical implementations of SR-SHG constitute the extent of super-resolution label-free imaging of collagen.

Super-resolution using SHG-active structures as a label was implemented by Liu *et al.* (Liu *et al.*, 2014). They used barium titanate nanocrystals attached to a short oligonucleotide to probe the location of single copies of mRNA. The resolution was achieved in a SMLM-like fashion however here separation of emitters was achieved by rotating the input polarization such that only a few nanocrystals were excited at any one time. The authors report a resolution of 55.6 nm, approaching that of fluorescence SMLM methods. The advantage here however, is that as a parametric process the SHG intensity will not bleach, allowing for long-term imaging.

It is of note that all implementations of label-free SR-SHG thus far have either been based on SIM-like methods and therefore have a maximum improvement in resolution of 2x, or for the case of dark beam imaging, are still limited by diffraction but to ~λ/4, again giving an approximate 2x improvement over the conventional diffraction limit (Dehez, Piché and De Koninck, 2013). All of these applications require retrofitting of extra scanning mechanisms to the beam path or methods of modulating the beam profile to the existing SHG microscope. This is a non-trivial task for those inexperienced in optics, inhibiting the widespread adoption of these methods. The research in this chapter covers the development of an inexpensive and simple to implement addition to existing SHG imaging systems, that facilitates SR-SHG imaging. The method is capable of a greater than two times improvement in resolution and is broadly applicable to many multiphoton modalities.

Here the photonic nanojet (PNJ) phenomenon in employed to realise label-free SR-SHG imaging, as it does not rely on manipulation of fluorescence emission and is simple-to-implement. A PNJ is a localised focus of light with an intensity cross section narrower than the diffraction limit that is able to propagate over multiple wavelengths (Chen, Taflove and Backman, 2004). The most common method of generating a PNJ is to use a dielectric microsphere although other shapes have been explored (Minin, Minin and Geints, 2015; Liu *et al.*, 2018). Alongside the photonic nanojet, whispering gallery modes (Zhou *et al.*, 2017), elements of solid immersion lens theory (Lee, Li, Ben-Aryeh, *et al.*, 2013; Darafsheh *et al.*, 2014) and near field effects (Devilez *et al.*, 2009; Devilez, Bonod and Stout, 2010; Hao *et al.*, 2013) have also been suggested as contributing to the SR imaging capability of PNJ generating microspheres. The focal spot of a PNJ, when generated using a microsphere is dependent on multiple parameters including sphere size, imaging

wavelength and the refractive index contrast with the surrounding medium (Patel, Kushwaha and Swami, 2018b). For biological imaging, the contrast should be ideally maximised against the microscope immersion medium.

To image a sample using a microsphere generated PNJ the sphere is illuminated by an objective and focuses the light onto the sample. The objective is focussed at a distance z beneath the sphere-sample contact point and captures the virtual image created by the microsphere (Figure 26).

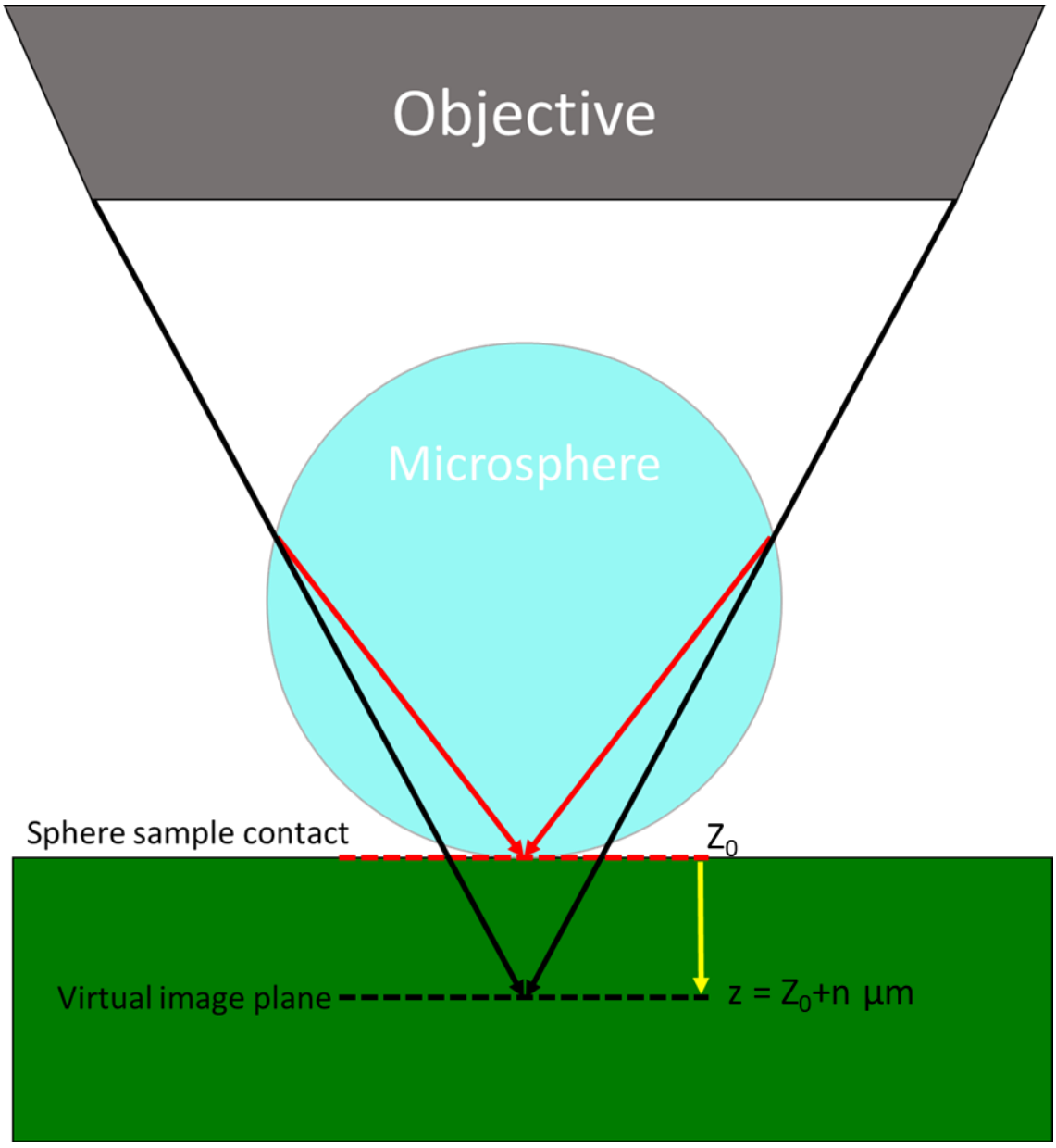

Figure 26: Schematic diagram of PNJ imaging using a microsphere.
The microsphere is placed between the objective and the sample. The objective illuminates the sphere (black arrows) which focuses the light into a PNJ (red arrows). The objective is focused at the virtual image plane (black dashed line), which is at a distance z (yellow arrow) below the sphere-sample contact Z_0 (red dashed line).

Imaging with PNJs has been typically performed in a widefield configuration where it has been used to achieve label-free super-resolution using a white light microscope (Wang *et al.*, 2011). It has also been used to image biological structures such as adeno viruses (Li *et al.*, 2013) using white light and sub-cellular structures such as centrioles and mitochondria using fluorescent labelling (Yang *et al.*, 2014). Similarly, Darafsheh *et al.* (Darafsheh, Guardiola, Nihalani, *et al.*, 2015) imaged fluorescently-stained glomeruli using a microsphere-embedded coverslip, using both brightfield and epifluorescence (Wang *et al.*, 2011; Yang *et al.*, 2014). Laser scanning imaging using PNJs was demonstrated by Yan *et al.* (Yan *et al.*, 2014) who imaged plasmonic gold nanostructures with a resolution of 25 nm. The ability of PNJs to improve multiphoton processes has been shown by Lecler *et al.* (Lecler *et al.*, 2007) reporting an up to 30% enhancement in TPEF signal for a Rhodamine B solution. Multiphoton imaging was briefly explored by Tehrani *et al.* (Tehrani *et al.*, 2018), however, a full characterisation and exploration of the potential of the technique is lacking.

In this chapter, the ability of PNJs generated by a microsphere are first verified for single-photon wide field and laser scanning geometries. SHG generated using PNJs is then verified and optimum imaging parameters established. Super-resolved SHG is demonstrated and quantified and a route to extended field of view of SR-SHG imaging is demonstrated. The origin of SR imaging using PNJs is investigated highlighting a critical near-field component. The polarisation properties of the photonic nanojet are also explored and characterised enabling polarisation-resolved SR-SHG (pSR-SHG). Nanoscopic anisotropy analysis enabled by pSR-SHG is used to detect underlying nanoscale changes in collagen during the development of lung fibrosis. Overall, the research heralds the role that label-free super-resolution techniques can play to unravel underlying biological phenomena and improve our understanding of disease mechanisms.

5.3 Materials and methods

5.3.1 Materials

FEP film (RS-online, FEP FILM 304X200X0.025MM). Barium titanate glass (BTG) microspheres (Cospheric LLC, Santa Barbara, CA) were obtained in 2 size ranges 5 µm-22 µm (small) and 55 µm-60 µm (large), the refractive index of the spheres is n=1.9. Due to the variation in size of microspheres particularly the small range, spheres used for imaging were selected by eye once deposited on the sample and those of sizes different to that desired were not used for imaging. Poly-L lysine was used at 1 mg/ml (MERCK). Paraformaldehyde 16% Solution (methanol-free) - 10x10ml ampoules diluted to 4% in PBS (Agar Scientific).

5.3.2 Lung Cell Culture Tissue Model

Primary lung fibroblasts from a patient with Idiopathic Pulmonary Fibrosis (IPF) were seeded in Transwell inserts under normal conditions for 24 hours before the media was replaced with that containing b-aminoproprionitrile (BAPN), which inhibits cross-linking of collagen fibres, or control conditions. After 6 weeks of growth under these conditions the spheroids were harvested, fixed in 4% paraformaldehyde, paraffin embedded, and 5 µm sections cut ready for imaging.

5.3.3 CT-FIRE Analysis

Collagen fibre analysis was performed using CT-FIREV1.3 (LABORATORY FOR OPTICAL AND COMPUTATIONAL INSTRUMENTATION, LOCI) (Bredfeldt *et al.*, 2014). This software uses a curvelet transform (CT) and a fibre extraction algorithm (FIRE) to computationally extract and analyse fibres from microscopy images. Four parameters were measured to describe fibre morphology: width, length, straightness and angle SHG intensity images were converted to 8-bit format before being batch processed using default parameters.

5.3.4 Development of a pSHG Imaging System

SHG efficiency depends on the relative orientation of the excitation polarisation and the harmonophores. The polarisation-dependent response can be characterised in multiple different ways including SHG polarisation anisotropy, $r = (I_{\parallel} - I_{\perp})/(I_{\parallel} + 2I_{\perp})$, where $I_{\parallel}$ and $I_{\perp}$ are the intensities recorded parallel or perpendicular to incident polarisation (Campbell and Tummino, 2014). It can also be used to measure the full polarisation response across 360 ° of excitation or

the SHG circular dichroism by measuring the ratio of right hand to left hand circularly-polarised light (Mazumder *et al.*, 2017). To exploit the polarisation-dependent properties of SHG, the existing multiphoton imaging system was modified to allow pSHG imaging. The first step in this process was to determine the linearity of the excitation at the sample plane of the microscope. To do this a near infrared polariser was placed at the objective focus and a power meter placed directly behind it. Figure 27 shows the result of rotating the analyser in 10° steps through 360°, it was seen that the polarisation at the output of the microscope was not highly linearly polarised but rather elliptic and had an extinction ratio of 0.42 without an objective lens in the beam path and this increased to 0.52 with a 63x/1.2NA objective used for SHG imaging. The objective was not designated as strain-free and therefore the purity of the polarisation will have been affected. This objective was selected as it had the highest NA of the water immersion objectives available. Water immersion was chosen to facilitate better refractive index contrast between microspheres and the immersion medium than would be possible with oil or glycerol immersion.

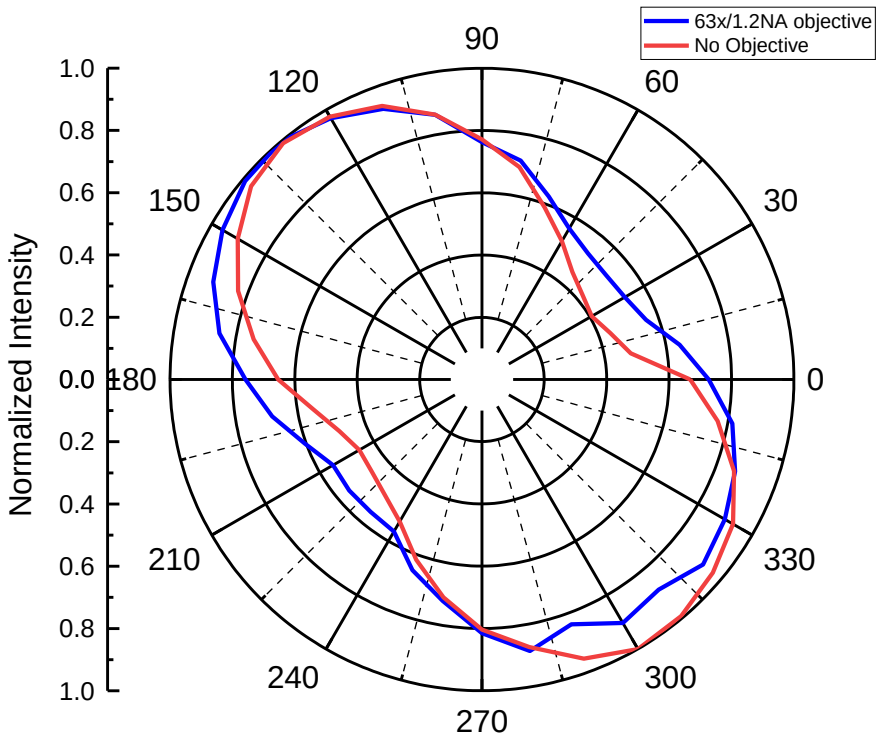

Figure 27: Power vs analyser angle at the microscope focus with and without 63x/1.2NA objective.
The objective reduces the linearity of the polarisation. Extinction ratios: 0.52 with objective 0.42 no objective.

To improve the degree of linear polarisation of the illumination beam at the objective focus and to introduce the ability to manipulate the orientation of the linear polarisation, a polarisation module was installed in the beam path. Figure 28**A** shows the polarisation module consisting of a

half-wave plate (λ/2)(Thorlabs, AHWP10M-980) and a quarter-wave plate (λ/4) (Thorlabs, WPQ10M-808); the λ/2 allows rotation of the linear polarisation and the quarter-wave plate allows pre-compensation of the beam to counteract the ellipticity introduced by the optics of the microscope.

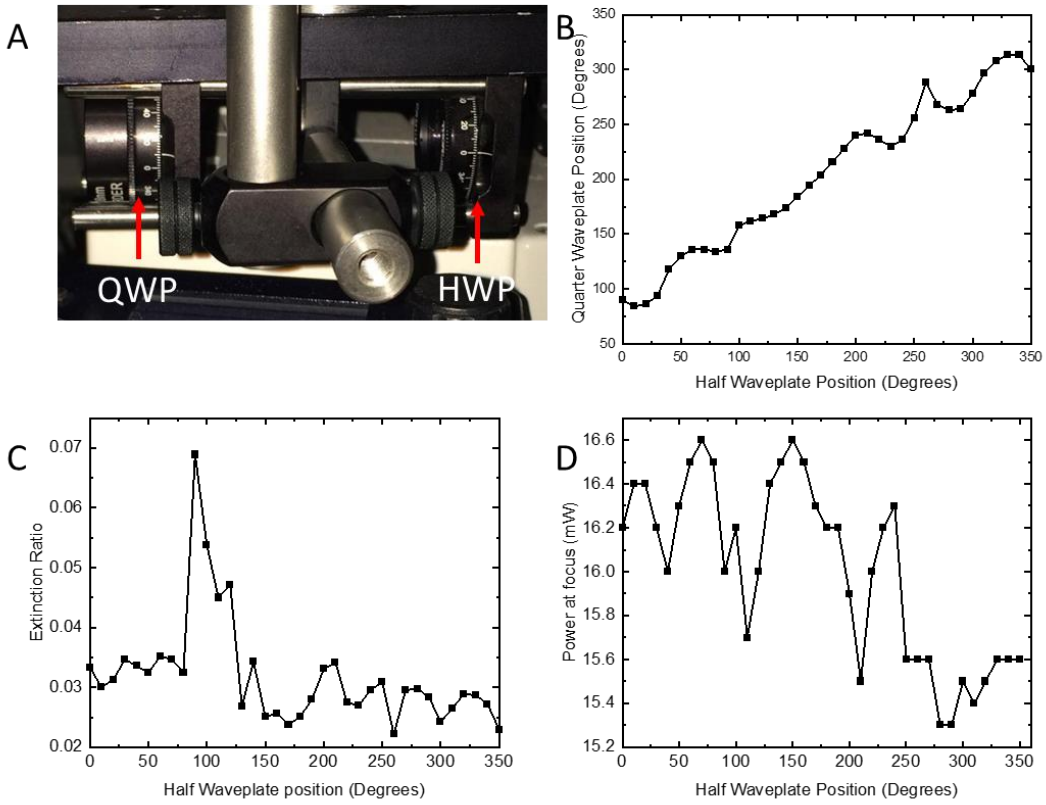

Figure 28: Polarisation compensation module.
(A)The polarisation module used to control polarisation at the sample: QWP = Quarter waveplate, HWP = Half waveplate. (B) The combination of λ/2 and λ/4 positions determined to give the required rotations in linear polarisation. (C) The extinction ratio achieved for each linear polarisation. (D) The variation in power at the sample plane with rotating polarisation.

To determine the optimum combination of λ/2 and λ/4 positions to allow 360 degree rotation of linear polarisation at the sample an analyser/power meter setup was placed at the objective focus as described previously. The analyser was moved in 10 degree steps and the positions of the λ/2 and λ/4 were adjusted to maximise the power measured. Figure 28**B** shows the relative positions of the two wave plates that gave maximum transmission. At each step the analyser was also rotated by 90° and the extinction ratio was calculated to evaluate the degree of linear polarisation (Figure 28**C)**. The extinction ratio was decreased to ~0.025- 0.035 for most polarisation positions, 20 times better than without the polarisation module. A few positions showed a marginally worse extinction ratio of 0.04 ~ 0.07 and this was deemed to be due to a small damaged region on the λ/2 that entered the beam path at certain angles of the λ/2. As polarisation oscillates with a

sinusoidal function the angles 0° to 180° are degenerate with the 180° to 360°, thus for all subsequent imaging experiments only the 180° -360° were used. A suitable combination of positions to achieve circular polarisation at the sample were also determined by fixing the position of the λ/2 and rotating the quarter-wave plate until the extinction ratio was 1. As SHG signal intensity has a quadratic dependence on the excitation power it was important to characterise the power at the sample for different polarisations as the excitation dichroic has different efficiencies for different polarisations. For the range of angles used there was a variation of ~6% in power at the sample (Figure 28**D**), this was deemed to be an acceptable amount of variation as this was within previously-measured fluctuations in the laser source intensity over time (not shown). For subsequent anisotropy measurements, this was also deemed acceptable as a fixed excitation polarisation was used for each pair of measurements.

5.3.5 One-photon Imaging of Test Structures

Before commencing label-free imaging using photonic nanojets it was necessary to perform preliminary investigations to verify the PNJ technique. Barium titanate glass (BTG) microspheres were suspended in filtered, deionised water and deposited onto the sample using a pipette for imaging using a water immersion objective (63x, 1.2NA), the sample was illuminated using a mercury lamp in an epi-illumination configuration. The chip size of the camera was 1200 x 1600 pixels and the physical pixel size was 7.4 μm^2, using the 63x objective the effective pixel size was 117 nm.

The first investigation was to image features on a silicon chip consisting of an array of straight line features that are larger than the diffraction limit (

Figure 29 **A/B**). When imaging through the spheres the straight-line features have been magnified relative to the image taken without a sphere in place. However, because the features are well above the diffraction limit this does not verify if PNJs are capable of super-resolution imaging. A common sample used in the literature is a Blue Ray disc (Upputuri *et al.*, 2014; Darafsheh, Guardiola, Palovcak, *et al.*, 2015; Lee and Li, 2015; Yang *et al.*, 2017; T. Chen *et al.*, 2018) as the lateral size of the ridges and grooves is on the order of 100 nm-200 nm. Blue Ray disc samples (Verbatim) were prepared by carefully removing the transparent reflective layer with scissors to reveal the feature-bearing recording layer underneath. Microspheres were then placed directly onto the recording layer surface. The size of the features on the disc were characterised using an Atomic Force Microscope (**D**), a line plot taken from the image showed the ridges to have a FWHM of 131nm (

Figure 29 **E**). Using the Rayleigh equation, the minimum resolvable distance using a 1.2 NA objective and the 436 nm line of the mercury lamp is given by

$$\frac{0.61 \times 436\ nm}{1.2} = 222\ nm$$

The lamp was used unfiltered however the camera chip contained an RGB filter which limited the detected wavelengths, therefore, the shortest wavelength detected was assumed to be the 436 nm band.

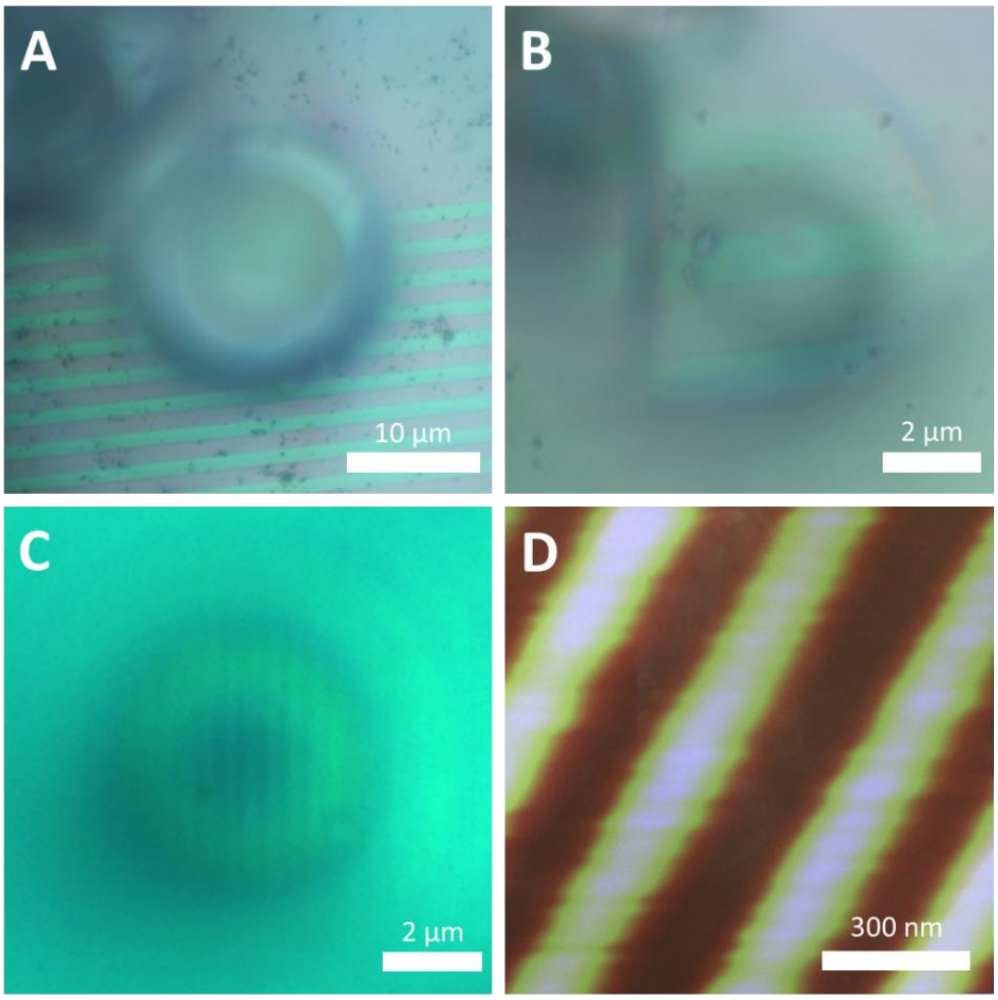
A
10 µm
B
2 µm
C
2 µm
D
300 nm

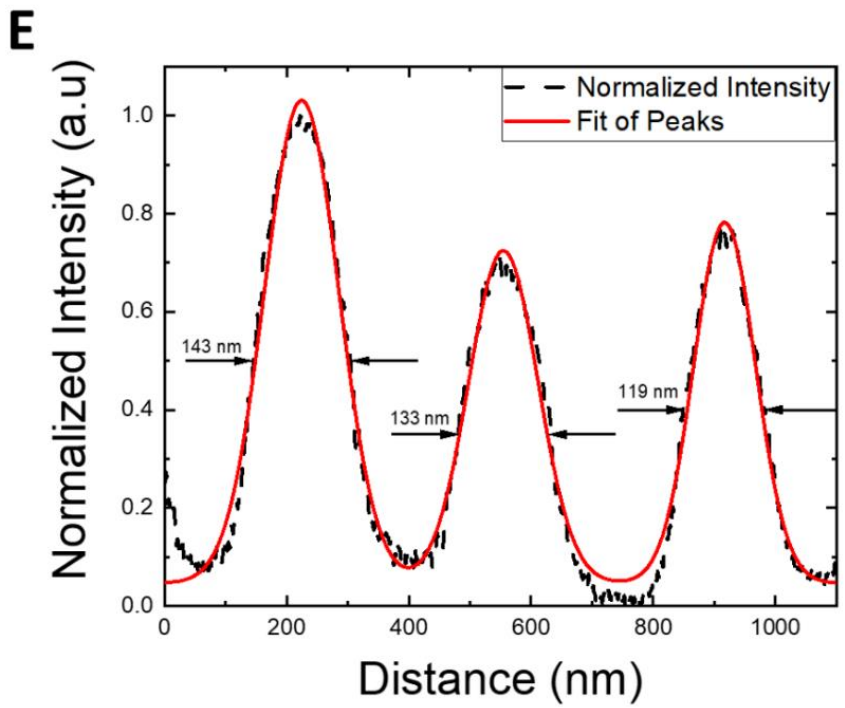
E
Normalized Intensity
Fit of Peaks
Normalized Intensity (a.u)
Distance (nm)
143 nm
133 nm
119 nm
0.0
0.2
0.4
0.6
0.8
1.0
0
200
400
600
800
1000

Figure 29: Validation that PNJ microscopy allows super-resolution imaging.
A: A diffraction-limited, reflected light image of line features of a Si chip. The 63x/1.2NA objective is focussed at the sample surface and the 20 µm diameter sphere can be seen in the centre of the image. **B**: The same location as in A imaged through the microsphere. This is achieved by focussing below the sample surface at the virtual image plane. An increased magnification of the line features can be seen. **C**: Bright field reflectance image taken through a 20 µm diameter sphere of sub-diffraction features on an unwritten bluray disc. The features are unresolvable without the addition of microspheres but can be resolved once viewed through a sphere. Image scaling takes into account the extra magnification given by the sphere. **D**: AFM image of the unwritten blue ray disc. **E:** peak fitting of line plot across the image showed an average FWHM of 132 nm and a peak-peak separation of ~330 nm.

Therefore, the features were smaller than the diffraction limit for the wavelength and objective lens used. At this wavelength (436 nm) it is noted that the 117 nm pixel size results in sub-Nyquist sampling of the image and may be the reason that the features of the disc could not be resolved. However, the mercury lamp also has major lines at 546 nm and 579 nm giving diffraction-limited resolutions of 277 nm and 294 nm respectively. At these wavelengths the signal is adequately sampled. As the collected signal was not spectrally filtered it is not possible to determine whether under sampling was the reason the features could not be resolved. Addition of the microsphere allowed resolution of the features of the disc (

Figure 29 **C**). This may be due to the extra magnification of the microsphere resulting in adequate sampling or the microsphere providing improved resolution, or both. Nevertheless, this result showed that microspheres were able to improve the resolution of our system.

5.3.6 Laser scanning and Second Harmonic Generation

After establishing PNJ imaging using spheres with wide field imaging it was necessary to confirm whether the technique would work under laser scanning, since SHG imaging is carried out using laser scanning. Although this has been shown before by Yan *et al.* (Yan *et al.*, 2014) using a confocal laser scanning microscope we wanted to establish it on our system. The multiphoton imaging system using a 63x/1.2NA objective was used. Figure 30**A** shows an image of Rayleigh scattering from 80 nm Au nanoparticles immobilised on a coverslip. The sample was generated by incubating 80 nm particles (BBI solutions) with coverslips coated with poly-L lysine for 24 hours at 4°C to allow some nanoparticles to adhere to the surface without aggregation to the extent possible. The image was taken with 800 nm excitation and the emission filter was removed to observe all signals from the sample. The dark spot in the centre of Figure 30**A** is where a microsphere is placed. Figure 30**B** is an image taken under identical conditions (objective magnification, optical zoom, laser power) as A, but imaged through the microsphere. The image was acquired at the virtual image plane, the sphere generates a magnified image. To determine whether the resolution was also improved and not just empty magnification, 80 nm particles were chosen as they are smaller than the diffraction limit for the fundamental wavelength and would therefore act like a point source. A common method for evaluating the resolution of a microscope system is to image a series of point sources and measure the full width half maximum (FWHM) of the point spread function. This is a convenient method for measurement of resolution however the width of the PSF does not necessarily equate to the minimum resolvable distance between two objects. If the point sources are separated by a defined distance measuring a dip in the intensity maxima between two neighbouring point sources can be used as a measure of the resolution. Unfortunately, it was not possible to determine the magnification or resolution improvement as the spacing between nanoparticles was not well defined and it was difficult to distinguish single nanoparticles from nanoparticle clusters.

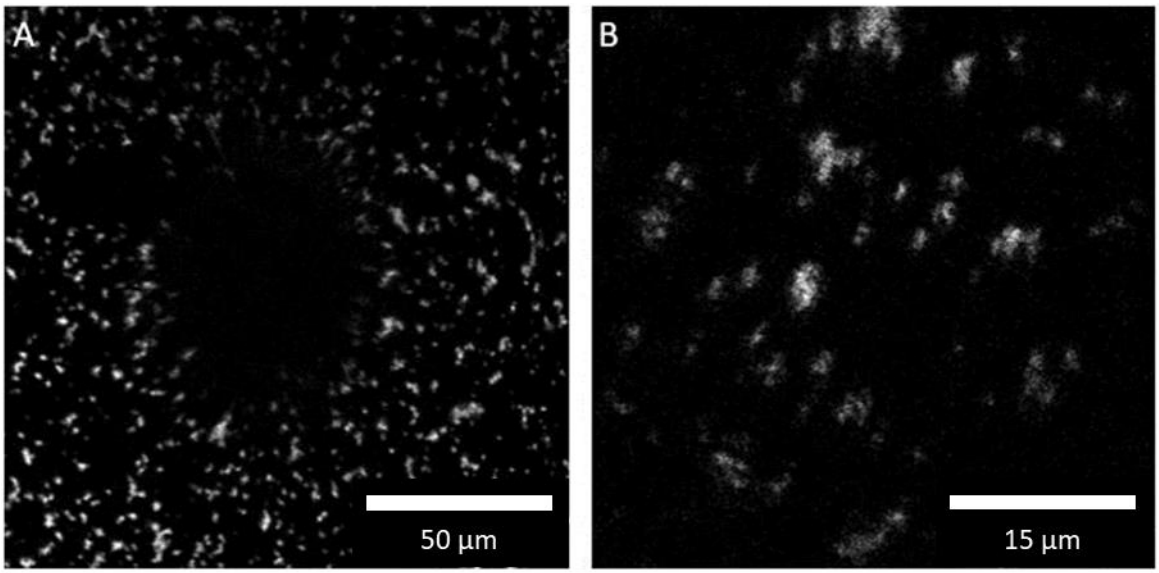

Figure 30: PNJ Imaging of AU nanoparticles
A: An image of laser scatter at 800 nm taken focussed at the sample plane, a dark circle can be seen where the BTG sphere is placed. The scanned FOV was 155 µm x 155 µm imaged onto 2048 x 2048 pixels giving an effective pixel size of 76 nm. The imaging objective was 63x/1.2NA **B**: An image taken through the BTG sphere, this is achieved by refocussing the objective at the virtual image plane and changing no other parameters. The image shows increased magnification relative to A however, individual nanoparticles can not be reliably identified and thus an improvement in resolution could not be determined.

5.3.7 PDMS Embedded Spheres

A major drawback of PNJ-assisted imaging is the limited field of view (FOV) of a single microsphere and the difficulty in locating a microsphere to a region of interest (ROI). Inspired by Darafsheh *et al*. (Darafsheh, Guardiola, Nihalani, *et al.*, 2015) a microsphere embedded film was developed to overcome this limitation. Dry microspheres were spread onto a clean microscope slide then a thin layer of polydimethylsiloxane (PDMS) was added carefully over the spheres. Once cured this resulted in a thin, flexible and transparent film (Figure 31**A**). A low density of microspheres was used so that the images formed by neighbouring microspheres did not overlap with each other (Figure 31**B**). The effect of close-packed spheres and overlap is discussed later (section 5.4.5). Larger spheres (60 µm) where used for these experiment as the aim was to maximise the effective FOV. The refractive index of PDMS (n = 1.43) is greater than water (n = 1.33), however due to the high refractive index of BTG spheres (n = 1.9), the refractive index contrast between microsphere and medium was still large enough to allow PNJ formation (Lee, Li, Wang, *et al.*, 2013; Xing *et al.*, 2017).

To test whether the microsphere film allowed SHG imaging, micrographs of a lung tissue sample were acquired with and without the use of the film. Imaging using the microsphere film was able to produce the expected magnified images of collagen structure (Figure 31**E/F**). The film allowed for simpler translation of the microspheres to a region of interest however some drawbacks of the film were observed: Not all microspheres within the film were able to produce an image, this was determined to be due to two reasons. For some of the spheres within the film the PDMS had crept underneath the microsphere resulting in the sphere not being in contact with the sample. Due to the requirement of close proximity of the sample with the PNJ this obstructed the imaging. For other spheres within the film it was observed that there was a thick layer of PDMS on top of the sphere. Because imaging using PNJs requires focusing of the microscope objective at a virtual image plane at distance z beneath the sphere-sample contact point; the combined thickness of the PDMS layer, microsphere and z must be less than the working distance of the objective lens. For the high NA (1.2) objective used the working distance is 220 µm. The combined thickness of the microsphere and z was determined to be ~130 µm leaving only 90 µm spare for PDMS and hence, in cases where the layer thickness is more than this it is not possible to focus the objective at the required axial plane. As the objective used had coverslip correction, a desirable thickness for the PDMS layer would be such that the optical pathlength could be matched to that of a standard coverslip. A N°1.5 coverslip has a thickness of ~170 µm and a refractive index of 1.52 giving an optical pathlength of 258.4 µm, PDMS has a refractive index of 1.4 therefore it should be ~185 µm thick to have a matched pathlength. If this could be achieved, then it should act to help minimise aberrations that may be introduced by operating without a standard coverslip. Other

implementations of PDMS-embedded spheres have used spin coating to create the PDMS layer (Yang *et al.*, 2017). Using this method creates a thin layer of PDMS and therefore avoids the issues encountered above. However, as simplicity was a key aim for the SR-SHG method it was decided to investigate other methods of improving the PNJ FOV.

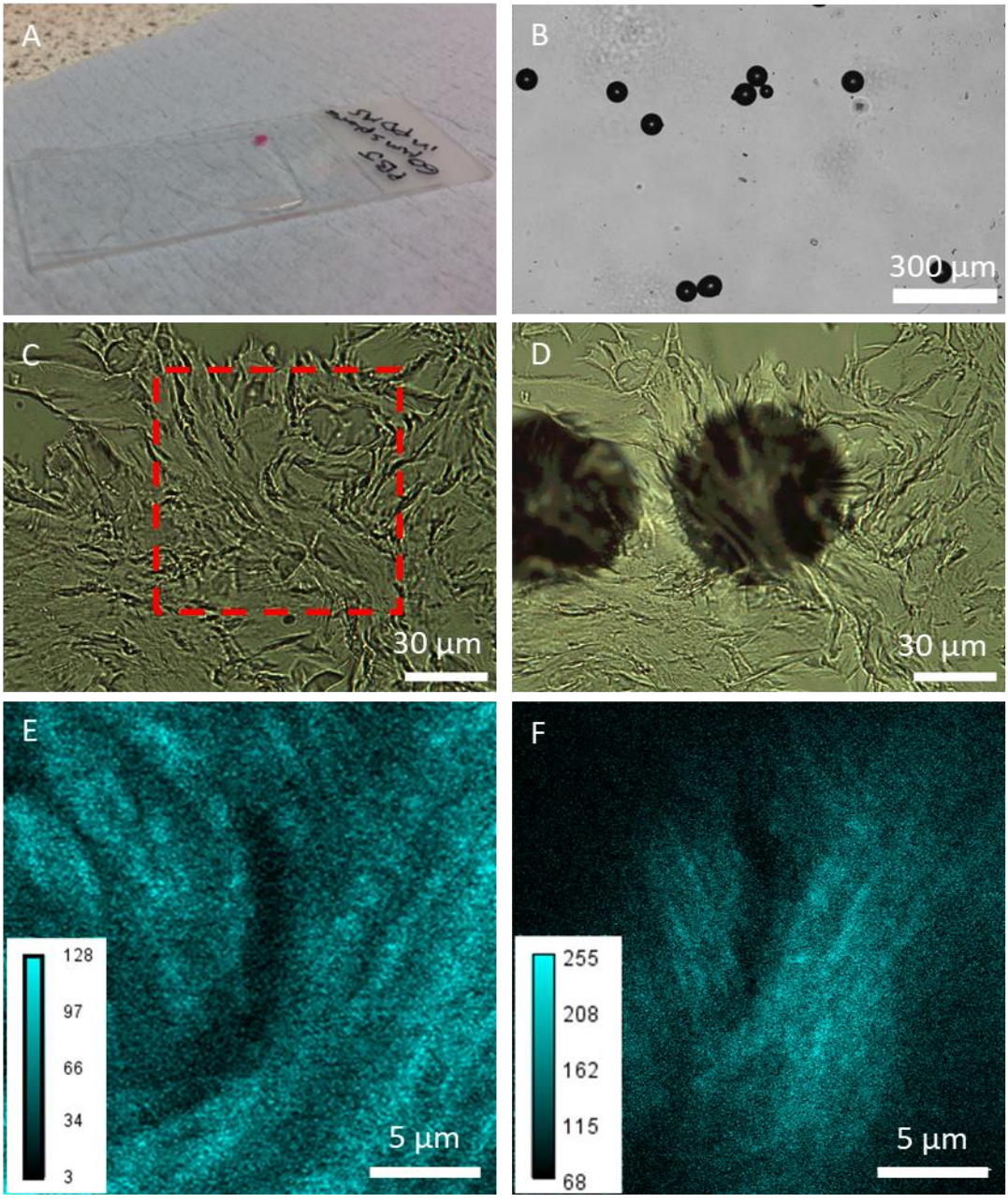

Figure 31: Development of a sphere embedded film.

(A) Macro image of the PDMS film containing microspheres on a microscope slide. (**B**) Brightfield image showing sparsely distributed spheres embedded in PDMS. (**C**) Bright field image of a lung tissue sample. (**D**) The same location as C but with PDMS embedded sphere in place. (**E**) SHG image of red square marked in C. Acquired using 63x/1.2NA objective with an effective pixel size of 101 nm, the displayed FOV have been cropped to match the FOV in F. (**F**) SHG image of the same FOV as E, taken through the sphere in D. This was achieved by refocussing below the sphere without changing any other imaging parameters.

Page left intentionally blank.

5.3.8 Microsphere Objective Adaptor

Inspired by the literature (Darafsheh, Guardiola, Palovcak, *et al.*, 2015; Xing *et al.*, 2017) a custom objective adaptor was designed to locate the microsphere in front of the objective such that it can be moved independently of the sample allowing precise location of the SR FOV using normal translation of the microscope XY stage. In order to hold the microsphere in front of the objective the microsphere was heat bonded to a 25 µm thick film of fluorinated ethylene propylene (FEP). FEP was chosen as it is durable, transparent and has a refractive index of n = 1.34 which is closely matched to water. The close matching of the refractive index of FEP and water minimises the effect of the additional material interface on PNJ focussing. Microspheres were attached to the FEP film in the following way. Microspheres were dispersed onto a clean dry microscope slide covered by a FEP film. These elements were then placed into an 80° C oven for 10 minutes whilst pressure was applied using a 1 kg aluminium block. Heating the FEP to 80 °C brought it to the glass transition temperature such that it formed around the microsphere. This method of adhesion avoided the use of any adhesives which may interfere with PNJ focussing, it also avoided extra layers of material which may affect the ability to focus at the virtual image plane as observed with the PDMS-embedded microsphere film. The FEP film was then attached to an SM1 retaining ring (Thorlabs) which was screwed into a single axis micrometre translation mount (SM1Z, Thorlabs). The objective lens was then mounted behind the FEP film using 30 mm cage optics (Thorlabs), this entire assembly could then be attached to the microscope objective port

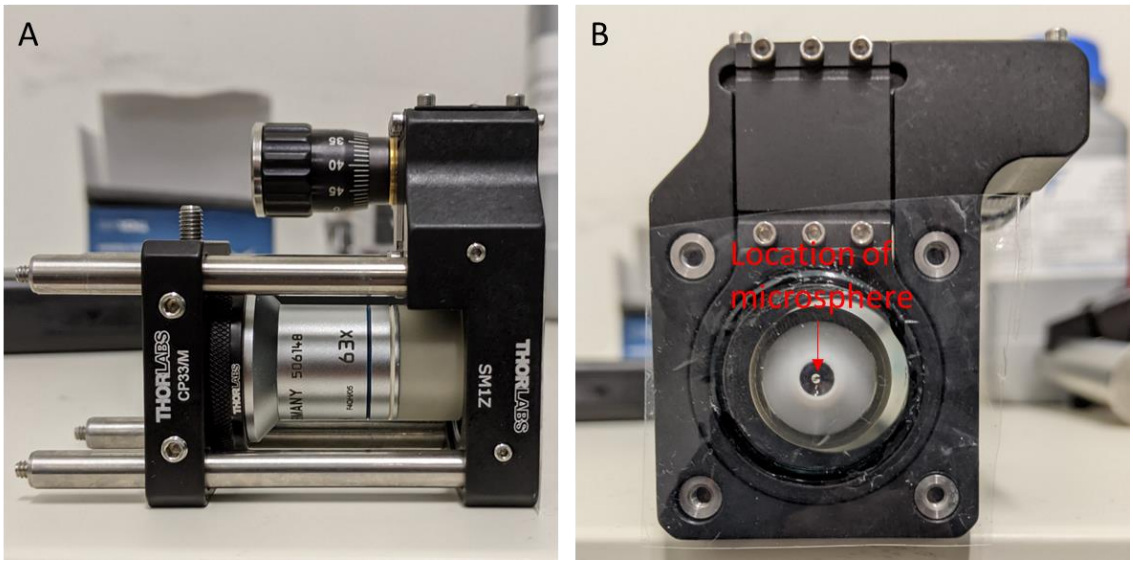

Figure 32: Microsphere Objective Adaptor.
(A) Side and (**B)** front view of the custom objective adaptor designed to hold the microsphere in a FEP film in front of the objective whilst the position of the microsphere along the optical axis can be adjusted.

The z axis translation mount allowed precise control of distance between the objective lens and the microsphere such that the objective could be focussed at the virtual image plane as is required for PNJ imaging. It was hoped that translation of the FEP film in the XY plane would allow placement of the microsphere along the optical axis however, it was found that this was too coarse to achieve acceptable alignment. It is possible to position the microsphere-FEP film in XY using a precise micrometre mount however, this removes the ability to translate the sample in z. Three axis mounts are also available (Thorlabs, CXYZ05/M) however the clear aperture at the centre of these mounts is only 12.7 mm wide and therefore can't accommodate the microscope objective. As a focus of this work was to develop a simple and easily implementable method or SR-SHG other routes to expanding the usable FOV were explored.

5.3.9 Self-assembled Sphere Array

To aid simplicity and maximise FOV, rather than locating a single sphere to an ROI and taking multiple images by moving the sphere each time, it is also possible to locate multiple spheres onto the sample surface and take an image incorporating multiple SR FOVs in a single frame. To maximise the sample area covered by SR FOVs the microspheres should be arranged in a close packed formation. Manual manipulation of the spheres to achieve this end is time consuming and may result in microscopic damage to the sphere surfaces that will affect imaging quality. It was found that ø = 60 µm spheres held in suspension in water within a glass vial (MERCK, Z188719), when inverted and gently returned to the correct way up, formed a raft on the meniscus of the water (Figure 33**A**, red circle). It was possible to transfer this raft to a coverslip or a sample whilst maintaining most of the close packed nature of the raft. To improve the transfer of the raft to the sample the glass vial was modified to remove the base and the sample was used as the base of the vial. After formation of the raft by inversion the vial was gently lifted to allow most of the water to escape, the remaining volume of water was dried at room temperature leaving the sphere array deposited on the sample surface. Using this method is was possible to cover large sample areas with an array of microspheres , greatly improving the effective super-resolution field of view (Figure 33**C**). Smaller microspheres (ø = 5-22 µm) did not form rafts on the meniscus of the water, this may have been due the larger range of sphere sizes in this batch of spheres, which affects the ability to form an ordered sphere array. With suitable sorting of spheres into more monodisperse groups it may be possible to create sphere arrays with smaller spheres. It is noted that the sphere array doesn't account for surface topology and as such the FOVs generated will potentially be at different axial planes to each other. Additionally, there are blank regions between neighbouring spheres that are not imaged. Therefore, the sphere array provides a

method of imaging multiple smaller super-resolution FOVs, not a method of creating one larger stitched FOV.

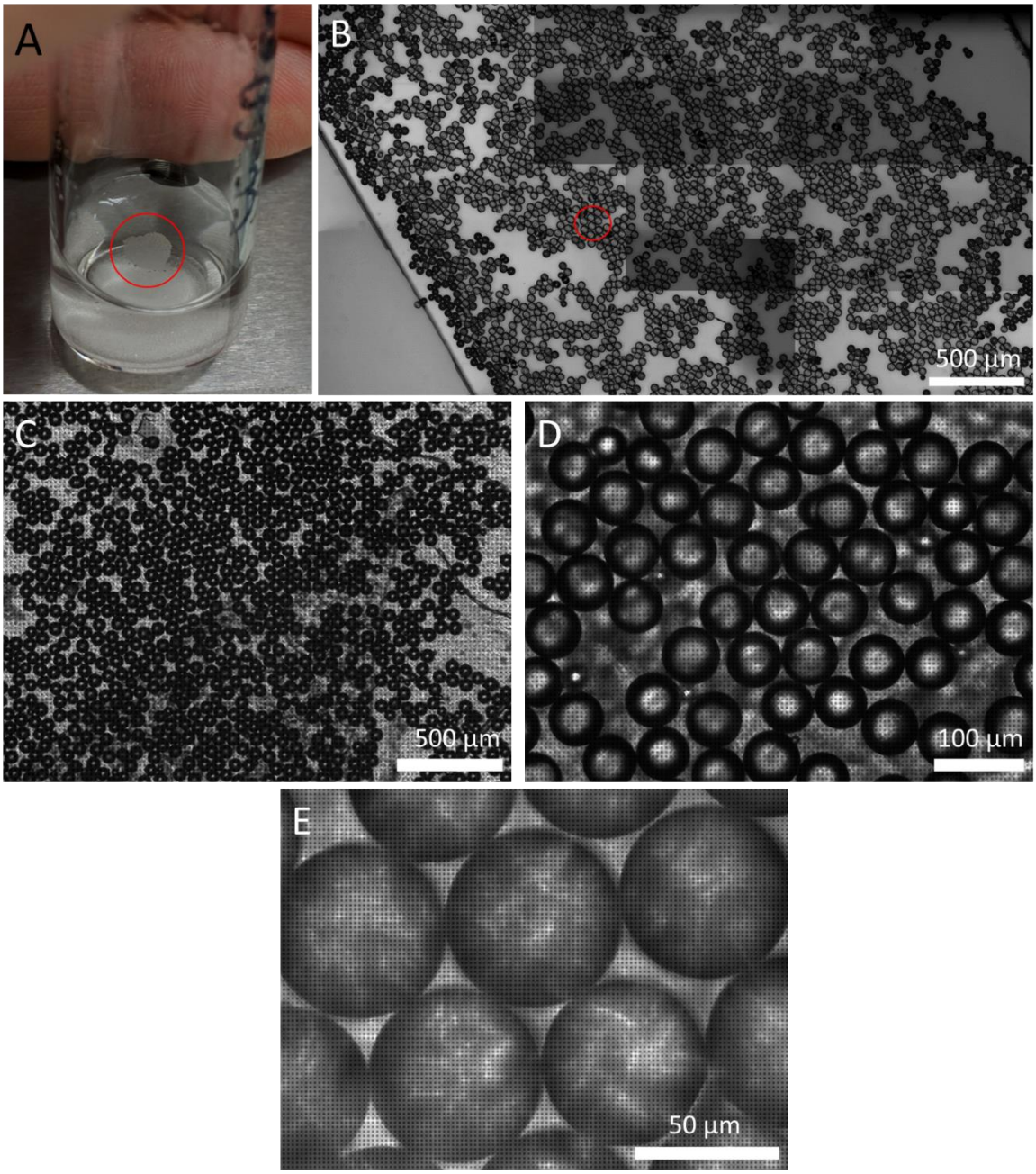

Figure 33: Self assembled sphere arrays
(**A**) Microsphere raft formed on the water meniscus in a glass vial. (**B**) Sphere rafts can be transferred to a coverslip whilst maintaining much of their close packed nature. **C-E**, the raft can be transferred directly to the sample surface allowing for multiple SR FOVs to be located within one FOV of the objective lens, even at high magnification.

5.4 Results

5.4.1 Confirmation of SHG Signals Excited Via Photonic Nanojet and Optimization of Parameters for PNJ-Assisted SR-SHG

Achieving super-resolution SHG (SR-SHG) imaging can have applications in understanding nanoscale biology and evolution of SHG-active materials such as fibrillar collagen in disease processes. The SHG signals observed by exciting via a PNJ showed the expected 2nd order dependence on power on imaging barium titanate nano-crystals (Figure 34 **A-B**). SHG was excited at 800 nm and emission was collected at 400 nm, this is true of all SHG images in this chapter unless otherwise stated. In the context of SHG from single collagen fibres it has been shown that with higher excitation power, sensitivity to smaller fibre diameters is achieved (Bancelin *et al.*, 2014). It was clearly also seen that at higher power the signal to noise ratio improves in PNJ-assisted SHG (Figure 34 **C-E**).

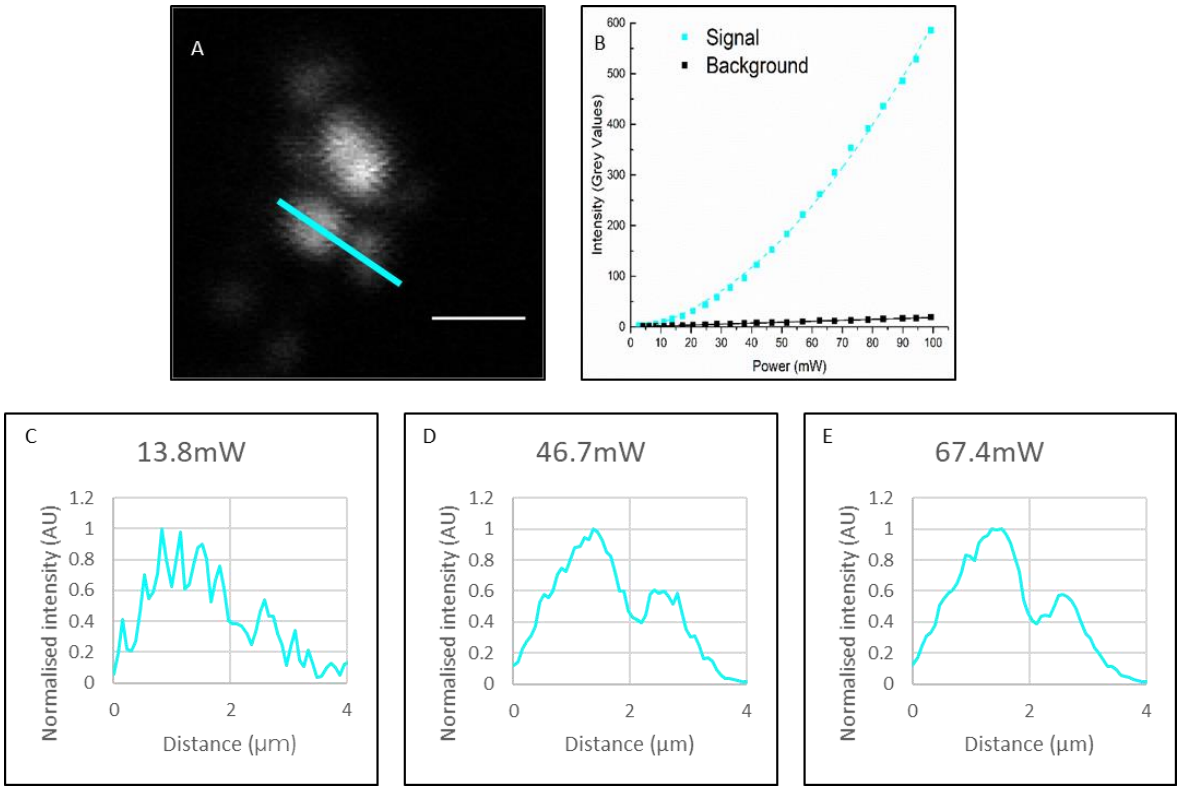

Figure 34: Characterisation of the SHG response when using PNJs.
(**A**) an example image of barium titanate nanocrystals imaged through a microsphere at increasing incident powers. Scale bar 2 µm. (**B**) Plots of signal and background against incident power, the signal shows a quadratic relationship to power whereas the background increases linearly confirming the signal as SHG. C,D,E Intensity plots taken along the cyan line marked in A as power is increased (C→E) the signal to noise ratio increases and the peaks become more easily resolved.

Since SNR is inherently linked to resolution, further experiments were conducted at the highest excitation power possible (typically <30 mW) within the damage threshold of the sample to obtain the highest resolution within the imaging conditions. Damage was assessed by the appearance of

amorphous bright regions in the laser scanning images that grew in size with repeated scans. They also appeared in the longer wave length channel (520 nm) as well as the SHG channel (400 nm).

Previous studies have shown that the degree of magnification depends on the distance n(Figure 26) between the objective focus and the sphere-sample contact (Lee and Li, 2015), where smaller z results in less magnification. The improvement in resolution generated by a PNJ from a microsphere is dependent on the sphere size, where smaller spheres give better resolution (Darafsheh *et al.*, 2012). To characterise this for PNJ-assisted SHG imaging, a patterned sample of known dimensions was fabricated in a 200 nm thick silicon film (Figure 35). The pattern consisted of a grid of repeat slit patterns (Figure 35**A**) where one repeat unit consisted of a series of slits cut into the film using focussed ion beam (FIB) milling (Figure 35**B**), the interface between the crystalline-silicon and the immersion water that filled the slit provided the ordered lack of inversion symmetry required to be SHG-active. The slits were cut in a non-symmetrical pattern of a single shorter wider slit next to two longer narrower slits, this allowed us to determine whether the observed signal came from the slits or from the remaining silicon. The PNJ-assisted image showed a single shorter, wider stripe next to two longer narrower stripes mimicking the pattern of the slits cut into the silicon indicating that signal arises from the slits and not the remaining silicon in between (Figure 35**B/C**). The wider slit appeared to produce a stronger signal than the narrower slits, this may be as the width of the slit (210 nm) was close to a harmonic of the SHG wavelength (400 nm) thus, it is possible that a resonance was established producing a brighter signal.

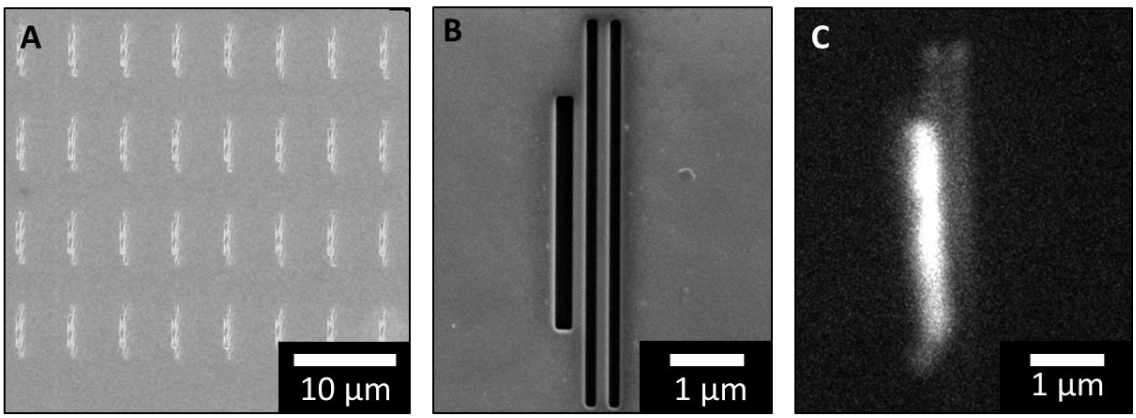

Figure 35: SHG active resolution sample.
(**A**) SEM image of a grid of repeat slit patterns milled into a silicon film substrate. (**B**) SEM of a single repeat unit from A. The shorter slit was 3 µm x 0.21 µm and the longer slits were 5 µm x 0.15 µm. The slits were separated by a distance of 0.15 µm. (**C**) SHG image of the same location as B, imaged through a 20 µm sphere. The distribution of intensity indicates the signal comes from the slits and not the silicon.

The imaging properties of 2 sizes of microsphere were investigated Ø = 22 µm and Ø = 60 µm (these size spheres were visually selected from the purchased ranges (5-22 µm and 55-60 µm) after deposition on the sample) by taking a series of images at increasing distance between the sphere-sample contact and the objective focus (z). The distance separating the signal between two slits was known and was used to calculate the degree of magnification due to the microsphere at different objective focus positions. Figure 36 **A-C** shows 3 example images at different z values imaged using a 60 µm diameter microsphere; PNJ behaviour consistent with previously published results (Lee, Li, Ben-Aryeh, *et al.*, 2013; Lai *et al.*, 2016) was observed. Smaller microspheres showed greater magnifications than larger microspheres and the range of values of n within which a focussed image could be generated (PNJ imaging range) was smaller than for larger spheres (Figure 36**D**). The large range of n positions over which a signal could be detected for such a thin sample was unexpected, this may be due to a combination of 2 factors. Firstly, a large movement of the objective focal position results in a comparatively small shift in the PNJ formation position (Figure 46). Secondly, PNJs have been shown to have an extended axial profile compared to a Gaussian focus (Chen *et al.*, 2019), which would increase the range of objective focal positions for which the PNJ can form an image . The PNJ imaging range is also shifted closer to the sphere-sample interface for smaller microspheres than for larger spheres which is in agreement with the literature that shows that the PNJ forms closer to the sphere surface with decreasing sphere size (Yang *et al.*, 2016, 2017).

For thicker samples, excitation not contributing to the PNJ creates a strong background over which the signal is not observable. Therefore, the relationship between imaging range and sample thickness must be considered when selecting a sphere size to use. Sphere size also affects the achievable resolution in SR-SHG with smaller spheres providing better resolution due to the narrower PNJ waist (Yang *et al.*, 2016) but with a smaller field of view. Based on all these considerations, 14 µm spheres were chosen and used subsequently at the z-position n =+20 µm for highest magnification for establishing the limit of resolution of SR-SHG while for tissue imaging 60 µm spheres were selected to increase FOV whilst maintaining sub-diffraction-limited resolution.

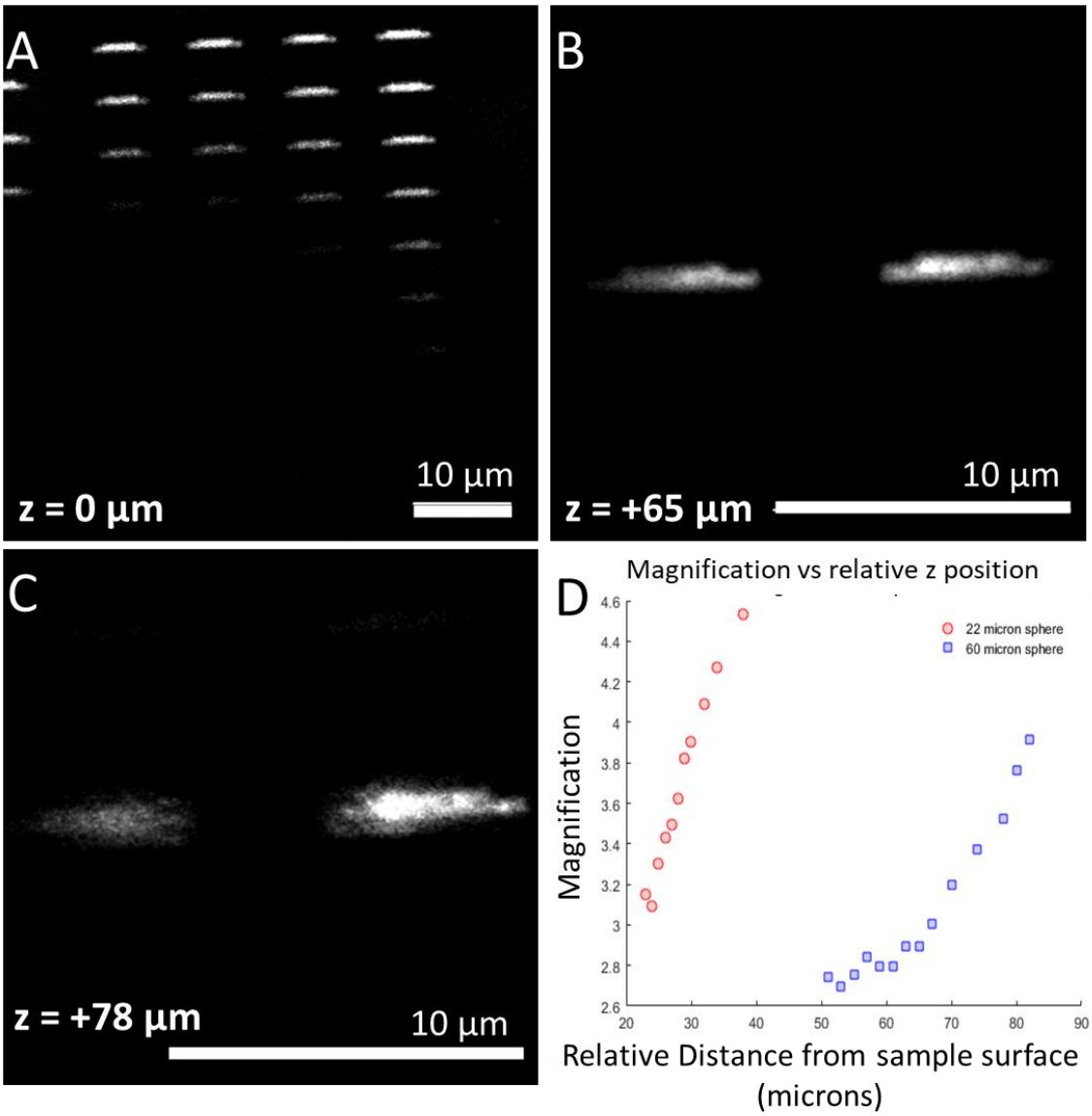

Figure 36: Relationship between magnification and objective focus position.
The degree of magnification by microspheres depends on the relative position of the objective focal plane (z) and the sphere sample contact (Z_0) and the size of the sphere.(Left) 3 example images taken through a 60 µm sphere. **(A)** is taken focussed at the sample surface ($z = 0 = Z_0$), the sample contains a grid of 4 x 8 triple-slit features, and the dark region indicates the location of the sphere. **(B)** is taken at z = +65 µm and **(C)** at z = +78 µm. They show that the image generated through the sphere increases in magnification as z increases. The z = +78 µm image also shows that the image becomes defocussed as z+ increases past the PNJ imaging range. **(D)** Images were taken through microspheres of 2 different sizes, 22 µm and 60 µm. The z-ranges for obtaining magnified images were 50-85 µm for the larger spheres and 20-40 µm for the smaller spheres. Smaller spheres produce a greater magnification than the larger spheres but over a narrower focal range. The focal range of smaller spheres occurs closer to the sphere than that of larger spheres. Scale bar 10 µm. Images were acquired using a 63x/1.2NA objective, the scan field without a microsphere was 53µm x 53µm imaged using 1024 x 1024 pixels giving an effective pixel size of 52 nm. B and C have been cropped to improve visualisation.

5.4.2 Establishing PNJ-assisted SHG Imaging in Biological Samples

Images were acquired of the same location of a tissue sample without and with PNJ excitation of SHG to investigate the extent of improvement over conventional, diffraction-limited SHG. The lung tissue sample was first verified to contain an abundance of fibrillar collagen using Sirius Red staining and polarized light microscopy (Figure 37), an unstained serial section was then used for SHG imaging.

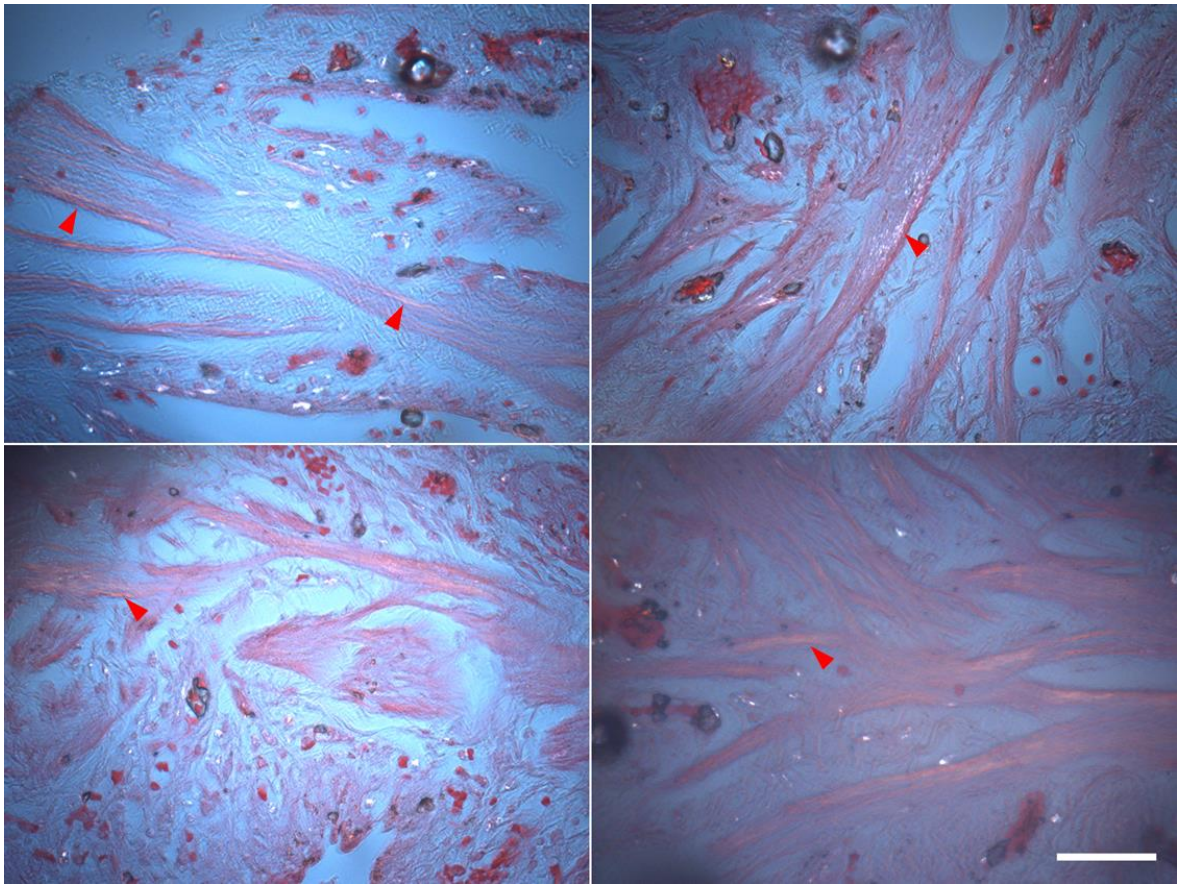

Figure 37: Verification of collagen content of lung tissue sample.
Example images taken of a lung tissue slide showing the distribution of collagen stained with Sirius Red and imaged using polarised light microscopy. Collagen fibres appear as gold/white on a pink and blue background, red arrows indicate areas of high collagen concentration Scale bar 50 µm.

The images acquired of the same location both with and without a PNJ indicate that PNJ-SHG of collagen in a biological sample is possible Figure 38**A/B**. When comparing the regions indicated by the red arrow in **A** compared to the red arrows in **B** it can be seen that when imaged using the photonic nanojet two separate features can be observed where without the nanojet only a single feature can be observed.

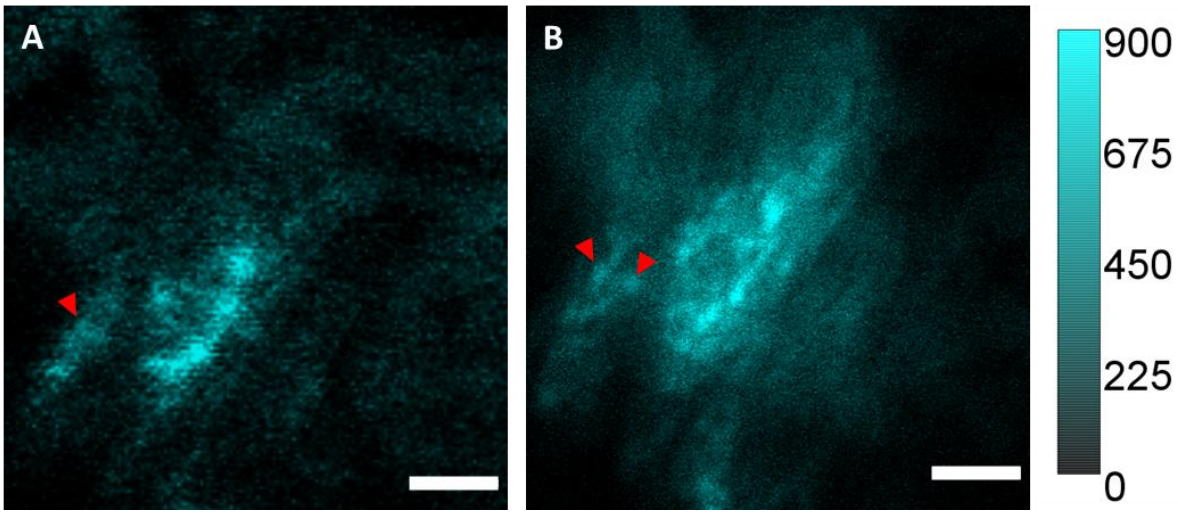

Figure 38: Verifying SHG signals in a biological sample using PNJs.
A: Diffraction-limited SHG signal from a fibrotic lung tissue sample containing collagen. **B:** SHG image of the same region taken using a PNJ. It is possible to resolve more fibres and their directionality. The red arrows highlight points where the PNJ images appears to resolve features that were not resolved in the diffraction-limited image, however, it is possible that the two images are from marginally different focal planes due to the ifferent focussing properties of the PNJ comparred to an objective alone.. Both images were acquired with a 63x/1.2NA objective objective with an effective pixel size of 101 nm, the displayed FOV in A has been cropped to match the FOV in B. Scale bar 1 µm.

5.4.3 Establishing the Limit of Resolution

To quantitatively evaluate the resolution of an imaging system two common methods are employed, one uses a sub-diffraction-sized object such as a fluorescent bead to act as a point source of light. When imaged it will appear as the point spread function of the system. Measurement of the full width at half maximum (FWHM) is then used as a measure of the resolution (Cole, Jinadasa and Brown, 2011). The second method uses a pair of slits as the emitters, the distance between the two slits is decreased until they are no longer resolved with an intensity drop satisfying one of the afore mentioned resolution criteria (You, Kuang and Zhang, 2016). A pair of long emitters can also be used in the same fashion as a slit, this is employed in commercial resolution test samples such as PSF check (https://www.psfcheck.com/psfcheck-slides). To determine the resolution of SR-SHG a well-characterised sample that produces an SHG signal was required.

Barium Titanate ($BaTiO_3$) nanocrystals (<100 nm) produce a strong SHG signal and therefore, were explored as a candidate for imaging a point source. $BaTiO_3$ crystals were suspended in 100 % ethanol before being sonicated for 5 minutes to break up any aggregates; the mixture was vortexed for 5 seconds to suspend the crystals. 10 µL of the suspension was deposited onto a clean glass coverslip, covered and allowed to dry at 21° C. 10 µL of the suspension was also deposited onto a silicon wafer as it has a highly smooth surface that is amenable to atomic force microscopy (AFM). AFM was

chosen as it has nanometre lateral and axial resolution and requires minimal sample preparation. Figure 39**A** shows the SHG images acquired for $BaTiO_3$ dried onto a coverslip. It was possible to obtain images with good contrast of aggregates (red circle) and presumed single crystals (red arrow). However, after imaging, small crystals could be seen to be moving in the immersion water indicating that some had detached from the surface. Due to this issue it was determined that drying crystals to the surface of a coverslip would not be suitable for generation of a resolution sample as imaged nanocrystals may move between correlative imaging with SR-SHG and AFM. Figure 39**C** shows an SHG image of the crystals dried onto silicon wafer. A distribution of crystals could be seen on the surface however, sample damage was also observed (Figure 39**D** Red arrow). To overcome these issues immobilisation of the nanocrystals in an optically transparent medium was explored.

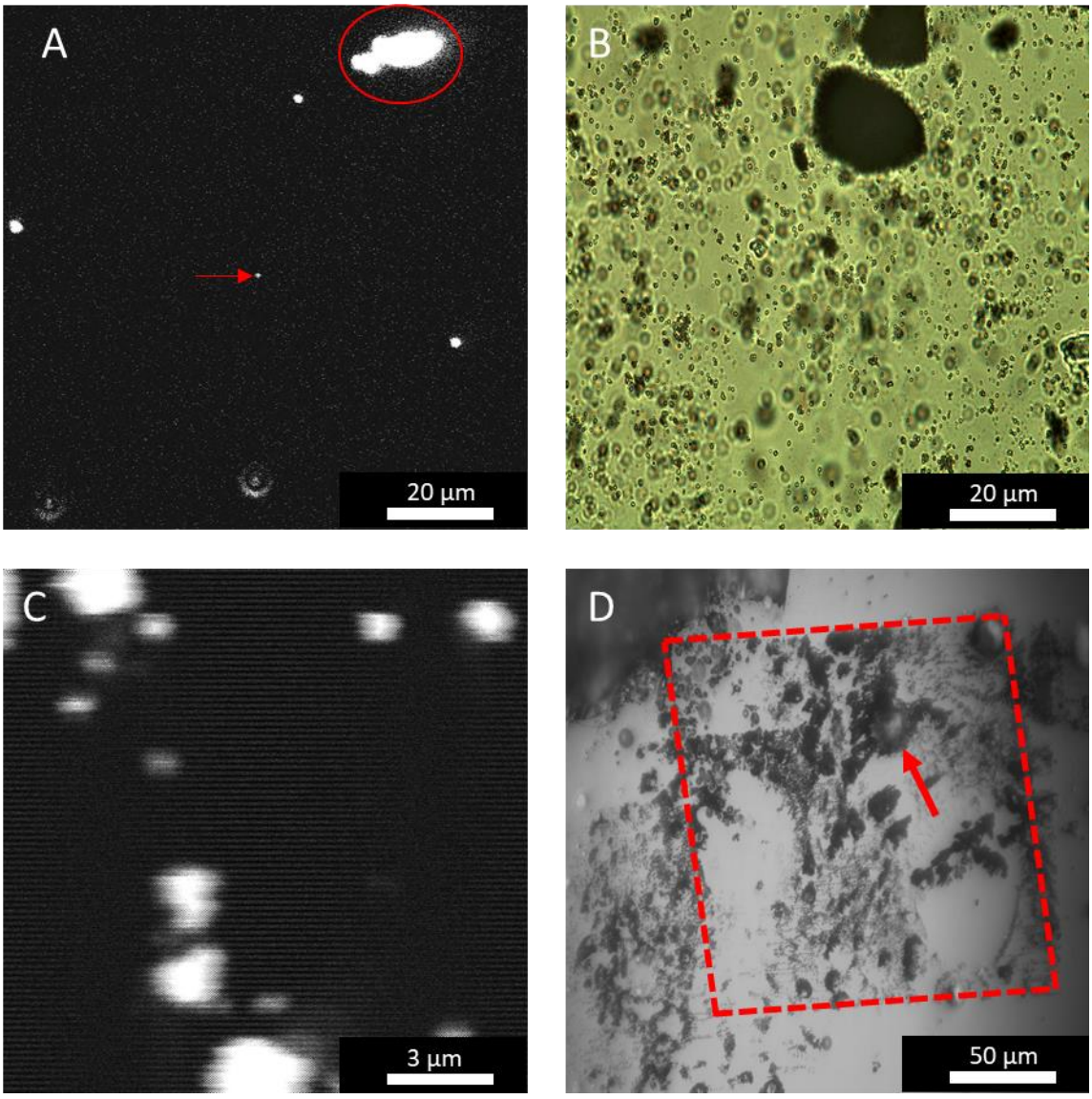

Figure 39: $BaTiO_3$ nanocrystals for resolution determination.
A: An SHG image of a sparse region of crystals dried onto a coverslip. Red circle, aggregate, red arrow potential single crystal **B**: A representative image of the distribution of crystals in PDMS, large aggregates and individual crystals can be seen. **C**: An SHG image of $BaTiO_3$ crystals on a silicon wafer. **D**: A bright field image showing sample damage. Red dashed line indicates straight

edges marking the edge of the scan field, red arrow points to sample damage. Images were acquired using a 63x/1.2NA objective.

A thin layer of PDMS was spread onto the surface of a microscope slide then a small amount of dry $BaTiO_3$ nanocrystals deposited on top before curing. Figure 39**B** shows a bright field image of the crystals suspended in PDMS. There are crystals at various planes of focus, with some clumped together and some existing as apparent individual crystals. Being optically transparent at the excitation wavelength (800 nm) the PDMS did not burn readily. However, it was found that the nanocrystals had sunk into the PDMS before it had fully cured and were covered by too much PDMS to be imaged using PNJs, due to the near field requirements of PNJ SR capability. Thus, other methods for developing an SHG-active SR test sample were explored.

Fibrillar collagen is also a strong SHG emitter and therefore formed the basis of the next resolution sample. 20 µl of bovine collagen solution (100 mg/ml, Sigma-Aldrich) was deposited onto a fresh layer of mica, dried under a stream of nitrogen, washed 3 times with deionised water, and then dried under a stream of nitrogen again. This dried sample was then imaged using AFM to investigate the distribution of fibrils to see if there were fibres separated by suitable distances (50 nm-200 nm) to test the resolution of SR-SHG. Figure 40 **A/B** shows the distribution of collagen fibrils when dried onto mica. Fibres separated by ~100 nm-200 nm were observed which fall within the expected range of spatial resolutions that SR-SHG is able to image. To verify whether the sample produced sufficient SHG signal to be used as a resolution standard, images were taken of collagen dried onto a coverslip. Very low levels of signal were observed Figure 40**C/D**, even at very low powers (<15 mW) sample damage could be observed (Figure 40 **C/D** red arrows). Sample damage was identified as points of high intensity that appeared across multiple wavelength channels and increased in size with multiple scans. As SNR is closely linked to resolution it was determined that the achievable signal levels would not be sufficient to find the limit of resolution for SR-SHG.

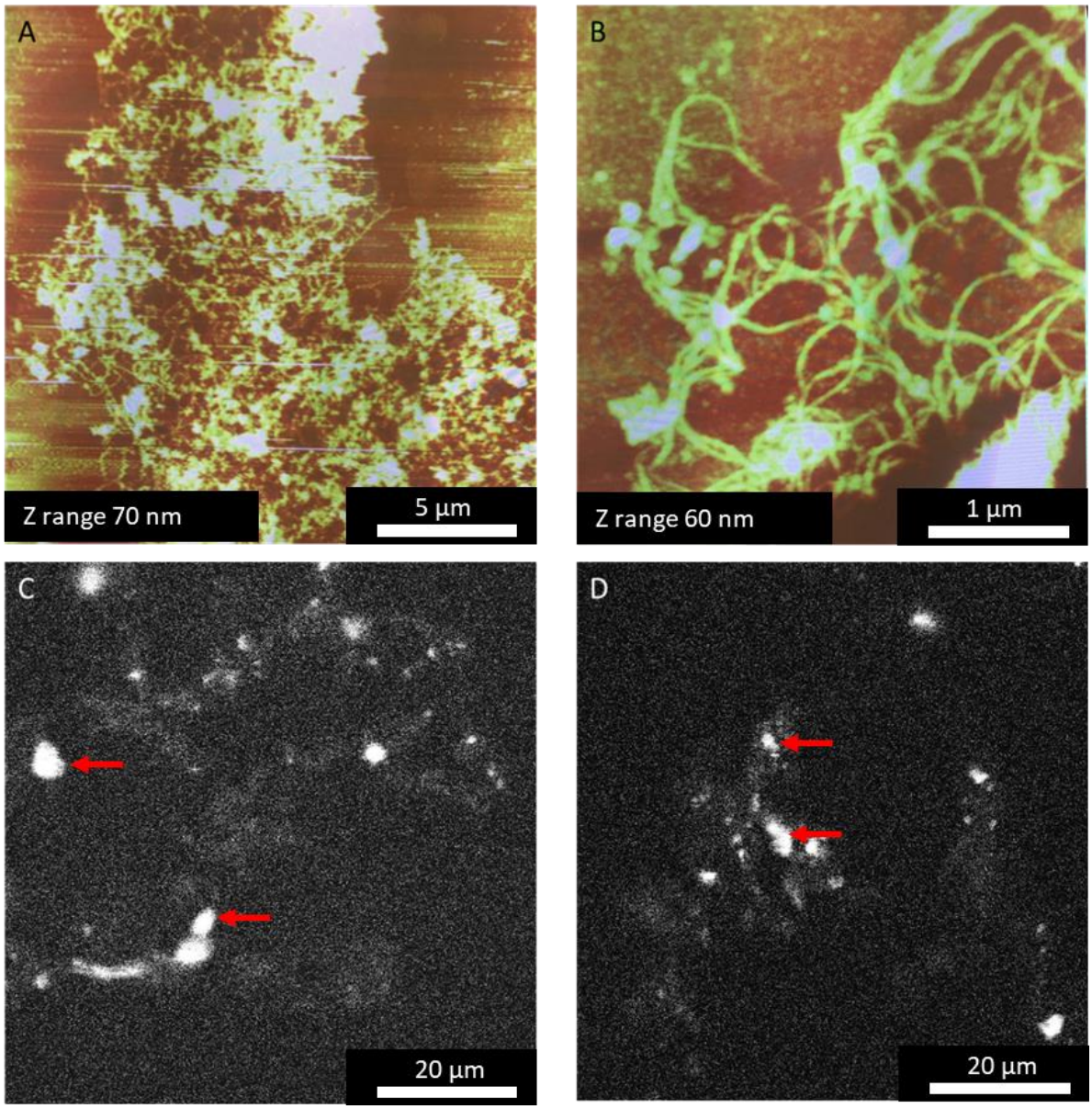

Figure 40: Collagen fibrils as a resolution sample.
A/ B, AFM images showing that the collagen fibrils accumulate into clumps but in B many fibrils remain separated by suitable distances. **C/D**: SHG images of collagen deposited onto cover glass, the signal is very weak, and locations of damage can be seen (red arrows). SHG Images were acquired using a 63x/1.2NA objective and an effective pixel size of 101 nm.

It was concluded that to determine the resolution of the system a more stable sample would be needed. Commercial samples are available (www.tedpella.com) however, these are expensive and it was unclear as to whether they would produce an SHG signal. Therefore, it was decided that a sample would be generated in house. To achieve this a sample was fabricated using focussed ion beam (FIB) milling into a silicon substrate, and surface SHG from this sample was detected as previously described in section 5.4.1 while describing the magnification properties of PNJ-assisted imaging. The first fabricated sample (Figure 41 **A/B**) consisted of a series of slits cut into a thin silicon film (200 nm thick). The slits were kept at a fixed width of 200 nm and the periodicity of the structure was varied at 1.2 µm, 1.0 µm, 0.8 µm and 0.6 µm. It was possible to resolve the features for all periodicities with an excitation wavelength of 800 nm collecting signal at 400 nm using a 1.2 NA water immersion objective therefore, a second sample with finer line spacing was made. It is noted that the white bands (signal) in Figure 41**A** are broader than the dark bands (not signal) this is in contradiction to the known relative sizes of the slits and silicon as determined in Figure 41**B**. This is possibly due to the light emanating from the slits, which are narrower than the diffraction limit for this combination of wavelength and objective, spreading due to diffraction and therefore appearing larger than their true width.

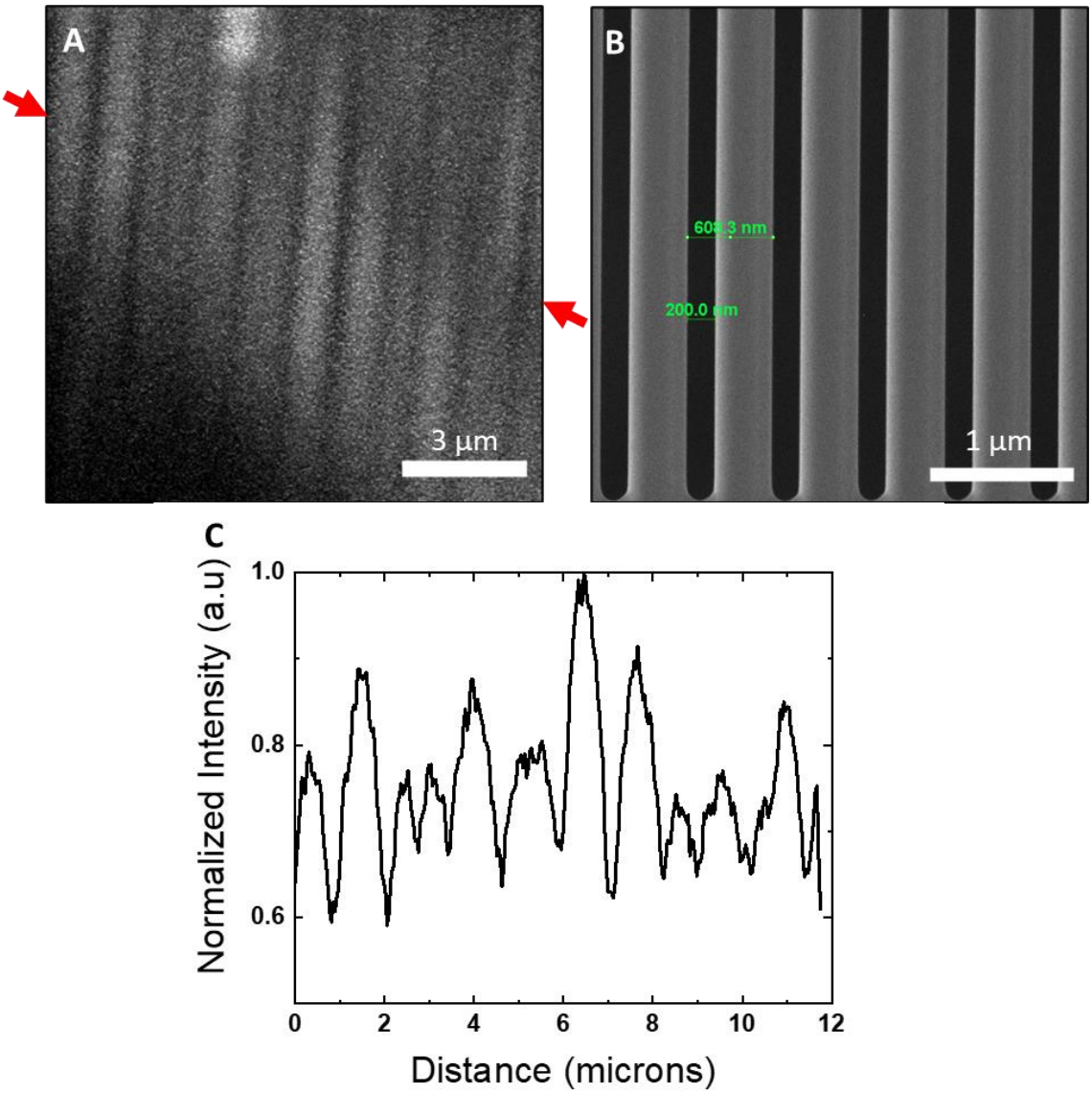

Figure 41: Resolution samples.
A: SHG image of resolution sample 1 taken without a sphere. **B**: SEM of A verifying the size of the cuts as 200 nm and the periodicity of the structure as 608 nm. **C** an intensity plot taken between the red arrow heads the periodic line structure can be resolved. SHG image (A), was acquired using a 63x/1.2NA objective, the diffraction-limited PSF size at the excitation wavelength used (800 nm) is 259 nm. (A) was acquired using 1024 x 1024 pixels over a 40 µm FOV giving an effective pixel size of ~39 nm. The image has been cropped for display purposes.

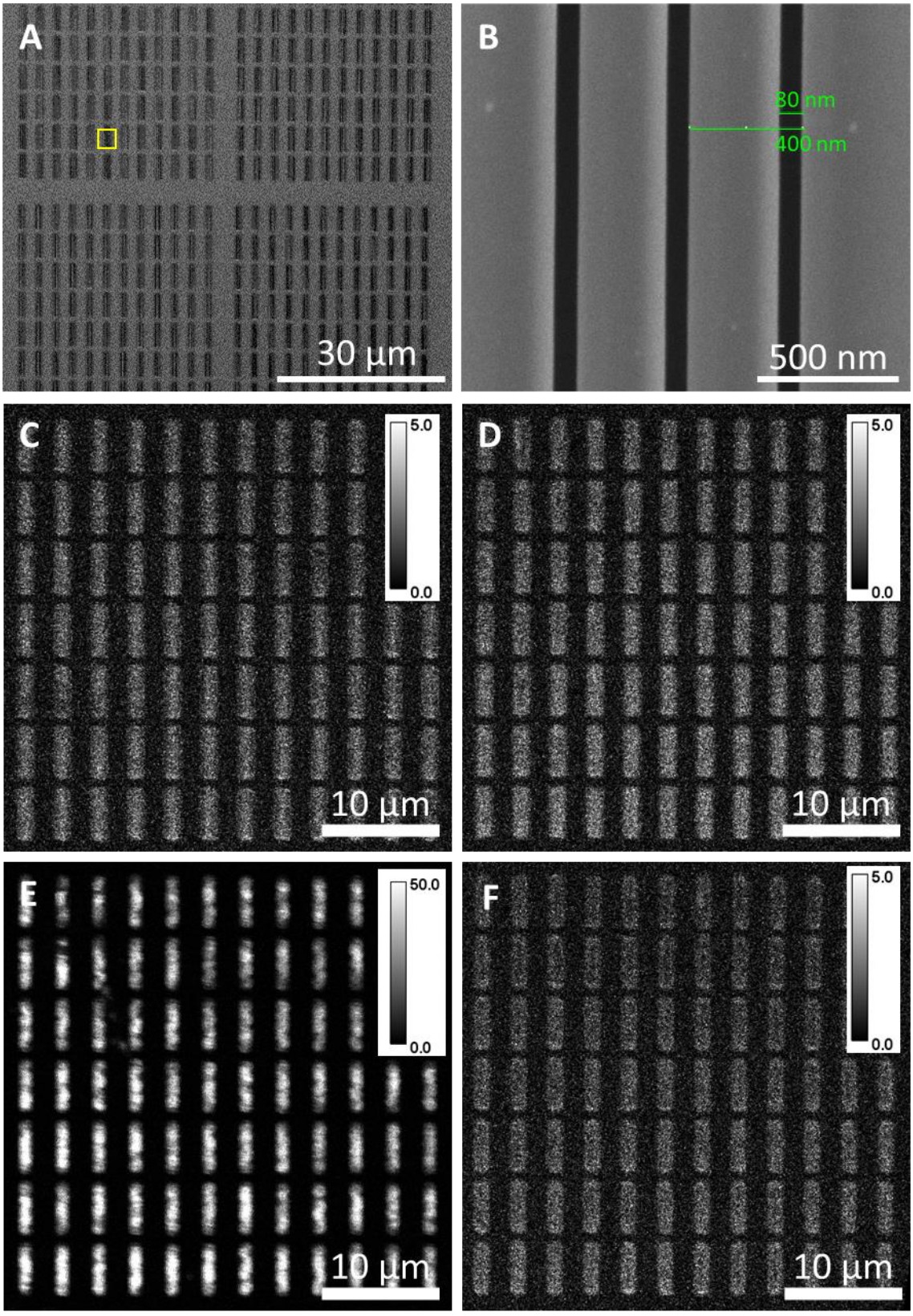

Figure 42: Resolution samples of different periodicities.
A SEM of the silicon sample showing the 4 squares made of repeat units of a triplet of cuts. **B** Higher magnification image of yellow box in A showing the 400 nm periodicity.**C-F S**HG images of the sample in A, the periodicities were 400 nm(**C**), 350 nm(**D**), 300 nm(**E**), 250 nm(**F**). SHG images were acquired using a 63x/1.2NA objective, the diffraction-limited PSF size at the wavelength

used (800 nm) is 259 nm. SHG images were acquired using 1024 x 1024 pix over a 53 µm FOV giving an effective pixel size of ~52 nm.

The second sample consisted of 4 large squares (35µm x 35µm) (Figure 42**A**), each square was made up of a repeat unit of three cuts (Figure 42**B**). The cuts were 80 nm wide and the periodicity of the repeat unit varied for each square, the periodicities being 400 nm, 350 nm, 300 nm, and 250 nm. It was observed that despite the samples being imaged under the same conditions (laser power, objective NA, wavelength, PMT gain) the signal strengths were not the same, particularly the sample with a periodicity of 250 nm (Figure 42**E**). As the slit widths were all the same (80 nm) it is unlikely that this variation is due to the width of periodicity of the slits, it is possible that the variation could be due to variations in crystallinity of the silicon substrate which would affect the second order susceptibility ($\chi^{(2)}$), thus affecting the efficiency of the SHG process.

Figure 43**A** shows a diffraction-limited SHG image of the sample with 300 nm periodicity, the diffraction-limited resolution at 800 nm and 1.2 NA is 288 nm ($0.61\lambda/\sqrt{2}NA$) (Gauderon, Lukins and Sheppard, 1998) and therefore the slits should be resolvable however they were not. This may be due to slight aberrations in the imaging system resulting in achievement of resolution less than the theoretical diffraction limit. However, when imaged using PNJ-assisted SHG this periodicity was readily resolved (Figure 43 **B**). In **B** there are images of slits from different spheres within the objective FOV, these images are overlapped even though the spheres are not. This is shown diagrammatically in Figure 44. A further sample of finer spacing was generated to find the absolute limit of resolution. The sample consisted of a series of slits each 100 nm wide whilst the spacing between them is 125 nm ($\lambda/6.4$) verified by SEM (Figure 43**C** inset). Figure 43**C** shows an image acquired through a 14 µm diameter sphere to generate a PNJ. This smaller sphere size was chosen as smaller spheres can achieve better resolution due to their narrower PNJ (Yang *et al.*, 2016). As shown in Figure 43**D** the slits were well resolved satisfying the Rayleigh criterion for slits (81% of peak)(Born *et al.*, 1999; Hecht, 2001). This showed that SR-SHG can be achieved with at least 125 nm resolution which is ~2.3 times better than diffraction-limited SHG. Even better resolutions may be achieved however, the surface-SHG used to image these samples is significantly weaker than bulk-SHG (Boyd, 2008). This could not be surmounted by applying higher laser powers given the low damage threshold for such thin samples. Hence, the actual achievable resolution with PNJ-assisted SR-SHG may be even higher.

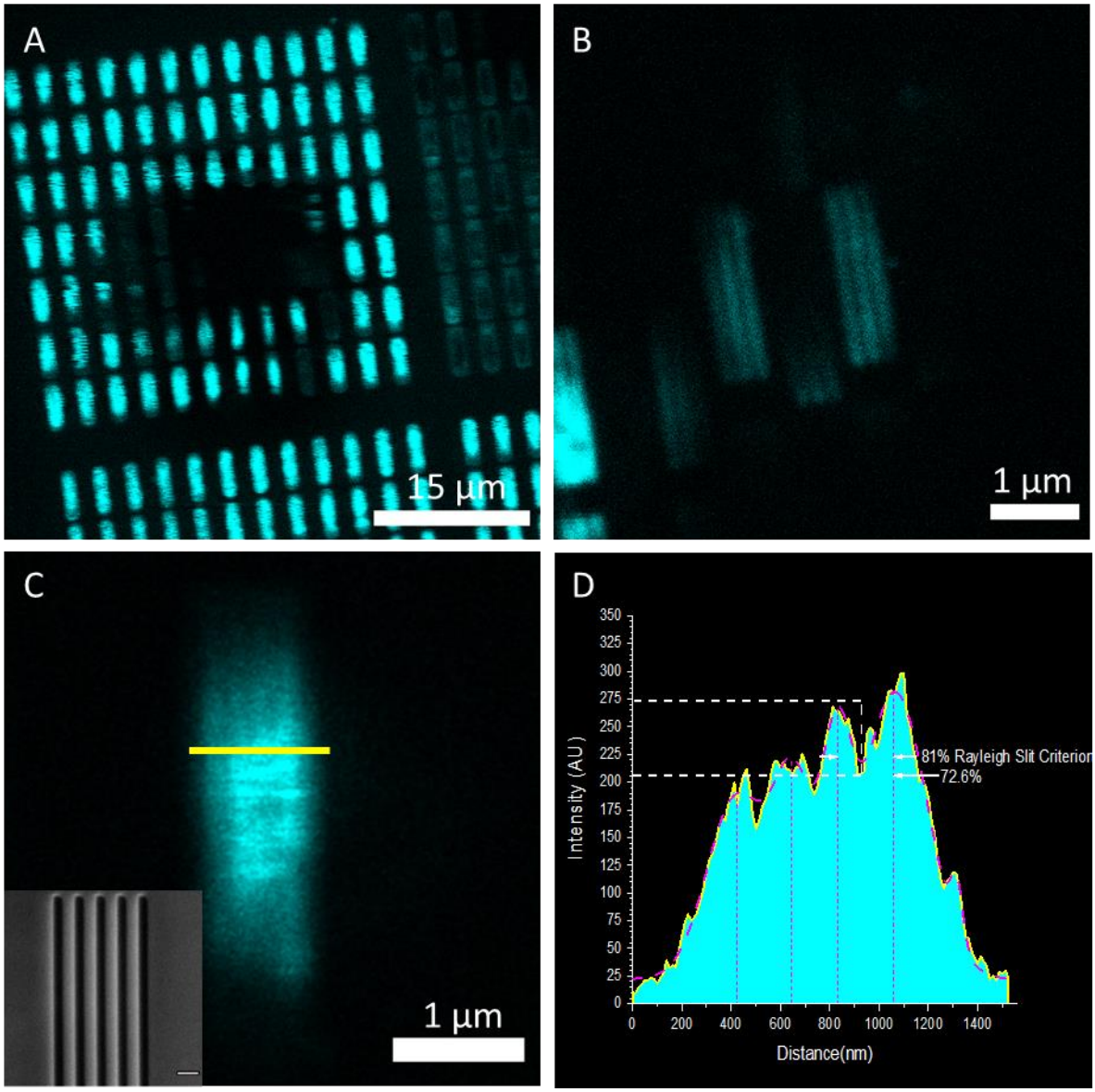

Figure 43: Determining the limit of resolution.
A: An image with the objective focused at the sample surface, the features of the triplet of cuts with 300 nm periodicity cannot be resolved. The dark area shows the location of 2 spheres. **B**, an image taken through the spheres in **A,** the features of the triplet can clearly be resolved. Multiple sets of offset triplets can be seen as the images from neighbouring spheres overlap. **C** Inset: An SEM image of the silicon sample, each dark slit is 100 nm wide and the slits are separated by 125 nm **C**: Image taken through a 14 µm sphere of the silicon slit sample, the sub-diffraction-limited features are resolved. Only 4 slits can be resolved, this is possibly due to the limited FOV and imperfect placement of such small spheres. The FOV for these small spheres needs full characterisation. **D**: An intensity plot taken across the yellow line in C. The plot shows 4 peaks corresponding to slits the peaks can be resolved with a drop to 72.6% intensity, satisfying the Rayleigh Criterion. Images were acquired using a 63x/1.2NA objective, 800 nm excitation 400 nm emission. Effective pixel size in A:52 nm, B:11 nm, C:12.5 nm

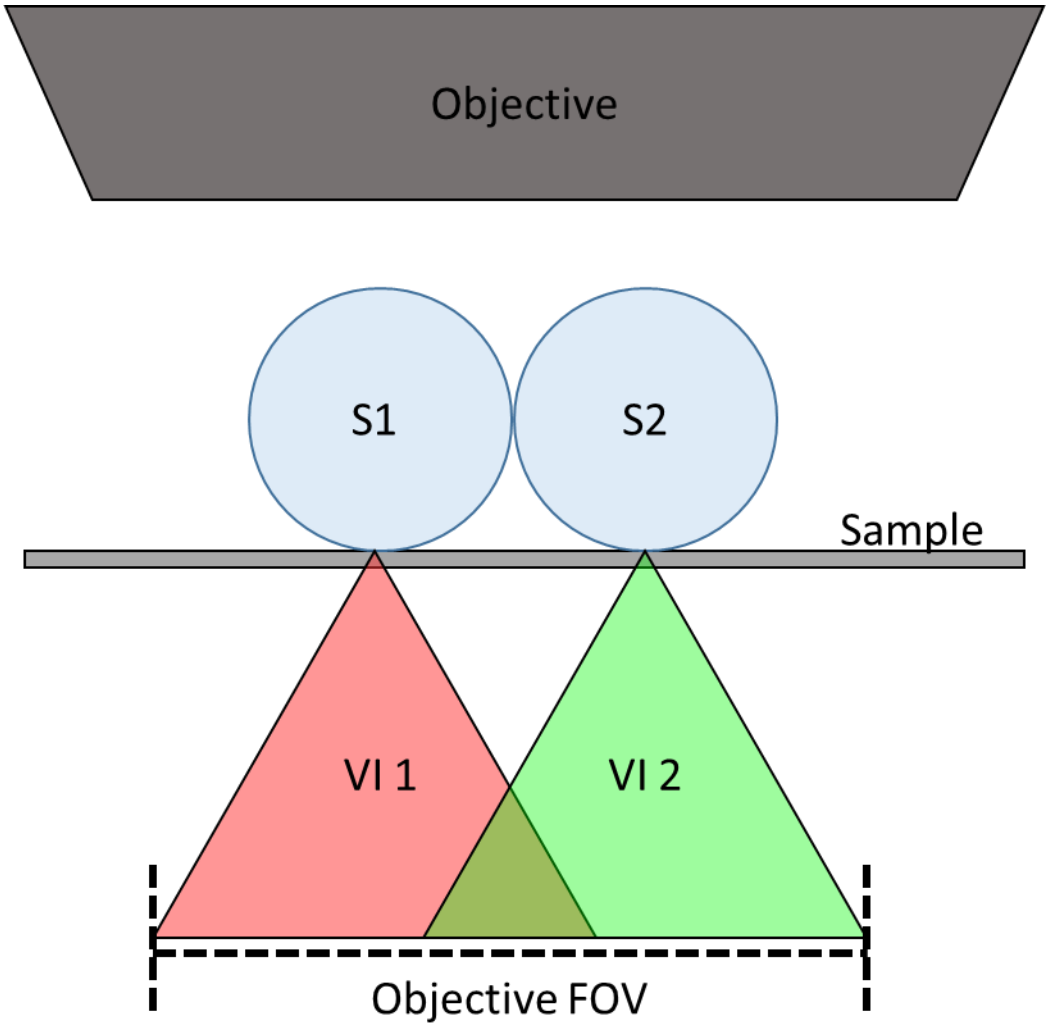

Figure 44: Origin of virtual image overlap.
The virtual image created by microsphere increases in magnification as the distance between the objective focal plane and the sphere-sample contact increases. When two or more spheres (S1 & S2) are located close to each other it is possible that the virtual images (VI 1 & VI 2) overlap even though the physical locations on the sample do not. This can create difficulty interpreting images from closely packed spheres unless caution is taken to only acquire images at an objective focal plane in which the images do not overlap. This is sometimes not possible as there is a limited range of objective focal planes within which the spheres produce an image.
.

5.4.4 Investigation of the Nearfield Origin of PNJ SR-SHG

Despite imaging occurring in the far field, it has been proposed that the super-resolution effect of PNJs has a strong near field component (Ben-Aryeh, 2012; Zhu and Goddard, 2019). To further understand this phenomenon, simulations were performed for both 14 µm and 60 µm diameter spheres using Gaussian beam illumination with a numerical aperture (NA) of 1.2 as used in experiments. In the simulations a PNJ formed both under plane wave and focused illumination conditions (Figure 45).

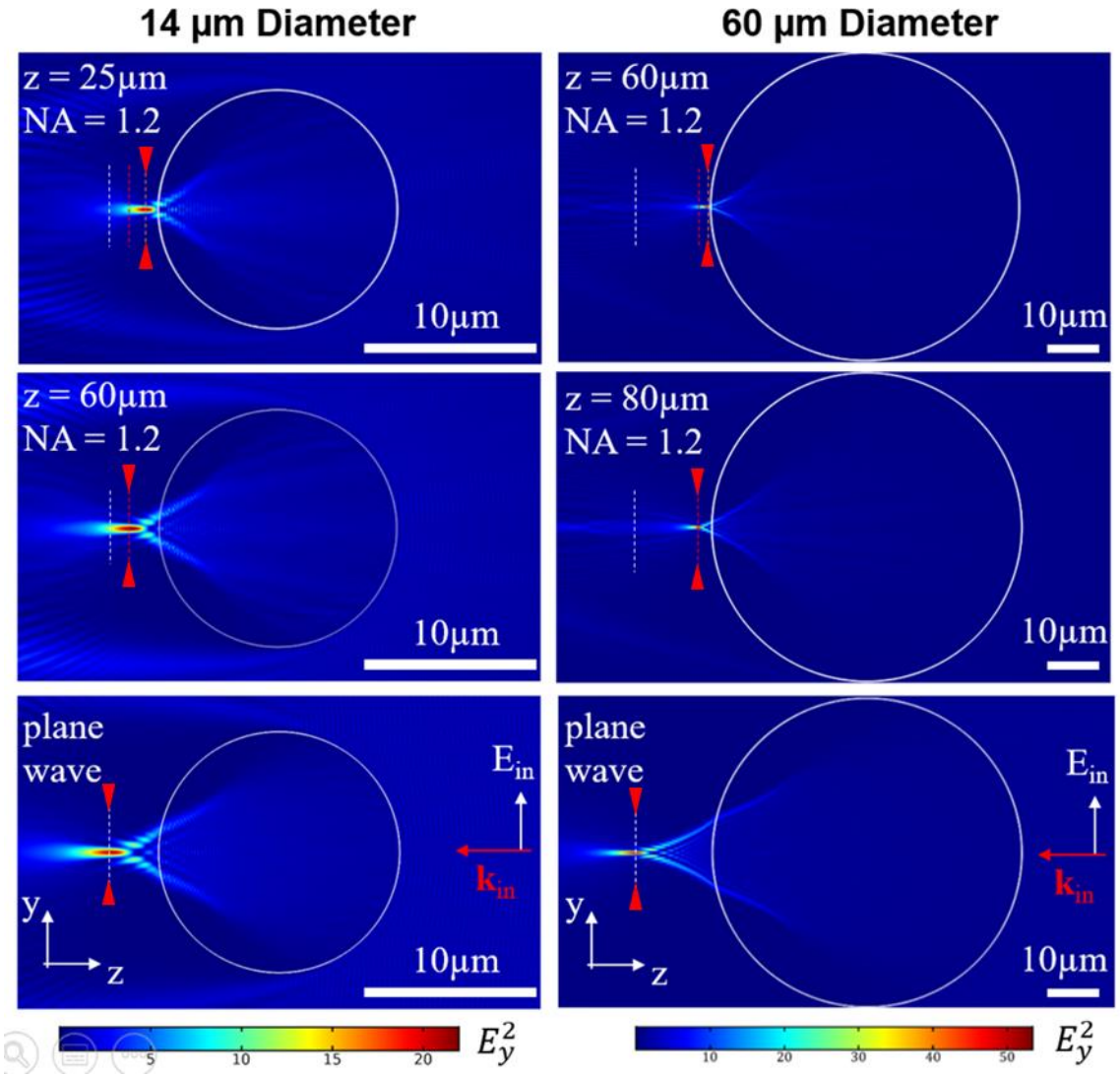

Figure 45: Simulations (2D) of photonic nanojet formation under plane wave vs Gaussian illumination

Using a numerical aperture (N.A.) of 1.2 for 14 µm diameter (left column) and 60 µm diameter (right column) spheres. Colour maps indicate field intensity in the y-polarization component Ey2 for different illumination conditions corresponding to plane wave illumination (bottom) and a focused Gaussian beam with NA = 1.2. Different distances of the illumination focus from the sphere end surface, z, are shown in middle and top rows as indicated in the figure. Coloured dashed lines bounded by red arrowheads represent the position of the maximum intensity of the PNJ for the three conditions for each sphere. Scale bars, 10 µm.

It was seen that the PNJ maximum moves much closer to the surface of the sphere under focused Gaussian illumination compared to plane wave illumination (Figure 46**A**). This behaviour can be understood as the effect of a compound lens consisting of both microscope objective and the microsphere where the effective focus is determined by the equation.

$$\frac{1}{f} = \frac{1}{f1} + \frac{1}{f2}$$

Where f is the focal length of the compound lens and f1 and f2 are the focal lengths of the objective and microsphere (ball) lens, the effective focus is shifted towards the sphere by the presence of the objective focussing. Here the distance of the sphere with respect to the focus of the microscope objective is a critical parameter, z representing the distance of the sphere-sample contact from the objective focus position in absence of the microsphere. The value of z for which the PNJ forms outside of the sphere for the two sphere sizes simulated matches or is close to the diameter of the sphere. The effect of gaussian illumination on the formation of PNJs has been investigated by Devilez *et al.* (Devilez *et al.*, 2009) and more recently by Huang *et al.* (Huang *et al.*, 2020). In the latter they noticed a similar trend to that in Figure 46, in that the PNJ focus moved further out of the sphere as the value of z increased, interestingly the value of z at which the PNJ focus was closest to the sphere-sample contact was when z was equal to the diameter of the sphere. As the properties of the Gaussian illumination used by Huang *et al.* were different to those used here, yet the same relationship is present, it may be more that coincidence and warrants further investigation. However, due to computational demand of the simulations and the focus of this project being a practical imaging method rather than fundamental PNJ research, the simulations were limited to those which represented parameters used in experiments.

As the PNJ moves closer to the sphere surface, the contribution of near-field components increases, resulting in a reduced spot size (Figure 46**B**). The smallest achievable single photon PNJ waist sizes in our simulations are 285 nm and 235 nm for the 60 µm and 14 µm diameter spheres respectively, due to the square-law dependence of SH generation the size of the effective point-spread function will be reduced by a factor of √2, giving approximate SHG spot sizes of 201 nm and 166 nm respectively. The diffraction-limited SHG resolution for a 1.2 NA objective at 800 nm is ~288 nm and therefore the achieved spot sizes from simulations are well below the diffraction limit for this system and provide insight into the improved resolution observed in the experiments, and is in line with previously published results (Yang *et al.*, 2016).

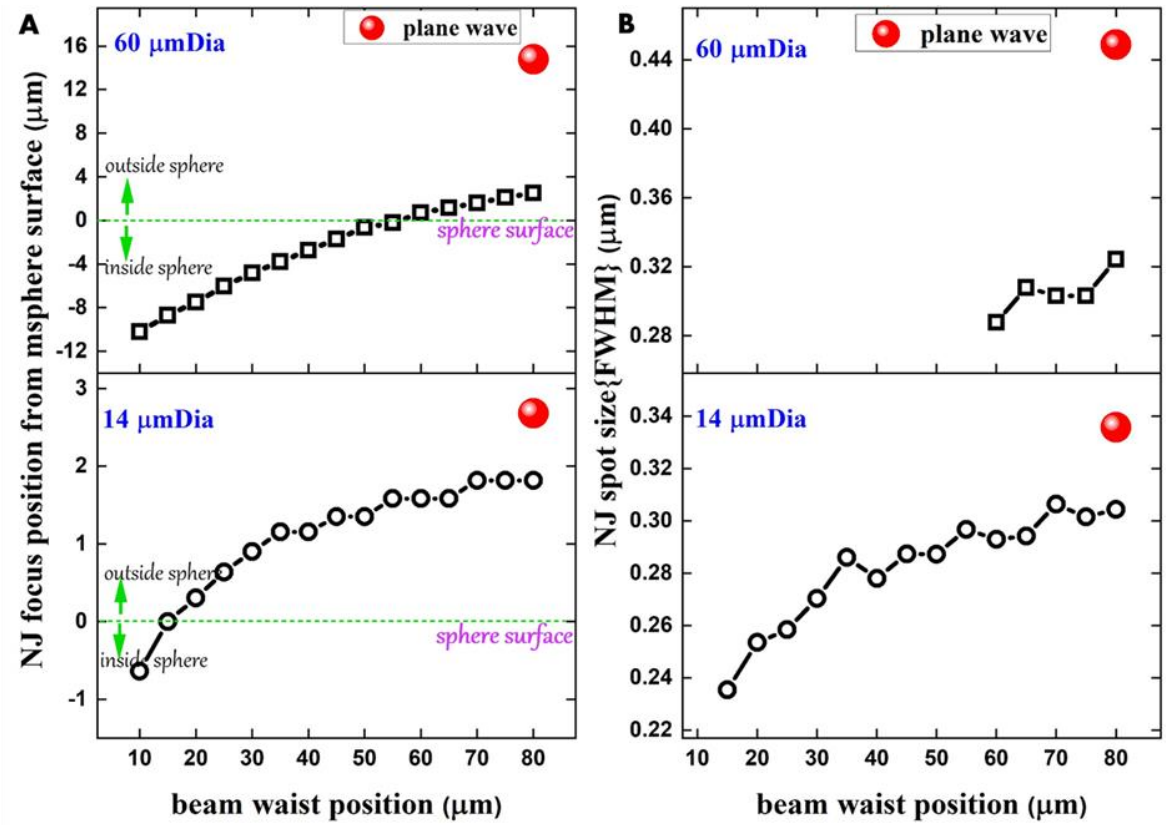

Figure 46: Analysis of simulations of nanojet formation under Gaussian illumination.
A: Nanojet focus position as a function of illuminating beam waist position. For a 60 μm diameter sphere the nanojet first forms outside of the microsphere when the illuminating beam is focussed 60 μm from the sphere surface. As the illumination focus is moved further from the sphere the nanojet focus also moves further from the sphere surface. The same trend is true for smaller spheres however the nanojet focus first forms outside of the sphere when the illumination focus is ~15 μm below the sphere surface. **B:** Nanojet spot size as a function of illumination focus position. The nanojet produced by both sizes of sphere is narrowest when the illuminating beam is focussed close to the microsphere surface. The narrowest achievable spots are 285 nm and 235 nm for 60 μm and 14 μm diameter spheres respectively. Spots of a narrower width than this form inside of the microsphere and therefore cannot be used for imaging.

Page left intentionally blank.

5.4.5 Improving Imaging Capacity Using Sphere Arrays

Having demonstrated the resolution improvement of PNJ-assisted SHG, a potential limitation is the restricted field-of-view (FOV) given by one sphere.

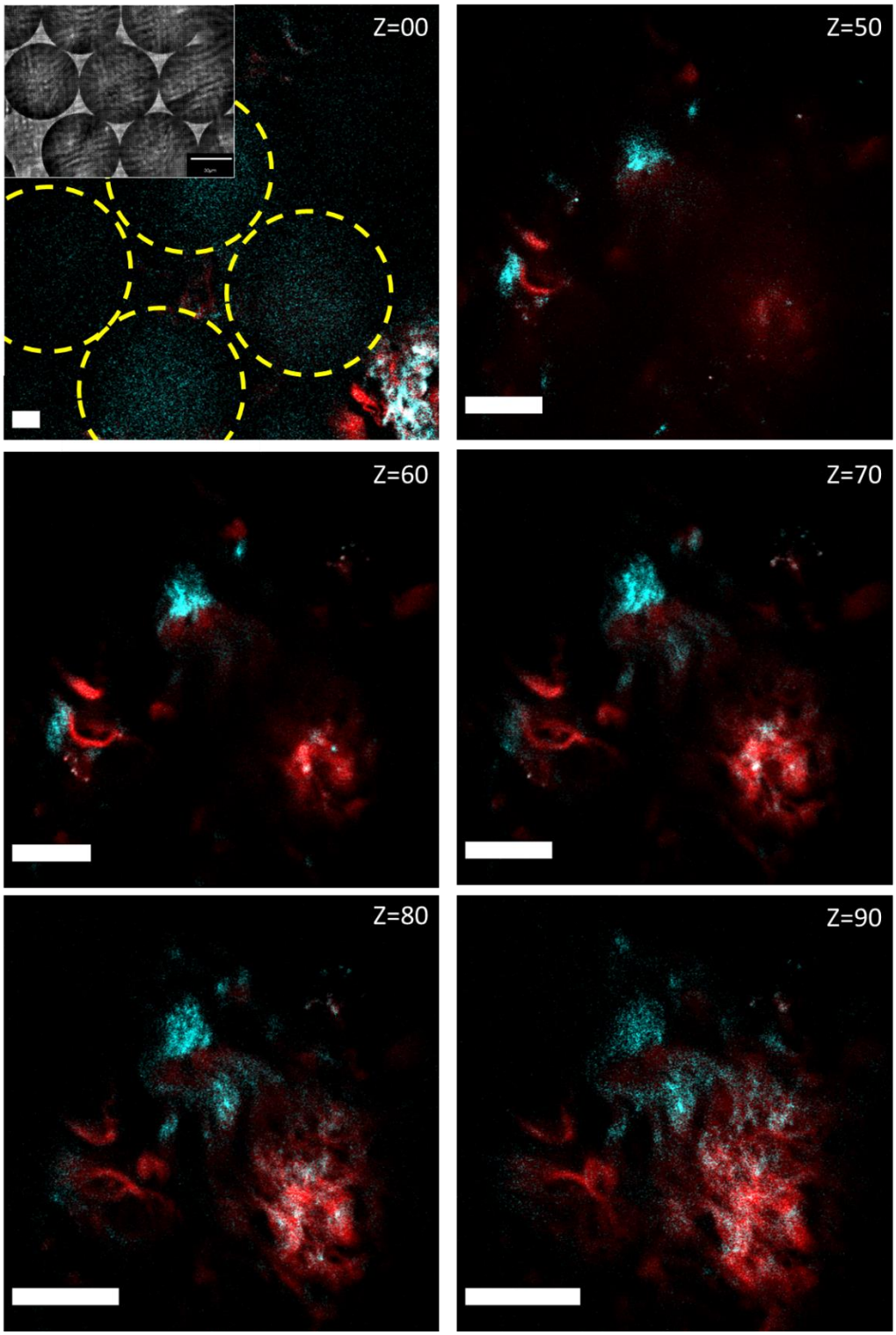

Figure 47 Arrayed spheres allow simultaneous acquisition of multiple images.
Images shown of a group of spheres deposited on a lung tissue sample, cyan signal is SHG at 400 nm, red signal is two-photon-excited autofluorescence (TPEAF) at 520 nm. In the Z=00 image the locations of 4 neighbouring spheres can be seen indicated by yellow circles, 3 of these contribute to clear FOVs when imaging through the spheres, the 4th sphere may not be located over a part of the sample that contains collagen of TPEAF producing molecules. As the focal position is changed (Z is increased) the magnification increases. At Z = 70 µm magnification is maximised whilst ensuring no overlapping FOVs. At greater values of Z overlap confounds image information from each sphere. Inset: Representative brightfield image showing 6 spheres packed together. Scale Bars 10 µm. Images were acquired using a 63x/1.2NA objective. The Z=00 image was acquired using 155 µm x 155 µm FOV scanned with 1024 x 1024 pixels. The same parameters were used to image the other z positions however, the magnification by the sphere alters the effective pixel size at the sample.

A simple multiplexing technique was employed to allow rapid acquisition of multiple SR-SHG images using self-assembled ordered arrays of spheres (Figure 47 inset) to overcome this limitation. Development of the sphere array system has been detailed earlier in section 5.3.9. The magnification achieved is dependent on the size of the sphere used and the focal plane z-position (Figure 36). Therefore, if taken with an array of spheres, the image from neighbouring spheres can overlap and hence needed to be optimised. With a 60 µm diameter sphere a focal position of z=70 µm was found to be the optimum to maximise resolution whilst avoiding overlap of images (Figure 47). It is important to note that the limited FOV of each sphere compared to the diameter of the sphere means that the FOVs of neighbouring spheres do not directly adjoin each other, i.e. there are unimaged regions between the spheres. As such, the sphere-array technique presented here is a way of imaging multiple smaller but separate fields of view in a single acquisition. Image stitching of multiple sphere images has been used previously to reconstruct composite FOVs (Yan *et al.*, 2015; Huszka and Gijs, 2018; Zhang *et al.*, 2019). To build a larger overall FOV from the sphere-array method, the sphere-array would need to be translated. For this to be possible the array would need to be embedded in a medium to maintain the arrangement of the spheres, to do this the simplicity of the self-ordered sphere-array system would be lost. The demonstrated self-ordered sphere array approach retains the advantage of simplicity whilst offering increased speed of data acquisition relative to single sphere approaches. Here it is demonstrated for label-free laser-scanning imaging and specifically for SHG.

5.4.6 Polarisation Resolved SHG Measurements

Having characterised the resolution of PNJ-assisted SHG and improved the utility of the technique by allowing simultaneous imaging of multiple SR-FOVs, the applicability of the approach to other SHG-based imaging modalities was explored. SHG signals are dependent on the relative orientation of harmonophores versus the polarisation of the excitation (Mazumder *et al.*, 2017) offering a measure of the disorder of a sample.

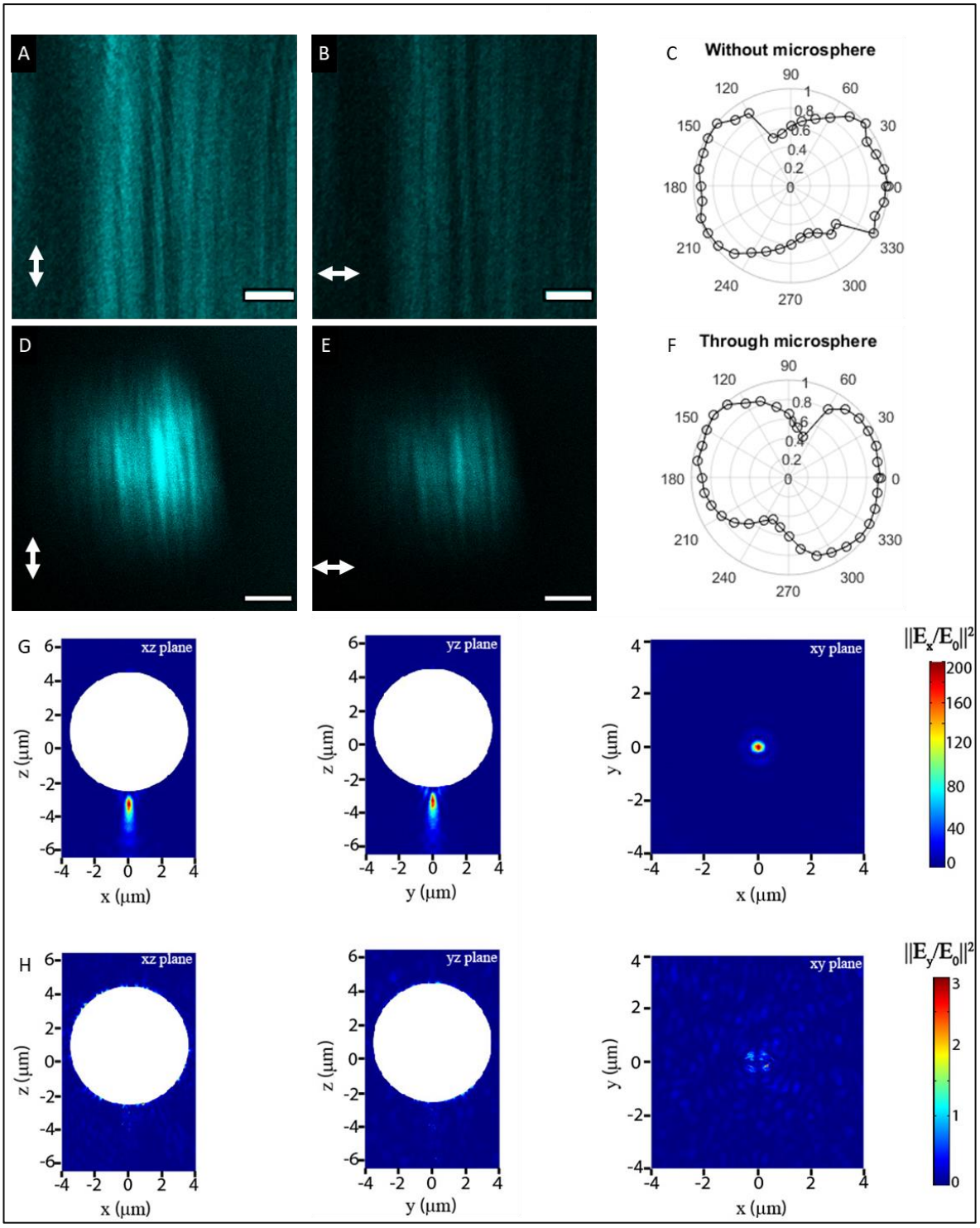

Figure 48: PNJs maintain the polarisation of light.
A and **B**, images of collagen fibres in mouse tail tendon with the excitation polarisation aligned parallel and perpendicular to the fibre orientation respectively. Images were acquired using a 63x/1.2NA objective. **D** and **E**, the same situation as **A** and **B** with imaging performed using PNJs. In both cases the intensity is at a maximum when fibres and excitation polarisation are aligned and at a minimum when they are perpendicular. **C** and **F** show polar plots of signal intensity against excitation polarisation for the diffraction-limited and PNJ cases respectively; the shape of the plots are the same, showing that polarisation is maintained through glass microspheres. Scale bars 3 µm. **G**: Simulation results-Colour map plot of the x-component of the electric field intensity (||E/E0||2) in various planes. The incident light was assumed to be x-polarised. The white shaded circular region represents the microsphere. The xz and yz corresponds to planes passing through the centre of the microsphere while the xy plane is plotted passing through the focal point of the generated PNJ, **H**: same as G but for the y component. The intensity of the y-component of the PNJ is approximately 2 orders of magnitude smaller than the x-component of the PNJ from the initially x-polarised illumination, indicating that the polarisation state of the illumination is not significantly affected when focussed into a PNJ. Simulation paramaters: Wavelength 800 nm, sphere refractive index 1.9, medium refractive index 1.33 (water).

Mouse tail tendon containing a high density of aligned collagen fibres was used to demonstrate this sensitivity to polarisation. Figure 48**A/B** shows images of the tendon taken with the excitation polarisation aligned parallel to and perpendicular to the major fibre axis, the intensity is greater in A than in B. Figure 48**C/D** shows the corresponding result when imaging using a PNJ and the same behaviour was observed. The polar plots (Figure 48**C**,**F**) show the full polarisation response over 360° of excitation rotation and gives the expected dumbbell shape for polarisation-dependent SHG signals (Yasui, Tohno and Araki, 2004).

However, the polarisation-dependent behaviour of SHG observed through a microsphere was unexpected. The experimental result suggested that polarisation is maintained despite the complex propagation conditions (whispering gallery modes, near-fields etc) that are taking place in the microspheres and that are responsible for the tight focussing. To investigate this result, 3D numerical simulations were performed to probe the polarisation state of the photonic nanojet of a microsphere. Figure 48**G** and **H** shows the x and y components of the electric field ($||E/E_0||^2$) respectively when the sphere is illuminated with linearly polarised light in the x plane. The intensity of the y component in the PNJ was approximately 2 orders of magnitude smaller than the x component indicating that the polarisation state of the illumination is not significantly affected when focussed into a PNJ. This large difference is much greater than the difference in intensity observed in the mouse tail tendon images. This can be attributed to the imperfect linear polarisation achieved at the sample (extinction ratio ~30:1, Figure 28**C**) compared to the perfectly polarised excitation in the simulation. Furthermore, collagen fibrils are not a perfect uniaxial crystal and therefore will not display a perfect polarisation-dependent response. However, these

results indicated that it should be possible to perform super-resolution, polarisation-resolved SHG measurements.

Polarisation-dependent changes can be measured by polarisation anisotropy, $r = (I_{\parallel} - I_{\perp})/(I_{\parallel} + 2I_{\perp})$, where $I_{\parallel}$ and $I_{\perp}$ are the intensities recorded parallel or perpendicular to incident polarisation. Polarisation anisotropy can vary between -0.5 and 1 where 0 is completely random emission, 1 is emission completely aligned with the excitation polarisation and -0.5 is emission aligned completely perpendicular to the excitation polarisation. Experimentally this was measured by taking two images with an analyser that was aligned parallel to, or perpendicular to, the excitation polarisation, placed in front of the PMT. Pixel-wise calculation of anisotropy can then be performed to generate images (Figure 49**B,** Appendix A.1) that show the spatial distribution of disorder within the sample.

Using the polarisation-dependence of SHG through measurement of anisotropy the information content of SHG images can be increased. Figure 49**A** and **B** show the diffraction-limited SHG intensity and corresponding polarisation anisotropy images. The polarisation anisotropy images reveal more structures than the respective diffraction-limited intensity images. Line profile plots in the anisotropy image reveals features that could not be identified using intensity alone. The anisotropy of SHG thus revealed the otherwise undetected fibres.

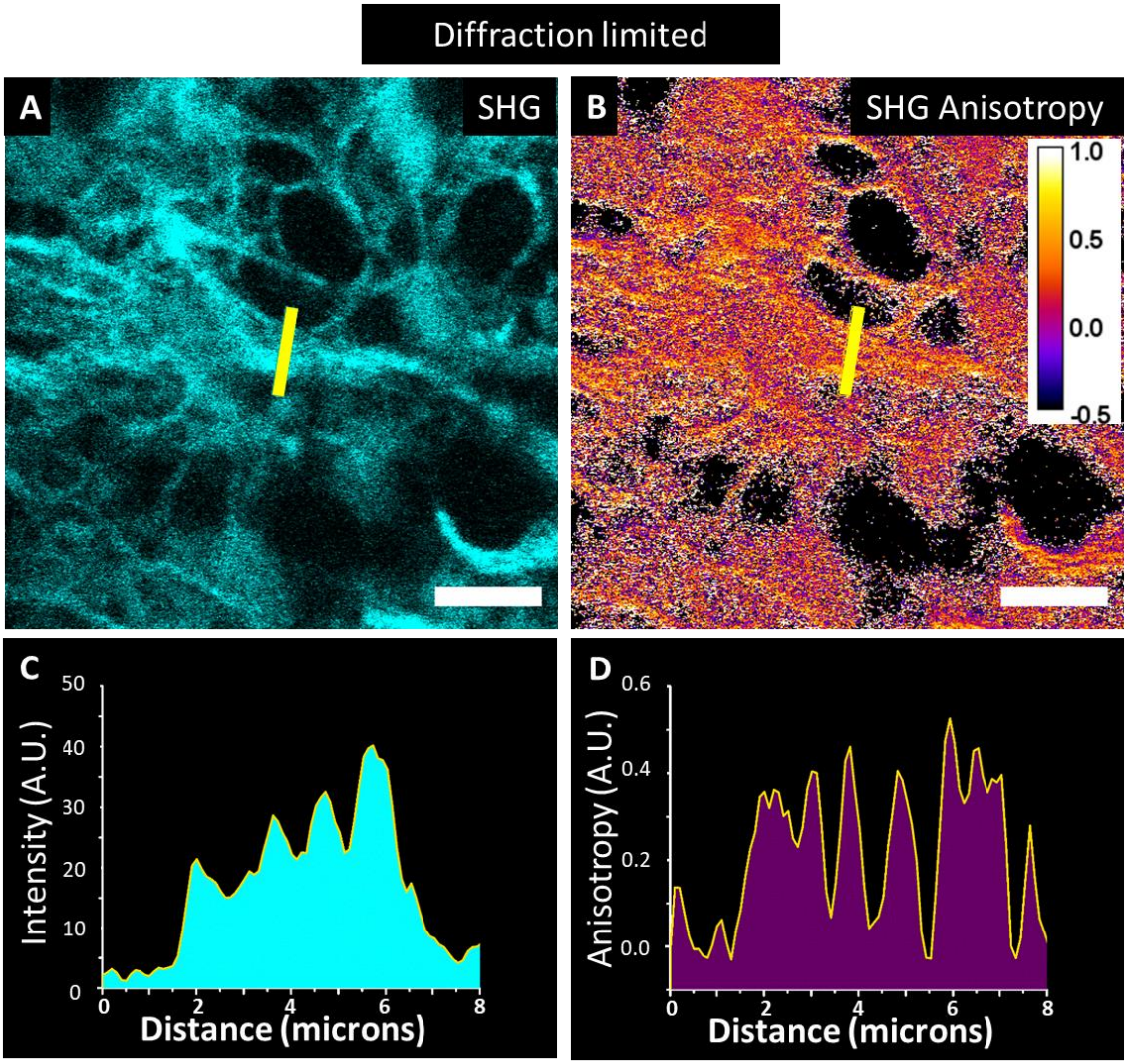

Figure 49 : Polarisation anisotropy reveals fibre features that cannot be identified by intensity alone.

A shows a diffraction-limited SHG image of collagen fibrils, the image is the sum of the two polarisations used to calculate the anisotropy image. **B** shows the corresponding polarisation anisotropy image (scale bars 10 µm). Intensity plots taken through the yellow lines in **A** and **B** are shown in **C** and **D** respectively. Polarisation anisotropy allows detection of fibre features that were not identifyable from intensity alone. Images were acquired using a 63x/1.2NA objective. The whole imaged FOV was 103 µm x 103 µm imaged using 1024 x 1024 pix. The displayed images have been cropped to aid visualisation of features.

Because the polarisation was maintained by the PNJ it was possible to perform the same measurements at a super-resolution scale. Figure 50**A/B** show example SHG intensity and polarisation anisotropy images acquired using a PNJ generated through a 60 µm diameter sphere. Like the diffraction-limited case, the polarisation anisotropy reveals hidden features that could not be detected by intensity. The decreased width of the PNJ allows detection of changes in anisotropy at an improved spatial resolution.

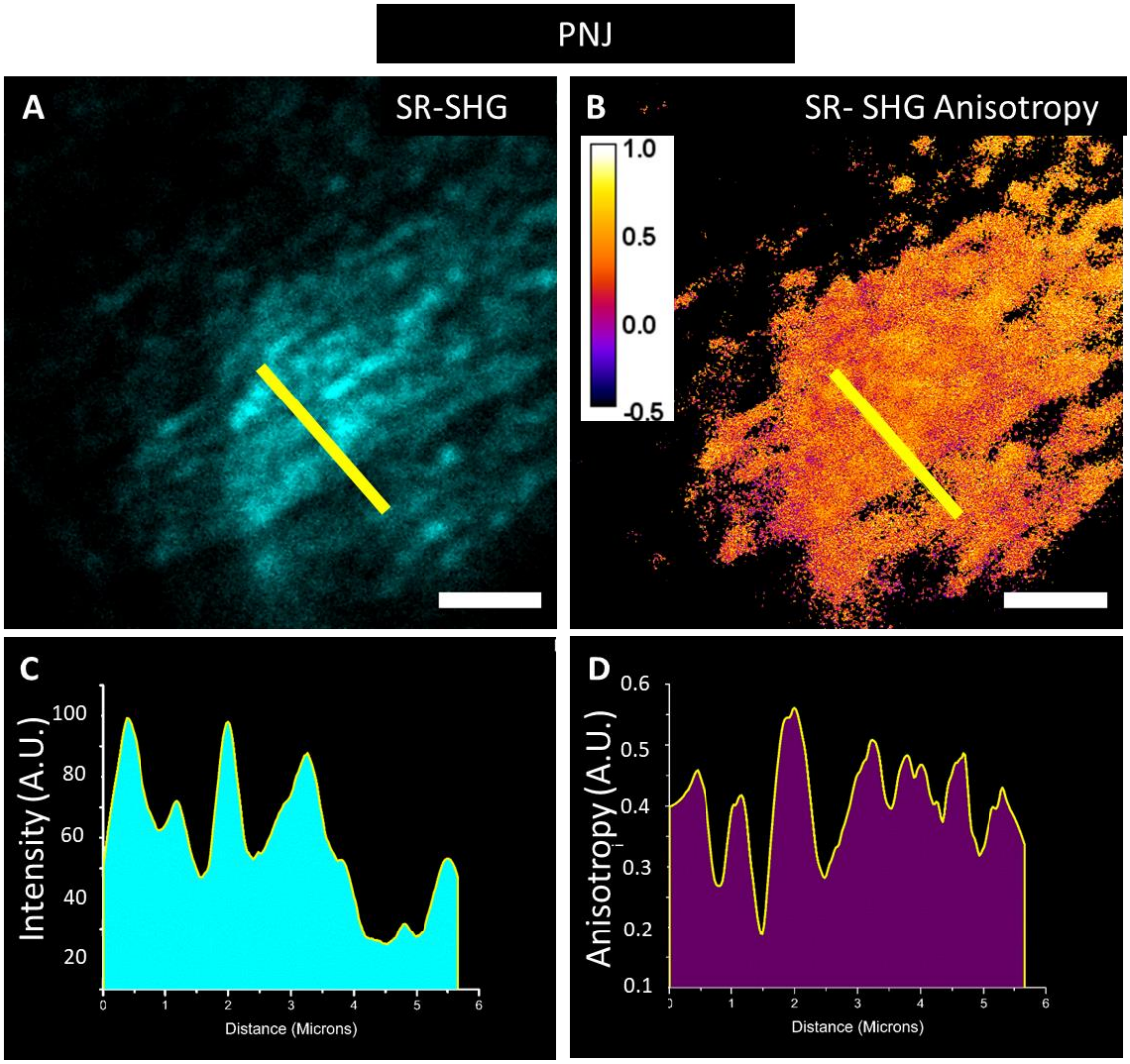

Figure 50: Polarisation anisotropy measurement using PNJs
A shows an SHG image of collagen fibrils,the image is the sum of the two polarisations used to calculate the anisotropy image. **B** shows the corresponding polarisation anisotropy image generated using PNJs (scale bars 3 µm). **(C/D)** Intensity plots taken through the yellow lines in **A** and **B** respectively. The polarisation anisotropy reveals hidden features that are not highlighted by intensity.Scale bar 3 µm. Images were acquired using a 63x/1.2NA objective and imaging through a 60 µm diameter sphere. The image was captured over 1024 x 1024 pixels and has been cropped to aid visualisation of features. Scale bars in A/B were calculated using the diffraction-limited scale and then multiplying this by the extra magnification of the sphere.

This demonstrates that polarisation-resolved SHG, herein using the anisotropy, can be performed using PNJs and therefore, with improved spatial resolution. We term these set of techniques as

pSR-SHG. Polarisation has been used previously to improve the resolution of diffraction-limited, fluorescence images (Gould *et al.*, 2008; Hafi *et al.*, 2014) by improving the localisation accuracy of the dye molecules used for labelling biological samples. The data shows that SHG polarisation anisotropy reveals additional information about fibrils. This is maintained even in PNJ-assisted SHG measurements whilst providing additional structural information and maintaining the benefits of label-free imaging.

5.4.7 Multiscale Imaging of Collagen Structure in a Lung Disease Model

The anisotropy of polarisation-sensitive SHG in diffraction-limited imaging is a powerful tool and can be used to delineate different stages of ovarian cancer (Campbell *et al.*, 2018) and differentiate between different collagen isoforms (Tilbury *et al.*, 2014). However, in many cases the changes are much more subtle and occur at the nanoscale such as in lung fibrosis (Jones *et al.*, 2018). By applying the super-resolved SHG imaging approach, particularly, pSR-SHG, we aimed to see whether such nanoscale changes in collagen could be observed directly.

Diffraction-limited, as well as PNJ-assisted, SHG images of sections from a tissue spheroid model (section 5.3.2) of the fibrotic lung disease, Idiopathic Pulmonary Fibrosis (IPF) were acquired. It has previously been shown using transmission electron microscopy that in this model the collagen ultrastructure changes significantly following treatment with lysyl-oxidase/ lysyl-oxidase-like (LOX/LOXL) inhibitor BAPN (b-aminopropionitrile) which inhibits cross-linking of collagen fibres (Jones *et al.*, 2018). Figure 51 shows diffraction-limited SHG images for both the control (A) and BAPN treated (B) sections. It has previously been demonstrated that the macroscopic collagen architecture becomes more disordered upon treatment with BAPN (Jones *et al.*, 2018) and here this can be seen by the loss of the "ring" of aligned collagen fibres at the edge of the sphere that is present in the control (Figure 51**A/B**), but not in the BAPN-treated sphere (Figure 51**C**). This "ring" is partially an artifact of the sample preparation process and is possibly a slice through a larger 3D collagen shell of aligned fibres surrounding the spheroid.

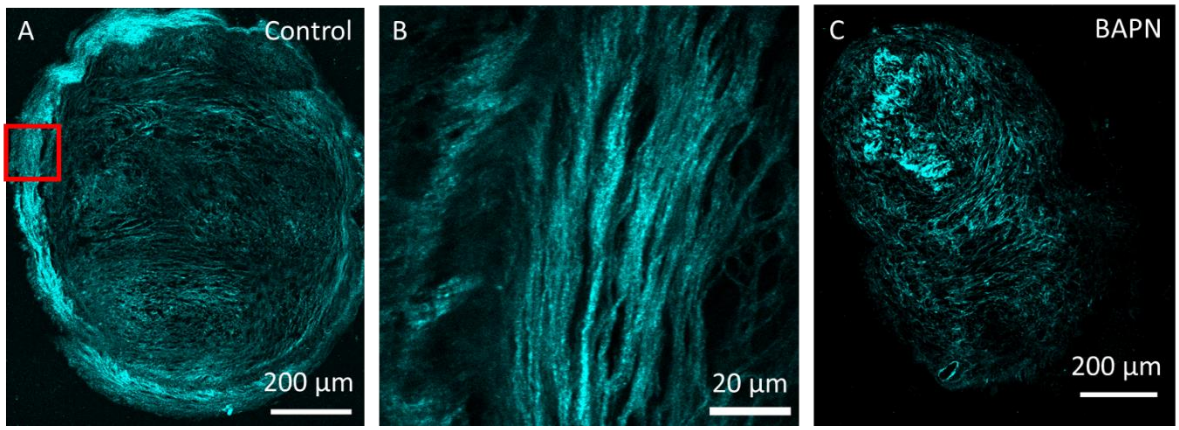

Figure 51: SHG intensity imaging of collagen changes.
(**A**) Tiled SHG image of control lung cell fibrosis model spheroid slices. (**B**) Zoomed image of the red boxed region in A, the laminar collagen structure at the edge of sample can be observed. (**C**) Tiled SHG image of a BAPN treated spheroid. The macroscopic collagen order around the edge of the spheroid is lost under BAPN treatment. Tiled images were acquired using a 20x/0.5 NA objective scaning a 250 µm x 250 µm FOV (per tile) to create a 512 x 512 pixel image for each FOV (tile). Image **B** was acquired using a 63x/1.2NA objective scanning a 103 µm x 103 µm FOV to create a 1024 x 1024 pixel image.

Page left intentionally blank

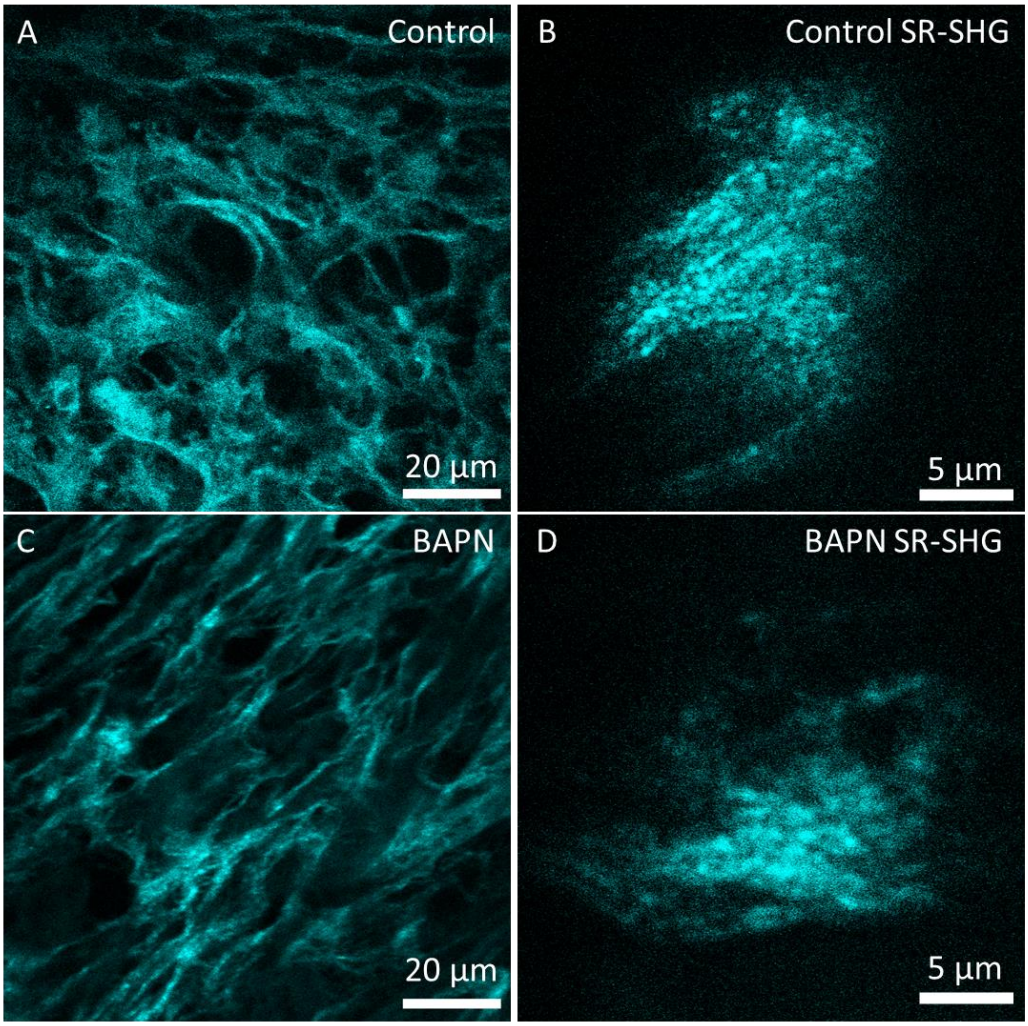
A
Control
20 µm
B
Control SR-SHG
5 µm
C
BAPN
20 µm
D
BAPN SR-SHG
5 µm

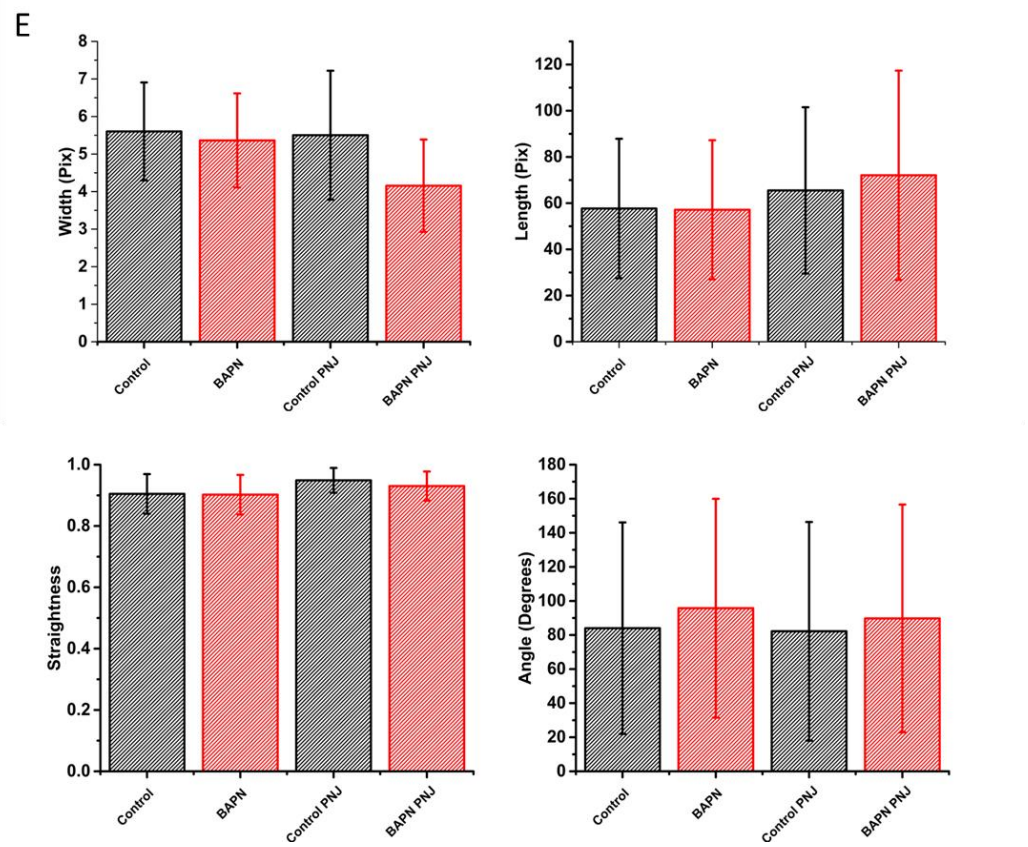
E
Width (Pix)
Length (Pix)
Straightness
Angle (Degrees)
Control
BAPN
Control PNJ
BAPN PNJ

Figure 52: Multi scale collagen morphology analysis.
Diffraction-limited SHG images of the collagen morphology within the centre of control **(A)** and BAPN-treated **(C)** spheroids. **B/D** show super-resolution images of similar regions for control and BAPN respectively. Collagen fibre analysis showed no differences in collagen morphology between the control and BAPN-treated spheres. Images were analysed for 4 parameters, fibre length, width, angle, and straightness. A total of 15 FOVs were tested for Control and BAPN diffraction-limited case and 20 FOVs for PNJ-assisted images. Error bars = 1 standard deviation from the mean. Images were acquired using a 63x/1.2NA objective. Diffraction-limited images were acquired by scanning a 103 µm x 103 µm FOV to create a 1024 x 1024 pixel image. SR images were acquired with the same parameters through 60 µm diameter spheres. Scale bars in B/C were calculated using the diffraction-limited scale and the multiplying this by the extra magnification of the sphere.

However, the central regions of the spheroids show similar collagen architecture when visualised with diffraction-limited SHG (Figure 52**A/C**) or by using PNJ-assisted SHG (SR-SHG) (Figure 52 **B/D**). These observations were further quantified via image analysis using CT-FIRE (Bredfeldt *et al.*, 2014) of fibres using a number of parameters: length, width, straightness and angle (Figure 52**E**). No significant changes were observed between Control and BAPN treated for any of these parameters.

The SHG polarisation anisotropy is able to indicate changes in collagen ultrastructure that affect the disorder of the collagen fibrils. The measured anisotropy from diffraction-limited images was unchanged (Figure 53**E**). In contrast, pSR-SHG showed that there is a significant decrease in anisotropy between the control and BAPN treated sample (Figure 53**F**) highlighting an increase in collagen disorder. This is consistent with previous observations using transmission electron microscopy of dysregulation of collagen fibril nano-structure in the spheroid model (Jones *et al.*, 2018).

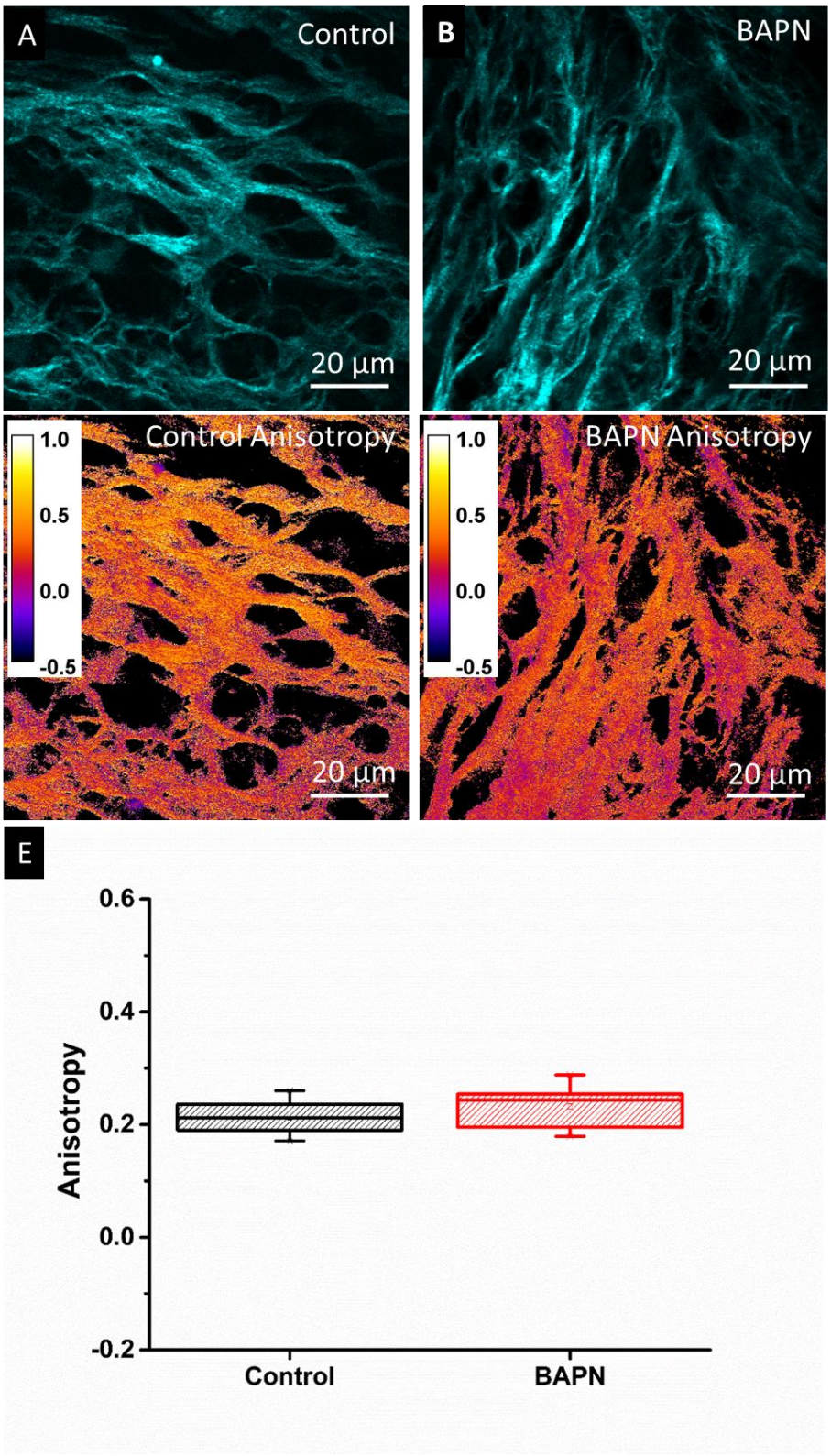

Figure 53: Anisotropy reveals increase in collagen disorder.
Example diffraction-limited SHG intensity and corresponding polarisation anisotropy images of control (**A**) and BAPN-treated (**B**) cell spheroid samples. The anisotropy images show that when measured using diffraction-limited imaging no change in anisotropy was detected, which is quantified in **E**, the mean anisotropies being 0.2132 and 0.2322 for control and BAPN-treated respectively (15 FOVs for control and BAPN).

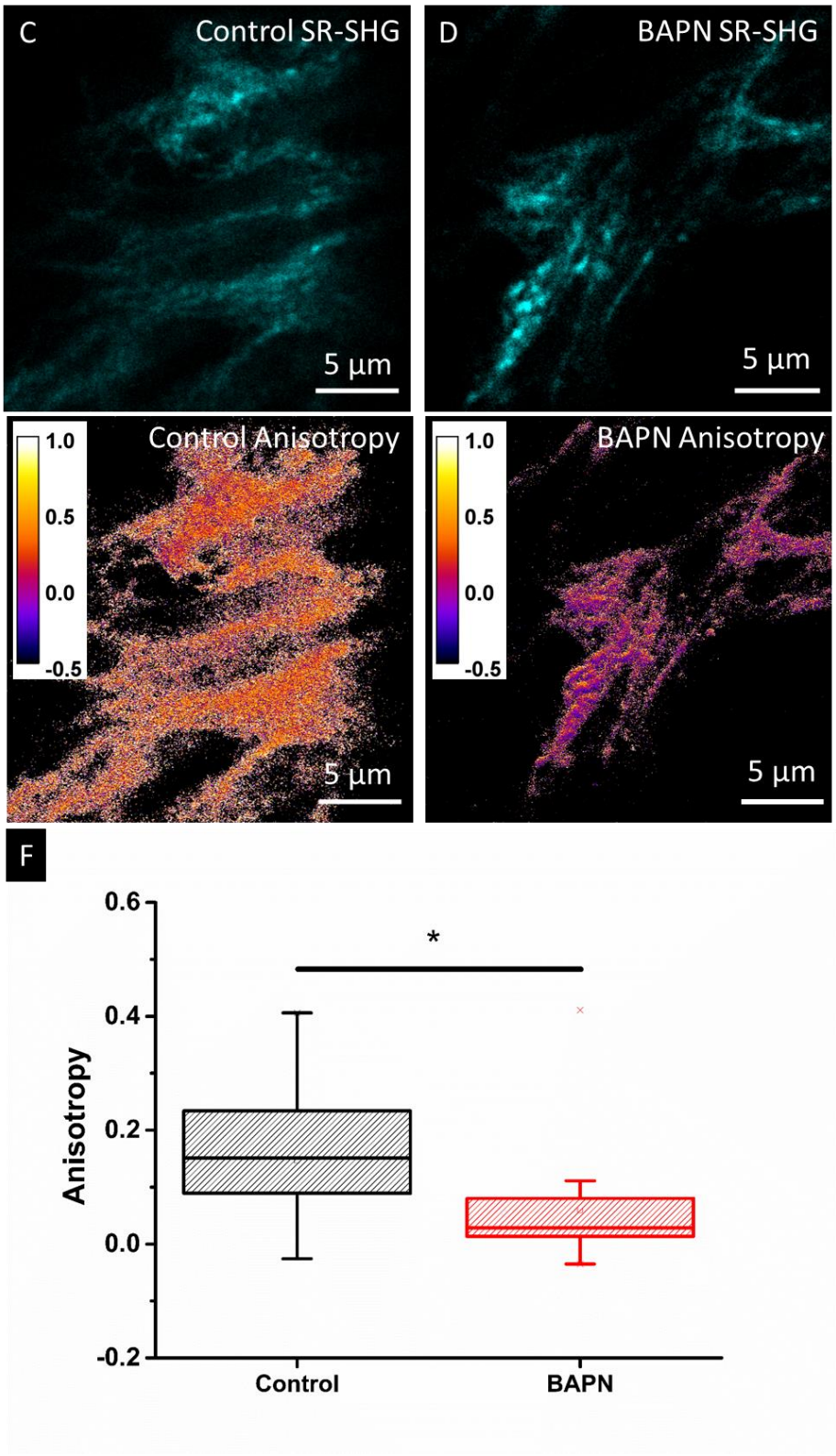

(**C/D**) SR-SHG images show that the gross morphological similarities exist at a SR scale; however, the SR-anisotropy (**F**) measurements highlight a significant difference in the mean anisotropy. Control-0.1471 (29 spheres) BAPN-0.0600 (20 spheres). BAPN moves the anisotropy towards 0 showing an increase in disorder. Significance tested using a one-way ANOVA, P = 0.0131. Images were acquired using a 63x/1.2NA objective. Diffraction-limited images were acquired by scanning a 103 µm x 103 µm FOV to create a 1024 x 1024 pixel image. SR images were acquired with the same parameters through 60 µm diameter spheres.

To further test the application of pSR-SHG in probing the changes that occur in IPF, SR anisotropy measurements were taken of lung biopsy samples from patients with healthy lung and those diagnosed with IPF. Figure 54 **A/B** shows example images SR-SHG images of healthy and IPF lung respectively; as with the collagen distribution within the lung cell spheroid sample (Figure 53 **C/D**), it is difficult to separate the tissues on morphological features. However, when compared using pSR-SHG (Figure 54 **C/D**) some regions that looked morphologically similar had a clear difference in anisotropy. To investigate this further, a series of SR images were acquired across 3 healthy lung tissue samples and 3 IPF tissue samples each taken from separate patients. Analysis of the mean anisotropy (n=30 FOVs) revealed no significant differences between the Healthy lung and IPF tissues (Figure 55).

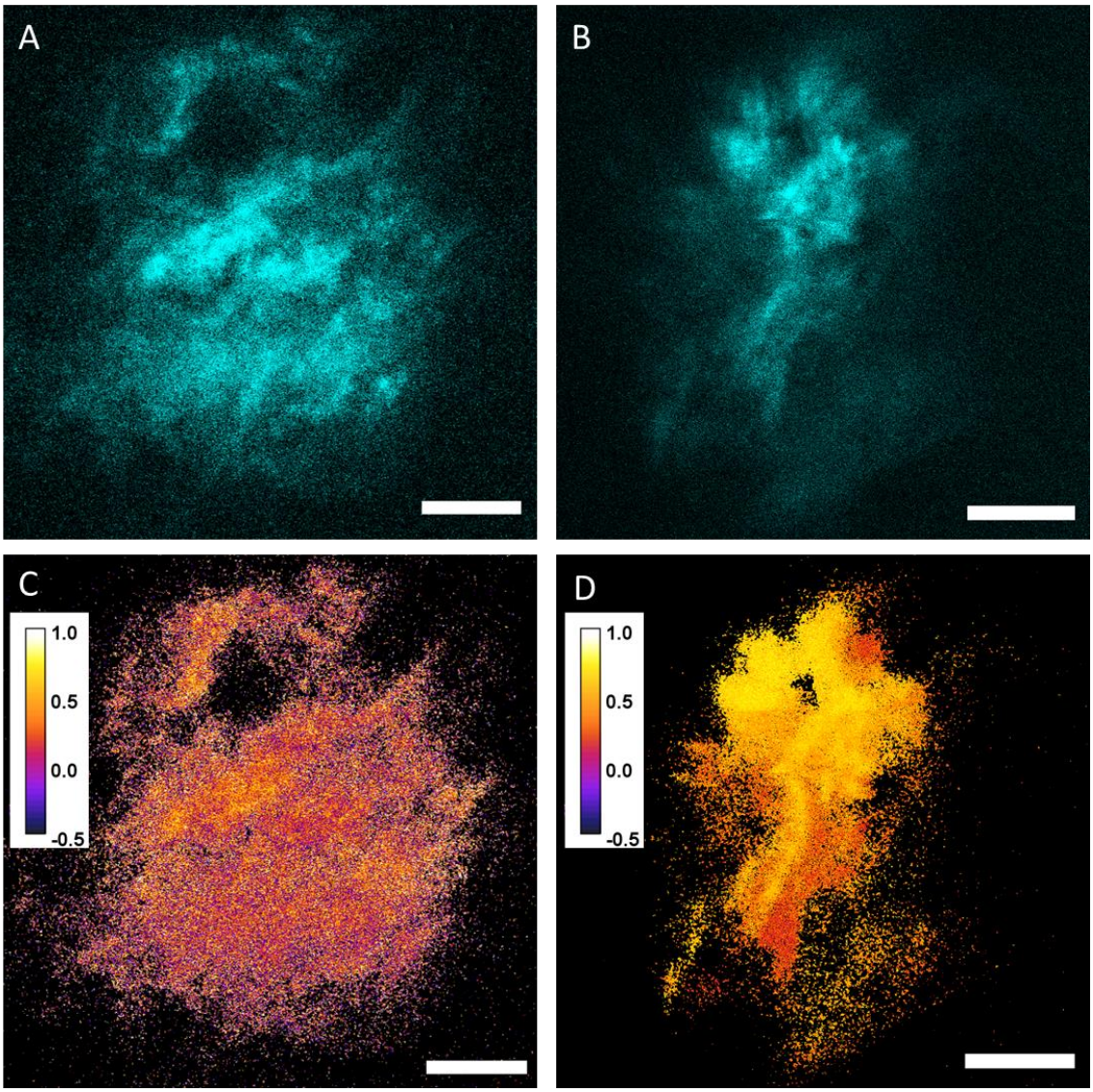

Figure 54: SR-Anisotropy of Human Lung Tissue
Example SR-SHG intensity images of **A**) healthy lung and **B**) IPF tissue. Corresponding pSR-SHG images **C/D** respectively. A difference in the general anisotropy can be seen between the two cases. Scale bar 5 µm. Images were acquired using a 63x/1.2NA objective, without the addition of a microsphere the FOV is 103 µm x 103 µm imaged onto 1024 x 1024 pixels, these parameters were then used to image through a 60 µm diameter microsphere.

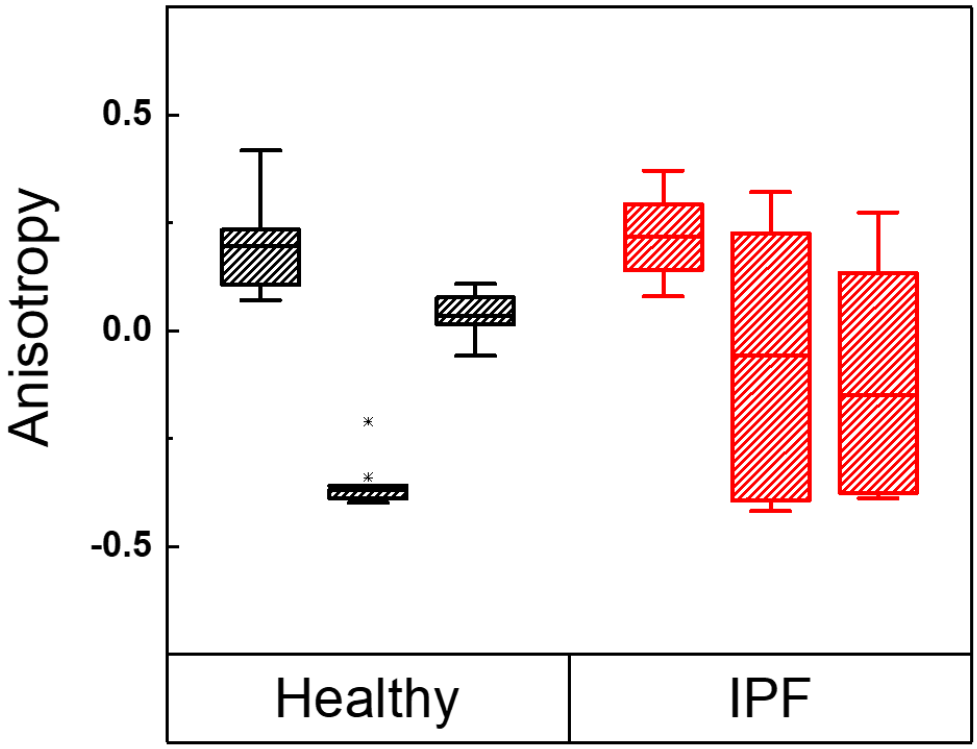

Figure 55: SHG anisotropy in lung tissue.
pSR-SHG anisotropy measurements from 3 healthy lung tissue samples (Black boxes) and 3 samples from patients diagnosed with IPF (red boxes). Both healthy and IPF tissue show a broad distribution of anisotropy values with no significant difference seen between the healthy and IPF groups when considered as single groups. Boxes show mean anisotropy and 25%-75% bounds, whiskers show range excluding outliers, outliers marked by * Measurements taken from 10 FOVs for each case, n = 30 FOV Healthy, n = 30 FOV IPF.

Both the healthy and IPF tissues show a broad range of anisotropy values when considering all measured values, the healthy lung tissue shows a much tighter distribution for all FOVs measured within the same sample but displays large differences between the mean anisotropy measures for each sample. In contrast the IPF tissues display a greater range of anisotropy values within each sample and a smaller distribution when comparing the mean anisotropy for each sample. Interestingly the complete range of anisotropy values observed in the Healthy lung and IPF tissues is largely similar.

A potential explanation for these observations is the heterogeneous distribution of pathology observed in IPF; as shown in Chapter 4, the collagen distribution in healthy lung and IPF tissue can be distinctly different, for example collagen surrounding an artery compared to a fibrotic focus. Therefore, sampling bias may result in measurement of significantly different polarisation

anisotropy values. However, within the same IPF tissue sample there will be regions of collagen distribution that fall broadly into 3 categories: A) healthy tissue with expected collagen morphology, B) fibrotic tissue with distinctly altered collagen morphology (e.g. a fibrotic focus) and C) tissue that appears healthy by morphology but contains ultrastructural changes to collagen. This morphologically-fine but ultrastructurally-changed tissue may be found surrounding clearly fibrotic tissue as the production of ultrastructurally-dysregulated collagen spreads from a nucleating type location. However, it may also be located within regions of primarily healthy tissue where morphologically there is no difference but ultrastructural changes detectable by pSR-SHG may be present, similar to that observed using F_{SHG}/B_{SHG} ratio by Kottmann *et al.* (Kottmann *et al.*, 2015). As IPF progresses, the degree of change to collagen ultrastructure will also change. Thus, when imaging IPF tissue using pSR-SHG it is possible that there will be a wide range of anisotropy values reflecting FOVs located at different stages of fibrosis progression. To further increase the utility of pSR-SHG, each imaged FOV could be further characterised using TEM or AFM to assess the degree of ultrastructural change associated with a given anisotropy value. In this way a calibration curve can be generated such that pSR-SHG measurements can give an indication of disease severity by mapping the anisotropy and thus, the collagen dysregulation. However, this presents a significant amount of work and due to the even smaller FOV of TEM and/or AFM techniques, would be even more sensitive to sampling bias than the pSR-SHG technique. Additionally, locating the same FOV in separate imaging methods is highly difficult making this process non-trivial and possibly impractical for contributing to a research or diagnostic tool.

The sensitivity of polarisation anisotropy measurements using pSR-SHG may be further improved by implementation of a forward detection scheme, this method of detection is more often used in other pSHG measurement as it affords (in general) greater signal collection due to the directionality of SHG. Also, as a significant proportion of backward-detected SHG is generated by the secondary scattering of forward-generated SHG photons, it is important to consider that some of the scattered light will become depolarised with respect to the excitation field. The detection of these SHG photons will alter the detected value versus the true generated value for the polarisation anisotropy. A common method used to remove the component of the light that is no longer polarised with the excitation is to place an analyser in front of the detector oriented with the polarisation of the excitation, however this is not compatible with anisotropy measurement where the measurement of 2 polarisations is used. For example, when detecting photons that are polarised parallel to the excitation polarisation it is not possible to know whether these photons were generated with parallel polarisation or were generated with a different polarisation and have then changed polarisation due to secondary scattering. To help overcome this, again,

forward detection may be useful as a greater proportion of the detected photons are generated in the forward direction and have not undergone secondary scattering, leaving the polarisation state unaffected. However, the issue of depolarisation is still present in forward detected signal and the effect of optical clearing on the SHG anisotropy has been explored by Nadiarnykh (Nadiarnykh and Campagnola, 2009) showing that optical clearing reduces the chance of secondary scattering events, thus increasing anisotropy sensitivity. For the case of pSR-SHG, the utility of optical clearing is limited as the sample thickness used is thin (10 μm) compared to the scattering mean free path, resulting in limited depolarization of both the excitation and signal. This is further compounded by the tight localisation of the PNJ to the sphere surface, limiting the effective penetration of the excitation to a few microns at the sample surface. Forward detection would, nonetheless, improve detection sensitivity but is non-trivial to implement. In a forward detection scheme a high NA (~1.2) condenser lens is used to collect the signal and a combination of a dichoric-mirror and bandpass filter used to separate the excitation from the signal and direct the signal onto a PMT. In this scheme the detection volume of the high NA condenser lens must be spatially overlapped and aligned with the SHG excitation volume. Due to the narrow width of the PNJ excitation, precise alignment with the detection volume would be complex and highly sensitive to drift in alignment. Therefore, the epi-detection scheme is preferable for simplicity.

It is also important to consider the resolution of a forward detection scheme. As the overall resolution of a system is a convolution of the excitation and the detection point spread functions, it is possible that the forward detection scheme will not benefit fully from the super-resolution focussing of the PNJ. Although the simplest implementation of PNJ imaging is using an epi-detection scheme, detection in transmission using microspheres has been demonstrated (Wang *et al.*, 2011; Li *et al.*, 2013); in these implementations white light is transmitted through the sample and collected by the microsphere. To date there has been no demonstration of SR focussing of the excitation light by a PNJ and subsequent detection of the emission in a transmission geometry. Thus, a full exploration of the resolution in this case is yet to be performed, particularly for the case of coherent imaging modalities which have inherent emission directionality.

5.5 Conclusions

SR-SHG is able to improve the resolution of a conventional SHG microscope and facilitate label-free super-resolution imaging via a simple addition to an existing multiphoton microscope. In this chapter, both qualitative and quantitative demonstrations of PNJ-assisted SR-SHG were shown, indicating a ~2.3X improvement over diffraction-limited imaging. While imaging in the far-field it was shown that near-field components of the photonic nanojet contribute to the sub-diffraction-limited spot sizes to enable super-resolution SHG observed with this method. However, the important difference between the PNJ SHG technique and conventional scanning of near-field probes is that in PNJ SR-SHG the probe is not scanned mechanically, nor does it capture the near-field feedback, but rather far-field laser scanning is used to obtain useful sample information. This makes the nanojet much faster for imaging samples. With the availability development of suitable resolution standards for SHG imaging and using smaller spheres to generate PNJs, even higher resolutions than those demonstrated could be achieved. The key parameters affecting SR-SHG imaging were characterised and optimised including the effect of sphere size, and distance from the focal plane. A method to increase throughput by using an array of self-assembled spheres to image multiple SR FOVs simultaneously was presented. It was also demonstrated that, despite the tight focussing properties of microspheres, the polarisation state is maintained in PNJs, allowing pSR-SHG imaging, wherein polarisation anisotropy of SHG signals can be measured. Measurement of anisotropy improved detection of hidden fibre features in both diffraction-limited as well as PNJ-assisted SR-SHG. pSR-SHG was applied to observe changes in collagen disorder in lung tissue spheroid sections and human tissue biopsy samples that were not detected by diffraction-limited SHG imaging. Currently, imaging of nanoscale changes in collagen is carried out by electron microscopy (EM) (Starborg *et al.*, 2013) and occasionally with atomic force microscopy (AFM) (Wen and Cynthia Goh, 2006). While higher resolution is possible with these methods, they do not allow for the potential imaging of live cells and cannot match the throughput of optical techniques. Using (p)SR-SHG methods developed in this chapter, significantly high resolution can be achieved without the complexity of sample preparation. Furthermore, in electron microscopy heavy metal stains need to be used to generate contrast (Tzaphlidou, Chapman and Meek, 1982) while for AFM analysis the collagen needs to be isolated (Viji Babu *et al.*, 2019) and analysis of native tissue is unrealistic. The (p)SR-SHG technique overcomes some of the issues of sample preparation associated with AFM and EM techniques and is label-free. It can be performed directly on cells and native tissues (and their sections) making it suitable for biomedical research and clinical translation. (p)SR-SHG can provide unprecedented nanoscale insight into biological harmonophoric-structures such as collagen and thus has the potential to improve our

understanding of a wide range of diseases and of the effects of treatments including in cancers and fibrosis.

Chapter 6 Multimodal Label-free Imaging of Extracellular Matrix

This chapter presents work in a manuscript under preparation: "Multimodal, Polarisation-Resolved Label-free Imaging of the Extracellular Matrix Ultrastructure in Pulmonary Fibrosis" *Peter Johnson, Christopher J. Brereton, Konstantinos Bourdakos, Kerry Lunn, James JW Roberts, Donna E Davies , Mark G Jones and Sumeet Mahajan*

Contributions: P Johnson performed all experiments, data processing and analysis, and designed experiments and the study. C J Brereton, K Lunn, J JW Roberts, D E Davies and M G Jones provided lung tissue model. K. Bourdakos built and helped maintain the imaging system. S. Mahajan conceptualised, designed, and coordinated the study. P. Johnson and S. Mahajan wrote the manuscript.

6.1 Abstract

The extracellular matrix (ECM) is composed of a complex collection of molecules that provide a diverse set of functions to multicellular organisms. These include structural support and mechanical and biochemical cell signalling. Deterioration of ECM components is a defining feature of many diseases including lung fibrosis. Two key lung ECM components are elastic fibres and fibrillar collagen. They perform complementary roles in defining tissue structure and mechanical properties. Here, multiphoton imaging was used to investigate the spatial organisation and interaction of these proteins, finding a close association between collagen and elastin. Photonic nanojet (PNJ) imaging was employed to improve the spatial resolution of these measurements observing fibre widths in agreement with previous electron microscopic data. Using polarisation anisotropy measurements, the ultrastructural organisation was investigated. Surprisingly, elastic fibres displayed a high degree of molecular order similar to that observed for collagen fibres, giving new insight into elastin organisation. The application of multimodal, label-free, super-resolution to the study of ECM proteins holds the potential for new biophysical insights and disease research.

6.2 Background

In the structural hierarchy of biology, individual cells form defined arrangements in tissues, which in turn arrange to form organs. To create such arrangements, cells secrete a number of proteins into the extracellular space. These proteins comprise both an insoluble scaffold, and soluble enzymes and glycoproteins, collectively called the extracellular matrix (ECM) (Kular, Basu and Sharma, 2014). The composition of the ECM can vary greatly from tissue to tissue as it is defined by the demands of the tissue and its physiological state (Frantz, Stewart and Weaver, 2010). The ECM is made of two key groups of macromolecules: fibrous proteins and proteoglycans (Järveläinen *et al.*, 2009; Schaefer and Schaefer, 2010). Proteoglycans provide a diverse set of functions depending on the specific tissue. These include force buffering, filtration and hydration (Järveläinen *et al.*, 2009). The main fibrous proteins of the ECM are collagens, elastins, fibronectins and laminins. Fibronectins and laminins both play important roles in cell adhesion and cell signalling, interacting via cell surface receptors (integrins) (Kular, Basu and Sharma, 2014). Additionally, fibronectin is key to the wound healing response (Lenselink, 2015). Collagen and elastin are closely interlinked within the ECM playing different, but interconnected, roles (Kular, Basu and Sharma, 2014). Collagens are the main structural component of the ECM providing tensile strength, regulating cell adhesion and migration and guiding tissue development (Rozario and DeSimone, 2010). Elastin is the key component of elastic fibres in association with fibrilin-microfibrils (Koenders *et al.*, 2009). The primary role of elastin is to provide elastic recoil, allowing tissues to return to their original shape after deformation. Due to this property elastic fibres can be found in the ECM of tissues that undergo regular structural deformation, such as the dermis of the skin (Eckes, Nischt and Krieg, 2010), blood vessels (Cocciolone *et al.*, 2018) and the lung (Mecham, 2018). Collagen is often found in close association with elastic fibres, to prevent the overextension of elastic fibres (Lemos *et al.*, 1997). Changes in the structure and components of the ECM are both the cause and effect of many diseases such as fibrosis (Parker *et al.*, 2014; James *et al.*, 2019) and cancer (Walker, Mojares and del Río Hernández, 2018). Thus, methods of studying the ECM are highly desirable.

Multiphoton microscopy provides an ideal tool to study the ECM in a label-free manner (Zoumi, Yeh and Tromberg, 2002). Many extracellular components are autofluorescent with ultraviolet excitation making them readily excitable by UV light or common multiphoton, pulsed-lasers using two-photon-excited fluorescence (TPEF) (Zipfel *et al.*, 2003). Elastic fibre autofluorescence is primarily attributed to the crosslinks present in elastin (Deyl *et al.*, 1980) and has a relatively high quantum yield compared to other autofluorophores (Monici, 2005). Collagen fibres contain an ordered helical structure giving rise to a high nonlinear susceptibility, making them a good target

for imaging via second harmonic generation (SHG) (Campagnola, 2011). Due to the close association and interconnected roles of these fibrous proteins, the ability to image both in a label-free manner is of research and diagnostic significance.

Loss of the delicate balance between the opposing roles of collagen and elastin is an underlying mechanism of fibrotic disease. Idiopathic pulmonary fibrosis (IPF) is a prototypic fibrotic lung disease that displays drastic changes in ECM structure (Kristensen *et al.*, 2014; Richeldi, Collard and Jones, 2017). Multiple studies using SHG microscopy have been performed investigating the changes in collagen structure and function in IPF (Tilbury *et al.*, 2014; Kottmann *et al.*, 2015; James *et al.*, 2019). By contrast, investigation into changes in elastin during disease progression using TPEF has been minimal. Analysis of histologically-stained lung sections has shown that there is a positive correlation between the amount of elastic fibres and the severity of IPF progression (Enomoto *et al.*, 2013). The distribution of elastin has also been shown to become more disorganised through disease progression (Tilbury *et al.*, 2014). Recently, Jones *et al.* (Jones *et al.*, 2018) developed a 3D in vitro model of lung fibrosis using cultured fibroblasts. They showed that dysregulation of collagen ultrastructure mediates pulmonary fibrosis. The ability to control the environment of fibroblast cells, which produce ECM components, makes this an ideal model to study changes in other ECM structures. In this chapter multiphoton, label-free imaging is used to probe the structure and organisation of ECM proteins in this model.

6.3 Materials

All materials have been listed previously in Chapter 3.

6.4 Experimental methods

6.4.1 Solution spectra

The fluorescence spectroscopy setup has been detailed previously. Elastin powder was dissolved in 0.2 M TRIS at pH 8.8. Spectra were acquired with 5 nm excitation and emission slit widths and PMT gain set to high. Presented spectra are an average of 3 analytical repeats with no further processing.

6.4.2 Elastic Fibre Staining

Elastic fibre staining has been detailed previously (section 3.13)

6.4.3 Multiphoton and PNJ Imaging

Details of the multiphoton imaging system have been described previously (section 3.3). All images were acquired using a 63x/1.2NA objective (HC PL APO 63x1,2 W CORR UVIS CS2). All diffraction-limited laser-scanning images were acquired using 1024 x 1024 pixels scanning a 103 µm x 103 µm field of view. This gives an effective pixel size of 101 nm. The diffraction-limited focal spot size of the system at the shortest wavelength used for multiphoton excitation (710 nm) is 230 nm (FWHM) thus Nyquist sampling was satisfied. Images acquired using microspheres were acquired through 60 µm diameter microspheres, the objective was refocussed 80 µm below the sample surface to capture the virtual image formed by the sphere. This refocus distance was chosen as microsphere FOVs were measured individually, therefore overlap of images from neighbouring spheres was not an issue and the greater magnification provided by this refocus distance could be exploited. The scale of the microsphere image was calculated by taking the scale of the image without a microsphere and applying the additional magnification of the microsphere (3.8x) (Figure 36 **D**). This gives an effective pixel size of ~27 nm.

6.4.4 Polarisation Anisotropy imaging

The method for polarisation anisotropy imaging has been described in detail in Section 5.3.4. Briefly Images were acquired at 2 orthogonal linear polarisations one parallel and one

perpendicular to an analyser placed in front of the detector. Anisotropy images were calculated on a pixel-wise basis and the mean anisotropy extracted for analysis. Anisotropy images were acquired sequentially for both autofluorescence and then SHG.

6.4.5 Lung Fibroblast Spheroid Sample

Primary lung fibroblasts from a patient with Idiopathic Pulmonary Fibrosis (IPF) were seeded in Transwell inserts under normal conditions for 24 hours before the media was replaced for control conditions. After 6 weeks of growth under these conditions the spheroids were harvested, fixed in 4% paraformaldehyde, paraffin embedded, and 5 μm sections cut ready for imaging.

6.4.6 Multiphoton Excitation Spectra

Elastin was sealed under a coverslip in powder form and imaged without further processing. Multiphoton excitation spectra were acquired using the multiphoton imaging system described in section 3.3.1. Samples were imaged at 10 nm wavelength intervals. The intensity of a region of interest was plotted against wavelength to generate spectra. All presented spectra are an average of 2 ascending and two descending wavelength scans.

6.4.7 Fibre Size Analysis

Fibre size was analysed using a line intensity plot along the longest axis of the fibre for fibre length and perpendicular to the longest axis for fibre width. Line width was set to 3 pixels.

6.5 Results

6.5.1 Methodology Establishment for Elastin Imaging

Despite being one of the most common autofluorescent molecules in the ECM, the reported wavelengths used for imaging elastin vary widely (Table 1). It is reported that there may be multiple fluorophores within elastin (Deyl *et al.*, 1980), which may lead to a complex fluorescence profile. Different fluorescence profiles also exist for different isomers and maturities of elastic fibres (Blomfield and Farrar, 1969).

Sample	Molecule	Excitation	Emission	Ref
Breast cancer	Elastin	890	583	(Tilbury *et al.*, 2014)
Lung	Elastin	860	490	(Débarre *et al.*, 2006)
Lung	Elastin	290/325	340/400	(Vishwanath and Ramanujam, 2011)
Lung	Isotropic Elastin	880	~500	(Abraham and Hogg, 2010)
Lung	Mature elastin	810	515-555	(Kottmann *et al.*, 2015)
Murine trachea	Elastin	750	454	(Mazumder *et al.*, 2019)
Human Skin	Elastin	740	480	(Zipfel *et al.*, 2003)
	Powdered elastin	"UV"	480	(Yasui, Tohno and Araki, 2004)

Table 5: Reported autofluorescence wavelengths for elastin, a large variation in both excitation and emission wavelength are reported.

Due to the variation in the literature, the autofluorescence profile was first confirmed using isolated elastin powder in solution (Figure 56**A**). The one-photon fluorescence profiles had a peak excitation at 340 nm and a broad emission with a peak centred at 430 nm. Using this information as a guide, a multiphoton excitation profile was acquired using the same powder. A strong excitation peak was observed at 720 nm and a smaller peak at 840 nm when the emission was measured at 425±13 nm. 720 nm was used for further imaging of elastin within tissues (Figure 56**B**). Due to the lack of a continuously-variable detection filter in the multiphoton imaging system a range of available bandpass filters, spanning the emission range observed under one-photon excitation (380 nm – 660 nm), were tested to determine the optimum band for signal collection (Figure 56**C**). A bright and structurally-distinct signal was observed at the band surrounding 430 nm (Figure 56$\mathbf{C_2}$) which agreed with the one-photon profile. A bright signal was also observed at longer wavelengths (650±10 nm) (Figure 56$\mathbf{C_6}$). This signal did not appear to match the same structure as the signal in the other wavelength bands. This may have been an artefact from the elastin extraction process. The pyridinoline fluorophore in elastin is known to be unstable and yields several fluorescent degradation products (Deyl *et al.*, 1980) the signal observed at the longer wavelengths was not considered to represent the elastin fluorescence.

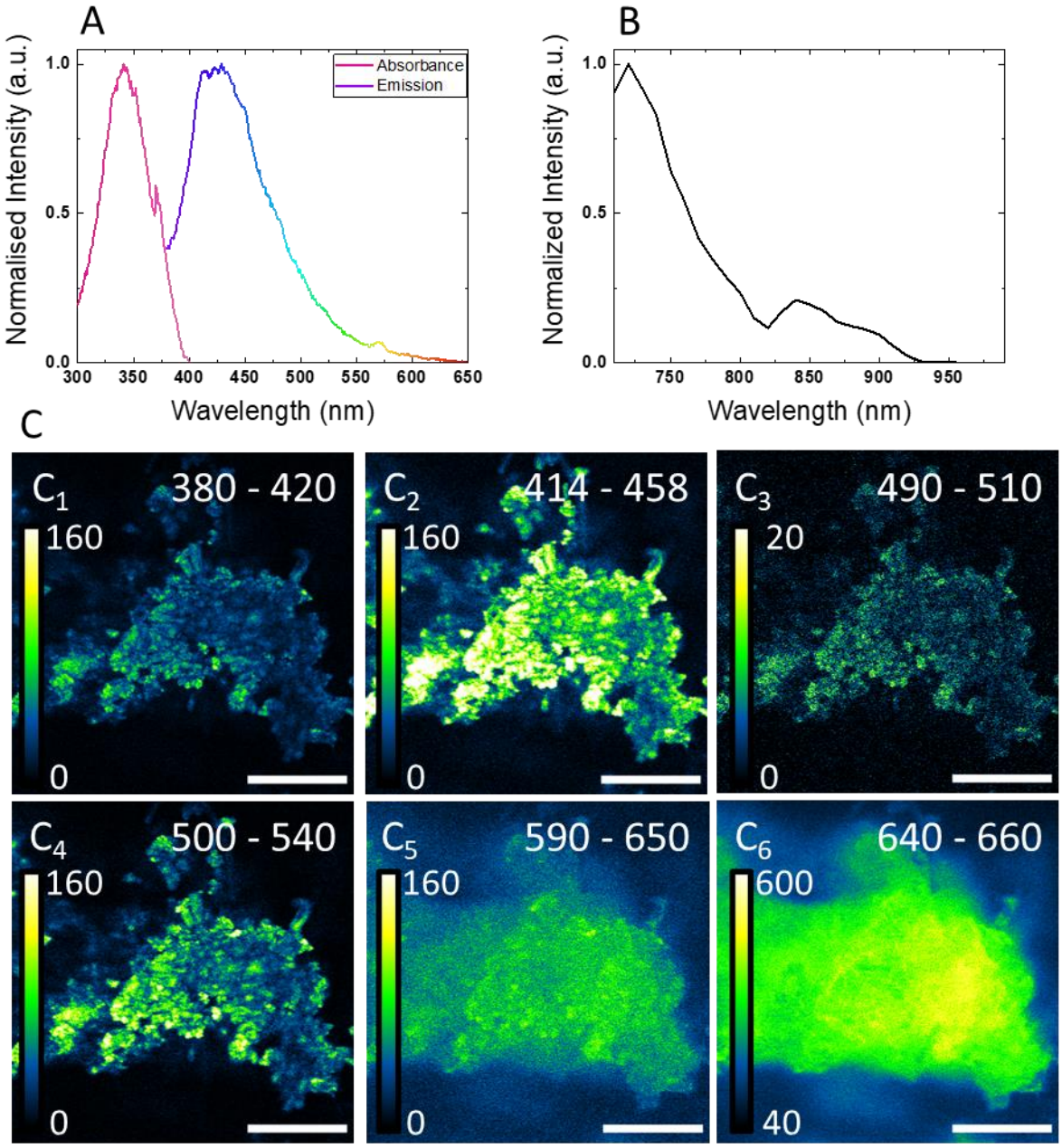

Figure 56: Establishing elastin imaging
(A) One-photon Absorbance/Emission spectra of elastin powder. Peak absorbance was observed at 340 nm and peak emission at 430 nm. (B) TPEF excitation spectrum of elastin powder, peak excitation was observed at 720 nm. (C) Elastin powder imaged using two-photon excitation at 720 nm and the emssion collected using bandpass filters indicated on images. The brighest signal considered to be from elastin was observed at 414 nm – 458 nm (C_2) in agreement with the spectrum in A. A bright signal that did not highlight the same features was observed in the 640 nm - 660 nm band (C6). Scale bar = 30 µm.

As the fluorescence of elastin can depend on tissue type and maturity (Blomfield and Farrar, 1969), the same band pass filters were tested to image the lung cell spheroid sample (Section 6.4.5). For the 3 shorter wavelength bands (Figure 57 top row) fibrous structures could be observed with the brightest signal centred at 436 nm. At 520 nm the same fibrous structures could be observed but with additional bright punctate spots. At 620 nm primarily the bright spots

could be observed and at 650 nm a diffuse signal was observed. The bright spots remained unchanged with multiple scans of the same FOV and therefore were not considered to be sample damage as observed in previous multiphoton imaging (e.g. Figure 40)

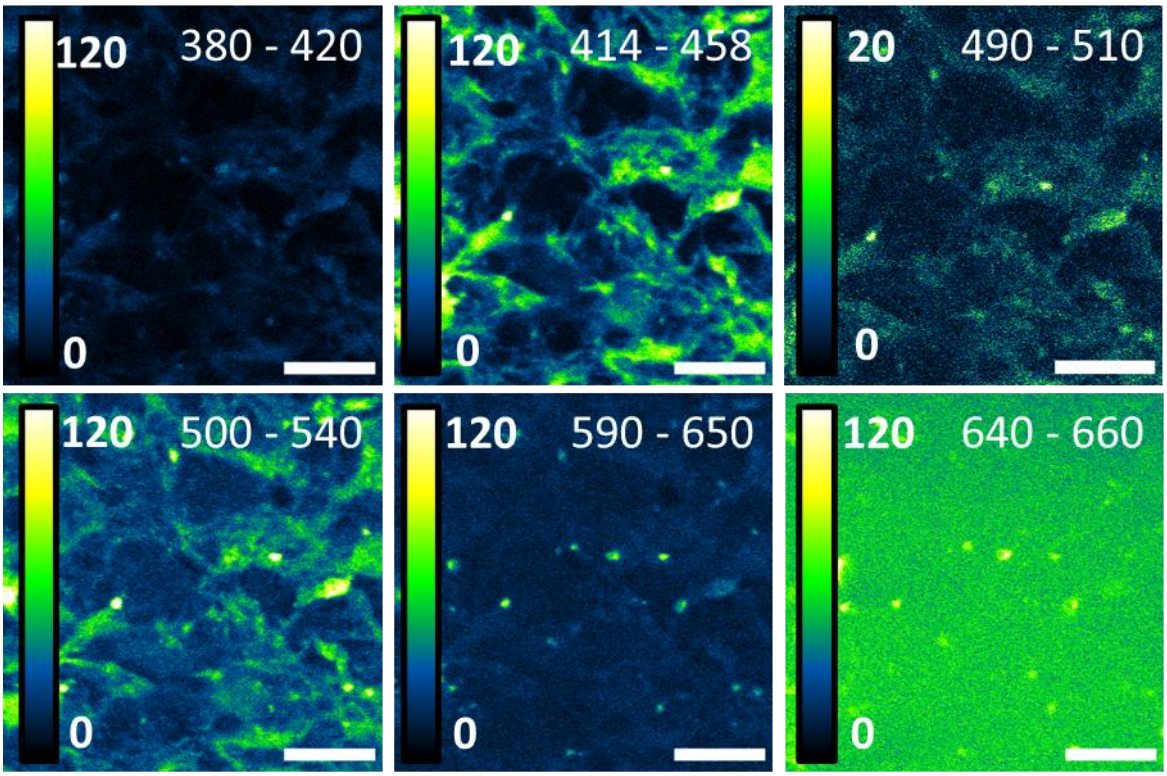

Figure 57:Testing of identified wavelengths in unstained spheroid sample tissue.
TPEF images were acquired at 720 nm excitation and emission collected at the bands indicated in the images. The strongest signal was observed for the 414 nm – 458 nm band. The resolved structures in this band had a fibre-like morphology suggesting that elastin fibres were being imaged. The intensity of the 490 nm-510 nm band was much weaker and has been displayed on a linearly adjusted LUT to aid visualisation. In the 590 nm – 650 nm band bright spots could be observed. In the 640 nm - 660 nm band a diffuse signal or potentially higher background could be observed. Scale bar = 15 µm.

To verify that the fibrous structures imaged at 430 nm were in fact elastin fibres, a tissue section was stained using Verhoff-Van Geission stain for elastic fibres. This stain was chosen as it is simple to perform and has high sensitivity for elastic fibres (Kazlouskaya *et al.*, 2013). With this stain nuclei and elastic fibres are stained black, collagen stained red and cytoplasmic elements are stained yellow. The black stained nuclei can be observed in Figure 58 (Left). As the stain results in black colouration, the dye displayed strong absorbance of the laser resulting in damage to the sample when heavily stained. Thus, a minimal staining procedure using extensive differentiation was employed to highlight elastin fibres whilst maintaining the ability to image the TPEF signal (Figure 58 middle). Qualitative co-localisation was observed between the stain and the TPEF signal (Figure 58 right). It was noted that the black spots of the Verhoeff Stain colocalised with structures in the TPEF channel suggesting the signal may be (in part) from the Verhoeff stain. Due

to the limited availability of samples it was not possible to perform a confirmatory experiment where the same FOV was imaged using TPEF before and after the staining procedure, or to antibody label for elastin using a fluorophore that is spectrally shifted from the TPEF emission. As the structures in Figure 58 (middle) showed a similar fibrous nature to those observed in Figure 57 (414 nm -458 nm band) it was decided that the TPEF signal was primarily from elastin.

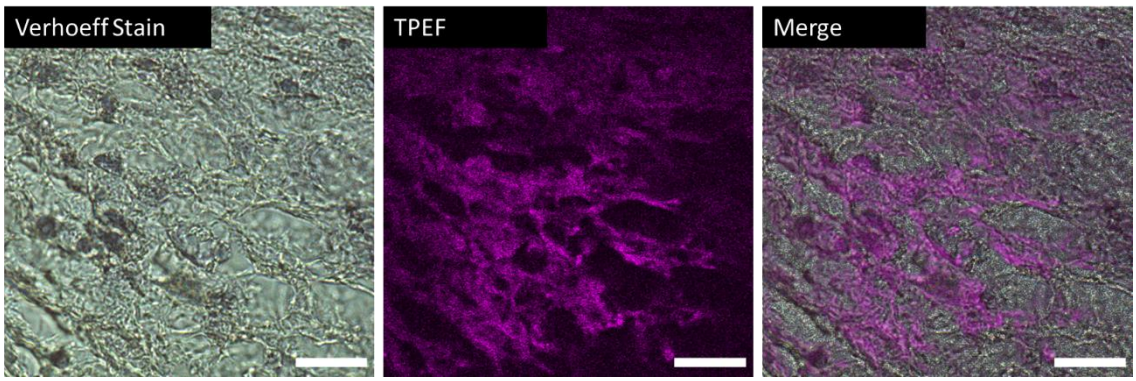

Figure 58: Verification of observed autofluorescence signal.
Images of the same sample location acquired using Verhoeff staining and TPEF excited at 720 nm and collected at 436 nm. Verhoeff staining highlights the nuclei in black and the elastin fibres as a paler black. The merged image shows good qualitative agreement between the elastin staining and the TPEF signal. The Verhoeff staining was performed before the TPEF imaging. Scale bar 20 µm.

Having established the conditions required to image elastin fibres, this was combined with SHG imaging to investigate the changes in ECM structures. As SHG occurs at half the wavelength of the excitation and TPEF is red-shifted relative to half the two-photon excitation wavelength it is possible to simultaneously acquire SHG and TPEF signals. This is achieved by matching the excitation wavelength to the excitation of the fluorophore and matching the emission channels to the fluorescence emission and exactly half the excitation wavelength. For the determined elastin excitation maximum at 720 nm the two-photon-excited autofluorescence emission is at 436 nm and SHG signal will be produced at 360 nm. In this implementation, the SHG signal would have been recorded on PMT1 and the TPEF signal on PMT2 (section 3.3.1), the two signals were separated by a dichroic mirror with 405 nm cut off. When imaging in this configuration it was observed that the SHG signal was weaker than observed in other SHG imaging experiments, therefore, further investigation was performed. Using the same sample as Figure 51**B**, which has previously been confirmed to contain the observed fibrillar collagen structure (Jones *et al.*, 2018), SHG images were acquired at 360 nm emission and 404 nm emission, this was performed sequentially on the same imaging channel and thus the same PMT (PMT1). The dichroic mirror used to direct the SHG signal to PMT1 was changed between the 360 nm and 404 nm acquisitions. It was observed that the SHG signal detected at 360 nm (720 nm excitation) was weaker than that at 404 nm (808 nm excitation) (Figure 59). The latter conditions were used previously for collagen imaging (Section 5.4.6).

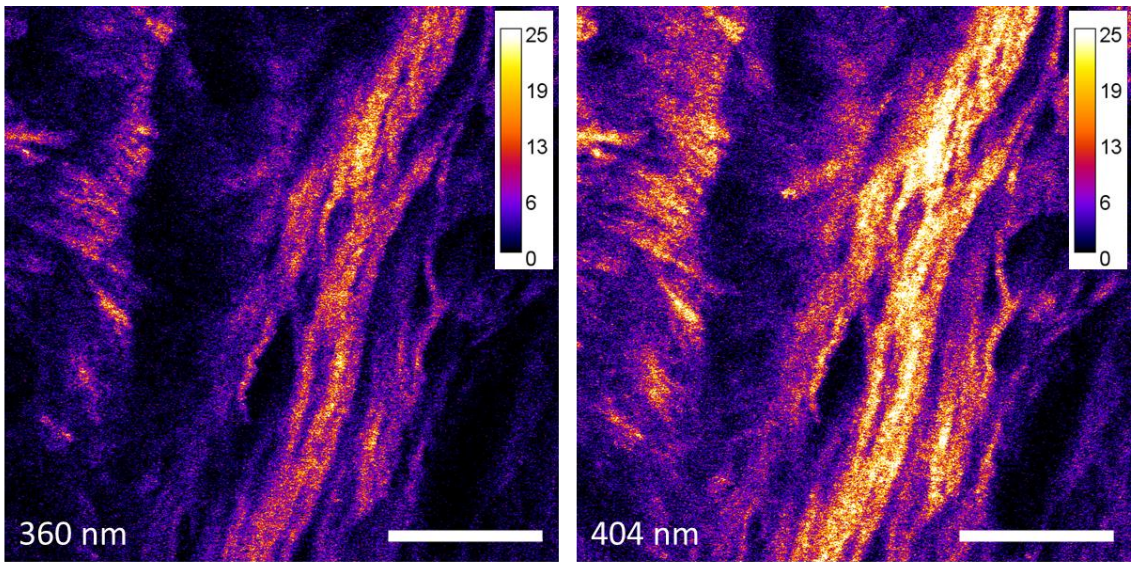

Figure 59: Comparing SHG intensity at different wavelengths
SHG images of fibrillar collagen in a lung cell spheroid sample section. (Left) excited/collected at 720 nm/ 360 nm and (Right) 808 nm/404 nm. Images were acquired sequentially using the same PMT. The signal recorded at 404 nm was approximately 3 times stronger than that for 360 nm. Scale bar 20 µm.

It has previously been shown that the SHG intensity for collagen increases with decreasing wavelength between 700 nm and 800 nm (Zipfel *et al.*, 2003) thus this result was counter

intuitive. Reasons for the weaker detected signal at 360 nm may include the relative transmission of glass components in the microscope, including emission filters, at 360 nm and 400 nm and the detection efficiency of the PMT which peaks at 400 nm (Appendix C **PMT 1**). However, the PMT1 sensitivity is only 1.14 times greater at 400 nm than 360 nm, thus the lower detected signal was assumed to be primarily due to the efficiency of the other optics in the detection path at these two wavelengths. Hence to minimise misinterpretation and the influence of the optics and detectors, we henceforth acquired multimodal imaging signals sequentially, tuning the laser wavelength between acquisitions. The detection filters were also swapped so that both SHG and TPEF signals were collected using the same PMT which had the greatest detection efficiency of the available PMTS at the 400 nm – 440 nm wavelength range (Appendix C **PMT1**).

Collagen is known to have a TPEF profile that can be excited at 720 nm with a broad emission including the selected elastin imaging wavelength (436 nm) (Zoumi, Yeh and Tromberg, 2002). To check whether this signal would interfere with elastin imaging, images were acquired of a pure collagen gel. The SHG signal was acquired at 808 nm excitation and 400 ± 20 nm emission (Figure 60 Top), and the TPEF signal was acquired at 720 nm excitation and 414 nm – 458 nm emission (Figure 60 middle/bottom). The SHG signal was approximately 10 times stronger than the TPEF signal. The excitation power used was 20 mW at the sample which was also used for future multimodal imaging. The SHG and TPEF signals observed in multimodal imaging were of comparable intensity indicating that the TPEF signal came from a different, brighter molecule.

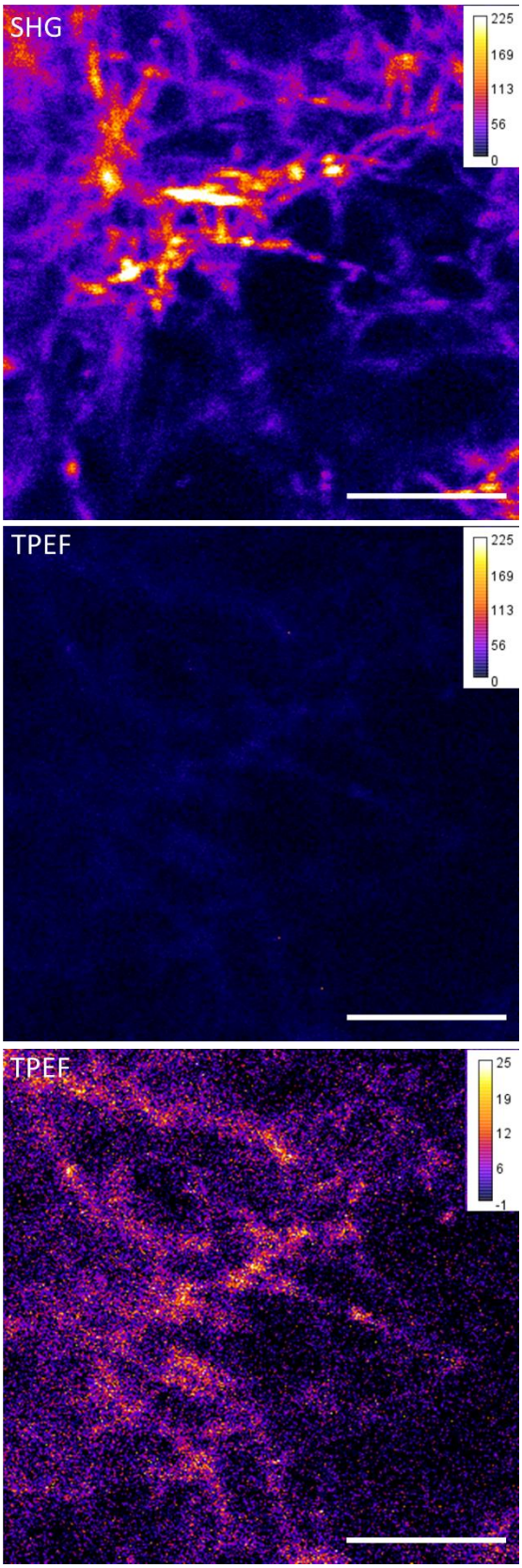

Figure 60: Comparing signal strength of SHG and TPEF for collagen.
Top: An SHG image of a pure collagen gel excited at 808 nm and emission collected at 400 ± 20 nm. **Middle/Bottom**: the same gel imaged using TPEF excited at 720 nm and emission collected at 414 nm – 458 nm. The TPEF signal is approximately 10 times weaker than the SHG signal. Scale bar 10- µm.

Page left intentionally blank

6.5.2 Multimodal Imaging of the Extracellular Matrix

TPEF/SHG intensity images (Figure 61**A/B**) showed a general agreement in spatial location between the elastin and collagen fibres (Figure 61 **C**). It has been observed previously that elastic fibres in tissues follow the predominant direction of collagen fibres (Green *et al.*, 2014). The elastin signal observed at the same location as the collagen signal (Figure 61 **D/E**) showed less defined fibrous structures than the collagen signal. Elastic fibres are known to contain a combination of amorphous elastin and microfibrils (Montes, 1996), in contrast to fibrillar collagen which has a highly organised hierarchical structure (Deniset-Besseau *et al.*, 2009). These underlying structural differences between the two imaged structures may be the reason for the observed difference.

The collagen fibres shown by SHG had a discontinuous structure along the length of the fibre (Figure 61 **E** red arrows), that was not observed in elastic fibres. The discontinuous signal has been seen before in images of rat tail tendon (Williams, Zipfel and Webb, 2005) and cornea (Han, Giese and Bille, 2005). In rat tail tendon the fibres are highly aligned and therefore can be mounted such that they run parallel to the imaging plane. This discounts the possibility that the discontinuity is due to neighbouring fibrils oriented perpendicular to the imaging plane. Fibril discontinuity was observed more prominently in backwards detected SHG and was attributed to immature collagen fibrils produced during fibrilogenesis. Immature fibrils are known to have a smaller diameter and therefore generate more backwards detected SHG than larger fibrils (LaComb *et al.*, 2008), this may explain the observed discontinuity/segmentation observed in the images acquired.

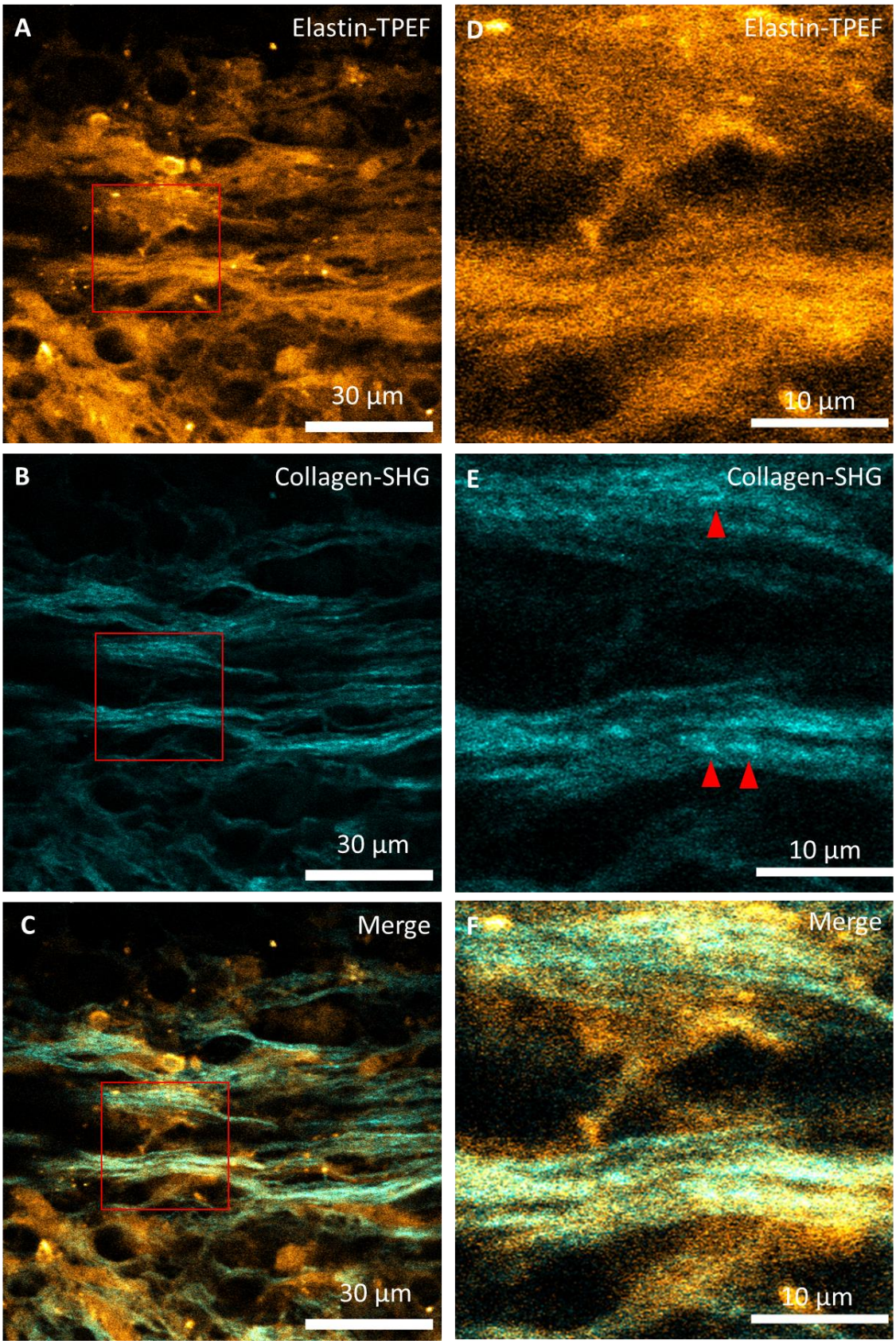

Figure 61: Diffraction-limited multimodal imaging.
(A) Elastin and (**B**) collagen fibres imaged using TPEF and SHG respectively. The merged image (**C**) shows a spatial overlap of the two signals. (**D/E/F**) zoomed images of the red boxes in (**A/B/C**). The elastin signal (**D**) shows less defined fibres than the collagen fibrils in (**E**). The collagen fibres shows a segmented structure (red arrows), where the signal intensity shows bright regions and

dim regions when observed along the length of the fibre. (**F**) Merge image of D/E, the close spatial arrangement of collagen and elastin is clearly shown.

As fibrosis is characterised by the aberrant and excessive generation of new collagen fibrils, the length of the segments were analysed as described in (section6.4.7). Analysis of the fibril lengths revealed that most fibrils were below 2 µm in length with a peak around 0.6 µm in length (Figure 62). Williams *et al.* report segment lengths of "a few microns or less" (Williams, Zipfel and Webb, 2005). As a more detailed characterisation of segment length was not reported direct comparisons cannot be made. Furthermore, the sample in their case was an immature rat-tail tendon whereas this sample was produced by human lung fibroblasts. The level of maturity will affect the degree of fibrilogenesis and thus the length of observed fibrils (Parry, Barnes and Craig, 1978; Craig *et al.*, 1989). Other factors including species and sample preparation may have also affected the observed fibre lengths compared to those observed by Williams *et al.* As the analysis of apparent fibre length was only performed in two dimensions it is possible that many of the observed segmented fibres represent cross-sections of fibres that orientated at an angle to the imaging/sample plane. The polarisation-dependent nature of SHG means that only those components of the fibres that are orientated parallel to the polarisation of the excitation will be imaged (Figure 63). Those components extending axially with respect to the imaging plane will not be efficiently excited unless longitudinal excitation polarisation can be achieved at the sample by focussing a radially-polarised beam with a high NA objective. Thus, there is a potentially caveat to the observed apparent fibre lengths.

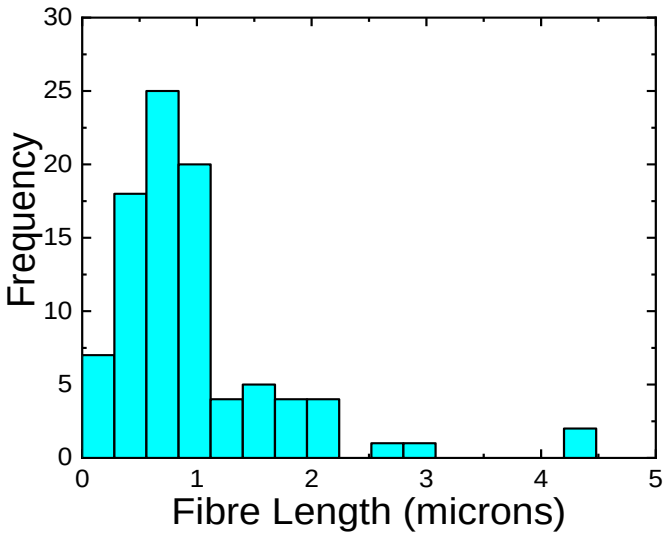

Figure 62: Analysis of punctate fibril length.
Most fibrils had a length less than 2 µm long with most fibril lengths centring around 0.6 µm long. Bin width 288 nm (0.61λ/√2NA). Fibril lengths of 100 fibrils analysed over 5 FOVs.

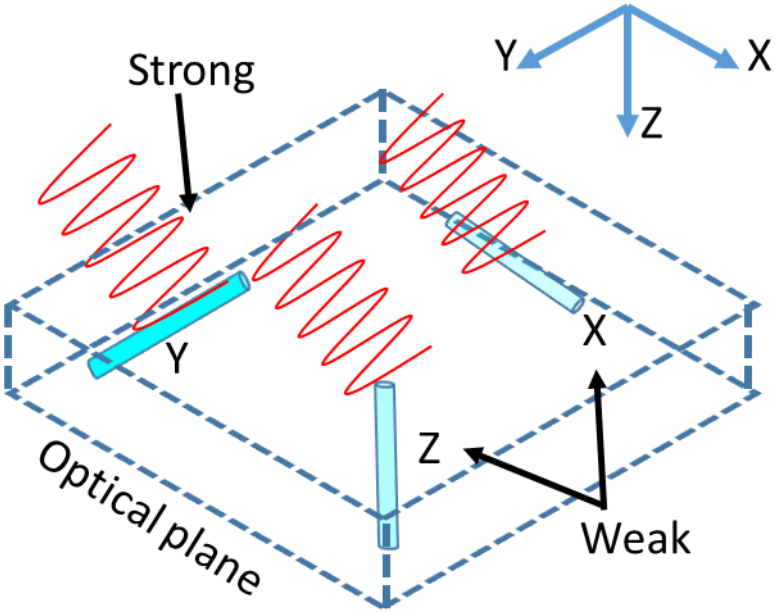

Figure 63: Schematic of fibre orientation vs. polarisation and effect on SHG signal
Fibres aligned parallel to the excitation polarisation (in this case Y polarised) generate strong SHG signal. Fibres oriented perpendicular to the excitation polarisation are weakly excited, this can be both within (X) or through the optical plane (Z).

The observation of segmented fibrils suggested the presence of immature fibrillar components of the ECM. As collagen and elastic fibres mature they undergo cross linking (Eyre, Paz and Gallop, 1984). In collagen, intramolecular crosslinking occurs between alpha chains of the same collagen triple helix and intermolecular crosslinks form between laterally adjacent triple helices staggered by a quarter of the triple helix length (Friess, 1998). In elastin, crosslinking occurs between tropoelastin monomers to form mature elastin and happens in a more disordered fashion (Schräder *et al.*, 2018). Errors in crosslinking have been implicated in the progression of lung fibrosis (Kristensen *et al.*, 2014). In collagen, crosslinking affects SHG harmonophore alignment and structural disorder (Lutz *et al.*, 2012; Jones *et al.*, 2018). To further probe the disorder for both collagen and elastic fibres, polarisation analysis was employed, specifically the polarisation anisotropy. The polarisation anisotropy is given by the equation $r = (I_{\parallel} - I_{\perp})/(I_{\parallel} + 2I_{\perp})$ where $I_{\parallel}$ and $I_{\perp}$ are the intensities recorded parallel or perpendicular to incident polarisation, as discussed in Chapter 5. It can indicate the degree of disorder within the sample (Latour *et al.*, 2012). In the case of fluorescence it can also indicate the degree of rotational freedom of the fluorophores (Lakowicz, 1999).

The polarisation anisotropy of collagen and elastin was investigated using the multimodal nature of the imaging system (Figure 64**A/B**). The mean SHG anisotropy was 0.18 ± 0.03 whilst the TPEF anisotropy was 0.14 ± 0.12. There was no significant difference observed between the TPEF and SHG anisotropy values (students t-test p = 0.235).

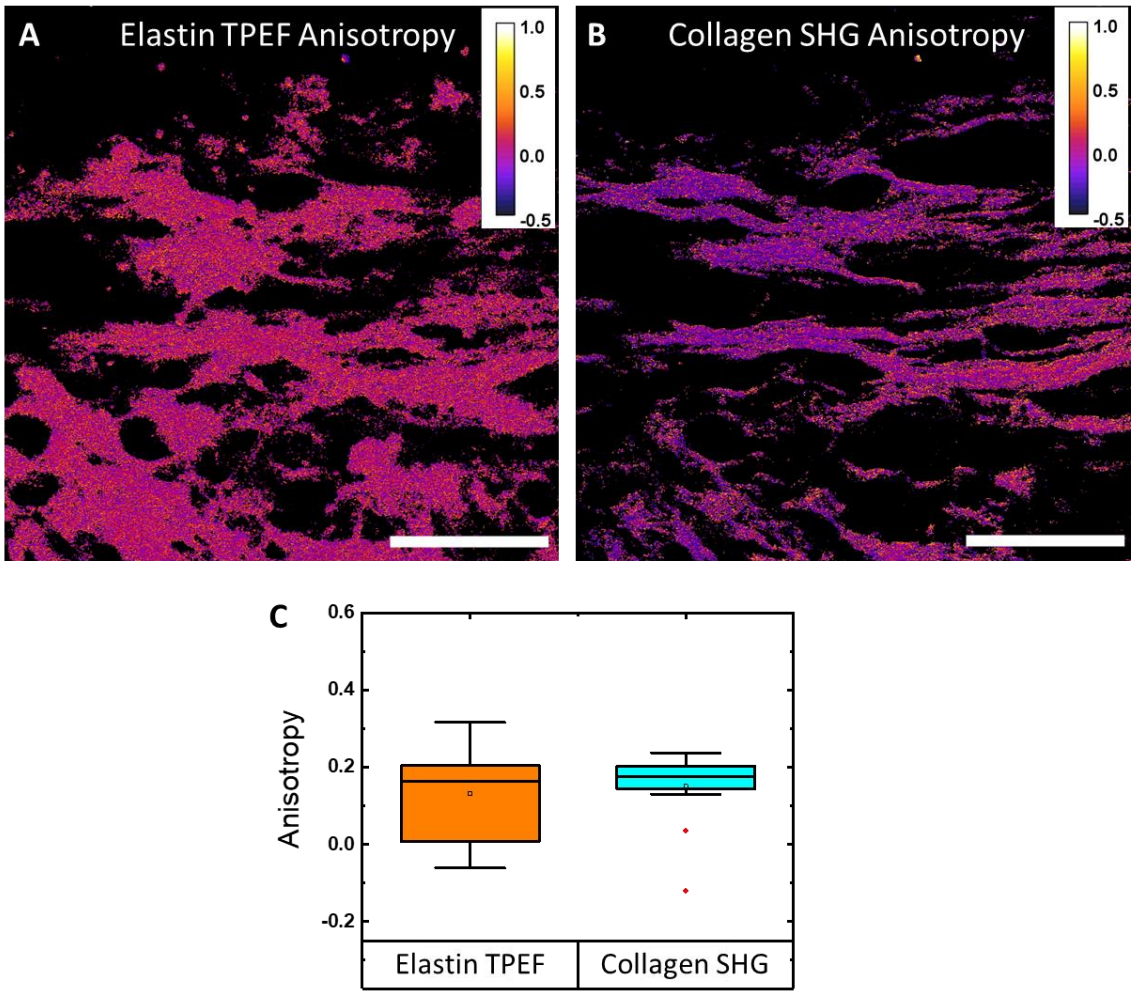

Figure 64: Polarisation Anisotropy.
(Elastin) TPEF (**A**) and (Collagen) SHG (**B**) anisotropy images of the same region. Scale bars 30 µm. (**C**) Comparison of the anisotropy values of elastin TPEF and collagen SHG; no significant difference was seen between the TPEF and SHG. Measurements were made over 14 FOVs. Tested using a students t-test p = 0.235.

Having probed the structural differences and similarities at a diffraction-limited scale, super-resolution imaging was employed to gain further insight into the ECM of the cell culture model and to determine whether differences in orientation or arrangement may exist at the nanoscale between elastin and collagen. Super-resolution imaging has previously been able to detect changes in anisotropy for collagen fibres that were not detectable at the diffraction-limited scale (Figure 53).

6.5.3 Photonic Nanojet Imaging

SEM studies show that elastic fibres contain structural organisation below the optical diffraction limit (Kadar, 1977). To see if these structural elements could be resolved optically the photonic nanojet phenomenon (Section 2.5.5) was employed. As the PNJ method does not rely on specific properties of the contrast mechanism (TPEF or SHG) multimodal SR imaging was possible. Figure 65 shows an example image of the previously used cell spheroid section, taken using photonic nanojets.

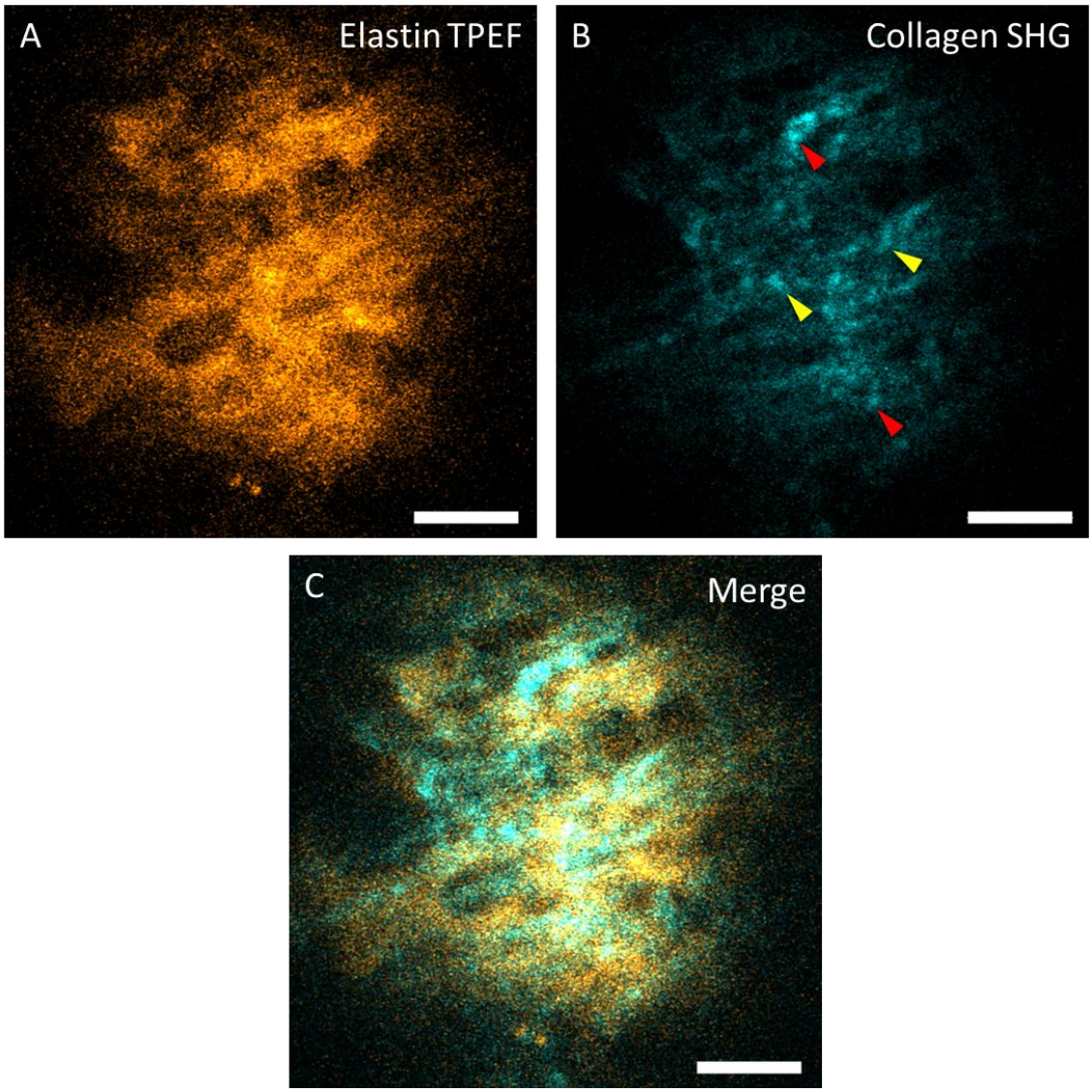

Figure 65: Multimodal PNJ imaging.
(**A**)TPEF image of elastin in the ECM, broad structures can be observed (~1-6 µm wide). These structures may be large fibres or many small fibres arraned togeter in mats/sheets. (**B**) SHG image of collagen, a punctate distribution fibrils (red arrows) is present. Some collagen fibrils can run across the major collagen/ elastin structure direction (yellow arrows) (**C**) The merged image shows that the many of the collagen fibrils overlap with the elastin fibres. The structures observed at different wavelengths may occupy different axial planes due to chromatic shifts in the PNJ. Scale bar 5 µm.

The TPEF image of elastin (Figure 65**A**) shows broad elastin structures with dimensions between 1 µm and 6 µm. SEM imaging of purified elastin has shown cylinder-like fibres of 1- 3 µm in diameter, that can organise in a parallel or sometimes in a branching pattern (Kadar, 1977). The fibres are made of fibrils with diameters of 0.2 µm (Green *et al.*, 2014) that were not observed during PNJ imaging. The sub-fibre structures observed by Green *et al*. where only observed due to "fraying" of the rope like organisation of elastin fibres from the isolation process. This may explain why they were not observed optically in these intact samples. Alternatively, the elastin-based structures observed may be a more disordered arrangement fibres creating "sheets" of elastic tissue like the structures observed in Figure 61 **A/B**. The SHG images showed a similar punctate distribution of collagen fibrils as seen with diffraction-limited SHG (Figure 65**B red arrows**). Collagen and elastin appear to be associated in the merged image (Figure 65**C**). However, due to potential uncompensated chromatic shift in the PNJ these images may be acquired from slightly different axial planes, thus, close association of the two components (elastin and collagen) cannot be concluded. 3D imaging in an achromatic system may be able to help elucidate the degree of association between the two ECM components but is not currently possible with the PNJ system. Some collagen fibrils appear to run across the main collagen / elastic fibre direction (Figure 65B **yellow arrows**). It has been observed previously that collagen fibrils are embedded into, and bridge between larger elastic fibres(Kadar, 1977). It is suggested they help to maintain the organisation of elastic fibres. Label-free observation of these small fibrils highlights the sensitivity of the PNJ imaging method.

To further probe the organisation of the elastic and collagen fibres, polarisation anisotropy measurements were made. As the PNJ maintains the polarisation state of the excitation field; it is possible to perform anisotropy measurements within the sub-diffraction volume of the nanojet, increasing sensitivity to changes in ultrastructure. Figure 66 shows example images used for anisotropy analysis. A-C shows total intensity images created by combining the intensities recorded with parallel and perpendicular analyser orientations. D/E show the anisotropy images of A/B respectively. In the displayed images the fluorescence anisotropy values show a similar distribution to the SHG anisotropy values. Statistical analysis of the TPEF and SHG anisotropy at the sub-diffraction scale resulted in mean anisotropies of 0.26±0.11 and 0.29±0.08, respectively. There was no significant difference between the fluorescence anisotropy and the SHG anisotropy (students t-test $p = 0.391$).

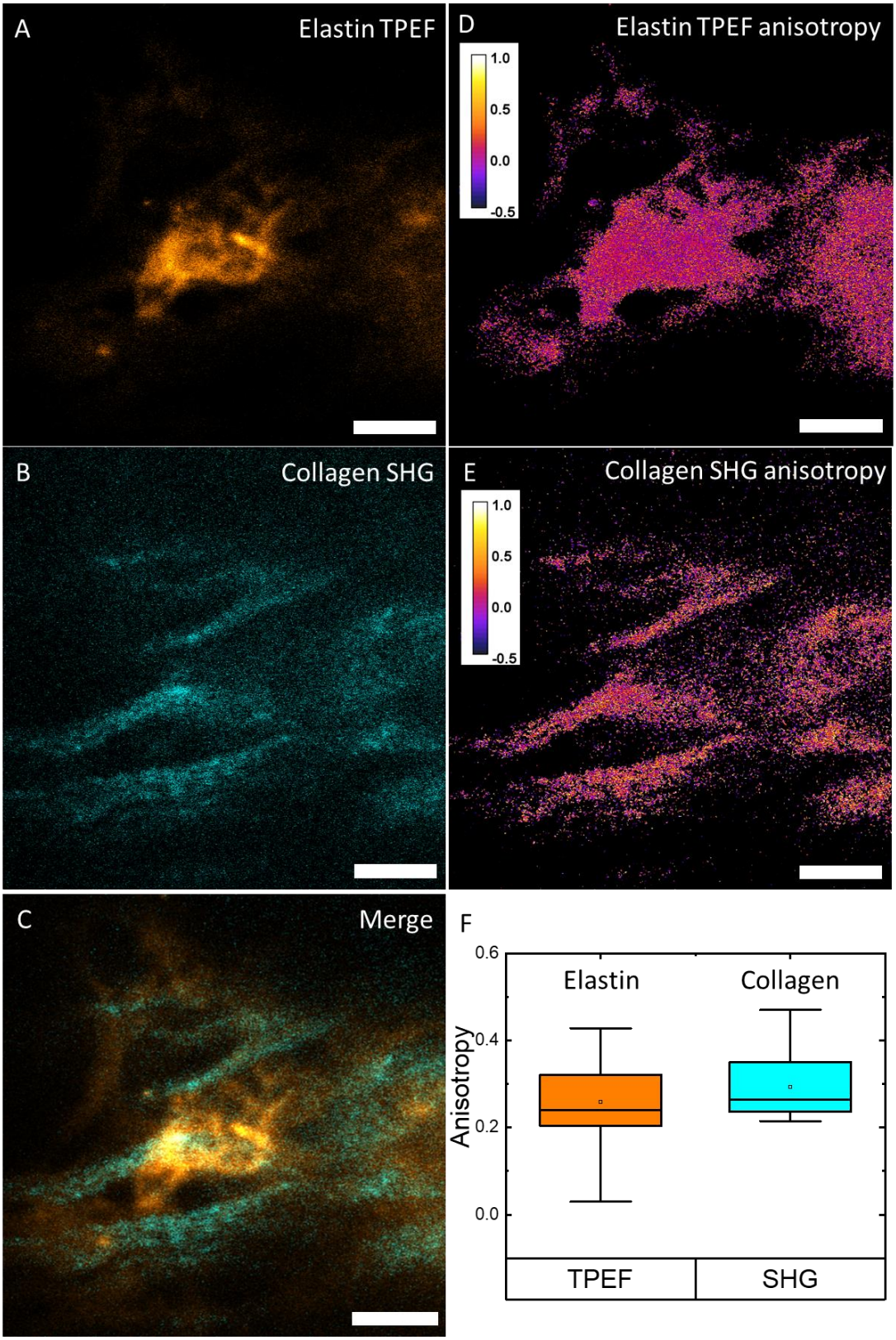

Figure 66: PNJ polarisation anisotropy measurements.
PNJ SR total intensity images of TPEF (**A**), SHG(**B**) and a merge (**B**) highlighting multimodal SR. TPEF (**D)** and SHG (**E**) anisotropy images of the same region. Scale Bar 5 µm for the PNJ FOV. **F** Statistical analysis of the PNJ-assisted TPEF and SHG anisotropies. There was no significant difference between the two cases tested by students t-test ($p = 0.391$). Analysis was performed for 14 super-resolution FOVs.

The measured anisotropies for both TPEF and SHG using PNJs were higher than those measured at the diffraction limit (Figure 64**C** vs. Figure 66**F**). This could be due to the reduced FOV size of PNJ imaging which would result in a smaller area of the whole tissue section being sampled and thus less averaging of anisotropy values. Anisotropy measurements were made over 14 FOVs covering a total of ~10,206 μm^2 (27 µm x 27µm FOV of each sphere) when using PNJs and 148,526 μm^2 for diffraction-limited imaging. This observation may also be due to the different excitation volume of the photonic nanojet compared to the diffraction-limited case. The axial and lateral FWHM of two-photon excitation volume for 808 nm excitation and a 1.2 NA objective are 262 nm and 669 nm respectively, calculated from (Zipfel, Williams and Webb, 2003). Whereas, the simulated proportions of the PNJ formed under the conditions used in these experiments (wavelength = 808 nm, sphere diameter = 60 µm, sphere refractive index 1.9, immersion medium refractive index = 1.33, NA of objective = 1.2, focal point of objective below sphere = 80 µm) are 232 nm laterally and 1400 nm axially. Due to the limited improvement in lateral resolution of the PNJ and the deterioration in axial resolution, the PNJ method should be used with caution only where the axial resolution sacrifice is acceptable or useful. The extended axial profile of the PNJ compared to the Gaussian focus will allow the PNJ to probe a larger axial distribution of collagen fibrils. The intensity of backwards generated SHG depends on the axial-size and axial-distribution of emitters within the excitation volume (LaComb *et al.*, 2008), and the anisotropy is calculated by measuring intensities at two, orthogonal polarisations. Thus, an altered axial excitation profile can be expected to alter anisotropy measurements in non-uniform materials such as biological samples.

6.6 Discussion

The similar anisotropy values observed for TPEF at both the diffraction-limited and sub-diffraction scale was unexpected as PNJ-SHG had been able to previously reveal differences that were not observed in diffraction-limited imaging Figure 53. The epi-detection geometry may affect the SHG polarisation measurements, decreasing the observed anisotropy. This is because backwards-detected SHG in tissue contains both a quasi-coherent and an incoherent component due to secondary scattering (LaComb *et al.*, 2008) whereas fluorescence is emitted isotopically (Masters and So, 2008). SHG is a structurally-selective technique that requires ordered arrangement of harmonophores with each other and the excitation polarisation, making it highly sensitive to ultrastructural changes in disorder (Chen *et al.*, 2012). Fluorescence is also excited most efficiently when the dipole orientation and excitation polarisation are aligned; however, it does not require ordered arrangement of fluorophores to generate signal (Lakowicz, 1999). Thus, the measurement of fluorescence anisotropy values similar to those measured for SHG suggests a

degree of fluorophore alignment similar to the degree of alignment in collagen fibres. The observed alignment of fluorophores suggests an arrangement of elastin with a similar degree of order to fibrillar collagen. Although TEM images have previously shown elastic fibres to contain an amorphous elastin component in their centre (Montes, 1996), it is now believed this may be an artefact of the sample preparation procedure (Kozel and Mecham, 2019). More recent studies using SEM show that elastic fibres have an ordered structure much like twisted ropes (Green *et al.*, 2014). Using deep-etch electron microscopy Kozel and Mecham (Kozel and Mecham, 2019) showed a densely packed network of fine filaments 5-7 nm in width. Recent work has given insight into the origin of ordered elastin assembly. The elastin precursor tropoelastin is transported to the cell surface where it forms small aggregates. The tropoelastin primary sequence contains motifs required to facilitate self-assembly, aligning lysine-containing domains ready for crosslinking by lysyl oxidase (LOX) (Muiznieks *et al.*, 2014). Association with Fibulins may help to facilitate cross linking and limit the size of these aggregates. The aggregates remain at the cell surface whilst they increase in size, this is microassembly (Wagenseil and Mecham, 2007). Elastin aggregates are then deposited onto existing elastic fibres which aggregate hierarchically, that is, increasingly large segments are progressively connected (Czirok *et al.*, 2006), this is termed macro assembly. This deposition and aggregation has been shown to be guided by fibrilin-microfibrils (Kozel and Mecham, 2019) that are believed to act as a scaffold onto which elastin is deposited. The elastin to microfibril ratio has been shown to increase with fibre maturity (Albert, 1972). The removal of microfibrils is proposed to reveal hydrophobic residues required for continued fibre assembly. They may also play a regulatory role in elastin deposition, ensuring that aberrant, excessive self-assembly of elastin is avoided (Kozel *et al.*, 2006) and signalling to cells where to deposit new elastin (Kozel and Mecham, 2019). Cell movement and associated mechanical forces have also been shown to play a role in elastic fibre construction (Kozel *et al.*, 2006). Cells stretch existing fibres, shaping the fibre network and guiding deposition of new elastin. The measured fluorescence anisotropy values indicate that the hierarchical assembly of elastic fibres, controlled by the mechanisms outlined above, confers a high degree of order to elastic fibres similar to that seen in fibrillar collagen.

It has been shown previously in this model that a loss of collagen cross linking leads to a decrease in the SHG polarisation anisotropy (Section 5.4.7) (Johnson *et al.*, 2020). This indicates an increase in disorder, which has been verified by TEM (Jones *et al.*, 2018). Tropoelastin undergoes crosslinking by the same set of enzymes as collagen, the lysyl oxidase (LOX) family (Eyre, Paz and Gallop, 1984), during maturation. The fluorescence of elastin has been attributed to these pyridolamine crosslinks (Deyl *et al.*, 1980; Zipfel *et al.*, 2003), thus the elastin fluorescence is expected to change under treatment with crosslinking inhibitors such as β-aminopropionitrile

(BAPN). Further study of the fluorescence polarisation anisotropy using elastin of different maturities and/or treatment with BAPN, will be informative of the effect of crosslinking on elastin fibre disorder. Multimodal anisotropy measurement of both SHG and TPEF therefore provides a tool to probe ECM quality in minimally processed samples.

Changes in ECM quality have been implicated in the progression of the lung disease idiopathic pulmonary fibrosis (IPF) (Kristensen *et al.*, 2014; Kulkarni *et al.*, 2016), with the amount of elastic fibres predicting prognosis (Enomoto *et al.*, 2013). Kottmann *et al.* (Kottmann *et al.*, 2015) used the TPEF emission of elastin in combination with SHG in a study of multiple types of lung fibrosis. They found that the ratio of mature elastin to collagen was decreased in both usual interstitial pneumonia (UIP) and cryptogenic organizing pneumonia (COP) versus healthy lung. They linked this to a process of "fibroelastosis". Alongside changes in collagen architecture, mature elastin is broken down and replaced with deposition of immature elastin lacking crosslinks. The method employed by Kottmann *et al.* only informs about changes in the amount and distribution of elastic fibres. The method presented in this chapter is also able indicate the level of disorder present in elastic fibres. Thus, the PNJ-based multimodal imaging method described above increases sensitivity to subtle alterations in the quality of the ECM that were not previously detectable.

6.7 Conclusions

The work presented in this chapter detailed the application of the photonic nanojet phenomenon for label-free, multimodal imaging-based studies of the extracellular matrix at a super-resolution scale. The conditions required for selective imaging of collagen and elastin were established and thereafter, multimodal investigation of these key ECM components was performed. The polarisation-maintaining properties of photonic nanojets were exploited to perform anisotropy analysis. Interestingly, the fluorescence anisotropy values were similar to those of SHG, despite the greater dependence of SHG on material order. This indicates autofluorophore alignment within elastic fibres that was not previously known. Changes in the ECM occur in many diseases, thus the ability to selectively detect subtle changes in the structure of multiple components has wide implications for the study of disease progression via detection of ultrastructure and orientation through multimodal anisotropy imaging.

Chapter 7 Fluctuations-based Super-Resolution

This chapter presents work in the manuscript under preparation: “Label-free super-resolution lightsheet imaging using autofluorescence fluctuations” *Peter Johnson, Niall Hanrahan, Simon Lane, Krishna Agarwal, Sumeet Mahajan.*

Contributions: P Johnson Performed imaging experiments, data processing and analysis, cell culture and sample preparation. N Hanrahan and S Lane developed and maintained the lightsheet microscope. K Agarwal provided image pre-analysis script and guidance on data processing. S Mahajan conceptualised, designed, and coordinated the study. P Johnson and S Mahajan wrote the manuscript.

7.1 Abstract

The desire to understand the living world at increasingly fine spatial detail has led to the development of super-resolution (SR) optical microscopy techniques. Most SR methods rely on specific manipulation of fluorescent label properties, limiting their application to label-free modalities. One branch of SR techniques uses inherent fluctuations in the optical signal to determine emitter location beyond the diffraction limit, creating the potential for label-free super-resolution. The Multiple Signal Classification Algorithm (MUSICAL) is one such method, capable of super-resolved imaging in live cells. Here, MUSICAL is applied to label-free imaging of mitochondria for the first time. The performance of the method was first characterised and optimised using an organic standard and labelled, adherent cells. Multiphoton excitation of the autofluorophores nicotinamide adenine dinucleotide (NADH) and flavin adenine dinucleotide (FAD) using lightsheet microscopy allowed potential resolution of organelle sub-structure. The ability to image mitochondria with super-resolution will become an invaluable tool for the study of cellular metabolism and health in a wide range of disease and therapeutic contexts. Importantly, this technique has no specific requirements on the imaged fluorophores, making the technique broadly applicable to label-free imaging in cellular and tissue contexts.

7.2 Background

7.2.1 Fluctuations-based Super-Resolution Microscopy

Single Molecule Localisation Microscopy (SMLM) has been implemented in multiple ways and constitutes some of the most widely used SR fluorescence techniques. Having seen significant success in biological imaging, they boast some of the highest resolutions achieved in far field optical microscopy (20-50 nm) (Betzig *et al.*, 2006; Rust, Bates and Zhuang, 2006; Hell *et al.*, 2015). Despite this success, localisation microscopy comes with significant drawbacks. These techniques work by detecting discrete fluorophore emissions and using a fitting model to calculate the most likely sub-resolution fluorophore location. To identify discrete emissions a large series of images (1000s of frames), containing only a few, sparsely-activated fluorophores in each frame must be acquired to catch most fluorophores in a "dark state" within a frame (section 2.1.1). Firstly, this decreases the temporal resolution of such techniques, prohibiting the study of fast dynamic processes such as those in live cells; secondly, specialist fluorophores must often be used that exhibit blinking or that can be forced into a dark state. To achieve this it is often necessary to add thiol reagents and oxygen scavenging buffers to promote blinking (Van De Linde *et al.*, 2011) and/or to use a high intensity pulse of light to force the fluorophores into a dark state (Sahl, Hell and Jakobs, 2017). Both impose limitations to non-perturbative, live-cell imaging and label-free applications.

These limitations have led to the more recent development of a new set of techniques that do not rely on localising individual emitters but on fluctuations in emission to achieve SR. Each of these techniques differs in the method of achieving super-resolution but all require the acquisition of an image stack, containing temporally fluctuating signals. These stacks are like those in traditional SMLM but in general require fewer frames (50-1000), do not need strict on/off states, and work with high emitter-density datasets. These techniques have been shown to achieve resolutions of 49 -130 nm, a summary is presented in **Table 6**. The most prominent fluctuations-based super-resolution microscopy techniques (FSRM) so far are: Entropy based super-resolution imaging (ESI) (Yahiatene *et al.*, 2015), Super-resolution optical fluctuation imaging (SOFI) (Dertinger *et al.*, 2009), Super-resolution imaging with autocorrelation two-step deconvolution (SACD) (Zhao *et al.*, 2018), Super-resolution radial fluctuations (SRRF) (Gustafsson *et al.*, 2016), Bayesian analysis of blinking and bleaching (3B) (Cox *et al.*, 2012) and Multiple signal classification algorithm (MUSICAL) (Agarwal and Macháň, 2016).

Technique	Resolution (retrieved from original publication)	Pros	Cons
SOFI (Dertinger *et al.*, 2009)	55 nm	High-resolution possible Can be quantitative	Sensitive to noise High number of frames (2000) needed for best resolution Requires static sample
ESI (Yahiatene *et al.*, 2015)	130 nm	Noise removal	High number of frames (2000-5000) needed for best resolution
SACD (Zhao *et al.*, 2018)	64 nm	Very low number of frames needed (16) Good for rapidly moving samples	Impacted heavily by poor SNR
SRRF (Gustafsson *et al.*, 2016)	49 nm	Low number of frames needed Good at identifying fibrous structures	Affected heavily by movement Many user-defined parameters Common “over slimming” artefact
3B (Cox *et al.*, 2012)	50 nm	High resolution possible	Computationally intensive
MUSICAL (Agarwal and Macháň, 2016)	50 nm	Low number of frames needed High resolution possible Can use any signal fluctuations as input	Can interpret sample dynamics as fluctuations confounding interpretation Best performance achieved for large signal fluctuations

Table 6: A comparison of the current FSRM techniques

Of the methods presented above MUSICAL has key advantages. MUSICAL needs as few as 49 frames to achieve super-resolution (Agarwal and Macháň, 2016). ESI and SOFI require a larger number of frames due to the iterative processing steps involved. The size of the temporal stack is halved at each iteration meaning to achieve the best resolution stacks of ~1000

frames are needed. Using bright emitters, frame rates on the order of ~1 KHz can be achieved (in a camera-based system), (Agarwal and Macháň, 2016), this would allow 1000 frames to be acquired in 1 s, thus, limited sample movement can occur over the course of acquisition. However, sample brightness due to choice of available fluorophore and limitations on illumination intensity may necessitate longer pixel dwell times (~100 ms) and therefore lower frame rates (~10 Hz). This may increase the total acquisition time to hundreds of seconds, where sample motion becomes an increasingly likely problem. Thus, algorithms that need fewer frames to achieve super-resolution are desirable.

SACD reduces the number of required frames by using auto-correlation between combinations of frames in multiple steps, a method the authors call *multi-plane autocorrelation* (MPAC). The authors do however highlight that the performance of SACD is heavily impacted by low signal to noise ratio; thus, this algorithm may not be suitable for label-free imaging data sets where signals such as autofluorescence can be comparatively weak compared to traditional fluorescent labels. SRRF is capable of reaching ~50 nm resolution with as few as 100 frames, a significant improvement over ESI and SOFI but greater than that required for MUSICAL. SRRF analysis is also one of the fastest FSRM analyses to run due to GPU optimisation. However, SRRF assumes a radially-symmetric emission from the sample. This is true of fluorescence emission, but it is not true of the emission from some coherent events such as second harmonic generation (SHG) which shows highly directional emission. 3B is also not suitable for label-free SR due to high computational demand of modelling the state of each fluorophore and hence it will have limitations for imaging with an extra dimension such as temporal stacks. Without access to specialist computing hardware 3B is only useful over very small areas (~ 5 µm x 5 µm) whilst maintaining reasonable computation times (Cox *et al.*, 2012). Hence, given the future potential for generalised applicability of MUSICAL with the larger palette of label-free techniques such as SHG and other scattering-based techniques we investigated it for label-free SR. As with many of the FSRM methods, there are drawbacks to MUSICAL. As MUSICAL uses fluctuations of any kind to generate a super-resolution image, it is possible that microscopic, rapid movements of the sample can contribute to the final image. This may prove beneficial for tacking nanoscopic movements in the sample but also adds a potential confounding factor to interpretation. User-defined parameter selection is also a feature common to many of the FRSM methods including MUSICAL. When a potentially subjective step is placed in any data analysis protocol, there is the potential for unconscious bias or “cherry picking” of data to match that which is expected. Furthermore, incorrect selection of these parameters may lead to artefacts in the output data. Therefore, caution should be executed when interpreting results produced by

FSRMs. SRRF has up to 8 parameters defined by the user, increasing the chance of incorrect parameter selection and therefore, artefacts. In MUSICAL there are three key parameters selectable by the user, the threshold value, the value alpha and the number of subpixels. Selection of the incorrect value for these parameters can lead to either loss of fine detail from the super-resolution reconstruction, or inclusion of fluctuations generated by noise leading to erroneous patterns in final SR image. The effects of these parameters are investigated in section 7.3.3. Evaluating the considerations above, MUSCIAL was determined to be the most suitable FSRM method to use to achieve label-free super-resolution.

A common assumption when interpreting data from the FSRM techniques listed above is that the fluctuations in signal at a given pixel location are not due to fluorophore/structure movement within the duration of the acquisition. To ensure that this criterion is satisfied either images must be acquired on fixed samples or, for live samples, the overall acquisition time must be minimised. This is achieved by increasing the frame rate and minimising the number of frames required. Increasing the frame rate (in general) will have a negative impact on the signal to noise ratio, potentially influencing the quality of the SR reconstruction. Many of the methods above have been demonstrated to work on synthetic data sets and data sets acquired using wide field illumination, often in a total internal reflection fluorescence (TIRF) microscopy configuration. This minimises background contributions improving SNR.

TIRF microscopy uses a specialist illumination scheme to illuminate the sample using only the evanescent field. The evanescent field decays exponentially with distance therefore, typically, it only penetrates a few 100 nm into the sample (Fish, 2009). Key advantages of TIRF illumination are the greatly decreased light dose to the sample and the significant decrease in background, making it the closest real case to an ideal 2D PSF. Often TIRF illumination is achieved using a high NA objective (NA >1.45), therefore, a key limitation to the technique is the limited FOV. However, chip-based methods of evanescent field illumination that alleviate this limitation have been demonstrated (Diekmann *et al.*, 2017). The key disadvantage of TIRF comes as a result of its key advantage. The limited penetration of the evanescent field away from the coverslip, means TIRF can only image structures within a few 100 nm of the coverslip surface and therefore imaging of samples thicker than this is not possible.

The use of widefield illumination allows for rapid acquisition of the required frames, minimising motion artefacts. Multiphoton microscopy relies on the tight focussing of light to generate non-linear interactions (Diaspro, 2002). In general, this necessitates the use of a point scanning system and this is the most common implementation of multiphoton microscopy (Masters and So, 2008). However, this imaging scheme is not suitable for FSRM

methods as the frame rate is significantly reduced. For example, a camera of 2048 x 2048 pixels and a frame rate of 10Hz has an exposure time of 100 ms. To achieve the same frame rate in a point scanning system with the same number of pixels, the pixel dwell time becomes 100 ms/2048^2 = 2.384 µs. Scanning at this speed results in decreased signal and an increase in scanning artefacts resulting from the acceleration/deceleration of the scan mirrors (when using galvanometric scanners). The scan field can be reduced (by decreasing the angular deflection of the mirrors) to improve image acquisition speed at the expense of FOV size, therefore, if super resolution over a large FOV is desired point scanning may not be a suitable option.

To overcome this issue, it is possible to use a lightsheet illumination scheme which provides a wide-field view and yet minimises background. A working understanding is provided below but for details the reader is referred to the following review (Girkin and Carvalho, 2018). In lightsheet microscopy a single plane is illuminated by focussing the light in a single axis. This is achieved using a cylindrical lens or by rapid scanning of the beam using a resonant scanner (Keller *et al.*, 2008) or tuneable acoustic gradient-index (TAG) lens (Zong *et al.*, 2014) forming a scanned or digital lightsheet. A cylindrical lens illuminates the entire sheet simultaneously, theoretically reducing the required exposure time compared to a digital lightsheet where the camera exposure must be long enough for all scan points to be integrated into the same frame. However, by spreading the power over a greater area, a cylindrical lens system lowers the power density at any point compared to a digitally scanned sheet. This may result in the need to increase the exposure time in order to accumulate sufficient signal. In the case of multiphoton excitation, the available power from the laser may be insufficient to achieve suitable power density at the sample to excite nonlinear effects. Therefore, in multiphoton imaging a digitally scanned light sheet is often necessary. The generated signal is detected orthogonally to the sheet usually by a second objective (Figure 67), however many single objective lightsheet systems exist (Meddens *et al.*, 2016). In general, the sample is then moved through the sheet to generate a z-stack, however physical movement of the sample is slow and can, in some cases, be considered rate-limiting for volumetric imaging. Therefore, systems that sweep the lightsheet through the sample using a galvanometer- or polygonal-mirror have been developed (Bouchard *et al.*, 2015). These provide more rapid volumetric imaging but can only image smaller volumes compared to sample-moving systems.

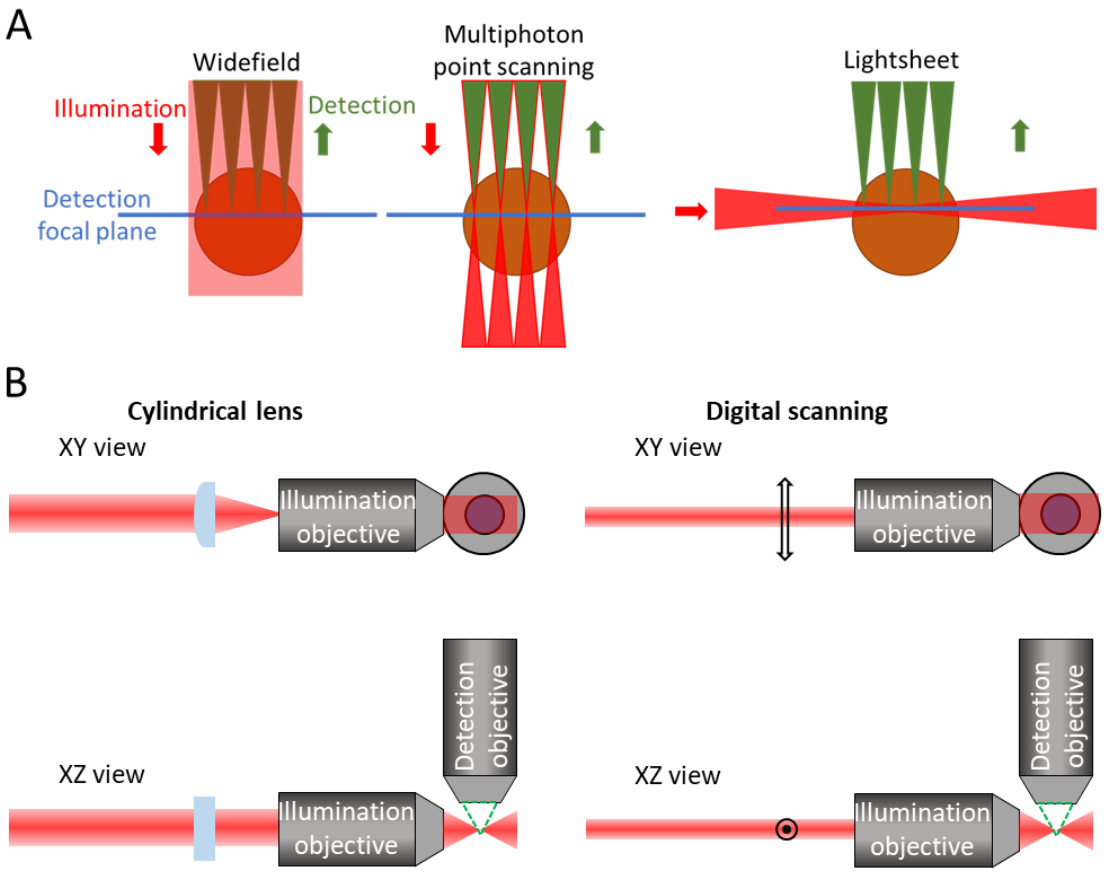

Figure 67: Lightsheet microscopy.
A In conventional widefield imaging the whole sample is illuminated and imaged at once, resulting in out-of-focus illumination and emission but rapid frame acquisition. In multiphoton point-scanning a focal point is scanned across the sample, excitation is confined to the same plane as detection, but image acquisition is slower. In lightsheet, a single plane is illuminated at once and the entire plane is imaged in a single camera frame combining the advantages of widefield and multiphoton point scanning. **B** Lightsheet microscopy using 2 orthogonal objectives for illumination and detection. The lightsheet can be generated either by a cylindrical lens or by scanning the beam to form a digital lightsheet. The latter is preferable for multiphoton imaging (see text).

Lightsheet (LS) microscopy holds many advantages over traditional widefield or point scanning microscopy techniques. Firstly, as mentioned above lightsheet is much faster than point scanning; given a strong enough signal, acquisition is limited only by the frame rate of the camera and/or the scan rate of the resonant mirror in a digital lightsheet. Secondly, because lightsheet only illuminates a single plane of the sample at a time there is minimal light dose, lowering phototoxicity to the sample as a whole (Figure 67**B**). The lack of out-of-plane illumination also lowers the background, improving the signal to noise ratio (SNR). These effects are compounded further when using near infrared (NIR) illumination and observing multiphoton phenomena (Truong *et al.*, 2011). The longer wavelengths used are less damaging to biological samples and due to decreased scattering versus visible

wavelengths, penetrate further into thick samples. These attributes highlight multiphoton lightsheet microscopy as one of the techniques best suited to rapid, live, 3D imaging of biological samples. In this work multiphoton lightsheet imaging is used to explore label-free super-resolution via FSRM.

7.2.2 Mitochondrial imaging and cell status

Mitochondria are often referred to as “the powerhouse of the cell”. Determined to be the result of assimilation of a prokaryotic lifeform, they now function as the source of energy for nearly all eukaryotic cells (Roger, Muñoz-Gómez and Kamikawa, 2017). As well as their role in energy production, mitochondria have also been shown to be involved in regulation of apoptosis (programmed cell death), free radical generation and oxidative stress (Chang, 2010; Bock and Tait, 2020). Looking at the wide range of functions performed by mitochondria it is unsurprising that mitochondrial dysfunction plays a pivotal role in a wide range of diseases including cancer, developmental diseases and neurodegenerative conditions (Reddy, 2009; Falk, 2010; Zong, Rabinowitz and White, 2016).

7.2.2.1 Mitochondrial Organisation

Mitochondria are highly dynamic organelles altering their structure and organisation in response to metabolic demands and environmental and chemical stressors. Mitochondria exist as a vast, branched, 3D network. They are often misrepresented by TEM images that can only capture a thin slice of this network leading to a “bean-like” appearance. Two key processes in the remodelling are mitochondrial fission and fusion. Mitochondrial fusion (as the name suggests) involves the fusion of two parts of the mitochondrial network to form a more interconnected, elongated network, this facilitates exchange of DNA, proteins, lipids and metabolites (Pernas and Scorrano, 2016). This occurs as a response to various cellular cues and is thought to help couple the state of the cell with mitochondrial function. The opposing process to fusion is fission, wherein the mitochondrial network will divide to form a less interconnected network. This can occur for a number of reasons, such as to provide more numerous and more motile mitochondria that can localise within a cell to areas of high energy demand such as during chemotaxis (Campello *et al.*, 2006). Mitochondrial networks also undergo significant fission (fragmentation) during apoptosis, before cristae structure breaks down and pro-apoptotic stimuli such as cytochrome C are released (Olichon *et al.*, 2007; Vaux, 2011).

7.2.2.2 Mitochondrial Structure and Function

Electron microscopic studies have shown mitochondria to have a double membrane structure (Figure 68). The outer membrane forms the smooth case of mitochondria whilst the inner membrane can be separated into three distinct zones: the inner boundary membrane, cristae junctions and cristae (Pernas and Scorrano, 2016). The inner boundary membrane is closely associated with the outer membrane at many locations. At these locations the inner membrane and outer membrane contain complexes of interacting proteins, including machinery used in protein transport (Reichert and Neupert, 2002), movement of metabolites and Ca^{2+} flux (Brdiczka, Zorov and Sheu, 2006). Cristae junctions represent the base of deep invaginations of the inner membrane called cristae. At these junctions the inner membrane folds into a narrow entrance of approximately 20 - 50 nm wide. It is thought that these junctions are present to prevent diffusion of molecules between the cristae and the peripheral outer membrane space, allowing controlled transfer of metabolites and proteins between the two compartments. The cristae protrude from the cristae junctions into the centre of the mitochondria. The membrane contains a diverse set of proteins including those for protein translocation and synthesis and, importantly, assembled complexes of the electron transport chain (ETC), key proteins in cellular energy production. The mitochondrial matrix contains a large variety of enzymes including those needed to produce reduced NAD (NADH), a fundamental co-enzyme involved in cellular respiration.

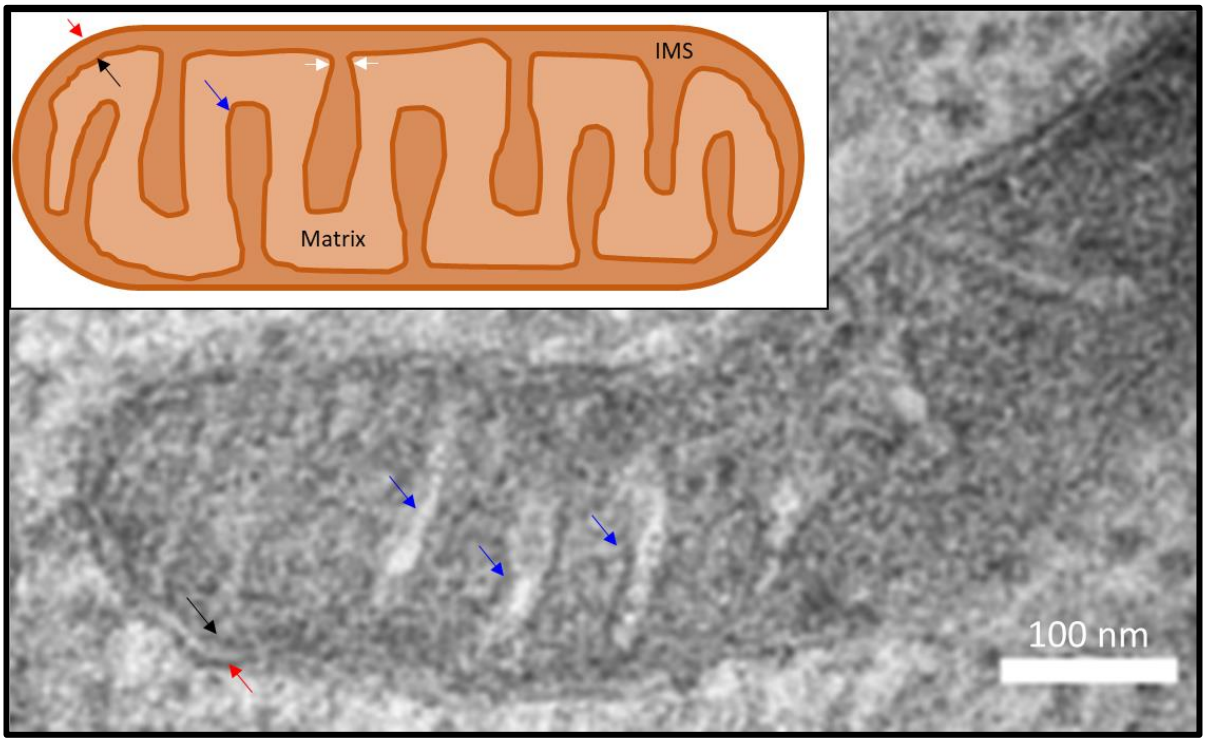

Figure 68: Diagram and TEM micrograph of mitochondrial structure.
Mitochondria observed by TEM have a bean-like appearance due to the sectioning required for imaging, which does not capture the extent of mitochondrial networks. Mitochondria have a double membrane structure wherein the outer membrane (red arrow) forms the outside casing of

the mitochondria. The inner membrane runs parallel to the outer membrane (black arrow), it also has many invaginations called cristae (blue arrows) gated by narrow openings called cristae junctions (white arrows). Cristae increase the inner membrane surface area, increasing space for proteins of the electron transport chain. IMS = Inter membrane space

Cellular respiration is the process of generating energy to drive cellular processes by converting glucose to adenosine triphosphate (ATP); an energy source that can be used to drive intracellular reactions vital to cell life. ATP is produced in a series of linked processes; first, glycolysis occurs in the cell cytoplasm and involves the conversion of one glucose molecule to two molecules of pyruvate, consuming 2 molecules of ATP and producing 4 molecules of ATP for a net gain of two ATP. Pyruvate is then converted to Acetyl CoA and fed into the second part of respiration which involves the Krebs cycle (also called the citric acid cycle or tricarboxylic acid cycle) which occur within the mitochondria. In the Krebs cycle acetyl CoA undergoes a series of chemical reactions, ultimately being converted into CO_2. The overall reaction is summarised below.

$$acetyl - CoA + 2P_i + GDP + 2NAD^+ + FAD \rightarrow CoA - SH + 2CO_2 + 3NADH + FADH_2 + GTP$$

At many of the intermediate steps in the cycle the co-enzymes nicotinamide adenine dinucleotide (NAD) and flavin adenine dinucleotide (FAD) are involved in a series of reactions, acting as an electron shuttle. The key output of the Krebs cycle is the generation of the reduced forms of these two molecules. They can then provide these electrons to a series of proteins situated in the mitochondrial inner membrane called the electron transport chain (ETC). As electrons move sequentially between these proteins the released energy is used to pump H^+ out of the matrix into the intermembrane space creating a chemo-electric gradient across the inner membrane. As protons flow back down this gradient, they provide the driving force (proton-motive force) for ATP synthase to convert ADP to ATP in the reaction below. This ATP is then used to power cellular reactions such as protein production and cellular signalling.

$$ADP + Pi + 3H^+_{OUT} \leftrightarrow ATP + H20 + 3H^+_{IN}$$

7.2.2.3 Mitochondrial Autofluorescence Imaging

The autofluorescence of the co-enzymes NAD (in the reduced form NADH (Chance, 1954; Schaefer *et al.*, 2019)) and FAD can be used for the label-free monitoring of mitochondrial dynamics within cells and tissues. As the primary location of both molecules is within the mitochondrial matrix (Chance *et al.*, 1979) it is possible to track fission and fusion events within cells without the addition of labels (Rodrigues *et al.*, 2011). Flavoproteins (proteins containing the FAD molecule) show strong fluorescence in their oxidised state whereas NADH is fluorescent in the reduced form. The signal from these two molecules can be separated by their excitation and emission.

NADH absorbs maximally at 335-350 nm range and shows peak emission between 440-470 nm (Rehman *et al.*, 2017). FAD shows two absorption peaks at 370 nm and 450 nm, peak emission is observed at ~530 nm (Cao, Wallrabe and Periasamy, 2020). Thus, ratiometric fluorescence readings from within cells can indicate the redox state of the cell. This redox state can be used to inform about cell metabolic status and stress. Redox imaging has seen significant success in cancer research including discrimination of healthy and diseased tissue (Xu *et al.*, 2016), determination of metastatic potential (Xu *et al.*, 2010; Alhallak *et al.*, 2016; Sun *et al.*, 2016), response to drug treatments (Walsh *et al.*, 2013; Shah *et al.*, 2014; Alam *et al.*, 2017; Xu *et al.*, 2019) and identification of macrophage heterogeneity in 3D tumour models (Heaster *et al.*, 2020).

Despite achieving subcellular resolution, label-free super-resolution is yet to see be reported for mitochondrial imaging. All information of mitochondrial substructure has come from electron microscopy (Mannella, 2008), or more recently by using SR fluorescence methods (Shao *et al.*, 2011; Stephan *et al.*, 2019). Both methods come with the caveats of extensive sample preparation protocols, and in the case of electron microscopy, the inability to perform live and therefore longitudinal monitoring of mitochondrial structure. Therefore, a tool capable of imaging mitochondrial structure at a SR scale in a label-free and non-perturbative manner is highly desirable.

7.3 Materials and Methodology Development

7.3.1 Materials

Ultra-low attachment coated 96 well plates (Corning, 7007). BacLight LIVE/DEAD viability kit prepared using manufacturer's instructions (Thermo Fisher Scientific, L7012). Fluorescently labelled tubulin was purchased from Cytoskeleton, Inc (www.Cytoskeleton.com). Tubulin Tracker Green (ThermoFisher Scientific). MitoTracker Orange CMTMRos (ThermoFisher Scientific). 110 nm fluorescent beads (Invitrogen, TetraSpeck, T7279).

7.3.2 MUSICAL pre-processing pipeline

To check if each image stack had sufficient fluctuations for MUSCAL it was run through a MATLAB script to calculate key parameters of the stack. An example is given in Figure 69, the imaged sample was an SHSY-5Y cell spheroid (section 7.3.4) labelled with mitoTracker Orange, the sample was excited at 561 nm and emission was collected at 620 nm. The sample was suspended in agarose and imaged using the lightsheet imaging system described in section 3.6. The sample was illuminated using a 20x/0.5NA objective and emission was detected using a 40/0.8NA objective. The full 2048 x 2048 pixels of the camera chip were used to image a 302 µm x 302 µm FOV. The effective pixel size was 147 nm.

The script calculates the average intensity over time for the stack (Figure 69B), the standard deviation (SD) of each pixel over time indicating the fluctuations (Figure 69C) and the SD/Average (Figure 69D).This last image indicates the strength of the fluctuation as a proportion of the average signal at that point. The SD/average image highlights regions that have strong enough fluctuations as a proportion of the average signal to be processed by MUSICAL, this value should be greater than 0.05 in ROIs. This quick step (<1 s) was undertaken initially before further analysis to indicate if acquisition parameters such as illumination power and exposure time were suitable. After fluctuation analysis, stacks were analysed for motion that may generate artefacts in MUSICAL processing.

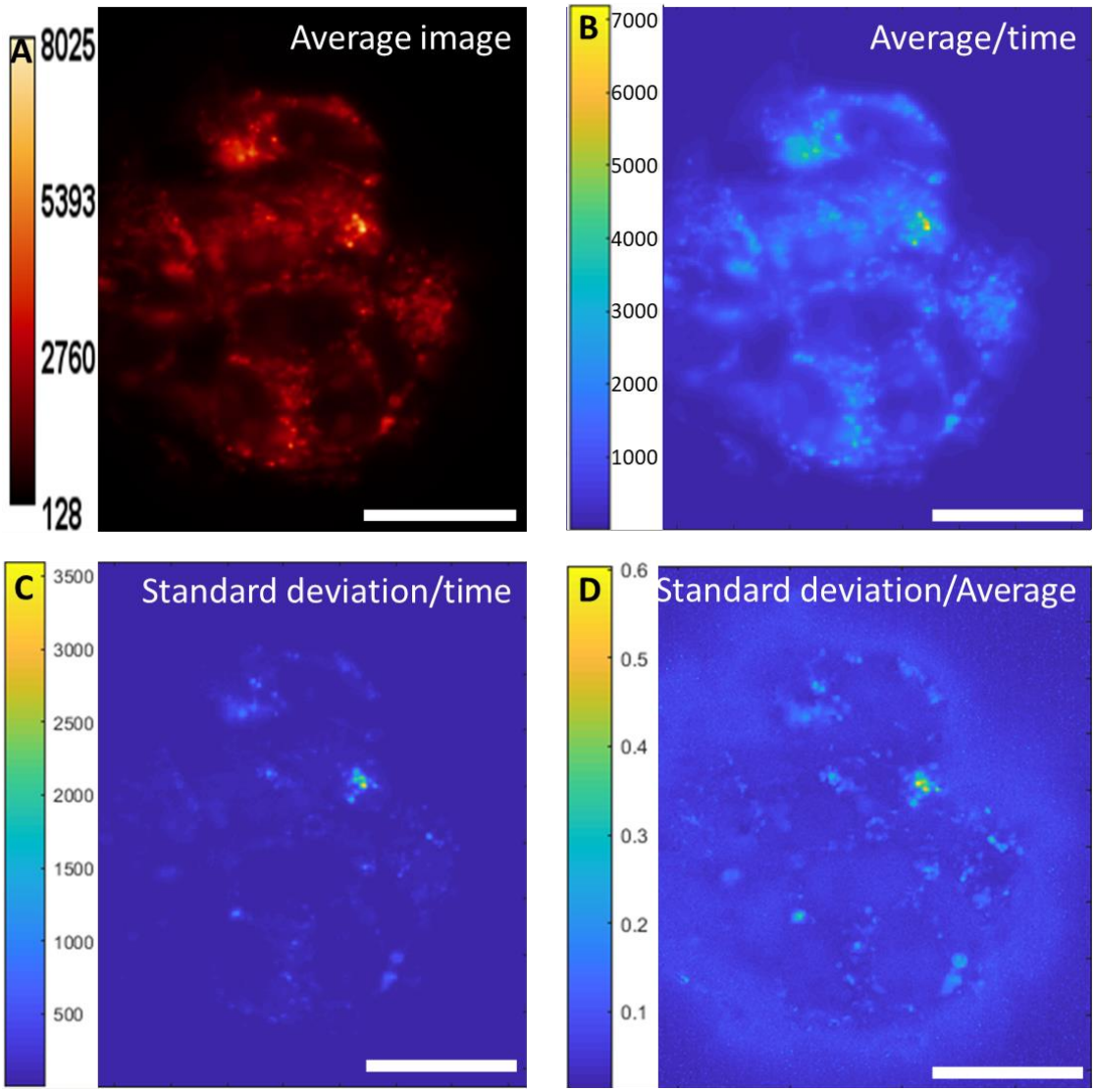

Figure 69: Analysis of image stack quality for processing
(**A**) Average intensity projection of a 50 image temporal stack taken of an SHYS-5Y cell spheroid, labelled with mitoTracker imaged using the light sheet imaging system. (**B**) Average/ time image to highlight if there is suitable SNR. (**C**) Standard deviation/time, this highlights fluctuations usable by MUSICAL. (**D**) Standard deviation/averagegives a quantitative evaluation of fluctuations useable by MUSICAL. This should be >0.05 in ROIs. Scale bar 20 µm.

Many cellular organelles including mitochondria are highly dynamic and can noticeably move within cells over a matter of seconds. Excluding single photon detection, every image acquired of a sample is an average from all locations of a given emitter within the exposure. When the exposure time is much lower than the timescale of the emitter motions the image is a representative snapshot. However, when the exposure time is greater than the timescale of the emitter motion then the image may contain artefacts of sample motion. This effect can be amplified for super-resolution algorithms such as MUSICAL where sample motion may be interpreted as sub-resolution emitter fluctuations. The time scales of emitter motion are dependent on the nature of the emitter. The motion of an entire mitochondrion will occur on a

much longer time scale (~<1 µm/s) (Frederick and Shaw, 2007) than the movement of a labelled membrane protein within the membrane or the diffusion of an unbound emitter (fluorescent protein or dye) within a cellular sub-compartment (~10 $\mu m^2/s$) (Xiang *et al.*, 2020). All of these motions have the potential to be interpreted by MUSICAL as fluctuations and can influence SR-image reconstruction. Methods to directly track the diffusion of individual molecules have been developed taking advantage of single molecule imaging methods (Xiang *et al.*, 2020). Local diffusion rates can be measured using techniques such as Fluorescence Recovery After Photobleaching (FRAP), Fluorescence Correlation Microscopy (FCM) and fluorescence anisotropy methods (Verkman, 2002). These techniques could be used help assess the impact of emitter diffusion on SR-image reconstruction. The more readily-observable movements of larger structures such as whole mitochondria ca be assessed using the acquired data stack.

To minimise the impact of these movements, the total exposure time for each super-resolution image should be minimised. The total exposure is a product of the individual frame exposure time and the total number of frames; even with optimisation there may still be regions of the image stack that contain significant, observable sample motion and should therefore be ignored for MUSICAL processing. To identify these regions an image processing pipeline was developed (Figure 70).

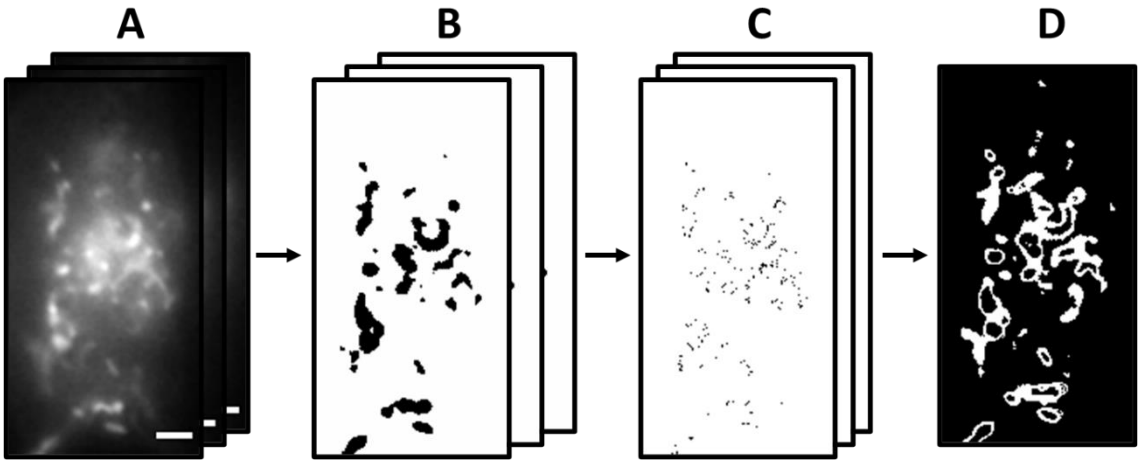

Figure 70: Identifying motion in MUSICAL stacks.
Raw stacks (**A**) are converted to binary images via background subtraction using a rolling ball with the ball size set to slightly larger than the size of the features of interest. Images are set to binary (**B**). Each image is subtracted from the subsequent image (**C**). Maximum intensity projection of the subtracted stack highlight points of motion as bright regions (**D**). This binary image is used as a guide to identify regions in the raw stack (**A**) that should be disregarded or excluded from analysis after MUSICAL processing. Example images are of mitochondria in a single, adherent SYSY-5Y cell labelled with mitotracker Orange. The raw images were acquired using the widefield imaging system described in section 3.4. Cells were imaged using a 60x/1.42 NA objective giving an effective pixel size of 107.5 nm. 25 ms exposure was used and 50 % LED power. Scale Bar 3µm.

First, image stacks (Figure 70**A**) were background subtracted and converted to binary images. Background subtraction was performed using a rolling ball with the ball radius set to be larger than the structure of interest e.g. mitochondria in Figure 70. Each image was then subtracted from the subsequent image in the stack to create a stack of "difference images". A maximum intensity projection of the difference image stack results in a single binary image. In this image an intensity of 1 corresponds to regions of sample motion in the original image stack and an intensity of 0 corresponds to static regions or background. The binary output image was used as a guide to interpret results of MUSICAL processing of the raw stack. Regions identified to contain significant sample motion were either disregarded and not put through the MUSICAL processing, or excluded from analysis after MUSICAL processing.

7.3.3 MUSICAL parameter selection

Suitable raw image stacks identified using the pre-processing steps above where used for MUSICAL processing. All MUSICAL processing was performed using the FIJI implementation which has recently been encompassed into a toolbox (MusiJ) for improved usability and throughput (Acuña *et al.*, 2020). When processing images using MUSICAL, it is possible for the user to modify key parameters that affect the outcome of the algorithm. These are the threshold (σ), alpha (α) and the number of subpixels. The threshold value is selected to separate the signal and null space for the MUSICAL algorithm. In MUSICAL, the acquired image stack is used to calculate a series of eigenimages, each eigenimage represents a pattern within the image stack and has an associated singular value. A large singular value indicates that the eigen image represents a prominent pattern in the image stack and a small singular value indicates a statistically less likely pattern. Patterns generated because of noise are statistically least likely (because they are random) and therefore have small singular values. Thus, by selecting a threshold singular value (σ_0) it is possible to use only those eigen images associated with signal for SR-image reconstruction. To select the value of σ there are two guidelines; if the SNR is well known then it should be selected such that σ_{Max}/σ_0 = SNR, where σ_{Max} is the maximum observed singular value and σ_0 is the selected threshold. As images in the raw image stack often contain a range of signal levels and it is not always trivial to determine an accurate SNR it is also suggested that the σ_0 value is selected to be slightly less than the knee point in the singular value plot (Figure 71**A**). Because MUSICAL uses a sliding window to process the raw image stack into an SR image, the singular value plot has a line for each sliding window. Each point on the line (not indicated) is the singular value associated with an eigen image calculated for that instance of the sliding window. The knee point is the point at which decay of the singular values changes from a steep slope to a shallow slope. This represents the point at which the singular values are associated with noise rather than signal. The singular value plot contains a single line for every position of the sliding window. As each position of the sliding window will contain a different number of emitters and fluctuations there is a range of singular values at which the knee point can be observed. The effect of σ_0 on MUSICAL processing was tested by selecting different values within this range. Selection of the highest value in the range (Figure 71**C**) reveals the SR features of the image. Selecting progressively lower values within the range (**D-F**) appears to reveal finer detail within the image. This finer detail corresponds to less prominent eigen images due to weaker fluctuations. Therefore, using a lower threshold value includes more information but this does not necessarily mean better SR, unless the weaker fluctuations can be definitively associated with smaller structures. Selection of a value too low incorporates information from noise into the MUSICAL reconstruction generating artefacts that appear as fine detail. Precise selection of the correct threshold had a smaller effect

in stacks containing high SNR. When image stacks contained lower signal to noise, selection of the threshold was performed for a series of values and an appropriate value selected by comparing the MUSICAL image with prior knowledge of the expected super-resolved structure.

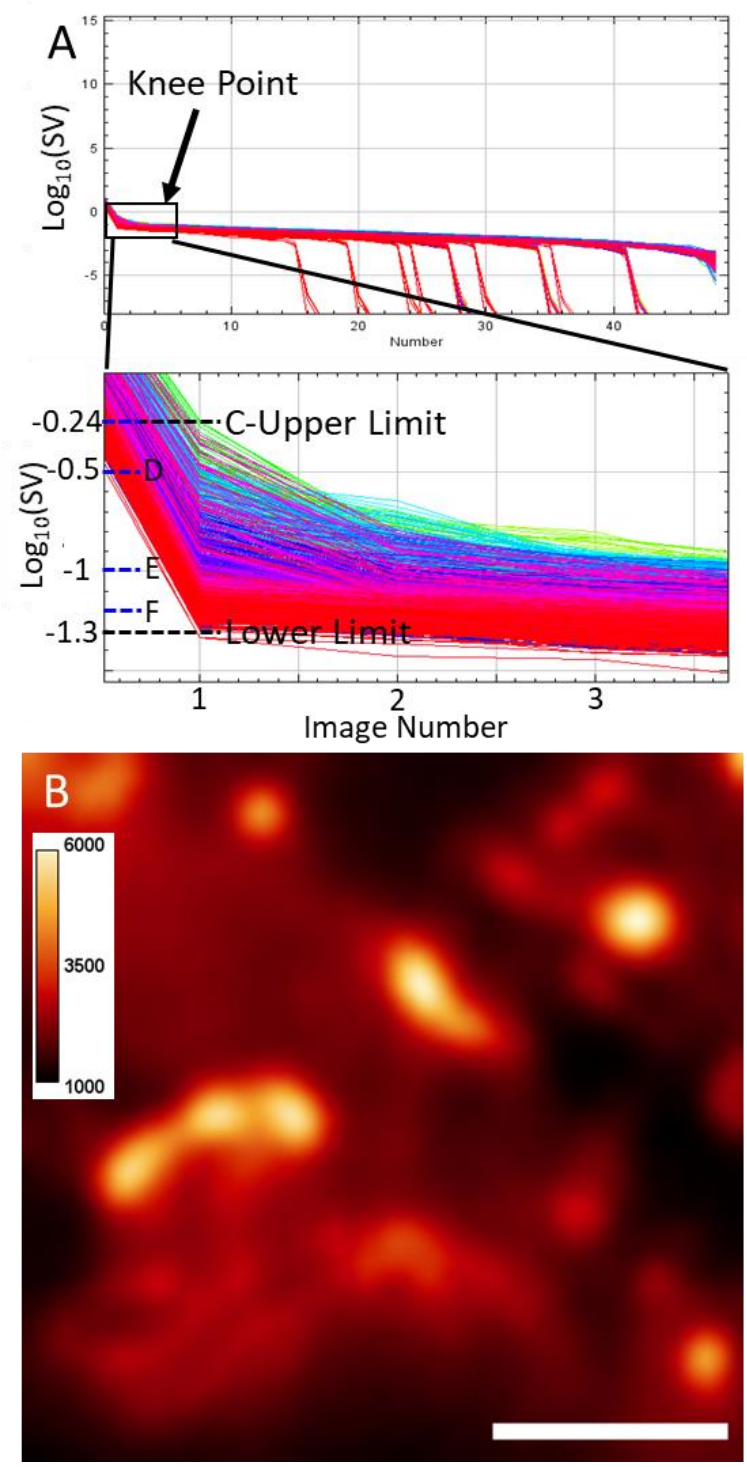

Figure 71: Choice of appropriate σ_0 threshold.
(**A**) An example singular value decomposition (SVD) plot for the image stack represented by the average projection in B. The Log of the singular value associated with an eigenimage is potted against the eigen image number. The SVD plot contains a line for each instance of the MUSICAL sliding window. The zoomed section highlights the knee point which contains appropriate σ_0 threshold values. Black dashed lines indicate approximate upper and lower limites for σ_0 selection. The positions of the vaules used in C-F are marked. (**B**) Average projection of 50 frames of mitochondria labelled with mitotracker orange.

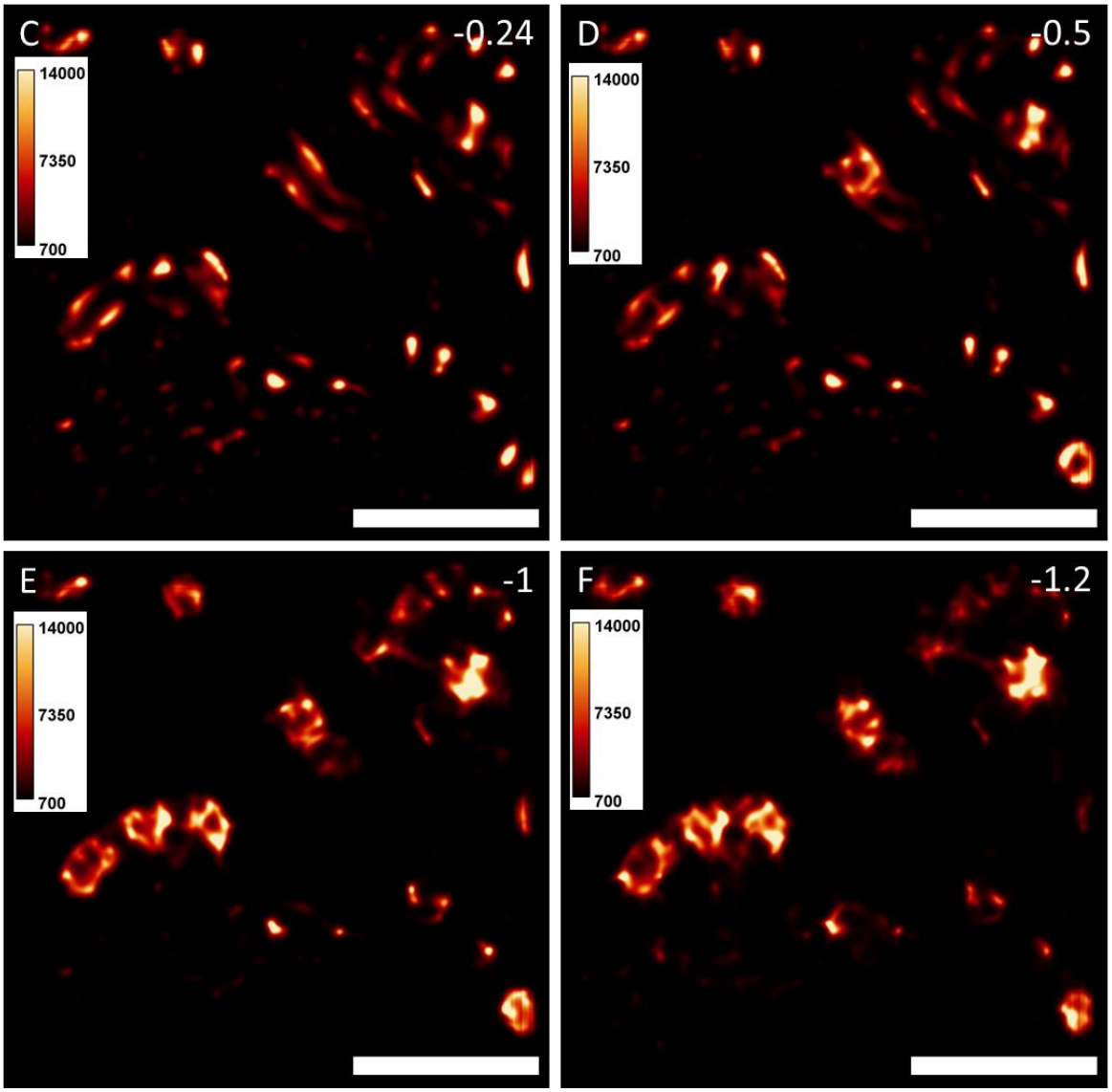

(**C-F**) MUSICAL images from the stack used in B using different σ_0 values. Lowering the value incorporates less prominent image patterns (potentially finer detail) in the MUSICAL image but also runs the risk of incorporating noise as an artefact. Scale bar 3 µm. Raw images were acquired using the lighsheet microscope with one-photon excitation and 100 ms exposure.The detection objective was 40x/0.8 NA with an effective pixel size of 147 nm. All MUSICAL images were calculated with $\propto$ = 4 and 20 sub-pixels per pixel.

The α value affects the degree of nonlinearity in the MUSICAL test function which is used to assign an intensity to a given location in the MUSICAL image. Changing the value of α has three effects on the final image, firstly it affects the contrast of the image. Secondly it affects the stitching of the sliding windows. Because MUSICAL is calculated for a series of sub-images (the sliding window), to form the final super-resolution image the individual MUSICAL sub-images must be stitched together. The sliding window encompasses the main lobe of the PSF and the MUSICAL intensity is calculated for a series of sub-pixel-spaced test points within the window. The centre pixel of the window is moved by a single pixel and a MUSICAL sub-image is calculated for a window centred on each pixel of the raw image stack. The MUSICAL image produced at a given pixel is influenced by noise the least when that pixel is the centre of the sliding window, when the pixel is one of the peripheral pixels in the window it is more greatly influenced by noise. The value of α affects the contribution of the MUSICAL images calculated at a given pixel, for the different relative positions within the sliding window, to the final MUSICAL image. Lower values allow greater contribution from off-centre sliding windows which are more susceptible to noise whilst higher values decrease this contribution. Finally, a high value of α non-linearly scales less prominent features. These features may be less prominent because they are not as bright or displayed fewer/weaker fluctuations, this can make them visually less obvious in the MUSICAL image. A low value of α will make fluctuations in the background more prominent making them difficult to separate from signal. Figure 72 shows the effect of varying α for a fixed $\sigma_{0.}$ For values <4 the background becomes very prominent and for values >6 the structures of the image start to disappear as the dynamic range of the image becomes too large to display. It was determined α = 4 was a suitable value to use as it provided an acceptable trade-off between the effects mentioned above. This is in agreement with the conclusion drawn by Agarwal and Machá (Agarwal and Macháň, 2016).

The number of sub-pixels determines the size of the MUSICAL processed image. Ideally it should be selected such that the pixel size is at least two times smaller than the finest features of the MUSICAL image, such that Nyquist sampling is maintained. As the expected resolution was unknown the default value of 20 subpixels per original pixel was chosen, this allows a potential 20-fold increase in resolution, which was expected to exceed the actual gain in resolution.

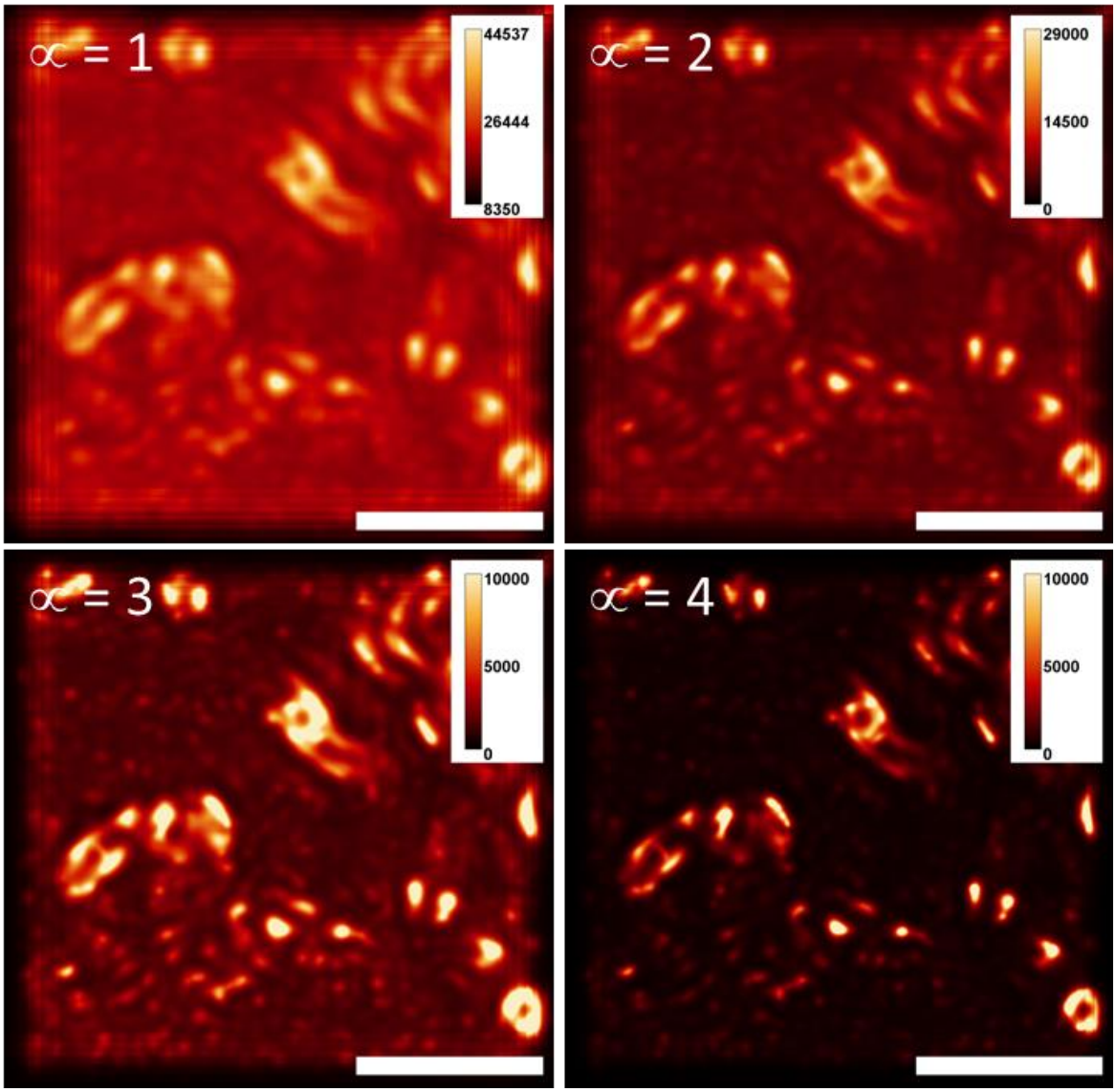
∝ = 1
44537
26444
8350
∝ = 2
29000
14500
0
∝ = 3
10000
5000
0
∝ = 4
10000
5000
0

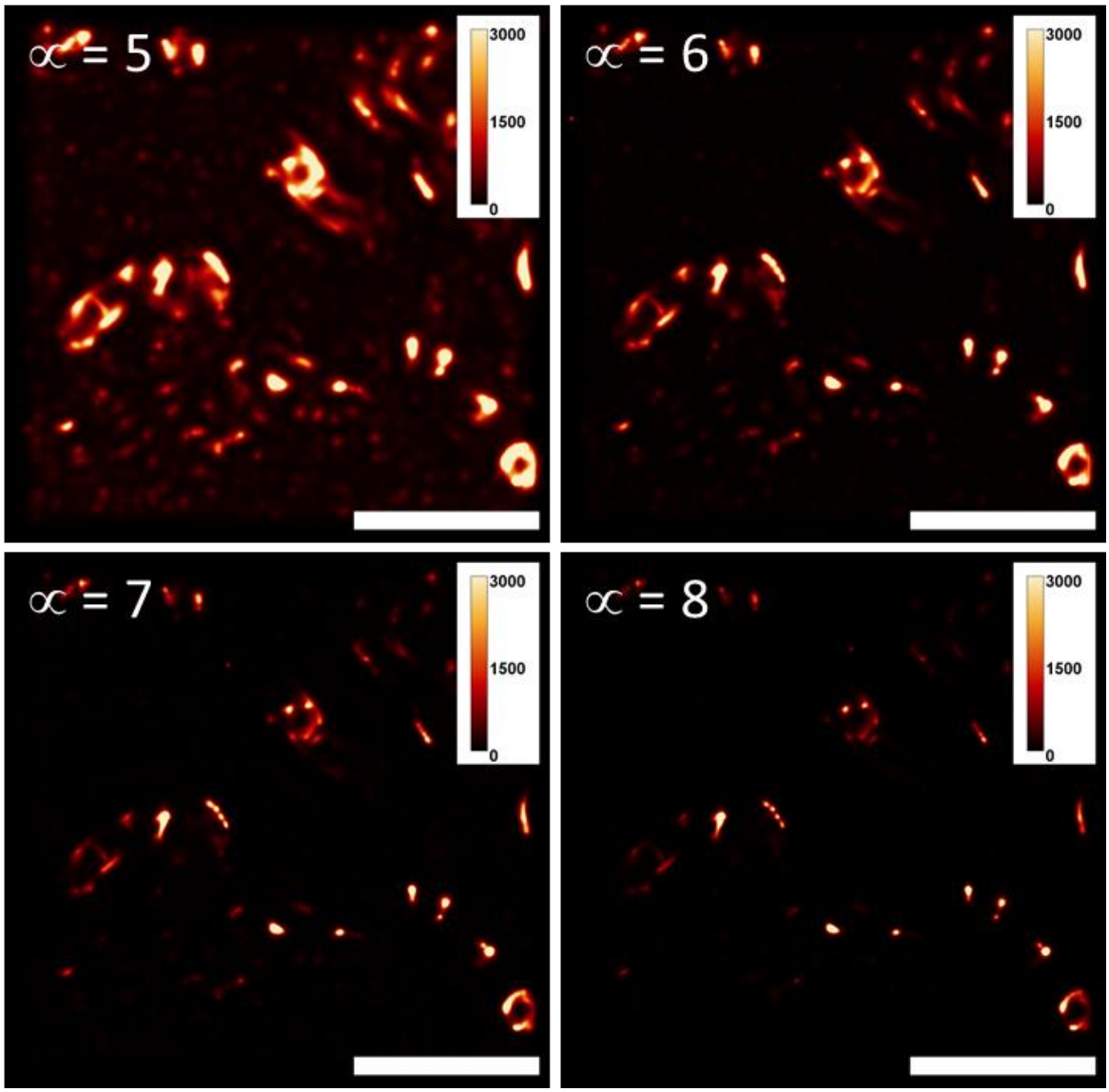

Figure 72: Choice of alpha value.
The ∝ value affects the non-linearity of the intensity given to each pixel in the MUSICAL reconstruction. Low values emphasise background/noise fluctuations making features difficult to resolve. High values of α non-linearly scales the intensity of less prominent features leaving only the strongest fluctuations visible. Scale bar 3 µm. MUSICAL images were generated from a 50 rawframe stack of mitochondria in a cell-spheroid labelled with mitotracker orange. Raw images were acquired using the lighsheet microscope with one-photon excitation and 100 ms exposure.The detection objective was 40x/0.8 NA with an effective pixel size of 147 nm. All images were calculated with σ_0 = -0.5 and 20 sub-pixels per pixel.

7.3.4 Development of a Suitable Test Sample

To evaluate the super-resolution capability of MUSICAL using the proposed lightsheet configuration a 3D cell spheroid sample of SHSY-5Y cells was developed. This allowed both labelled and label-free imaging of subcellular structures

7.3.4.1 Optimising Spheroid Formation

Two key parameters were investigated for the generation of cell spheroids suitable for 3D imaging, cell seeding number and spheroid formation time. SHSY-5Y Cells were detached from culture flasks as previously described (section 3.14) and the cell count determined using a haemocytometer. Serial dilutions of the starting cell suspension were made to created suspensions of ~$6.6x10^7$ – $6.6x10^3$ cells / ml. Wells of a 96 well plate that are coated with an ultra-low attachment coating were loaded with 150 µl of cell suspension resulting in spheroid seeding numbers of ~$1x10^6$ – $1x10^2$ cells in each well. The same spheroids were imaged using phase contrast microscopy after 24, 48 and 72 hours (Figure 73**A/B**), spheroid diameter was measured in Fiji. Spheroid size increased with increasing seeding number (Figure 73**C**). Wells seeded with ~10^3 cells produced spheroids with an average diameter of ~100-150 µm which was determined to be a suitable size for 3D imaging as this is the range over which the Airy beam profile is uniform (section 3.6.1). No significant change in size was observed after 48 or 72 hours (Figure 73**C**). It was determined that spheroids should be imaged 48-72 hours after seeding. Spheroids harvested earlier than this didn't display suitable mechanical stability to be transferred out of the 96 well plate for imaging.

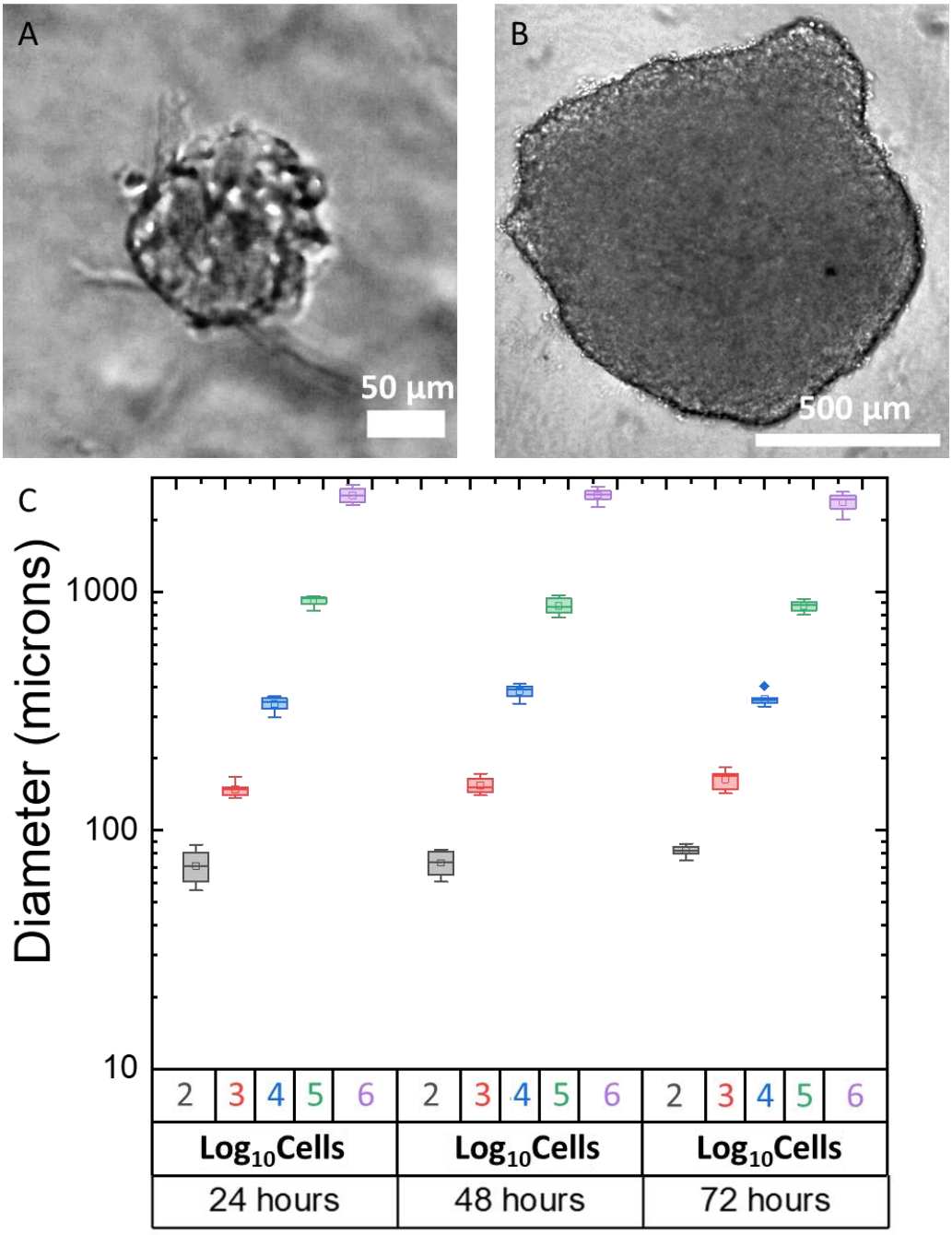

Figure 73: Characterisation of seeding density for cell spheroids.
Example images of cell spheroids seeded with ~$1x10^3$ (A) and $1x10^5$ (B) cells after 48 hours of growth. **C** Spheroid size increases with increasing cell number. Eight spheroids were analysed for each cell seeding number for three separate repeats totalling 24 spheroids analysed per seeding number. The same spheroids were measured at each time point.

7.3.4.2 Verifying Spheroid Viability

The viability of the cell spheroids after 72 hours was checked using the stains SYTO9 and Propidium Iodide (PI). SYTO9 is a cell-permeable dye that binds to DNA and is used for staining the nucleus. PI also binds DNA but is not able to cross the cell membrane and is therefore only able to penetrate dead cells where the membrane has been compromised. Widefield, one-photon excited fluorescence microscopy was performed on the spheroids using the DeltaVision microscope described in section 3.4. Images were acquired using a 20x/0.75NA objective, the effective pixel size of was 324 nm. A z-stack was acquired and 3D, iterative, constrained deconvolution was performed, details of deconvolution parameters can be found in Appendix D. Spheroids showed minimal PI staining after 48 hours but showed staining by SYTO9 (Figure 74), verifying the viability of cell spheroids at the point of imaging.

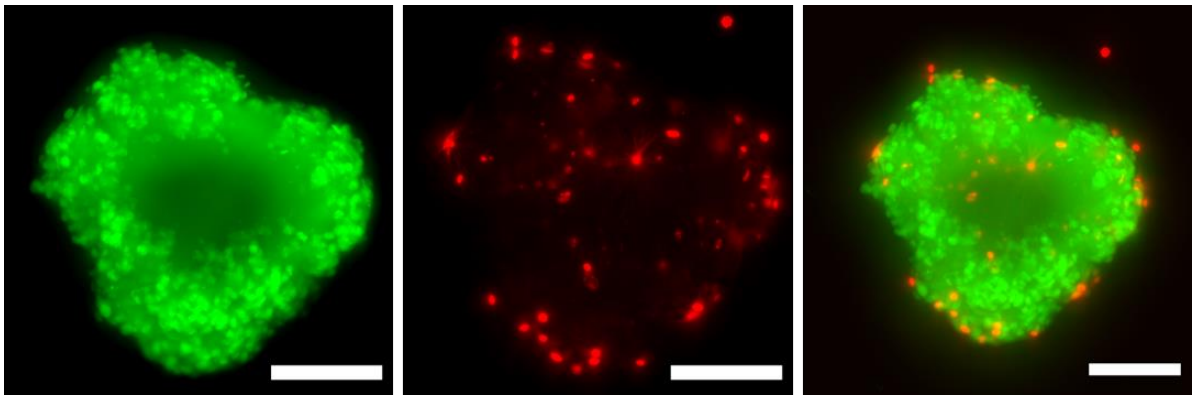

Figure 74: Verification of spheroid viability.
Representative maximum intensity projections of z-stacks taken from spheroids stained with a combination of SYTO9 **(A)** and Propidium Iodide (PI) **(B)**. Live cells are labelled green whilst dead cells are labelled red, an insignificant number of red stained cells were seen. Images were acquired using the DeltaVision microscope described in section 3.4 using a 20x/0.75NA objective. Scale bar 50 µm.

7.3.4.3 Optimising Cell Culture Conditions for Lightsheet Imaging

7.3.4.3.1 Lightsheet Sample Preparation Pipeline

Large variability in the signal-to-background ratio was observed between lightsheet imaging sessions of cell spheroid samples. To decrease this variability, issues in the sample preparation pipeline that could affect the signal to background ratio were identified and optimised. The sample preparation process is outlined in Figure 75. Once grown and incubated with a dye (if a dye was being used) in the 96 well culture plate (Figure 75-1), excess media is removed from the wells (2). The wells are then filled with liquid agarose and mixed with the media via gentle pipetting (3). The spheroid and some agarose (~50 µl) are sucked into the pipette (4) and deposited as a droplet on the sample pedestal of the custom sample holder (5). The sample was

inverted whilst the agarose cooled to encourage the spheroid towards the "top" edge of the agarose droplet (6). Once cool, the sample was transferred to the lightsheet, the sample bath filled with indicator-free media and imaged. Further details of the custom sample holder can be found in section 3.6.2.

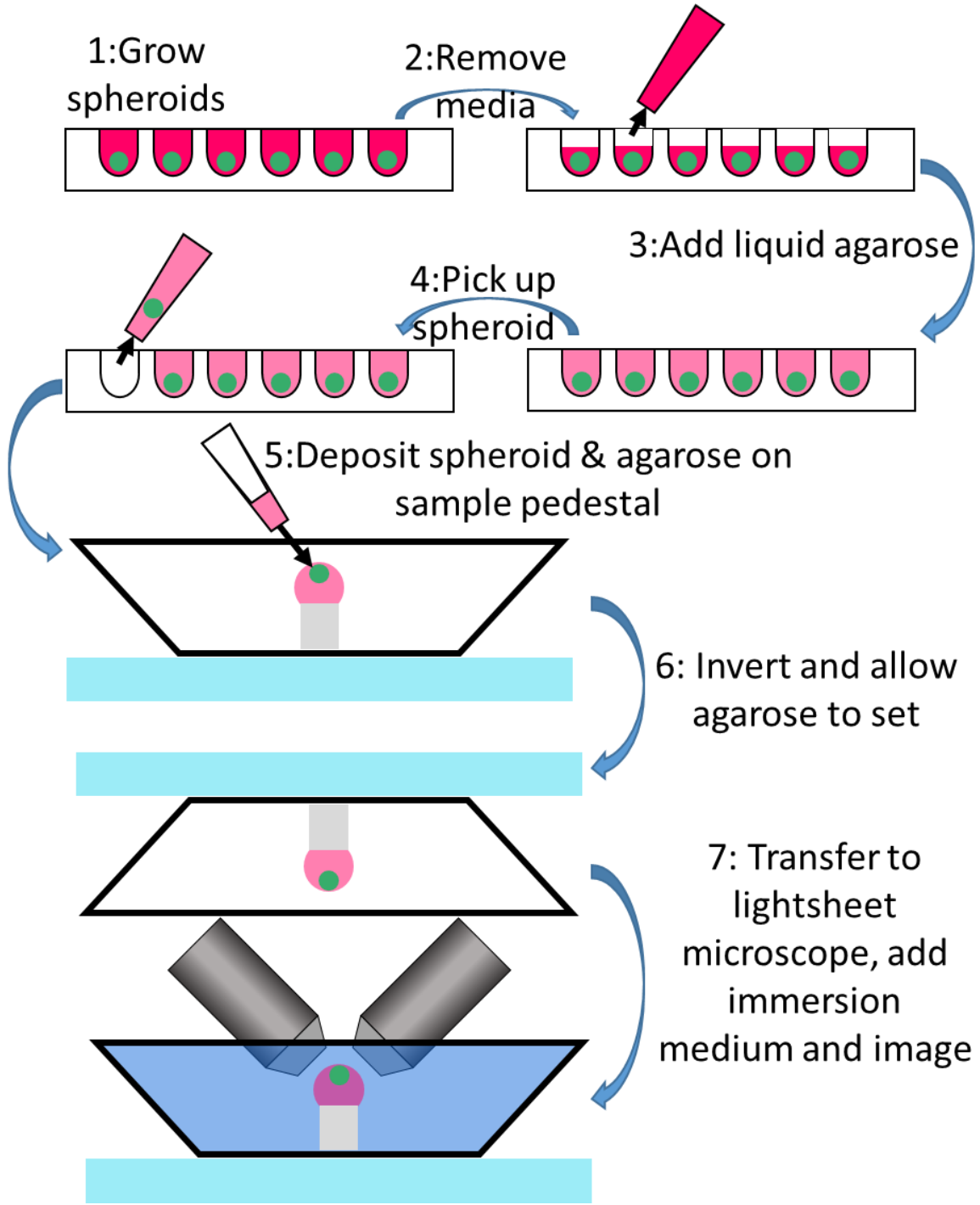

Figure 75: Lightsheet spheroid sample preparation.
(1)Once grown for 48 hours spheroids were incubated with a dye if a dye was being used. (2) Excess media was removed using a pipette. (3) Liquid agarose was then added to the well and mixed by very gentle pipetting. (4) The spheroid-in-agarose was picked up using the pipette, (5) and deposited onto a clean sample pedestal. (6) The pedestal was inverted to encourage the spheroid to move to the "top" edge of the droplet as the agarose set. (7) Once set, the

sample was taken to the lightsheet, the bath filled with immersion medium (indiator-free media) and imaged.

7.3.4.3.2 Absorbance From Components of Media

During the transfer of cell spheroids from the 96 well culture plate to the sample pedestal excess media must be removed before being replaced with agarose (2 and 3). The small size and density of spheroids made them highly mobile during these steps and easily lost into the volume of the pipette. To avoid this, a large volume of media must be left in the well of the 96 well plate (~30 µL) before addition of agarose. To investigate whether this residual volume of media, may be decreasing the observed signal the absorbance spectra of 4 formulations of media were acquired. The spectra were acquired as detailed in section 3.9. It was observed that the Phenol Red (PR) indicator-containing medium absorbed significantly more across the visible spectrum than indicator-free medium (Figure 76). The addition of foetal bovine serum (FBS) appeared to have a greater impact on the absorbance of the PR-containing media than on the PR-free media. This may be due to slight variations in the constitution of the FBS as it is an extracted not a manufactured product. There was minimal observed absorbance in the range 710 nm – 990 nm (the tuning rage of the multiphoton laser) indicating that the observed degradation in detected signal was most likely due to absorption of the fluorescence emission rather an absorption of the NIR excitation. As a result of this experiment general cell maintenance was performed using PR free media to minimise signal loss due to absorbance.

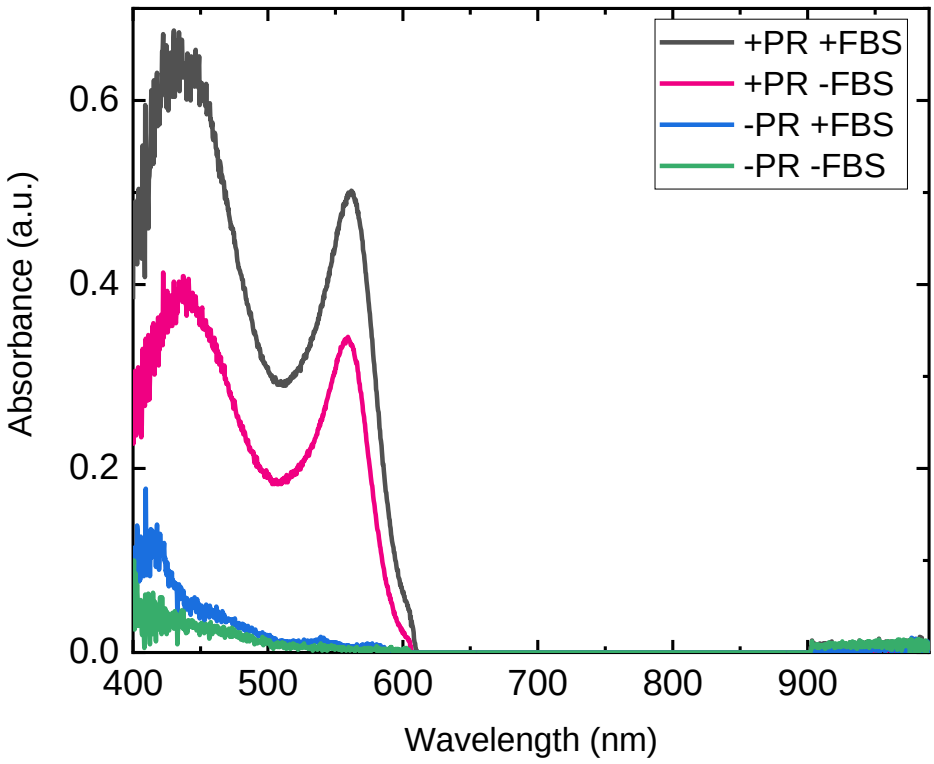

Figure 76: Absorption spectra of DMEM with different additional components.
Media containing PR showed much higher absorbance in the visible spectrum than PR free media. PR = Phenol Red FBS = Foetal Bovine Serum.

7.3.5 Microtubules

Cytoskeletal structures are often used in super-resolution microscopy to evaluate the resolution of a new SR method. The two key components: microtubules and fibrillar actin both form thin, elongated structures that have widths below the diffraction limit (Demmerle *et al.*, 2015). These can be used to calculate a line spread function and the FWHM used as an indicator of resolution. Due to the complex network like nature of these structures, the points at which two fibres cross can be used to establish the minimum resolvable distance. Microtubules were chosen for investigation due to their close interaction with mitochondrial networks, acting as roadways for transport of mitochondria around the cell (Wang *et al.*, 2015). The width of individual microtubules is well established as being 25 nm (Moores, 2008).

Prior to imaging intracellular microtubules, where networks are complex and highly dynamic, microtubules polymerised *in vitro* were imaged. Fluorescently-labelled tubulin was polymerised *in vitro* as described in section 3.16. Briefly, labelled tubulin was polymerised in the presence of 3mM GTP for 30 minutes then stabilised by the addition of taxol. Polymerised microtubules were imaged immediately after stabilisation. Example images of the polymerised microtubules can be seen in Figure 77. Successful polymerisation resulted in microtubules (or small microtubule bundles) of ~10 µm in length (Figure 77**A/B**) however, accumulation of microtubules into star-shaped bundles was sometimes observed (Figure 77**D**). As microtubules are of sub-diffraction-limited width they will appear at the size of the diffraction limit when imaged. Many microtubules may also form a bundle, yet still be below the diffraction-limit in width and will therefore also be imaged with diffraction-limited width. Thus, when imaging these structures it is important to consider the possibility that both individual and bundles of microtubules may be present. To establish the optimum wavelength for multiphoton imaging of labelled microtubules an excitation wavelength scan was performed (Figure 77**C**), 800 nm was used for all further multiphoton imaging of *in vitro* microtubules. The excitation scan was performed in an imaging format by taking images of polymerised microtubules at increasing excitation wavelength steps spaced 10 nm apart. The signal was collected at 520 ± 20 nm using a bandpass filter. The intensity in each image was measured and plotted against wavelength. The presented spectrum is an average of two ascending and two descending wavelength scans.

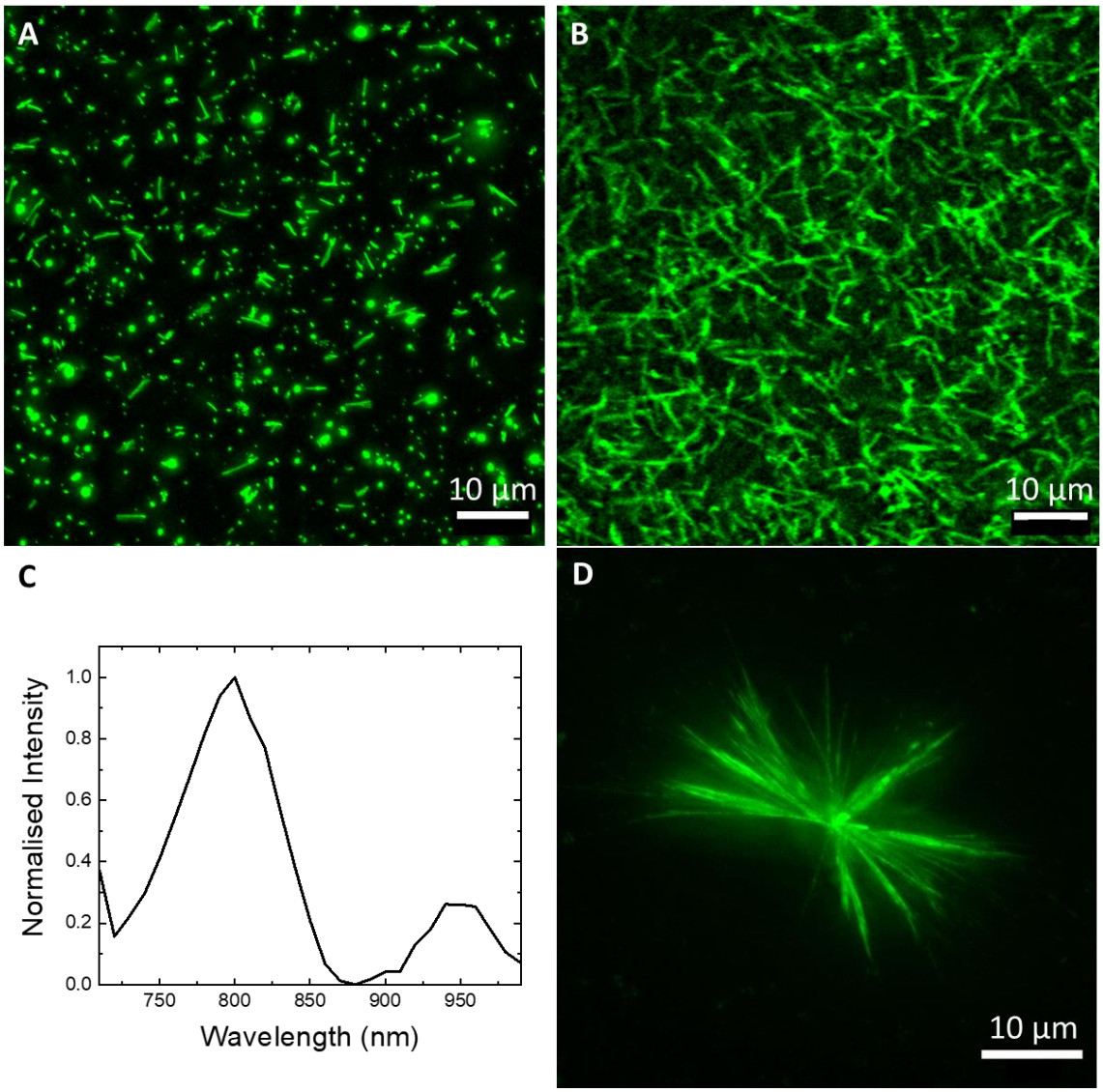

Figure 77: Imaging of *in vitro* microtubules
(**A**) OPEF image of *in vitro* microtubules (bundles) on a glass coverslip, multiple microtubules can be seen alongside small, round aggregates of un-polymerised tubulin. (**B**) TPEF image of similar tubules (bundles), a dense network of tubules (bundles) can be seen. (**C**) TPEF excitation spectrum of *in vitro* microtubules (bundles). (**D**) Example image of a star like aggregate sometimes observed in microtubule samples. **A/D** were acquired using the DeltaVision microscope using a 60x/1.42 NA objective, the effective pixel size was 107.5 nm and the diffraction-limited resolution was 226 nm. **B** was acquired using the multiphoton imaging system (section 3.3) using a 63x/1.2 NA objective. The imaged field was 78 µm x 78 µm and was imaged using 1024 x 1024 pixel, the effective pixel size was 76 nm.

The microtubules were observed to be highly dynamic in solution and thus not suitable for MUSICAL imaging, to overcome this issue microtubules were immobilised in agarose. However, this resulted in consistent formation of star shaped aggregates and other amorphous clumps of tubulin. The formation of aggregates could be advantageous as the points at which neighbouring sub-diffraction-limited width microtubule-bundles approach each other can be used to measure the resolution of the microscope and the improvement given by MUSICAL.

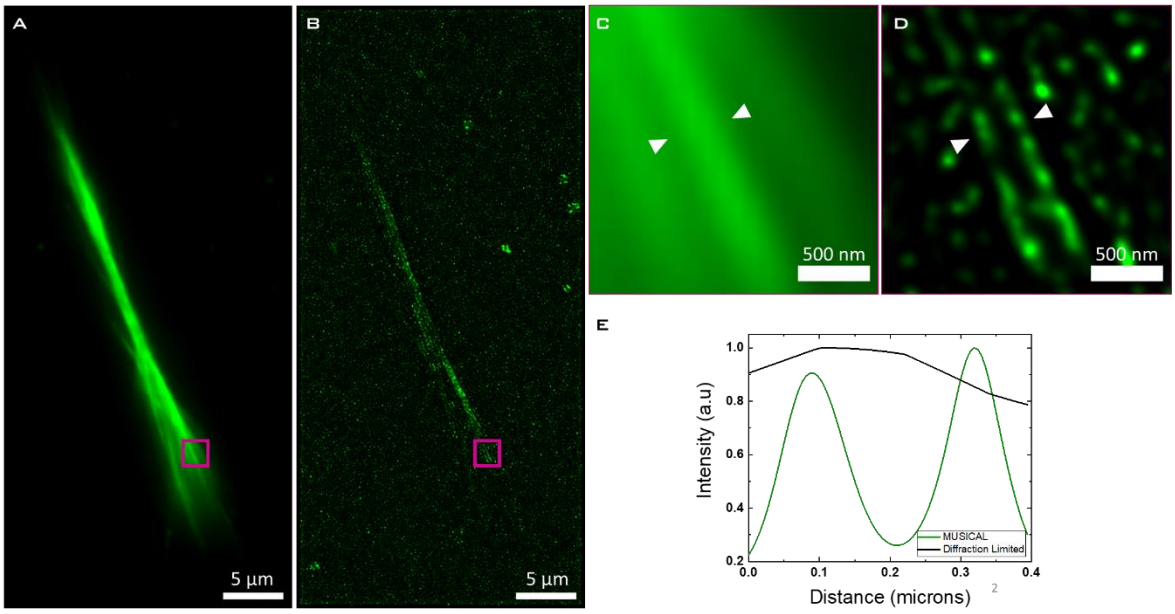

Figure 78: MUSICAL imaging of a microtubule bundle.
(**A**) diffraction-limited average of 50 frame time-stack of *in vitro* polymerised microtubules. The raw image stack was acquired using the DeltaVision microscope using a 60x/1.42 NA objective and an effective pixel size of 107.5 nm. Exposure was set to 20 ms and illumination power to 10 % (**B**) The corresponding MUSICAL processed image calculated with σ_0 = -0.866 and α = 4. (**C**) zoomed view of the magenta square in (A), a series of microtubules or microtubule bundles can be seen, the central tubule is in focus whilst the others are . (**D)** the corresponding MUSICAL processed image of the image in C, MUSICAL processing revels two neighbouring microtubules that appear as 1 in C. Intensity plots (**E**) between the white arrow heads in C/D show the separation of the two peaks to be 223 nm and the FWHM to be 96 nm and 84 nm.

Before imaging on the light sheet microscope, a microtubule bundle was imaged using widefield, one-photon excited fluorescence, as the imaging conditions were closer to the conditions used in the original application of MUSICAL (Agarwal and Macháň, 2016). The microtubule bundle resembled a twisted rope with frayed ends (Figure 78**A**). These ends contain the individual microtubules of interest. As the microtubule bundle extends in 3 dimensions, regions of the structure contain out-of-focus signal that acts to lower the contrast and by extension the resolution of the image. When processed by MUSICAL, much of this light is removed as the fluctuations are weaker, improving the contrast (Figure 78**B**). Closer inspection of the apparent individual microtubules at the end of the bundle (Figure 78**C/D**) revealed microtubules that appeared as a single strand under diffraction-limited imaging but were resolved as two separate strands after MUSICAL processing. The intensity plot taken between the white arrow heads in Figure 78**C+D** are plotted in E (black line and green line respectively). The FWHM of the two peaks measured from **D** were 96 nm and 84 nm and were separated by 223 nm. The diffraction-limited resolution at 527 nm with a 1.42 NA objective using the Rayleigh criterion (d = 0.61λ/NA) is 226 nm. At the limit of resolution, it would be expected to see a small intensity dip between two peaks however, a single broad peak is observed. This may be due to non-optimal imaging conditions, such as the immobilisation of the sample in agarose and imperfect adjustment of

coverslip correction causing aberrations and thus lowering the effective resolution compared to the ideal theoretical case. It may also be possible that the apparent single microtubule was, in fact, a bundle of microtubules and therefore the true separation between neighbouring microtubules was much less than the diffraction-limited resolution. In this case, the two microtubules revealed by MUSICAL may only represent a sub-selection of the microtubules that were present. These microtubules showed the strongest signal fluctuations and therefore, were best identified by MUSICAL. The microtubules in Figure 78**D** appear be discontinuous, as they are made from fluorescently-labelled tubulin this appearance is not due to a discontinuity in labelling. It is possible that the appearance is due to different fluorophores showing different degrees of fluctuations and therefore are assigned different intensities in the MUSICAL image. Those fluorophores displaying weak fluctuations may then be thresholded out with the background. Nonetheless, Imaging of *in vitro* microtubules indicated that they could be used as a suitable standard for measuring the performance under multiphoton excitation on the lightsheet microscope.

When lightsheet imaging of *in vitro* microtubules was attempted the only observed signal came from amorphous aggregates and the identification of individual microtubules or stars/bundles was not possible. This may be due to the comparatively weaker two-photon excitation compared to single photon excitation resulting in signal that was too weak for detection. For lightsheet imaging samples are suspended in a droplet of liquid agarose which is allowed to cool such that it sets. Transferring to the warm, liquid droplet (section 3.6.2) may also cause the depolymerisation of the microtubules and aggregation of labelled tubulin as microtubules are known to be highly dynamic and temperature sensitive (Wallin and Strömberg, 1995). The above detailed experiments were to verify the validity of imaging microtubules using *in vitro* samples. Once established, imaging of microtubules *in cellulo* was performed, initially on a widefield system using adherent cells, then using the lightsheet system using cell spheroids.

To image microtubules *in cellulo* the live imaging dye Tubulin Tracker Green was used. The label was added as a 1x stock as per manufacturer's instructions, pluronic F-127 solution was added to aid loading of the dye. The efflux pump inhibitor probenecid (Stefan and Wiese, 2019) was added to the imaging medium to prevent efflux of the dye. Figure 79**A** shows an example adherent cell imaged under widefield illumination using the DeltaVision system described in section 3.4. A 60x/1.42NA objective was used giving an effective pixel size of 107.5 nm. The complex network of microtubules was observed and showed suitable signal to noise ratio and fluctuations for MUSICAL processing.

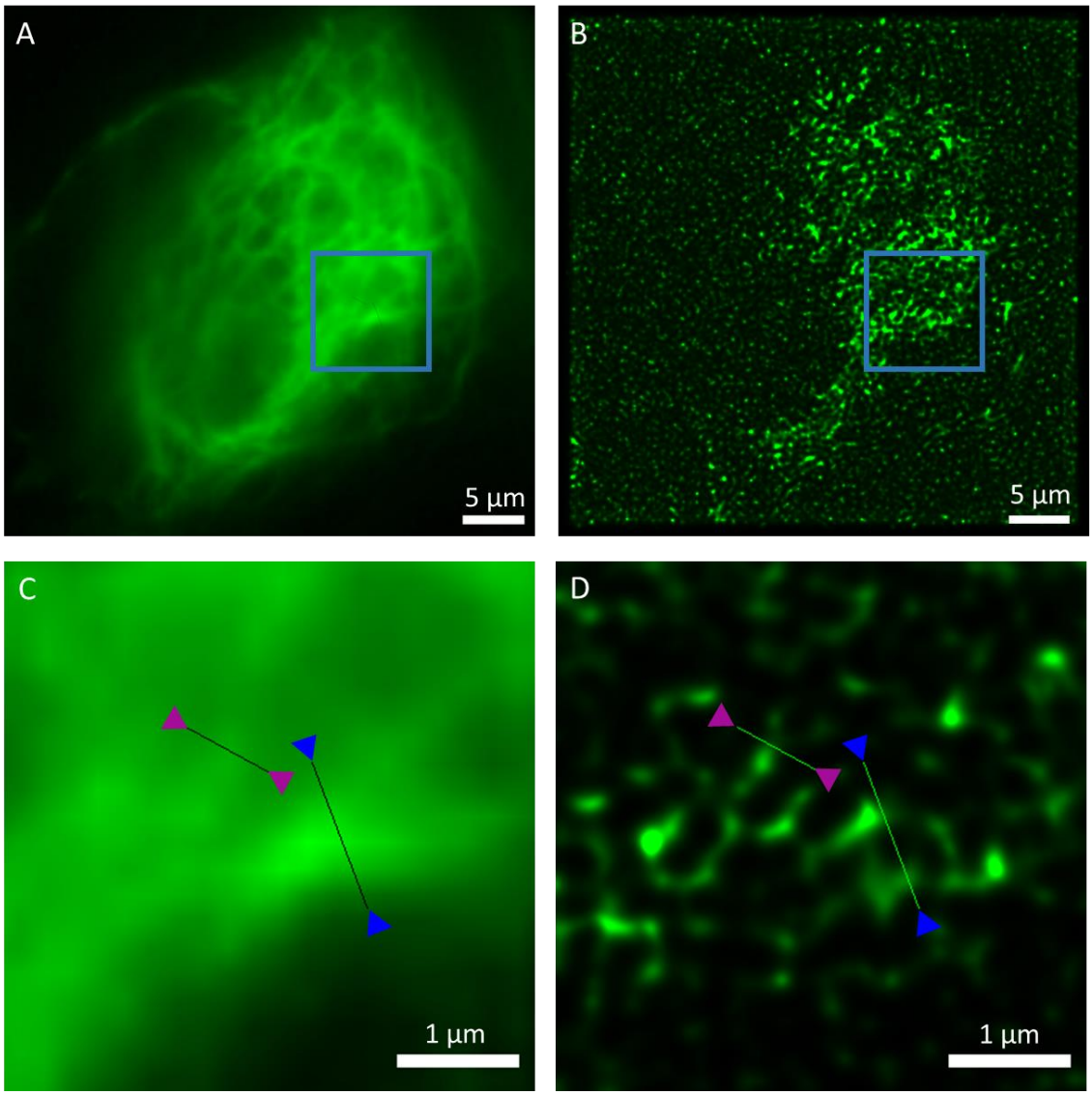

Figure 79: MUSICAL processing of wide field images of tubulin tracker green labelled cells. (A)Average projection of 50 diffraction-limited frames and (B) corresponding MUSICAL processed image σ0 = -0.7, α = 4. The raw image stack was acquired using the DeltaVision microscope using a 60x/1.42 NA objective and an effective pixel size of 107.5 nm. Exposure was set to 100 ms and illumination power to 50 % (C/D) zoomed-in views of blue boxed regions in A/B respectively.

As the images in Figure 79 were acquired using a widefield illumination scheme the raw images displayed a high amount of out-of-focus signal. As with the *in vitro* microtubule samples, the widespread and 3D network of microtubules resulted in a high degree of background in the widefield image, processing by MUSICAL removed this background (Figure 79**B**). However, many (fainter) punctate spots could be observed in the area surrounding the cell in the MUSICAL image. These may be a result of unbound die creating fluctuating background that was not separated from the signal by σ_0 selection. When observing a zoomed region of high microtubule-density (C) the out-of-focus background makes it difficult to identify parts of the microtubule network.

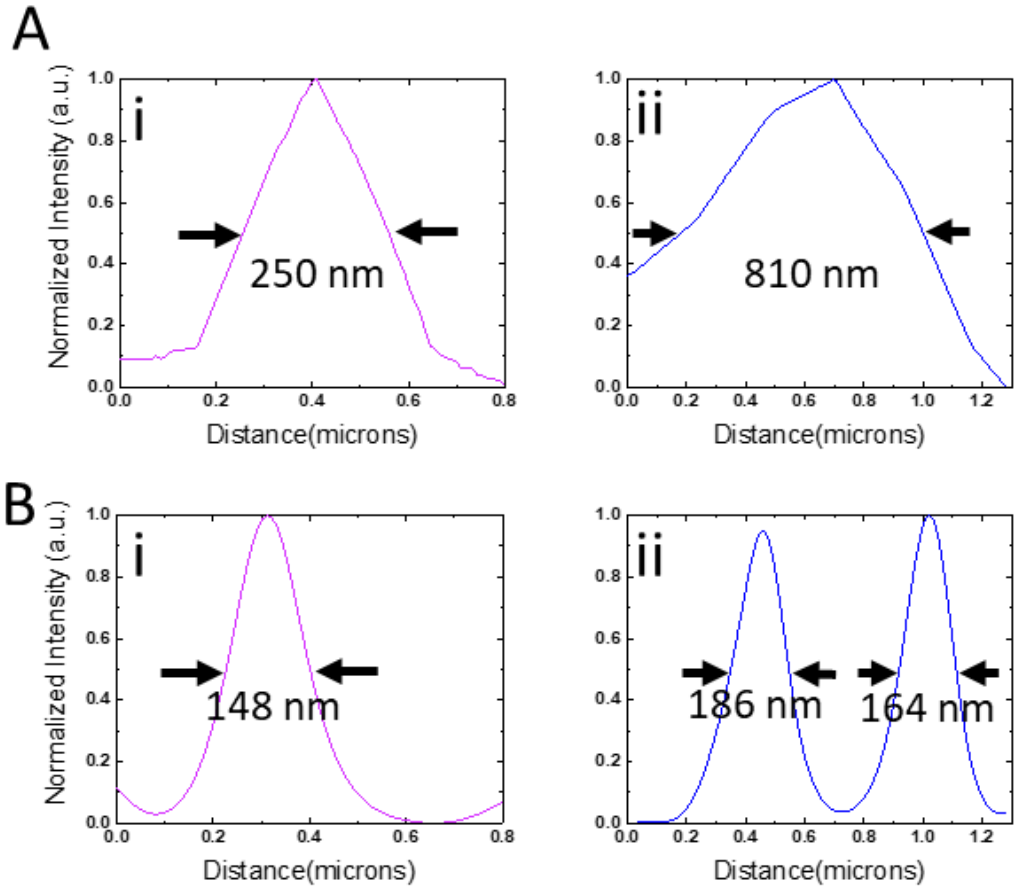

Figure 80: Line Plot analysis of tubulin tracker labelled features in Figure 79
(**A**) Intensity plots of the lines bounded by magenta (**i**) / blue (**ii**) arrow heads in C. (**B**) Intensity plots of the lines bounded by magenta(**i**) / blue (**ii**) arrow heads in D. MUSICAL processing decreased the FWHM of the peaks and resolved neighbouring microtubules that could not be resolved before processing.

After processing with MUSICAL (**D),** sharper/narrower features can be observed where the microtubules (bundles) appear to be in **C.** The image in **D** shows a complex network of intensity, this network may be resolved microtubules. However, due to the widefield acquisition scheme it is possible that some structures are a result of microtubules/dye moving into and out of the focal plane and therefore appearing as fluctuations used by MUSICAL. Intensity plots taken over an apparent single microtubule (bundle) and a pair (Figure 80 **A/B** respectively) of approaching microtubules (bundles) show that MUSICAL was able to reduce the measured peak width from 250 nm to 148 nm, an apparent 1.7 fold improvement in the resolution. It also allowed the resolution of two peaks separated by 567 nm that could not be resolved without MUSICAL processing. Having established that labelled microtubules could display suitable fluctuations for MUSICAL and observing the limitations of a widefield configuration with respect to background, the next steps were to image multiphoton excitation and using lightsheet illumination.

The optimum wavelength for multiphoton excitation for tubulin tracker green was established by imaging a labelled cell spheroid (Figure 81**A**) and was found to be 780 nm (Figure 81**B**). This was performed on the multiphoton imaging system described in section 3.3 using a 63x/0.9 NA water dipping objective. Imaging of the cell spheroid highlighted staining across the cytoplasm of cells with a dark hole possibly corresponding to the cell nucleus. No microtubule structures could be resolved. This may be due to the NA of the objective used (0.9) which has a diffraction-limited resolution of ~328 nm (FWHM) defined by the two-photon excitation volume (Zipfel, Williams and Webb, 2003). To investigate this, images were acquired of adherent SHSY-5Y cells labelled with tubulin tracker using the 60x/0.9 NA water dipping objective and the 60x/1.2 NA water immersion objective (Figure 81**C/D**). The microtubule network was resolved using the 1.2 NA objective, the network is not as readily resolved using the 0.9 NA objective however, some microtubules can be observed. As this is the same objective as used in Figure 81**A** it suggests that the microtubule network in spheroids is too close packed to be resolved using diffraction-limited imaging, needing SR to be resolved.

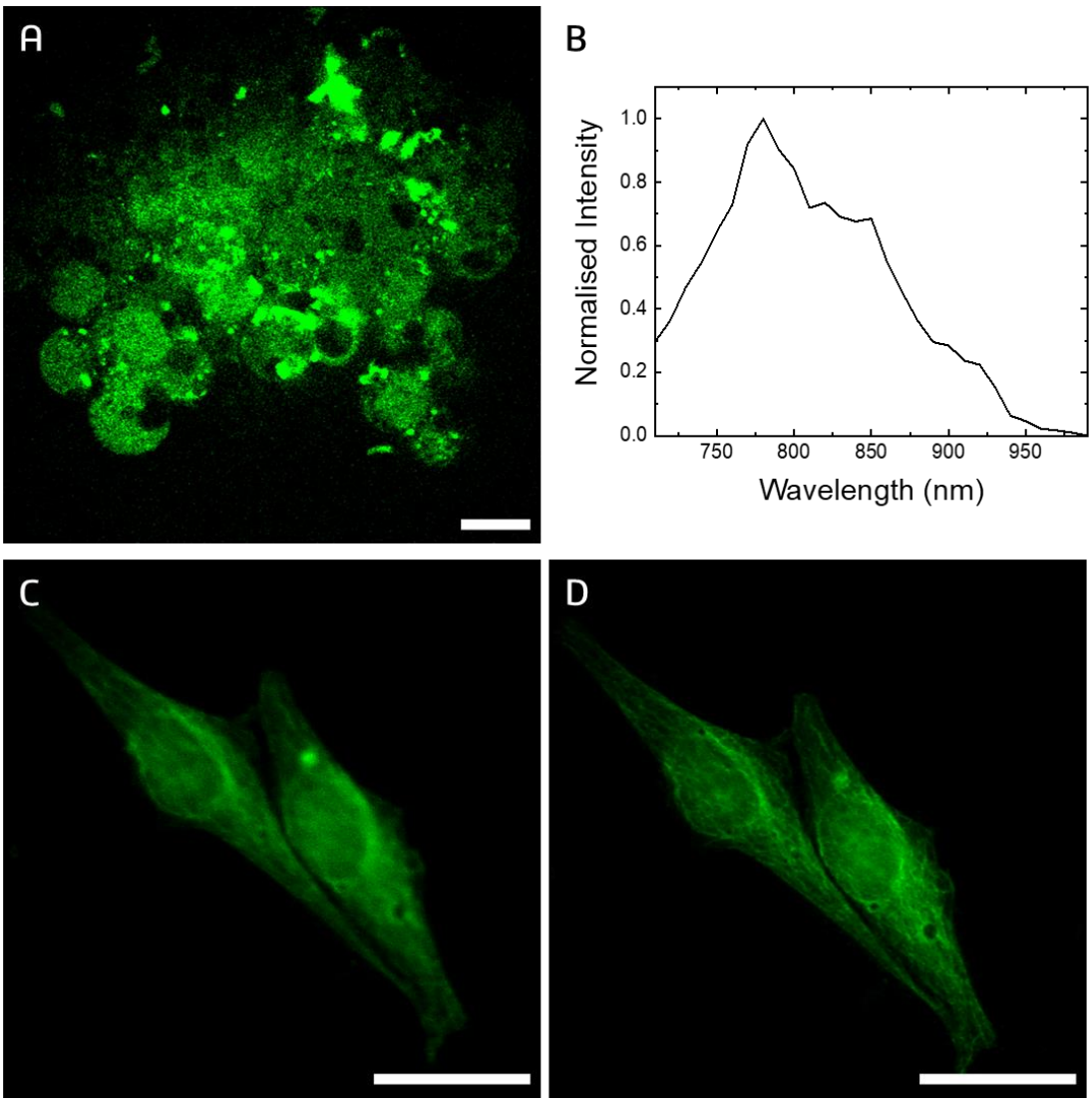

Figure 81: Multiphoton imaging of labelled microtubules.
(**A**) Example TPEF image of a Tubulin Tracker green-labelled cell spheroid imaged using laser scaning imaging using a 60x/0.9 NA objective. The cells show weak labelling and no microtubules can be resolved. Bright regions of dye aggregation can be observed. (**B**) TPEF excitation spectrum of Tubulin Tracker Green, peak excitation was achieved at 780 nm. (**C**) TPEF image of adherent cells labelled with Tubulin Tracker using 60x/0.9 NA (**D**) the same cells imaged using 60x/1.2 NA, the microtubules can be resolved. The imaged field was 103 µm x 103 µm imaged using 1024 x 1024 pixels, the effective pixel size was 101 nm. C/D have been cropped to aid display. Scale bars 10 µm

When processing images using MUSICAL, the lower the signal to noise ratio, the harder it is to separate signal fluctuations and background fluctuations when selecting the σ_0 threshold. MUSICAL processing of images acquired using widefield illumination (Figure 79) had highlighted that out-of-focus signal impacts MUSICAL processing, even in thinner sample such as adherent cells. As such, widefield imaging is not suitable for acquiring image stacks for MUSICAL in 3D samples. A key advantage of lightsheet imaging over conventional widefield imaging is optical sectioning due to the perpendicular arrangement of the excitation and imaging objectives. By using lightsheet imaging it was hoped it would be possible to process data acquired in 3D cell spheroids using MUSICAL and hence, resolve microtubule networks in cell spheroids. Figure 82 shows corresponding images of a cell spheroid taken using one-photon (A) and two-photon (B) excitation using the lightsheet imaging system described in section 3.6.

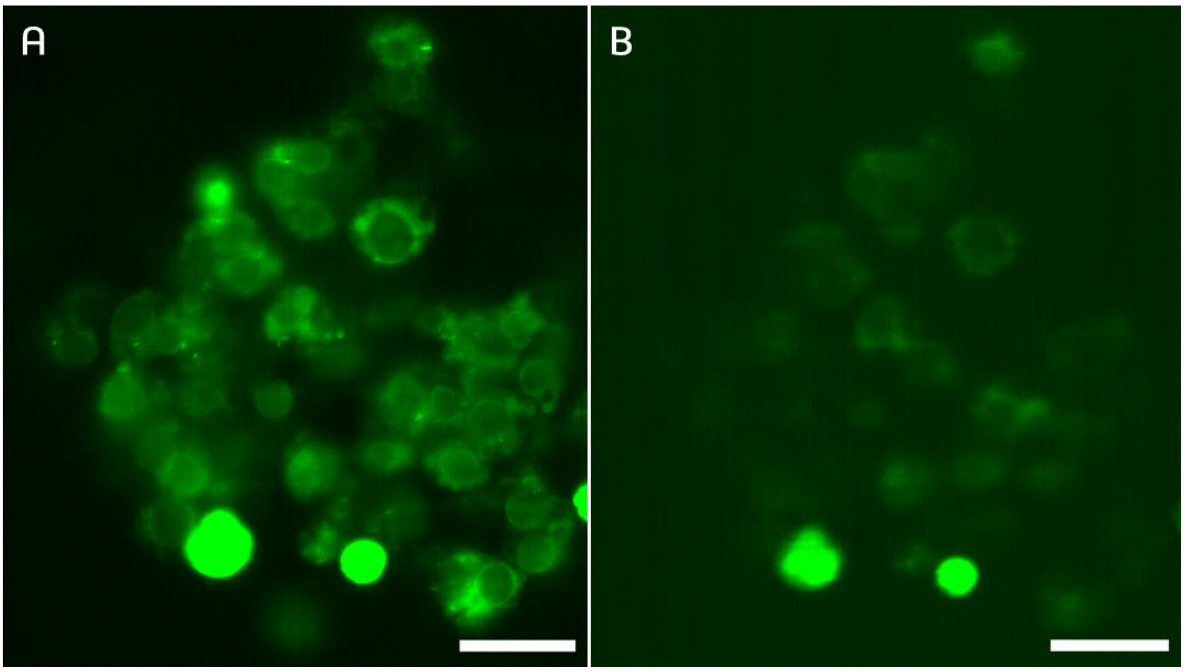

Figure 82:Lightsheet imaging of Tubulin Tracker Green in a cell spheroid
(**A**) OPEF image and (**B**) TPEF image of a tubulin tracker green-labelled cell spheroid. The SNR for OPEF is better than for TPEF. OPEF was excited using a 488 nm cw laser and TPEF was excited using 780 nm excitation. Exposure time 100 ms, effective pixel size 147 nm. Scale bar 30 µm.

When analysed using MUSICAL a complex, network-like structure was observed as would be expected for microtubules (Figure 83**B/D**). However, the nature of the structure looked very similar to artefacts observed when applying MUSICAL to data acquired using dyes for other structures such as SYTO9 for nucleic acids (Figure 83**E/F**), and to the background observed in regions outside of cells stained with tubulin tracker green (Figure 79**B**). During MUSICAL processing the final image is produced on a grid of pixels smaller than the original pixels, this allows the new image to accurately sample the potentially increased resolution in the MUSICAL processed image. The original images in Figure 83 A/C/E have been displayed on a resized pixel grid to match the MUSICAL processed images.

While Figure 83 showed that potentially MUSICAL could help achieve SR on a lightsheet the images needed to be correlated with ground truth. In the absence of ground truth, it is difficult to conclusively establish whether the observed structures were real or artefacts. However, obtaining ground truth for microtubules in cells in spheroids was very challenging and could not be established. Hence, instead of microtubules, mitochondria were chosen as intra-cellular biological targets for further development of super-resolution using MUSICAL.

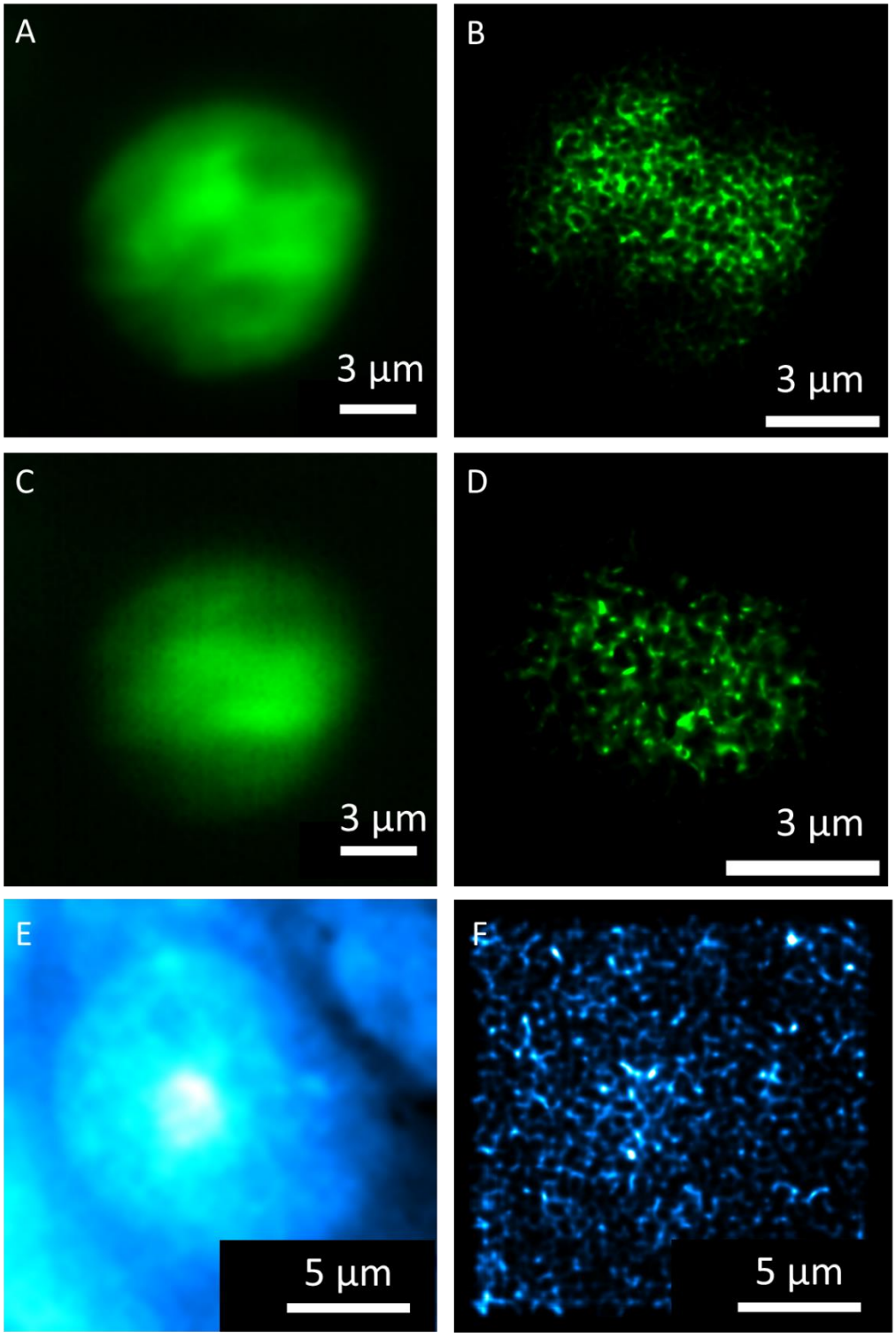

Figure 83: *In cellulo* microtubules imaged using lightsheet.
A) 50 frame average projection of a single cell from the upper surface of a spheroid labelled with tubulin tracker green under OPEF-lightsheet (488 nm excitation, 100 ms exposure). **B**) The MUSICAL processed image. **C**) The same as A but using TPEF-lightsheet (780 nm excitation, 100 ms exposure) and **D**) the corresponding MUSICAL image. **E**) Diffraction-limited average of a SYTO9-labelled nucleus imaged using TPEF-lightsheet (800 nm excitation, 50 ms exposure) and (**F**) the corresponding MUSICAL image. The patterns observed are due to poor threshold selection not true structures. A/C/E were recorded on 1024 x 1024 pixels giving an effective pixel size of 147 nm, MUSICAL processing resizes the image onto a new pixel grid 20 x larger 20480 x 20480. The effective pixel size in B/D/F is therefore 7.35 nm. A/B/C have been displayed on a resized pixel grid, 20 x 20 pixels per original pixel, to match the pixel size of MUSICAL processed images.

7.3.6 Mitochondria

Mitochondria are often used to demonstrate SR techniques as they contain a complex structure below the classical diffraction limit (section 7.2.2) and there are a large number of mitochondrial targeted fluorescent dyes available. MitoTracker Orange was selected as a suitable dye for multiphoton imaging of mitochondria within cells as the one-photon excitation spectrum indicated that it could potentially be readily excited by multiphoton excitation. Also, the emission did not significantly overlap with auto fluorophores such as nicotinamide adenine dinucleotide (NAD) and flavin adenine dinucleotide (FAD) (Monici, 2005) allowing evaluation of co-localisation of signals. An excitation scan was performed by imaging adherent SHSY-5Y cells labelled with 500 nm MitoTracker Orange to determine the optimum two-photon excitation wavelength for MitoTracker Orange (Figure 84). For all further TPEF imaging of MitoTracker Orange, 850 nm was used as the excitation wavelength.

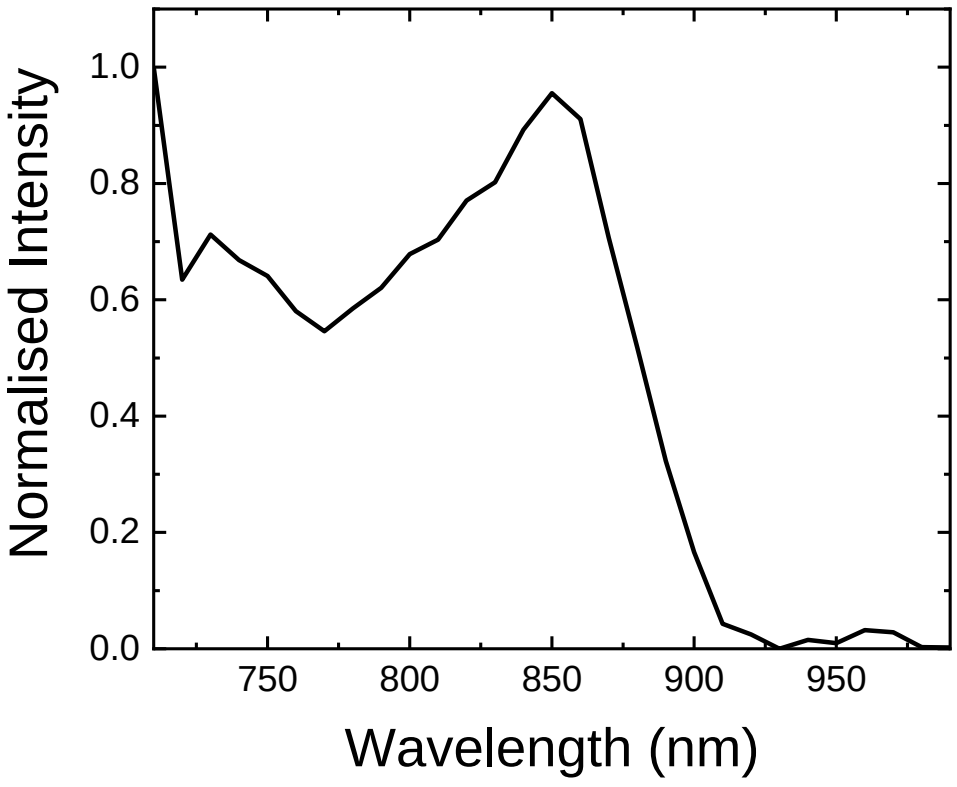

Figure 84: Two-photon excitation spectrum of MitoTracker Orange.
The spectrum was acquired by imaging adherent SYSY-5Y cells labelled with 500 nm MitoTracker Orange at 10 nm steps of excitation wavelength, emission was collected at 610 nm ± 10nm. Peak excitation was observed at 850 nm.

7.3.7 Verification of MUSICAL performance under widefield illumination

MUSICAL has been reported being used for datasets under widefield illumination. Before attempting to apply and characterise MUSICAL for multiphoton and label-free datasets it was important to verify the capabilities of the algorithm when using the same dyes and cell lines as would be used for multiphoton imaging. Optimising the temporal resolution of FSRM methods is highly important as sample movements can generate artefacts and mar the validity of the SR data. Mitochondria were observed to be highly dynamic in SHSY-5Y cells stained with Mitotracker Orange (Figure 85).

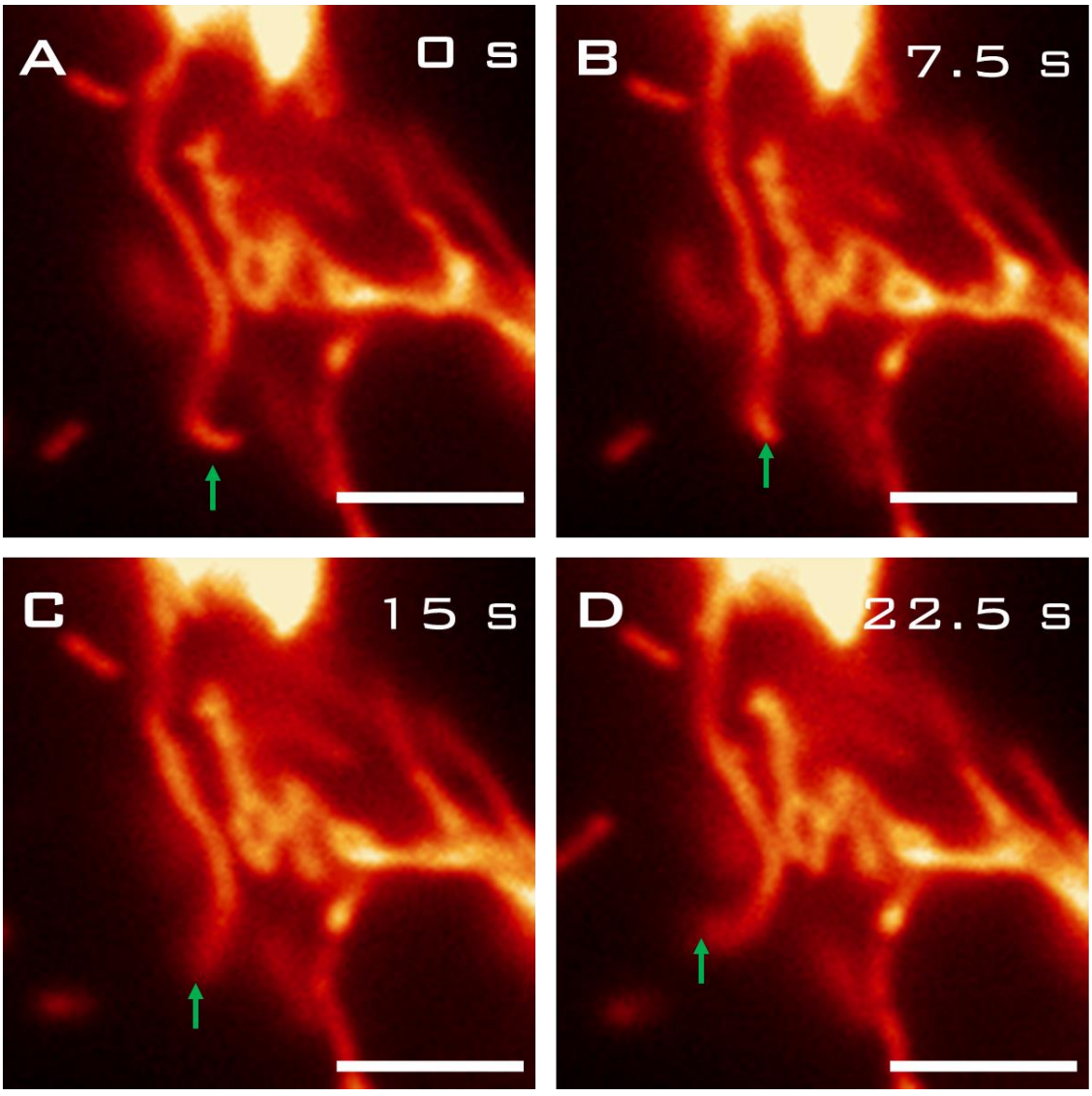

Figure 85: Mitochondria are highly mobile.
A time stack of mitochondria labelled with 500 nM mitoTracker Orange acquired using the DeltaVision microscope using a 60x/1.42 NA objective with an effective pixel size of 107.5 nm. The exposure time was set to 150 ms and the LED power to 10%. **A-D** show the frames 1, 50, 100 and 150 respectively. These correspond to 0, 7.5 s, 15 s and 22.5 s after the start of the stack acquisition. Mitochondria can be seen to move within the field FOV laterally and into/out of the plane of focus (green arrows). The image has been cropped to aid visualisation. Scale Bar 5 µm.

Mitochondria were observed to move laterally within the FOV and into/out of the plane of focus (Figure 85 green arrows). These movements occurred over the time scale of MUSICAL stack acquisition (a 7.5 s window) and therefore would affect MUSICAL reconstruction. These large motions can be identified by the pre-processing step in Figure 70 however, as these motions occurred over much of the data, this would result in a significant amount of excluded data. Thus, it was important to establish the minimum number of frames required by MUSICAL and the relationship between input frame number and achieved resolution. To do this a temporal image-stack of MitoTracker Orange-labelled adherent cells was acquired (Figure 86).

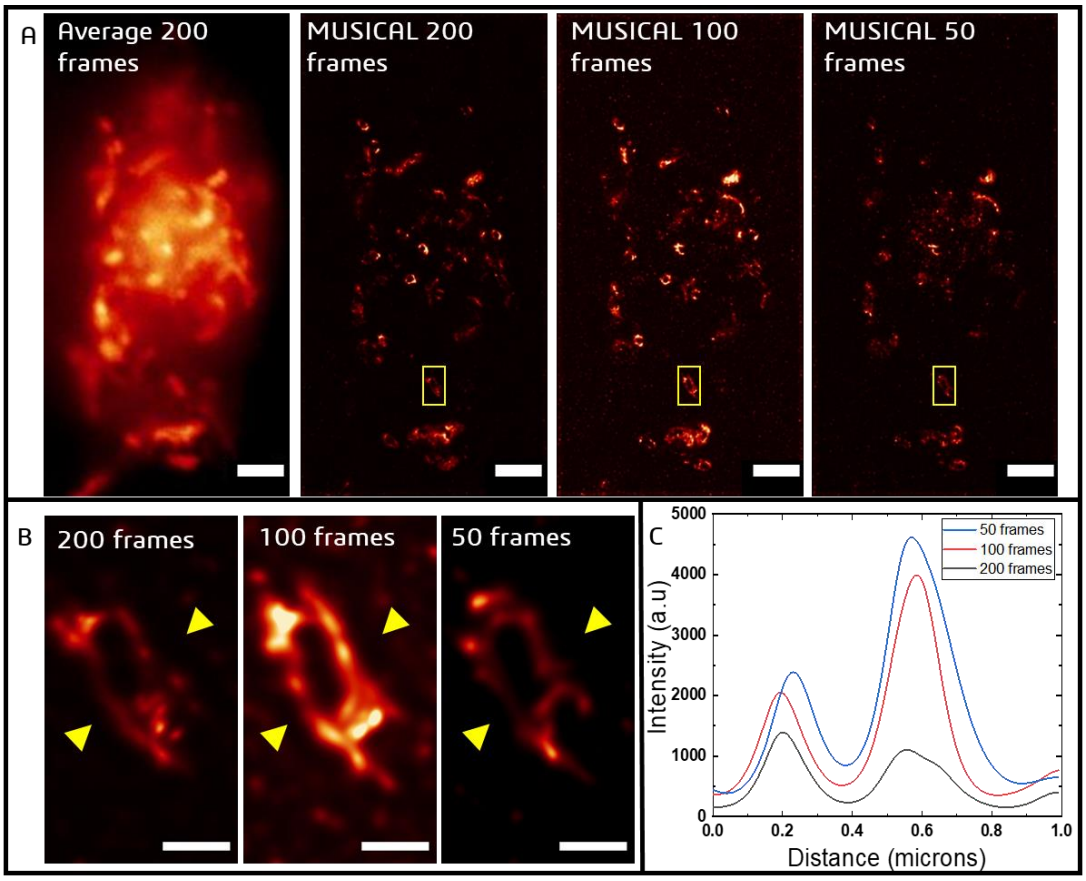

Figure 86: Verification of MUSICAL performance under widefield illumination for imaging mitochondria.
(**A**) Average intensity projection of a 200 frame image stack of single cell acquired with 25 ms exposure times. Left to right show the MUSICAL outputs for the first 200, 100 and 50 frames. Scale bars 3 µm. (**B**) Zoomed in view of the yellow boxed regions in A high lighting a single mitochondrion, MUSICAL processing appears to resolve the mitochondrial membrane. Scale bars 500 nm. (**C**) Resolution quantification by line spread function. Intensity plots of a line taken between the yellow arrows in B for 200, 100 and 50 frames. Gaussian fitting of the two peaks gave FWHM of 130/185 nm, 156/133 nm, and 135/205 nm for 200, 100 and 50 frames respectively. Images were acquired using the DeltaVision microscope using a 60x/1.42 NA objective with an effective pixel size of 107.5 nm.

Figure 86**A** shows an average projection of 200 frames of a single labelled cell, the image shows many mitochondria with a high density of mitochondria surrounding the nucleus. MUSICAL

processing was performed on the first 200, 100 and 50 frames of the image stack, the 3 different stack lengths gave qualitatively similar results. MUSICAL processing appears to resolve the mitochondrial membranes that were unresolvable under normal imaging. Resolution of this membrane is in agreement with previously published results for MUSICAL (Agarwal and Macháň, 2016), and with known information that MitoTracker is localised to the mitochondrial inner membrane (Shim *et al.*, 2012; Huang *et al.*, 2018),however, there is data contradicting this localisation (Misaad and Bewersdorf 2020) leading to cautious interpretation of these results. Some internal structure of the mitochondria could also be observed however consistent resolution of mitochondrial cristae was not achieved, this may be because the cristae structure is highly convoluted, and the separations of the folds are beyond the resolving power of the system even with MUSICAL processing. The resolved internal structures may be either lager cristae where more dye has accumulated, or they are points about to undergo mitochondrial fission and the membranes are closing off between two daughter mitochondria. However, as MUSICAL uses fluctuations to perform super-resolution image reconstruction it is possible that the outer membrane/edges of the mitochondria are being resolved is due to movements of this membrane being classified as signal fluctuations. The pre-processing pipeline developed in section 7.3.2 is able to detect lateral movements within the focal volume if they are greater than the diffraction-limit. However, if the movements are smaller than the diffraction-limit they will not be identified but can still be extracted by MUSICAL. Similarly, if the movements occur axially, such that the imaged structure becomes more/ less in focus over the course of the time-stack acquisition, they will not be highlighted by the pre-processing pipeline. These considerations present a potential limitation of MUSCIAL in mobile samples such as living samples, particularly when being used with a widefield imaging system which has greater out of focus contributions than other imaging modalities such as confocal microscopy or lightsheet.

To quantitatively evaluate the effect of decreasing frame number, intensity plots were taken of the same mitochondrion where the two membranes could be clearly resolved (Figure 86**B**). Gaussian fitting of the two peaks revealed FWHMs of 130 nm and 185 nm for the 1st and 2nd peaks respectively for the 200 frames image. Reducing the number of processed images to 100 yielded peak widths of 156 nm and 133 nm, reducing it further to 50 frames gave peak widths of 135 nm and 205 nm respectively (Figure 86**C**). The width of the first peak stayed more consistent with decreasing frame number whilst the width of the second peak was more variable and did not show a trend with relation to frame number. It has been shown previously that MUSICAL is capable of achieving similar resolution with either 10,000 or 49 frames (Agarwal and Macháň, 2016). The variation in the observed resolution within the range of frame numbers tested may be as a result of which frames contain suitable fluctuations for MUSICAL processing. It is possible that

the strongest fluctuations that would result in best MUSICAL performance are located within frames 51-200 of the stack. Therefore, because the 50 frame MUSICAL image was generated using the first 50 frames of the stack it has a worse resolution than the 100 and 200 frame reconstructions. This could be probed by investigating a sliding window of 50 frames i.e. frames 1-50, 2-51, 3-52 etc. and identify in which range the performance deteriorates. However, 50 frames performed similarly to 200 frames indicating that this number as a minimum frame limit is sufficient. Furthermore, a lower number of frames is advantageous as it also reduces light dose on the sample. Therefore, for further MUSICAL acquisitions 50 frames were acquired.

7.3.8 Artefacts of Laser Scanning are Enhanced by MUSICAL

As point scanning is the most common implementation of multiphoton imaging it was important to establish whether MUSICAL could improve the resolution of images acquired using such a system. Images were acquired using the multiphoton imaging system detailed in section 3.3 equipped with a 63x/0.9NA objective. A pixel dwell time of 8 µs was needed for enough signal to noise, to keep a fast frame rate, image size was reduced to 256 pixels^2 and the size of the scan field was reduced to 45 µ x 45 µm to maintain Nyquist sampling. With these optimisations, the frame rate was 1.9 Hz, approximately 21 times slower than the 40 Hz frame rate of the widefield system, resulting in a 26 s total acquisition time for a 50 frame MUSICAL stack. Analysis of the data stack revealed regions that contained suitable fluctuations for MUSICAL processing and did not show significant movement over the course of the acquisition (26 s). For this first pass attempt at using MUSICAL for multiphoton point-scanning microscopy the PSF computed by MUSICAL uses an Airy disc calculated using the Rayleigh criterion. For 610 nm emission this gives a FWHM of 413 nm, the lateral FWHM of the TPEF PSF is 358 nm. It has been shown that if the estimated PSF is wider than the true PSF of the imaging system the MUSICAL image appears sharper and more punctate (Agarwal and Macháň, 2016). This is a potential source of the artefacts observed in Figure 87 D/F. Close inspection of the average projection of the image stack (Figure 87**A**) revealed a “zigzag” artefact corresponding to the fast axis scan (Figure 87**C/E**). This artifact remained even after careful correction of the scan-phase when bi-directional scanning. It is possible that the issue could have been removed with uni-directional scanning, however this would have increased the acquisition time by approximately 2-fold increasing the probability of other sample- motion related issues. It is also possible that the artifact is a result of the zoomed in FOV and resultant altered angular deflection of the scan mirrors. MUSICAL processing of the image stack gave similar results to the widefield case, highlighting the outer edges of the labelled mitochondria (Figure 87**D/F**) however, it also made the scan artefact more pronounced. The “comet-tail” scan artefact appears to be identified as a fluctuation by MUSICAL and results in the

generation of localised points of intensity in the MUSICAL image (Figure 87**F** Blue arrows). The scan rate could be reduced to remove the scan artefact however, this would result in significantly longer acquisition times that are not compatible with fluctuations-based imaging in live cells due to potential movement of the sample. It was concluded that without significant alterations to the imaging setup such as the introduction of a resonant scanner (to remove scan artefacts at high scan rates), a point scanning system was unsuitable for fluctuations- based super-resolution. All further super-resolution experiments were therefore performed on a light-sheet imaging system.

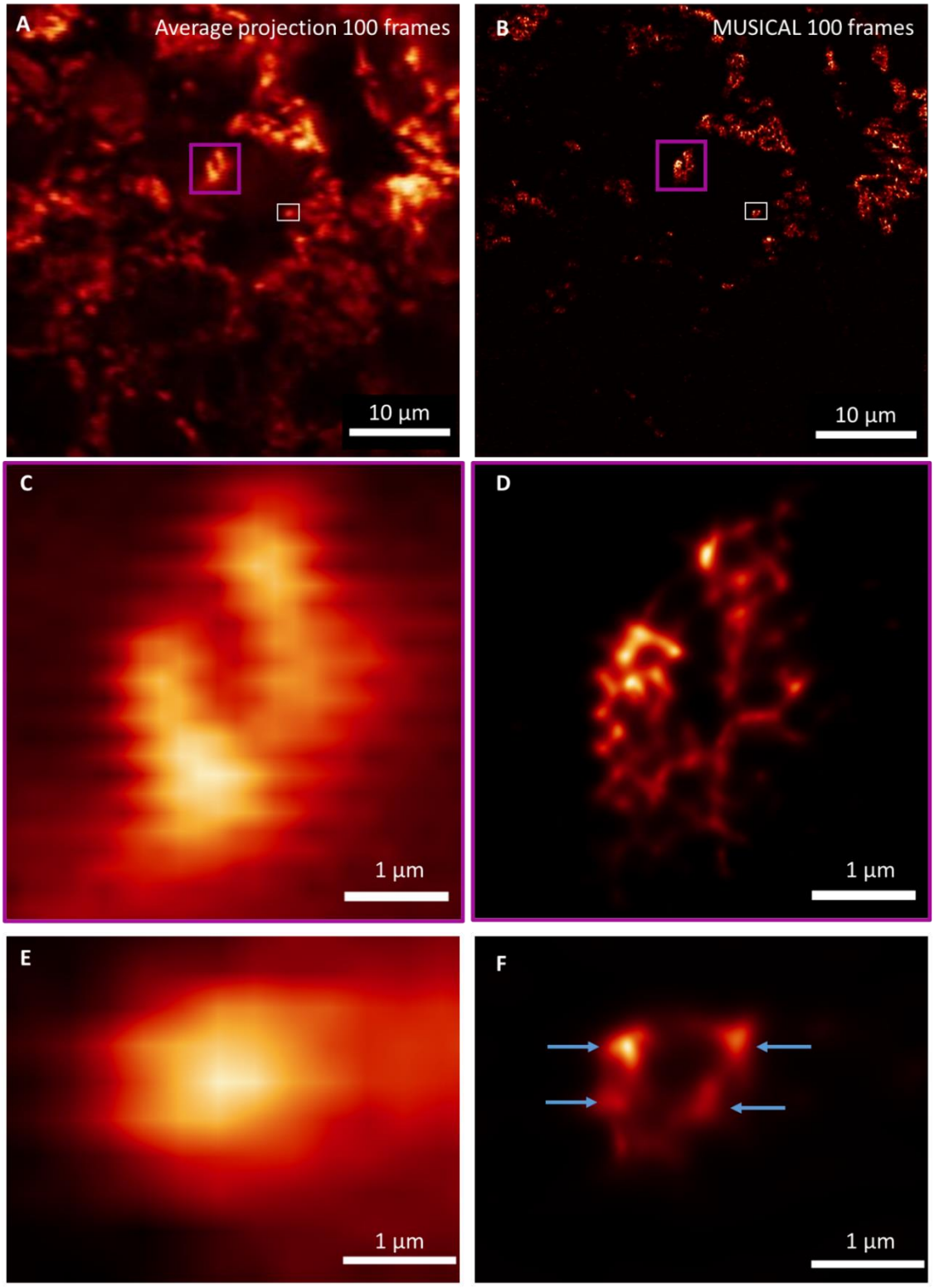

Figure 87: Scanning artefacts are exaggerated by MUSICAL
(**A**) 50 frame average diffraction-limited and (**B**) corresponding MUSICAL image of adherent SHSY-5Y cells labelled with 500 nm mitoTracker Orange, imaged using TPEF (850 nm excitation, 610 nm emission). σ_0 = -1.0, α = 4 .**C/D** Zoomed in view of the region highlighted in magenta in A/B respectively. The diffraction-limited image has a "zig-zag" scan artefact that is claerest at the edges of structures which prominent in the MUSICAL images. **E/F** Zoomed in view of the region highlighted in white in **A/B** respectively**.** The MUSICAL images suggest that it is possible to resolve mitochondrial membrane structure but contains artefacts due to the laser scanning (Blue arrows), that are emphasised by MUSICAL. C/E have been displayed on a resized pixel grid 20 x larger than the raw images to match the pixel resizing of MUSICAL.

7.3.9 Autofluorescence Lightsheet Acquisition Parameters

Autofluorescence (AF) lightsheet (LS) imaging was performed using 100 ms/frame exposure with ~130 mW at the sample. Shorter exposure times resulted in insufficient contrast for MUSICAL processing of images. The power was maximised for maximum SNR, power could not be increased further due to formation of bubbles in the immersion medium and agarose. Two-photon excited autofluorescence of NADH/FAD was excited at 740 nm.

7.3.10 Solution Fluorescence Spectra

Spectra of FAD and NADH were acquired at pH 7.2 in PBS. Spectra were acquired using high gain and 5 nm excitation and emission slit widths. Spectrometer details can be found in section 3.10.

7.3.11 Measurement of Lightsheet Point Spread Functions

PSFs were calculated from a 200 frame image stack of 110 nm fluorescent beads (Invitrogen, TetraSpeck, T7279), using 100 ms exposure. Single-photon excitation was performed with 561 nm and two-photon excitation was performed at 850 nm, emission was collected at 610 nm. The NanoJ SQUIRREL plugin for Fiji (Culley *et al.*, 2018) was used to identify and extract diffraction-limited, 2D PSFs from the average projection of a 200 frame image stack. The same detected beads were then individually extracted as ROIs using a home-written Fiji macro and MUSICAL was performed on each stack. An intensity profile was taken across each MUSICAL PSF and fitted with a Gaussian using the MATLAB “gauss1” function.

7.3.12 Lightsheet Thickness and Implications for MUSICAL

The 3D resolution of a lightsheet microscope can be characterised by the 3D point spread function (PSF), which is a convolution of the detection PSF defined by the detection objective and the excitation PSF defined by the excitation objective (Theer, Dragneva and Knop, 2016). Provided the centre of the axial extent of the detection PSF lies within the lightsheet plane, the lateral resolution is defined by the detection objective alone. The axial resolution is defined by the thickness of the lightsheet and the depth of focus (DOF) of the detection objective. If the lightsheet is thinner than the DOF then it defines the axial resolution (Remacha *et al.*, 2020). If the lightsheet is thicker than the DOF of the detection objective, then the sheet is truncated axially by the detection objective (Hosny *et al.*, 2020). For the planar Airy lightsheet used in this thesis (section 3.6.1) the beam that forms the lightsheet has multiple lobes, the main lobe forms the sheet and is at the centre of the DOF of the detection objective, secondary lobes are oriented above and below this plane. The depth of field of the detection objective limits the range of

efficient signal collection in the axial direction (due to the detection probability) such that minimal signal is collected from the secondary lobes (Hosny *et al.*, 2020). Furthermore, due to the quadratic power dependence of signal generation in two-photon-excited fluorescence (TPEF), the signal generated by secondary lobes becomes negligible (Hanrahan *et al.*, 2020). The lightsheet used for these experiments was simulated in MATLAB to allow observation of the XZ plane and measurement of the lightsheet thickness (Hosny *et al.*, 2020). The thickness of the sheet was calculated to be approximately 1.5 µm -2.5 µm dependant on the wavelength of excitation and whether one-photon or two-photon excitation was used. The optical sectioning provided by the lightsheet makes it superior to an epi-illumination widefield system for imaging in 3D samples, as it decreases out-of-focus contributions. However, as the lightsheet still has a thickness this has implications for MUSICAL. MUSICAL uses a projection of a 2D PSF during generation of super-resolution images. This assumption is true of synthetic data and close for data acquired in a total internal reflection fluorescence (TIRF) geometry. However, when the PSF has a larger axial extent there is the potential for out-of-focus contributions to contain fluctuations and contribute to artefacts in the MUSICAL reconstructions. These considerations must be kept in mind when interpreting MUSICAL data presented in this thesis. The 3D nature of the PSF on the lightsheet microscope will need to be taken into account in the MUSICAL algorithm in future work for a more accurate interpretation of resolutions achieved using the proposed method.

7.4 Results

7.4.1 Multiphoton Excitation Improves the Signal-to-Background Ratio in 3D samples

The lightsheet imaging geometry minimises the out-of-focus excitation, decreasing the background in images of 3D, thick samples compared to traditional widefield illumination. This is further enhanced by use of two-photon excitation and the quadratic dependence on excitation power ensures that excitation only occurs in the beam focus, improving the axial resolution and decreasing background. **Error! Reference source not found.** shows a 3D spheroid labelled for mitochondria, imaged using one-photon excited fluorescence (OPEF) and two-photon-excited fluorescence (TPEF) in a lightsheet configuration. The displayed XY slice was taken at 35 µm from the top surface of the cell spheroid; at this depth the excitation light must penetrate ~65 µm through the sample (left to right in images) due to the orthogonal light-sheet geometry. Comparison of the signal to background ratio (SBR) shows a 1.75 fold improvement when using TPEF compared to OPEF. The SBR was calculated as the mean signal divided by the mean background for an average of 3 ROIs. The same ROIs where used for both OPEF and TPEF. The yellow arrows in **Error! Reference source not found.A/B** indicate the direction of beam propagation when forming the lightsheet. The decreased scattering of the 850 nm two-photon excitation compared to the 561 nm one-photon excitation improves penetration to the shadow (right) hand side of the spheroid. This improves contrast across the image and facilitates imaging of larger and more highly scattering samples such as tissues and whole organisms. This was important for acquiring suitable data for MUSICAL processing where the SBR heavily influences the ability to detect suitable fluctuations for SR.

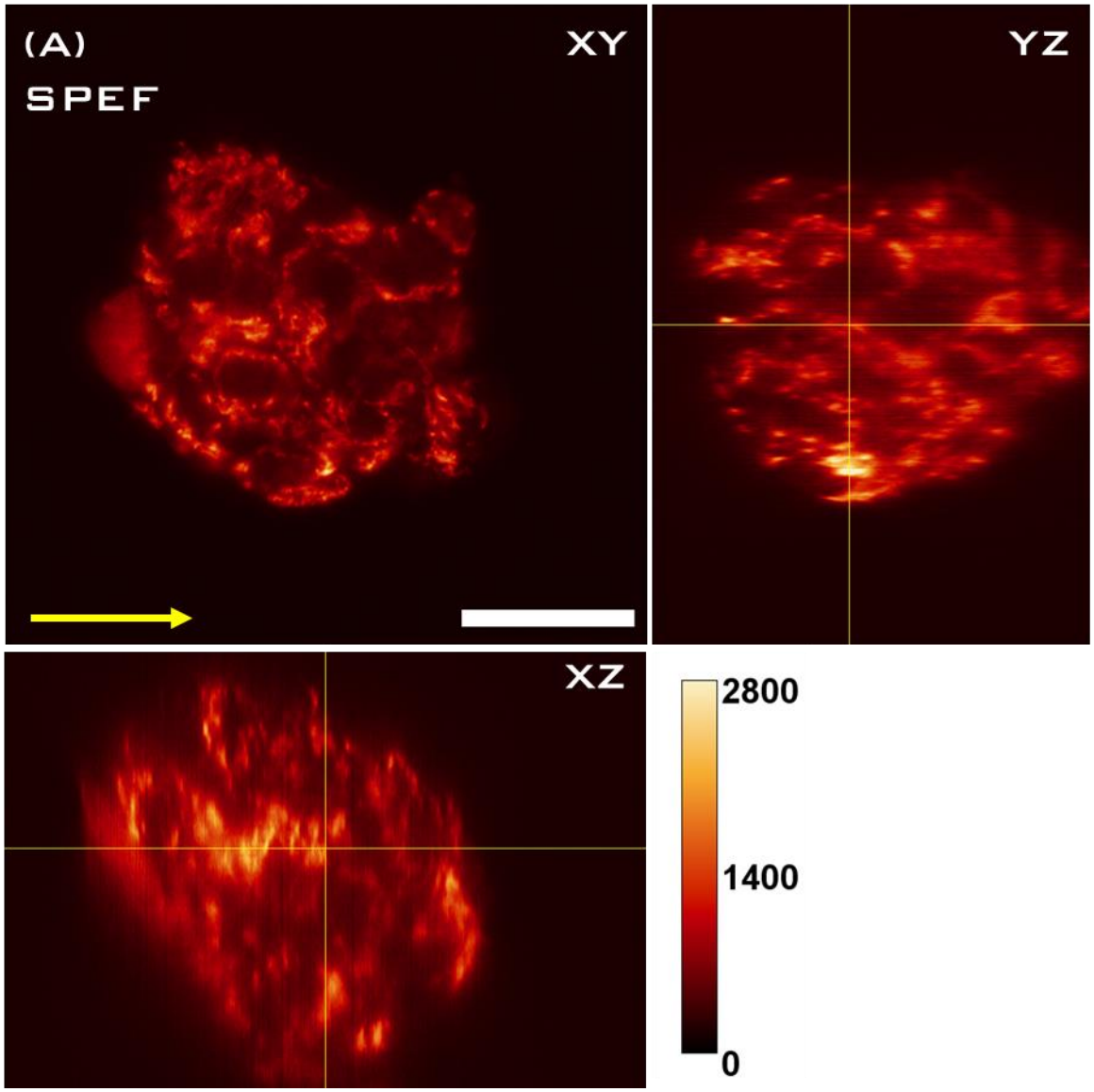
(A)
SPEF
XY
YZ
XZ
2800
1400
0

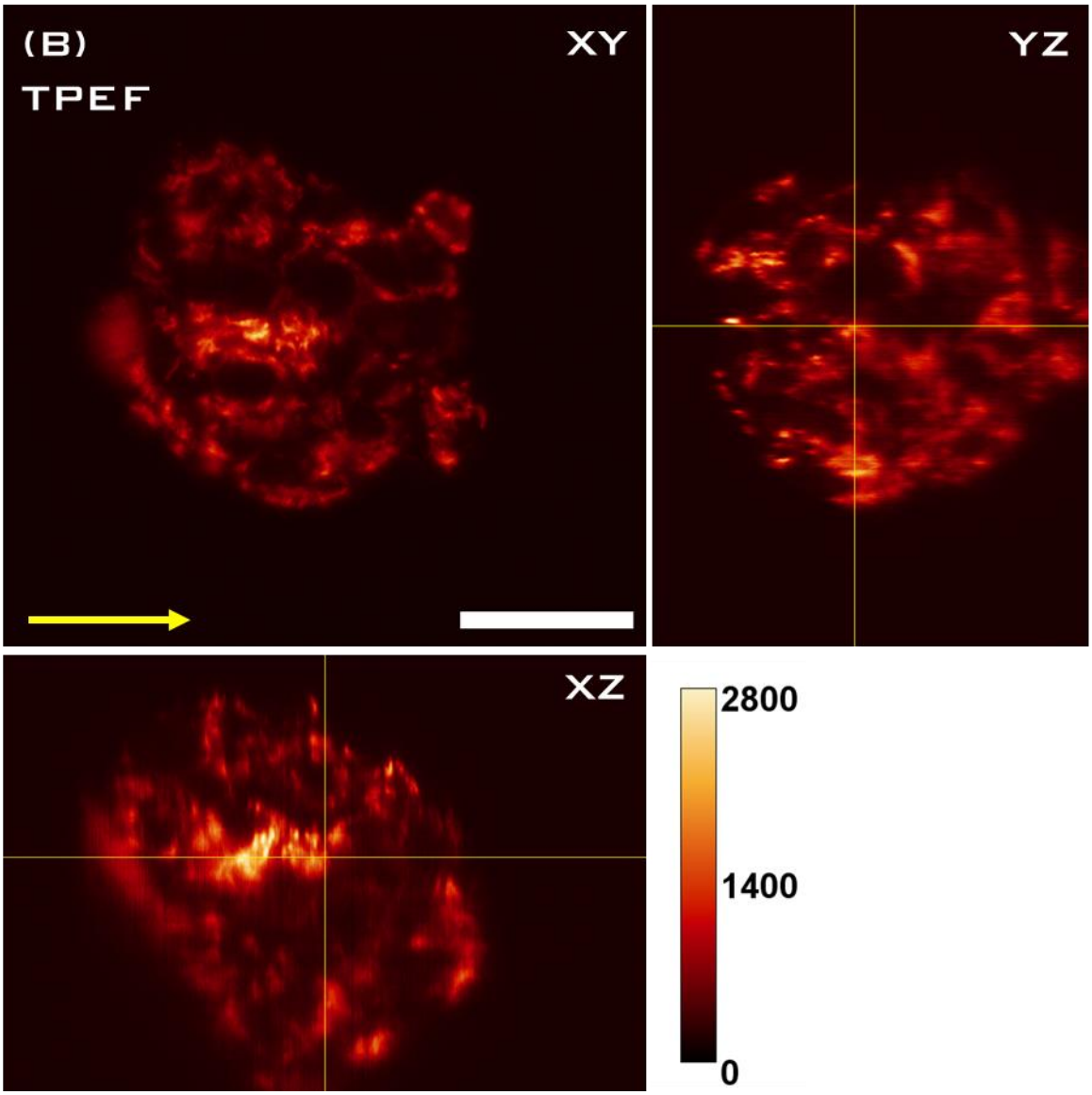

Figure 88: Multiphoton lightsheet decreases background.
(**A**)OPEF image of a cell spheroid labelled with 500 nmMitoTracker Orange,(**B**) the same spheroid imaged using TPEF. Intensity scaling is identical for both images, TPEF improves the SBR at depth in 3D samples compared to OPEF. Yellow arrow indicates direction of light-sheet propagation. Scale bar 30 µm. Images were acquired with 100 ms exposure time.

7.4.2 Quantitative Evaluation of Resolution Improvement Using MUSICAL

To quantify the resolution improvement achieved by MUSICAL on the lightsheet microscope a 200 frame image stack was acquired of 110 nm diameter fluorescent beads, suspended in 0.5% agarose using two-photon and one-photon excitation. The FWHM of the unprocessed PSFs were 477 nm and 486 nm for one- and two-photon respectively (Figure 89**A**).

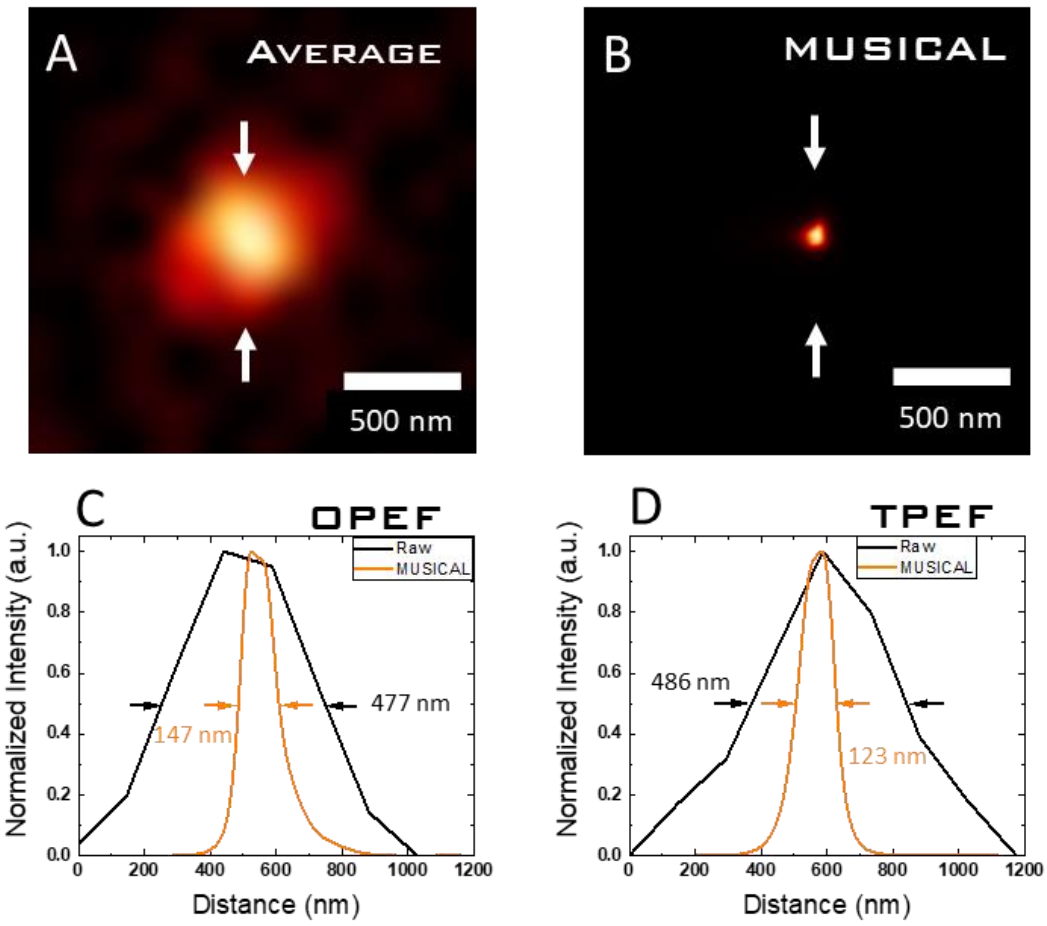

Figure 89: Quantification of resolution improvement.

(A) Diffraction-limited average of 200 frames of a single 110 nm diameter bead. The image has been displayed in a 20x larger pixel grid (40960^2 pix) to match the pixel size of the MUSICAL image. (**B**) The same bead after MUSICAL processing (α=4, σ=-0.4). Intensity plots taken between the example white arrows in A/C are presented for OPEF (**C**) and TPEF (**D**). intensity plots were measured from non-resized images for Raw measurements. MUSICAL narrows the apparent FWHM of the PSF from 477 nm to 147 nm, a 3.2 times improvement and from 486 nm to 123 nm a 4 times improvement from OPEF an TPEF respectively.

As the lateral resolution of a lightsheet microscope is affected only by the PSF of the detection objective it was decided that the same parameters (610 nm emission, 0.8 NA objective) for the PSF inputted to MUSICAL would be used for both OPEF and TPEF. This is supported by the small difference seen in the widths of the unprocessed PSFs for OPEF and TPEF. The mean MUSICAL PSFs were 123 nm ± 23 nm for TPEF and 147± 32 nm for OPEF, calculated over 42 beads. This

represents 4 times and 3.2 times improvement for TPEF and OPEF, respectively. The improvement in lateral resolution afforded by MUSICAL for TPEF is greater than that for OPEF. This may be because of the decreased thickness of the two-photon light-sheet excitation due to the quadratic dependence of two-photon excitation on excitation power. This would result in the true imaging PSF of TPEF, being a closer approximation to the ideal 2D PSF (used by MUSCIAL) that the OPEF point spread function. This would improve the quality of MUSICAL reconstruction.

The minimum number of frames required by MUSICAL is defined by the requirement for a higher number of receivers (pixels) and measurements (frames) than the number of fluorescent emitters (Agarwal and Macháň, 2016). Because the sliding window of the MUSICAL algorithm is set to 7 pixels by 7 pixels, to adequately sample the PSF, the minimum number of frames is set to 49 frames. To confirm whether this minimum frame limit could still improve resolution the MUSICAL PSF was calculated for the first 200, first 100 and first 50 frames from the same image stack. Reducing the number of frames did not appear to significantly affect the achieved resolution for either one- or two-photon excitation (Table 7). Having established that reducing the frame number to the algorithmically-allowed minimum did not significantly affect the achieved spatial resolution using standard bead samples; the biological applicability of MUSICAL was tested using well known cellular structures.

No of frames	OPEF	TPEF
1-50	140±50	125±32
1-100	143±54	121±25
1-200	147±32	123±28

Table 7: Effect of frames number on PSF width determined by MUSICAL.

7.4.3 Lightsheet Imaging Shows Labelled Mitochondria in a Large Spheroid Sample

As previously observed under widefield illumination, mitochondria are highly dynamic; they can move and/or change shape within the time scale of a MUSICAL stack acquisition(Figure 85). Due to this it was important to identify the minimum exposure time needed to achieve suitable contrast and fluctuations for MUSICAL processing. Stacks of 50 images were acquired using 30 ms, 60 ms and 100 ms exposures for one-photon and two-photon excitation. Figure 90 shows examples for OPEF and TPEF; in both cases MUSICAL revealed the outer edges of the mitochondria as observed in widefield imaging (Figure 90**F** Blue arrows). Similarly to widefield imaging the mitochondrial cristae/matrix was not resolved as it has been by other super-resolution imaging of MitoTracker dyes (Shim *et al.*, 2012), however, it is noted that MitoTracker Orange has also been reported to localise to the mitochondrial matrix (M'Saad and Bewersdorf, 2020). Therefore, the structures highlighted by the white and blue arrows in Figure 90 E/F and measured in G/H may not be true membrane structure but instead generated due to small motions not detected in the pre-processing of the stack. The fluctuations identified by MUSCICAL to resolve these structures may also be due to axial motion (with respect to the detection objective) of the mitochondria within the thickness of the lightsheet. Lightsheet imaging is advantageous over widefield imaging for MUSICAL as it allows imaging of an optical section within a 3D sample. However, the lightsheet still has a thickness (1.7 µm) and therefore it is possible for mobile samples to move axially within this thickness creating fluctuations in intensity. Such fluctuations would be identified by MUSICAL and used to resolve the edges of the mitochondria. This was not observed when processing images of fluorescent beads (Figure 89), the fluorescent beads did not move during the acquisition and therefore only intensity fluctuations due to fluorophore bleaching/blinking contribute to the MUSICAL reconstruction. Figure 90 D/F green arrows shows a point where a narrowing of the PSF, like that observed with fluorescent beads, is seen. This may be the "tip" of a mitochondrion or a small, spherical mitochondrion that has become better resolved as a result of MUSICAL. The similarity to the result observed with fluorescent beads suggests that this structure did not move during the acquisition of the raw stack. Most of the mitochondria observed in the raw image stacks used for this MUSICAL processing appeared to be round rather than elongated, this may be due to many of the mitochondria being orientated perpendicular to the lightsheet plane however this is unlikely. It is more probable that due to the lack of temperature control on the lightsheet microscope the cells in the spheroid were becoming temperature shocked/stressed, resulting in significant alterations to the mitochondrial network, potentially in preparation for apoptosis (Youle and Van Der Bliek, 2012).

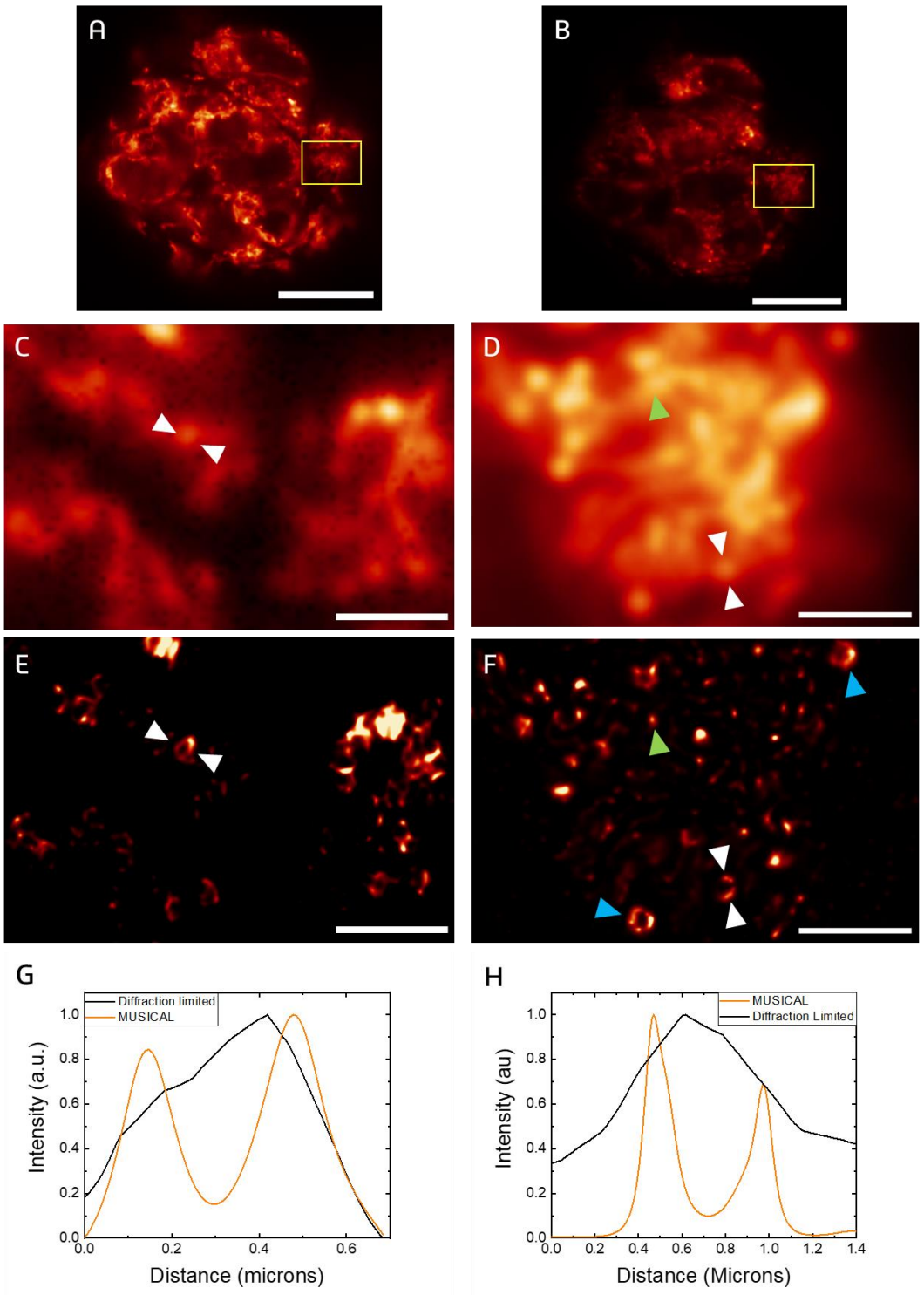

Figure 90: Mitochondrial SR in thick samples imaged by lightsheet
(**A**) OPEF and (**B**) TPEF images of mitoTracker Orange labelled mitochondria in a 3D cell spheroid sample, imaged using lightsheet. **C/D** zoomed images of the yellow boxed regions in A/B respectively; a complex network of mitochondria can be observed, but closely-spaced mitochondria cannot be resolved, and no sub-structure is resolved. **E/F** the MUSICAL processed images for C/D respectively, the edges of the mitochondria become resolved by MUSICAL (arrow heads) and closely neighbouring mitochondria can be distinguished. (**G**) intensity plots between the white arrow heads in C/E (black and orange lines respectively). (**H**) intensity plots between the white arrow heads in D/F (black and orange lines respectively).MUSICAL appears to resolve the mitochondrial membrane where it could not be resolved in the raw images. Some mitochondria appeared to be resolved to a smaller point (green arrows D/F) rather than a membrane-like structure. Scale bars A/B 20 µm, C-F 3 µm. MUSICAL parameters: E σ=-0.5 α = 4, F σ=-1.0 α = 4.

The effect of exposure time on MUSICAL reconstruction was evaluated by analysing the PSF of representative mitochondria for each MUSICAL image. Figure 90**E/F** (white arrows) show example locations where measurements were made. G/H show MUSICAL was able to produce similar results to those observed under widefield illumination (Figure 86). The results (summarised in Table 8) showed that lowering the exposure time did not affect the mean width observed for OPEF whereas for TPEF decreasing the exposure time decreased the achieved resolution of MUSICAL. Furthermore, 100 ms exposures were required for sufficient signal collection to detect NADH/FAD autofluorescence signals (section 7.3.9.).

Table 8: Average line spread functions measured for different exposure times and excitation conditions of MitoTracker orange-labelled cell spheroids. 3 representative mitochondria yielding 6 analysed peaks for each case

	30 ms	60 ms	100 ms
OPEF	187±39 nm	190±55 nm	193±68 nm
TPEF	235±76 nm	180±14 nm	141±24 nm

Due to the uncertainty as to the nature of the structures in mitochondria that are resolved by MUSICAL and whether the signal fluctuations were due to bleaching/blinking or microscopic movements of the sample within the thickness of the lightsheet, definitive conclusions on resolution cannot be made from these measurements. However, some suggestions as to impact of exposure time with respect to contrast, observed fluctuations and their potential impact on MUSICAL can be made. When comparing raw time-stacks acquired using OPEF- and TPEF-lightsheet a sharper decrease in contrast is observed when lowering the TPEF exposure time vs OPEF. As a more efficient excitation process, even at shorter exposures, OPEF generates sufficient contrast such that the performance of MUSICAL is not affected. Under two-photon excitation the contrast drops sharply with decreased exposure time, and thus, affects the performance of MUSICAL. Changing the exposure time may also have an effect by altering the detected fluctuations. At shorter exposure times, the chances of an emitter displaying a different intensity in different frames is increased, whereas with longer exposure times the chances of fluorophore intensity-fluctuations being averaged out within the exposure increases. During the pre-processing of image stacks, an image is generated when the pixel intensity corresponds to the standard deviation (SD) of the signal recorded at that pixel through the time-stack, divided by the mean signal (average) recorded at that pixel through the time-stack (Figure 69D). This image shows the strength of the intensity fluctuations at a pixel as a proportion of the average brightness of that pixel. By analysing the SD/Average images, it was observed that for OPEF the strongest fluctuations localised to mitochondria (Figure 91 top row). As the exposure time is decreased the SD/average in the background increased. This same effect can be observed in the

TPEF images (Figure 91 bottom row), however, for 30 ms and 60 ms exposures the difference between signal and background is much less whereas at 100 ms it is more like that of OPEF. When there is only a small difference in the fluctuations observed in the signal versus those in the background it is harder to separate the two via thresholding in MUSICAL. This potentially results in selection of a σ_0 value that removes structures associated with weaker fluctuations.

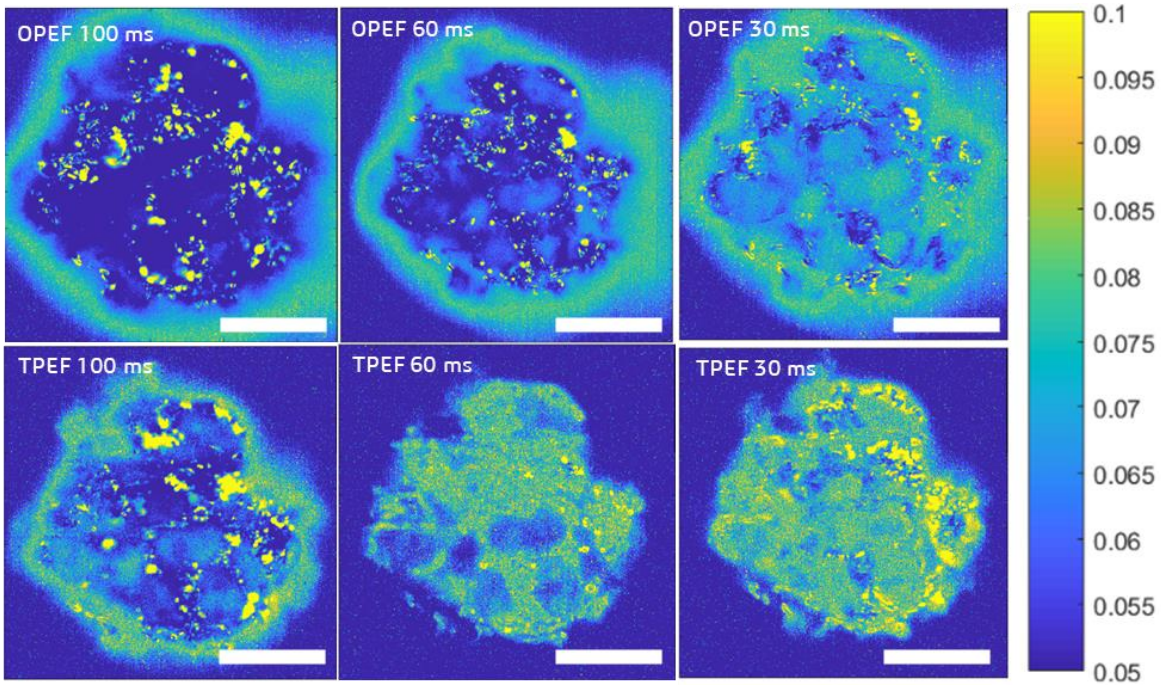

Figure 91: The effect of exposure time on fluctuations.
SD/Average images for OPEF and TPEF at different exposure times. Decreasing the exposure time lowers the SNR and makes distinction of fluctuations in signal and background more difficult. This effect is more pronounced in TPEF as the shorter exposure times are closer to a minimum exposure threshold to achieve suitable SNR for MUSICAL. Scale bar 20 µm.

As the SD/average image is not able to determine the source of the intensity fluctuation it is possible that the observed fluctuations are due to movements of the emitter that are below the size of the diffraction limit or occur axially (with respect to the detection objective) within the thickness of the lightsheet. As discussed in section 7.3.2, the movement of mitochondria is much slower than the random movement of diffusing dyes or inherent fluctuations in the intensity from the fluorescence process. Therefore, the effect of exposure time on the ability to detect fluctuations becomes more complex in the case of the diffusion scenario. Ideally the exposure time should be selected such that fluctuations can be detected by different frames. This depends on the timescale of the fluctuations that are being detected, which may be structure/emitter dependent. The exposure time must also be selected such that sufficient contrast is achieved in the raw images. Thus, the selection of the optimal exposure time for MUSICAL-based imaging will be dependent on many factors including sample dynamics, signal strength, signal fluctuation kinetics, detector sensitivity and available laser power. These factors mean that, for each new sample a range of exposure times should be explored with respect to the achieved signal-to-noise

ratio and the detected fluctuations. As the core aim of the PhD project was to develop label-free super-resolution techniques and previous lightsheet imaging had been performed on mitochondria, the autofluorophores nicotinamide adenine dinucleotide (NADH) and flavin adenine dinucleotide (FAD) were selected to be tested for MUSICAL imaging.

7.4.4 Autofluorescence Imaging of Mitochondria

The impact of cell metabolic status, stress and general health on the structure and organisation of mitochondria is well established, it can provide insight into the effect of drug treatments, environmental alterations and genetic modifications. Thus far the microscopic observation of mitochondria has been hampered by one of two limitations. On one hand, fluorescent labelling is used, allowing super-resolution imaging with established methods like STED or SMLM. However, many dyes dissociate from the mitochondrial membrane as it depolarises under stress and transfection can involve complex sample preparation. On the other hand, label-free imaging using autofluorescence avoids the issues with labelled imaging, but currently only allows for diffraction-limited resolution. Lightsheet-MUSICAL imaging presents itself as a way of achieving super-resolution, label-free imaging of mitochondrial dynamics.

To guide TPEF imaging of autofluorescent NADH and FAD, the single photon excitation and emission spectra of both compounds in solution were acquired. Figure 92 shows that both fluorophores are excited in the UV region. NADH has a single peak with maximum excitation at 340 nm whereas FAD has a double peaked excitation spectrum with peak excitations at 370 nm and 450 nm. The 370 nm peak of FAD shows significant overlap with the 340 nm peak of NADH. NADH emission peaks at ~460 nm with a long tail into green/orange wavelengths, whereas FAD emission peaks at ~530 nm, with emission tailing into the red wavelengths.

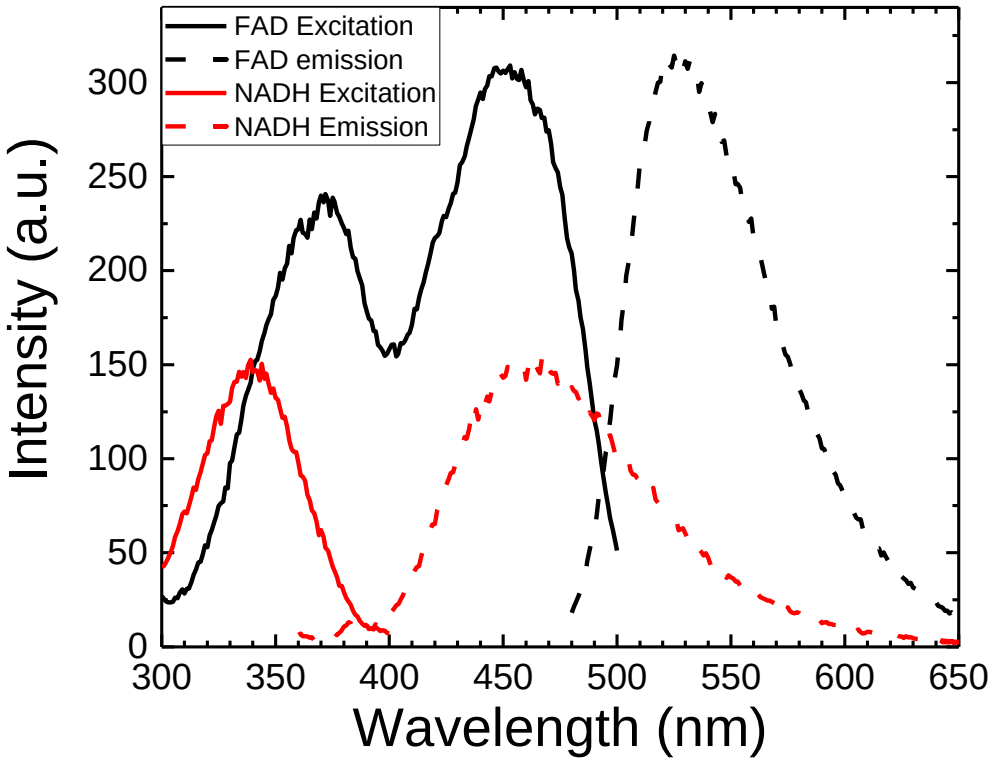

Figure 92: Excitation/ emission spectra of FAD and NADH.
NADH has a single peak with maximum excitation at 340 nm whereas FAD has a double-peaked excitation spectrum with peak excitations at 370 nm and 450 nm. NADH emission peaks at ~460 nm and FAD emission peaks at ~530 nm.

It has been shown that it is possible to selectively-image the distribution of either component by appropriate selection of excitation and emission combinations (Xu *et al.*, 2010). It is also possible to simultaneously acquire combined NADH and FAD signals by exciting at ~370 nm and collecting broad fluorescence from ~430 nm – 630 nm. This can be advantageous in situations of low signal or where excitation light dose should be minimised such as long term, live cell imaging. From the one-photon spectra it can be inferred that the two-photon excitation wavelengths should be at ~ 720 nm and 900 nm to image NADH and FAD, respectively. However, in practice when measured using the multiphoton imaging system (sectionr 3.11) it was found that maximum signals were observed on two-photon excitation at 740 nm (447 ± 30 nm emission) and 900 nm (520 ± 20nm emission). To verify that these signals originated from mitochondria, a cell spheroid was labelled with MitoTracker Orange and imaged using two-photon excitation (850 nm excitation, 650 nm ± 20 detection) on the point-scanning, multiphoton imaging system (section 3.3). The point scanning system was used as a lower magnification objective (4x) and brightfield illumination could be used to easily locate the spheroid before switching to the higher magnification objective (63x) and laser scanning imaging. Both NADH and FAD signals showed qualitative co-localisation with the MitoTracker signal (Figure 93), but were significantly (~10-fold) weaker than the

MitoTracker signal. Some small movements of the imaged structures (including potential changes in z into/ out of the focal plane) were observed as a result of the time taken to tune between laser wavelengths, match the laser power and manually change the imaging filters (approx. 1 minute). Selective FAD imaging gave better contrast of mitochondria over cellular background compared to NADH imaging. This agrees with the cellular locations of both co-enzymes where NADH is both mitochondrial and cytosolic whereas FAD is only mitochondrial (Heikal, 2010).

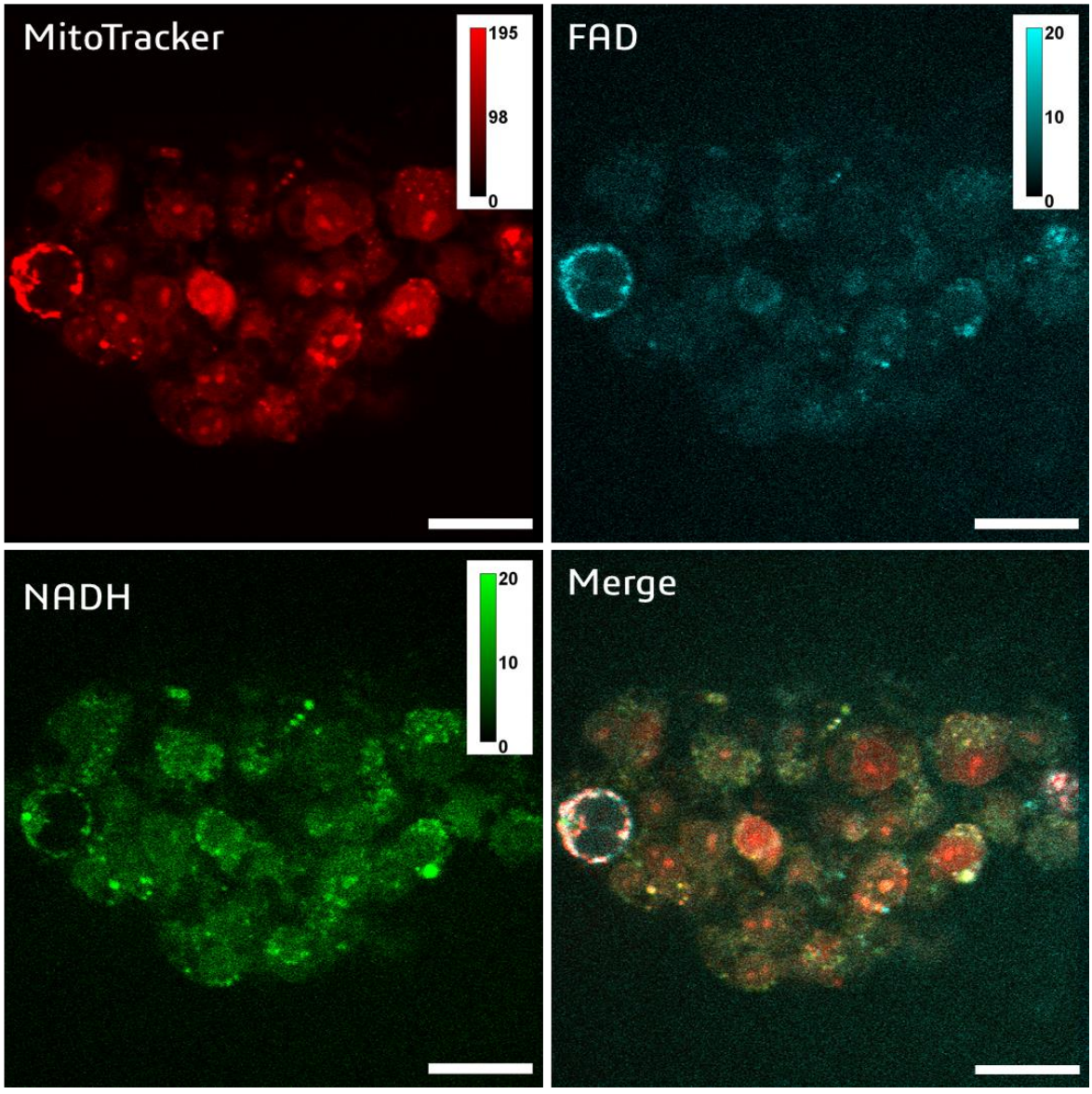

Figure 93: Verification of autofluorescence signal.
TPEF images of a SHSY-5Y cell spheroid labelled with 500 nM mitoTracker Orange. The spheroid was mounted in agarose as is done for lightsheet imaging and imaged using a 63x/0.9 NA objective. The whole scanned field was 103 µm x103 µm scanned using 1024 x 1024 pixels. MitoTracker signal was excited at 850 nm and detected at 650 ± 20nm to minimise contributions from NADH and FAD emission tails, the MitoTracker signal was observed to be ~ 10-fold brighter. FAD was excited at 900 nm and collected at 520 ± 20 nm, NADH was excited at 740 nm and collected at 447 ± 30 nm. The merged image shows co-localisation between the autofluorescence and MitoTracker signals, verifying the primarily mitochondrial origin of the autofluorescence signal. Scale bar = 20 µm.

Confirmation of the mitochondrial origin of the observed autofluorescence signal opened the opportunity to image mitochondria using MUSICAL. When imaging using the lightsheet microscope it was found that differential signals for NADH and FAD could not be observed. A strong autofluorescence signal was only observed under 740 nm excitation at collection wavelengths of either 500 nm – 540 nm, or in the wider pass band of 500 nm – 650 nm whereas no signal was observed at 900 nm excitation. This was possibly due to the lower power output of the laser at 900 nm which becomes too low for lightsheet imaging but not for point scanning. The autofluorescence signal was found to be much weaker (approximately 5-fold) than the signal from MitoTracker Orange (Figure 94). This is approximately half of the fold change seen in Figure 93 and is likely because in Figure 93 separate NADH and FAD signals were being detected and in Figure 94 the combined signal is being detected. There may also be variations in the staining efficiency of MitoTracker between the 2 experiments, and variations in the concentrations of NADH/FAD. To maximise signal for subsequent MUSICAL acquisitions fluorescence was excited at 740 nm and collected in the range of 500 nm – 650 nm, therefore the signal will be primarily composed of contributions from FAD provided a roughly equal concentration of each species.

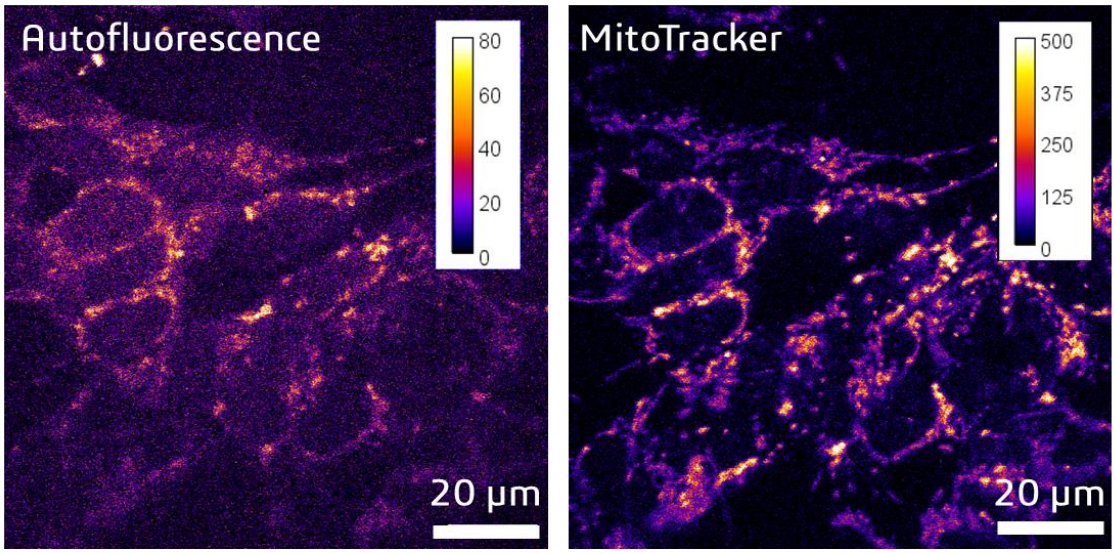

Figure 94: Comparison of signal strengths of two-photon excited autofluorescence from NADH/FAD and MitoTracker Orange.
The autofluorescence from mitochondria (740 nm excitation 420-540 nm emission) is approximately 5 times weaker than the signal from MitoTracker Orange (850 nm excitation, 590-630 nm emission) (see Figure 84). Measurements taken in adherent SHSY-5Y cells.

Figure 95**A** shows the average projection of 50 frames of a single, unlabelled cell imaged using autofluorescence lightsheet. The unlabelled cell was identified as having detached from a cell spheroid when being mounted in an agarose droplet for lightsheet imaging. Four distinct mitochondria can be seen. Analysis of the image stack showed a SBR of only 2:1 (Figure 95**D**) which is less that the desired >3:1 for MUSICAL processing. However, the fluctuations in the signal from mitochondria were significant and satisfied the ~>0.05 requirement for MUSICAL reconstruction (Figure 95**F**). Analysis of the intensity of the mitochondria over time revealed that the fluctuation in signal was primarily due to bleaching. However, similar structures were observed after MUSICAL processing as seen with MitoTracker labelling, such as the circularised mitochondrion. The apparent resolution of the outer mitochondrial membrane (Figure 95**C** white arrow) was not as clear as the MitoTracker image and instead appeared to highlight a weaker diffuse signal across the mitochondrion (magenta) and dense punctate points relating to areas of high fluctuations (white/orange spots). It was also observed that there was a different structure that had not been observed in the MitoTracker images (Figure 95C Yellow arrow). Here, an outer ring at the edge of the mitochondrion was not observed but instead the structure looked more like that which may be observed in the mitochondrial matrix. As the selected imaging conditions (740 nm excitation, 500 nm – 650 nm emission) incorporates signal from both NADH and FAD (primarily FAD, Figure 92) it is difficult to interpret the observed structures. Relating these observations from NADH/FAD atuoflourescence to the MitoTracker Orange observations, the differences may be due to different locations of NADH/FAD compared to MitoTracker. However, Mitotracker orange and NADH/FAD are both primarily located in the mitochondrial matrix (Chance *et al.*, 1979; M'Saad and Bewersdorf, 2020), therefore the differences in observed features is interesting. As with the MitoTracker-labelled images it is not possible to tell whether the identified fluctuations are due to intensity fluctuations of the emitters due to bleaching or whether there are also contributions from small movements of the mitochondrion within the thickness of the lightsheet. It is possible that the features seen in the MitoTracker data are a result of mitochondrial motion induced fluctuations which highlights the edges of the mitochondria. If these fluctuations were stronger than the fluctuations due to dye diffusion and bleaching/blinking then they would dominate in the MUSICAL processing. Having made observations of MUSICAL performance with two-photon excited autofluorescence lightsheet data from a single cell, the next step was to attempt imaging in a large 3D cell spheroid.

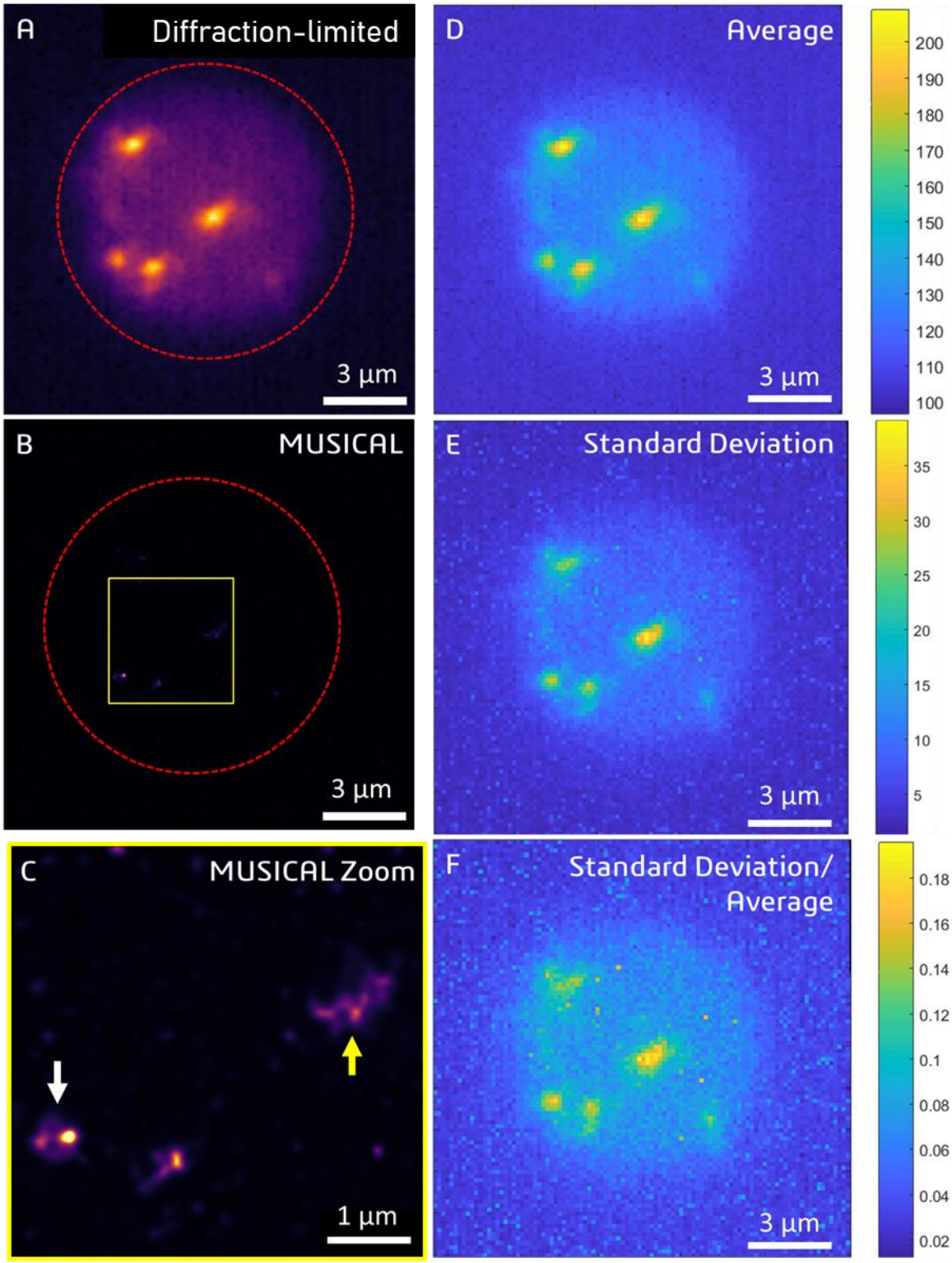

Figure 95: MUSICAL autofluorescence imaging of mitochondria in a single cell.
(**A**) Average projection of 50 diffraction-limited frames of autofluorescence signal corresponding to mitochondria in a single cell on a lightsheet microscope. Raw images acquired using 100 ms exposure time, 40x/0.8 NA objective with an effective pixel size of 147 nm. (**B**) the corresponding MUSICAL processed image, σ_0 = -0.5, α = 4. The red circle indicates the outline of the cell. (**C**) Zoomed view yellow square in B. MUSICAL has revealed features due to fluctiuations (white and yellow arrows). Right column: Pre-processing analysis images of the stack used in A. **D** = Average, **E** = Standard Deviation, **F** = Standard Deviation/Average. **F** highlights that despite a SNR of 2:1 (D) there are suitable fluctuations to use in MUSICAL processing.

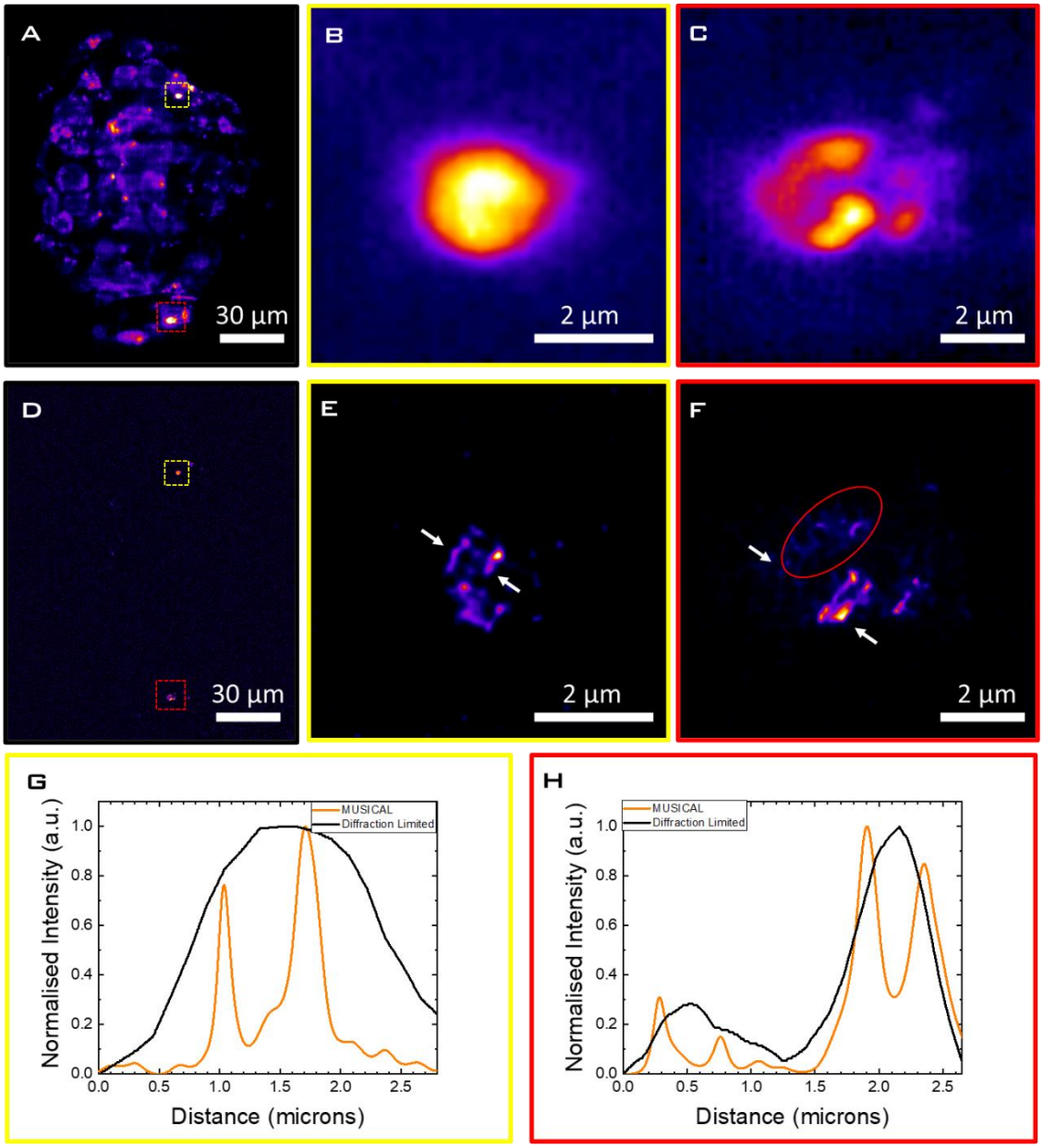

Figure 96: MUSICAL autofluorescence imaging in a whole spheroid sample.
(**A**) Autofluorescence image of an unlabelled cell spheroid, average of 50 diffraction-limited frames. Raw images acquired using 100 ms exposure time, 40x/0.8 NA objective with an effective pixel size of 147 nm. (**B/C**) zoomed views of the yellow/red boxed regions in A, they represent ~65 µm and 30 µm of penetration of the excitation light respectively.(**D**) MUSICAL processed image of the stack in (A) σ_0 = -0.7, α = 4. (**E/F**) zoomed views of the yellow/red boxed regions in D. (**G**) intensity plots taken between the white arrows in E and corresponding position in B. (**H**) intensity plots taken between the white arrows in F and corresponding position in C.

Figure 96**A** shows an image of a whole cell spheroid. The cellular distribution of autofluorescence allows for the identification of individual cells within the whole spheroid. Due to the weaker signal provided by autofluorescence compared to MitoTracker-labelling, many of the smaller and elongated mitochondria are only clearly identifiable in the average projection of 50 frames but not in individual frames, due to the averaging out of noise. Due to the SNR requirements of MUSICAL only the locations of highest intensity were suitable for processing, this can be seen by

comparing Figure 96**A** and **D**. Much of the signal was lost during MUSICAL processing, some of this is cytosolic autofluorescence that does not have a defined structure and therefore can't be resolved via MUSICAL however, other structures were also of similar intensity and showed similar fluctuations as the cytosolic signal, resulting in them being removed by MUSICAL thresholding.

The regions suitable for MUSICAL processing are shown in Figure 96**B/C**. This shows that there was a high degree of data loss from MUSICAL processing, with a more sensitive system (discussed below) this may be improved. Here, MUSICAL appeared to highlight the mitochondrial outer membrane (Figure 96**E/F**) rather than the punctate bright spots and diffuse circular signal observed previously (Figure 95**C**). Analysis of the point spread function of the peaks gave a mean peak width of 198±80 nm (Figure 96**G/H**), the narrowest resolved peak was 101 nm. As with previous observations of the outer-membrane-like structure by MUSICAL this may be due to movements within the lightsheet thickness and therefore it is not possible to draw direct conclusions from the PSF measurements. The measurements do indicate that MUSICAL can produce qualitatively similar results using mitochondrial autofluorescence to those observed with MitoTracker Orange labelling. Within the centre of the mitochondria a similar structure to that seen in Figure 95**C** (yellow arrow) was also observed (Figure 96**F**, red oval) however, this was of much lower intensity than the "outer membrane" like features.

7.5 Discussion

The work in this chapter presents important, early-stage, proof-of-concept and development of a label-free, super-resolution method. Thus far label-free imaging of intracellular components has been held back by diffraction. Only a handful of examples of label-free super resolution by autofluorescence exist. Dong et al (Dong *et al.*, 2016) used the fluorescence blinking of DNA to perform SMLM on unlabelled chromosomes. An intense pulse of 532 nm light was used to force most DNA molecules into a dark state and then 10,000 frames of blinking were recorded. Using this method they achieved a resolution of ~20 nm, which was further improved 2 years later to 6.2 nm by analysis of the spectral signatures of the emitters (Eshein *et al.*, 2018). Despite the impressive resolution, this technique requires a complex optical setup and the acquisition of extensive datasets as with other SMLM systems, impeding live cell imaging. Additionally, it is limited to imaging of DNA, which displays intrinsic autofluorescence blinking. Autofluorescence SIM has also been demonstrated for imaging lipofuscin in retinal tissue (Best *et al.*, 2011).

In this chapter a new method of label-free SR was demonstrated that does not have stringent requirements of fluorophore blinking and therefore should be applicable to any autofluorophore. MUSICAL appears able to potentially partially resolve the structure of complex organelles such as

mitochondria (Figure 97). Here the ground truth measurements were obtained with TEM and compared to MUSICAL images. They show a similarity in structural features observed by label-free LS-MUSICAL imaging. Clusters of small, fragmented mitochondria were observed, although these may be an artefact of the sectioning process. Larger, elongated mitochondria and wider, swollen mitochondria were also observed. The origins of these different structures may be a result of the sample preparation process such as the sectioning required for TEM imaging and the optical sectioning provided by lightsheet microscopy. It is noted that the thin sections required for TEM are approximately 200 times thinner than the lightsheet thickness (90 nm vs 1.7 µm) however, the same sectioning of the 3D mitochondrial network will occur but with lower resolution. The imaged autofluorophores NADH and FAD exist at different locations; NADH is found both cytoplasmically but also in high concentrations within the mitochondrial matrix, by contrast FAD (in the form of flavoproteins) is found bound to the inner membrane (Lienhart, Gudipati and MacHeroux, 2013). As the collected signal contained contributions from both autofluorophores it is difficult to interpret the SR images and the observed structures. In a system with increased sensitivity (discussed below) it may be possible to separate the signals such that the mitochondrial substructure can be imaged in a 2-colour fashion, and spatial location of the two signals can be determined. It is noted that the complex structure observed here is similar in nature to a common artefact observed in MUSICAL due to poor selection of processing parameters (Figure 83**F**). As such, interpretation of SR data produced from data sets containing weak signal and/or limited fluctuations should be performed with caution.

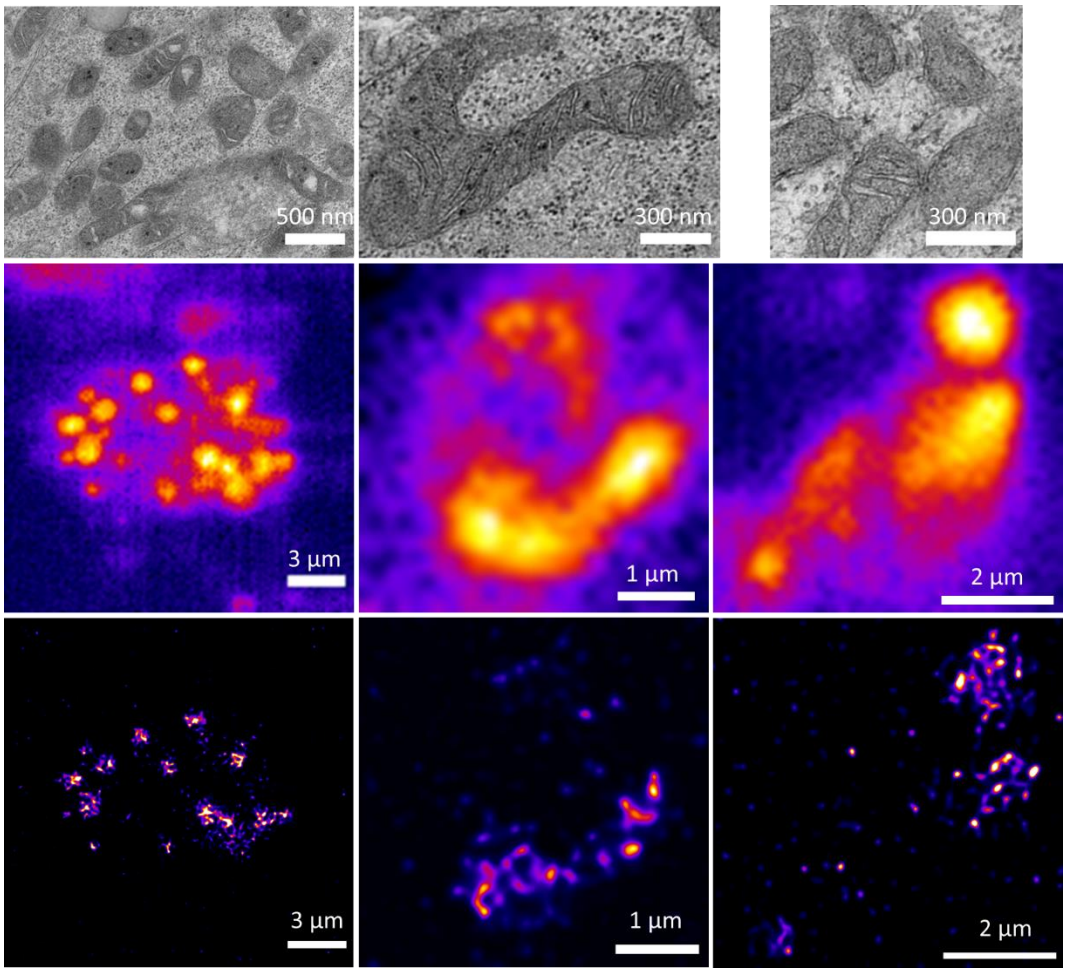

Figure 97: Comparison of MUSICAL with TEM images.
Top row, TEM images of mitochondria displaying different morphologies and distributions within a spheroid. **Middle row:** Diffraction-limited autofluorescence images taken from a similar spheroid. **Bottom Row:** MUSICAL processed outputs of the middle row images. In these images the mitochondria appear more elongated than in previous data sets, the resolved features also appear more like cristae structures although the approximate dimensions are larger than those observed by TEM.

In this chapter MUSICAL was applied to fluorescence microscopy data collected using a number of different microscopy methods. These were: one-photon widefield, two-photon point scanning, one-photon lightsheet and two-photon lightsheet. The original demonstration of MUSICAL was performed on a combination of simulated data and data collected in a TIRF illumination scheme (Agarwal and Macháň, 2016). In the simulated data, the data can be considered to be 2D and with TIRF illumination this can be considered to be one of the best approximations to 2D imaging for non-synthetic data. When MUSICAL computes the super-resolution image it uses a computed 2D-PSF. As such, is does not consider the possibility of intensity fluctuations that are the result of lateral or axial movement of emitters within and into/out of the focal volume. Thus, the MUSICAL processing of data acquired by other methods where the PSF deviates from the ideal 2D-PSF has the potential for artefacts. One-photon widefield has no optical sectioning and therefore would be expected to be most susceptible to artefacts, two-photon point scanning imaging and one- and

two-photon light sheet imaging both all have good optical sectioning compared to one-photon widefield, but still poor compared to TIRF imaging. Therefore, they may be less susceptible to artefacts (relating to the PSF axial extent) than one-photon widefield. A common potential artefact observed across all of the acquisition systems used, was the resolution of what might be interpreted as the outer membrane in mitochondria. It is possible in each of these cases the resolved structure is actually as a result of small movements of the mitochondria either laterally or axially that result in strong intensity fluctuations that impact the MUSICAL reconstruction process. Evidence in support of this is that MitoTracker Orange and NADH/FAD are known to be localised to the interior of mitochondria and not to the outer membrane (Chance *et al.*, 1979; M'Saad and Bewersdorf, 2020). The data acquired in this chapter suggests the potential power of MUSICAL for achieving label-free super-resolution. However, it has also highlighted the sensitivity of computational SR methods to deviations from ideal data collection parameters. Therefore, further characterisation of these artefacts with better defined standard samples will be necessary. Furthermore, it might be optimal to further develop the MUSICAL algorithm to consider a variety of PSFs that best reflect that of the imaging system used. In particular the ability to consider 3D PSFs and potential aberrations caused by scattering.

The generation of artefacts by computational SR algorithms is acknowledged and has led to error-mapping tools such as SQUIRREL (Culley *et al.*, 2018) which can be used to objectively evaluate the quality of a super-resolution reconstruction. The availability of these tools increases the strength of LS-MUSICAL as a super-resolution tool as it decreases the need to have knowledge of the underlying structure in the form of a ground truth. In exploratory biological studies this may not be available or is difficult to acquire. These were not explored in this thesis due to time constraints discussed in section 8.1.

Label-free imaging was demonstrated for a large 3D sample at ~65 µm depth of penetration of the excitation light (Figure 96**A**). Imaging of such cellular spheroid samples has become widely accepted as an intermediate between adherent cell samples and *in vivo* tissue imaging (Costa *et al.*, 2016), particularly in the context of tumour models, where nutrient and oxygen gradients through a 3D sample (such as a spheroid) play a key role in cellular activity and development (Jamieson, Harrison and Campbell, 2015).

Thus far, label-free imaging of these samples has been performed by optical coherence tomography (OCT), a method that uses interferometric detection to probe changes in phase introduced by changes in refractive index. Despite the large penetration depth and low light dose required in OCT, making it an attractive modality, it lacks the spatial resolution and selectivity of fluorescence microscopy. Quantitative Phase Imaging (QPI), allowing for the quantitative

measurement of the refractive index of cellular components, allows for more accurate identification of cellular components however this requires a specialist microscope setup not yet available to most biological labs (Park, Depeursinge and Popescu, 2018). High chemical specificity in spheroid imaging has also been achieved using Stimulated Raman Scattering (SRS) microscopy; using tissue clearing images at a depth of ~ 500 μm could be acquired (Wei *et al.*, 2019). SRS is reliant on point-scanning excitation and a complex multi-beam excitation scheme. The emission is also highly directional and is yet to be demonstrated in a lightsheet configuration, with most setups requiring transmission detection (Freudiger *et al.*, 2012; Tipping *et al.*, 2016). Super-resolution SRS imaging has been demonstrated for a specific molecule(1,4- diphenylbuta-1,3-diyne) (Gong *et al.*, 2019) where the SRS process can be saturated and, as such, the label-free suitability is lost.

LS-MUSICAL can overcome many of the limitations of the techniques mentioned above, potentially providing label-free super-resolution in a large 3D sample. The applicability of this method to several fluorophores both intrinsic (autofluorescence) and applied (fluorescent dyes) was demonstrated and the autofluorescence of metabolic markers used to potentially reveal structural detail of mitochondria. This resolution has been historically limited to electron microscopy (Mannella, 2008) and, more recently, super-resolution, labelled fluorescence modalities (Shao *et al.*, 2011; Stephan *et al.*, 2019). The resolution demonstrated for label-free mitochondrial imaging is not as good as that shown for conventional SR such as STORM. This could be improved by further optimisation of the lightsheet microscope in several ways. The current layout requires samples to be mounted in a droplet of agarose for imaging. Although every effort was made to minimise the scattering and absorption contributions of the agarose, this will still negatively influence the beam quality at the point of the sample as well as increasing scattering of signal reaching the camera. New innovations in single objective lightsheet microscope technologies have allowed open-top systems, facilitating conventional mounting techniques and removing the need for immobilisation in agarose such that refractive index matching can be optimised (Bouchard *et al.*, 2015; Theer, Dragneva and Knop, 2016; Sapoznik *et al.*, 2020). Another benefit of single-objective lightsheet systems is that high numerical apertures of >1 have been used; this automatically improves the diffraction-limited resolution but also improves signal collection efficiency due to the larger acceptance cone. Use of higher NA objectives in two-objective lightsheet systems (such as the one used in this thesis) is normally prohibited due to steric hinderance between the excitation and illumination objectives. In low signal samples, such as autofluorescence imaging, higher detection sensitivity will allow the reduction of excitation laser power and exposure time, improving the temporal resolution and the long-term imaging capabilities. Decreasing the exposure time and improving SNR will also improve

the quality of the MUSICAL reconstruction by allowing better separation of signal and noise and minimising potential artefacts due to sample motion. Another more modest improvement is the introduction of environmental control, in this thesis all lightsheet imaging was performed at ~21°C in imaging DMEM. It has been discussed that the appearance of many fragmented mitochondria can occur due to cellular stresses such as cold (Buser *et al.*, 1982). Thus, inferences from the biological data must be taken cautiously. Cold temperatures have been shown to increase NADH fluorescence however this effect is seen at temperatures well below freezing and cannot be used for live cell imaging (Zelent, Troxler and Vanderkooi, 2007). Of greater importance is the reduced production of NADH/FAD at cooler temperatures which will become altered as the cell cools from 37° C. Therefore, fixed samples may be better systems for some of the development work shown in this chapter, however, in my hands no autofluorescence signal was observed from fixed samples (data not shown).

NADH and FAD are only a few of many autofluorophores, in a tissue-imaging context many other autofluorophores exists such as elastin, collagen, retinol, lipofuscin and folic acid (Zipfel *et al.*, 2003). Because LS-MUSICAL does not have strict fluorophore requirements it is applicable to imaging these fluorophores in tissue with super-resolution.

7.6 Conclusions

The work presented in this chapter detailed the development of a new, label-free super-resolution imaging method. By developing a suitable imaging platform and sample production methodology a previously-established FSRM was applied to autofluorescence signals in mitochondria, potentially resolving internal structure at previously-unobtainable optical resolution. The method presented here is applicable to any lab with a multiphoton lightsheet microscope however, these are not common in most labs. The preliminary results regarding laser-scanning systems indicate that with further development this may be a suitable avenue for autofluorescence-MUSICAL imaging. As point-scanning multiphoton systems are more common than multiphoton lightsheet microscopes, and confocal microscopes with a UV laser more common again, these may be more broadly available systems for use with MUSICAL. As such, efforts to overcome the artefacts observed in this chapter are well warranted. These observations highlight the early stage of development of autofluorescence MUSICAL and further development is required. With these considerations, autofluorescence MUSICAL has widespread potential impact in the label-free monitoring of living systems, beyond the diffraction limit in a wide range of disease contexts.

Chapter 8 Conclusions and Future Perspective

The objective of this thesis was to explore and develop super-resolution (SR) optical imaging techniques for multiphoton, label-free imaging. In particular, this thesis focussed on the multiphoton modalities of second harmonic generation (SHG) and two-photon-excited fluorescence (TPEF) and their application to biological imaging. Two different methods were applied to achieve label-free super-resolution; the physical method of photonic nanojets (PNJs) generated using microspheres, and the computational fluctuations-based method MUSICAL.

By establishing the optimum conditions for SHG using PNJs the author was able to identify the limit of resolution, demonstrating a 2.7 x improvement over the theoretical diffraction limit for SHG excited at 800 nm. Furthermore, the polarisation properties of photonic nanojets were investigated and it was discovered surprisingly that they were maintained despite tight focussing. This was exploited to further improve the resolution by measuring the anisotropy of signals. The biological applicability of this method was demonstrated by measuring polarisation SHG (p-SHG) signals from a lung fibrosis tissue model and human lung samples. The author was able to show that inhibition of cross-linking disrupts collagen ultrastructure, an observation only previously achieved via electron and/or atomic force microscopy (Jones *et al.*, 2018). Structural alterations in collagen are present in a multitude of diseases including fibrosis and cancer, thus the ability to study these optically, with minimal sample preparation holds wide research potential.

Another key benefit of the PNJ method was demonstrated by applying it to the study of the extracellular matrix (ECM) protein elastin. As the PNJ method is independent of the source of contrast, both SHG and TPEF signals could be measured at a sub diffraction-limited scale. Building on the previous work, the author was able to show that TPEF emission from elastin has an unexpectedly high polarisation anisotropy similar to that of fibrillar collagen detected using SHG. This indicated a high degree of molecular order and is an important new insight into elastic fibre structure. It was previously shown that elastin was amorphous by electron microscopy (Kozel and Mecham, 2019). Further investigation of the elastin polarisation anisotropy in the disease model used will allow further understanding of the impact of treatments such as the stimulation and inhibition of cross-linking. This has direct research relevance as alterations in cross-linking have been implicated in lung fibrosis (Mecham, 2018) and cancer (Walker, Mojares and del Río Hernández, 2018). The demonstration of the multimodal ability of PNJ imaging opens the door for application to other multiphoton imaging methods including third harmonic generation and the coherent Raman techniques: Coherent anti-Stokes Raman Scattering (CARS) and Stimulated Raman Scattering (SRS) microscopy. This will increase the range of available structurally- and

chemically-specific super-resolution, label-free imaging techniques to further enable biomedical research.

The second avenue explored to achieve label-free super-resolution was the computational method MUSICAL. Through the optimisation of suitable imaging parameters MUSICAL was applied to conventional widefield one-photon excited fluorescence, point scanning, two-photon-excited fluorescence *and* both one- and two-photon-excited fluorescence in the lightsheet geometry. The author was able to demonstrate super-resolution in all cases, highlighting the versatility of the MUSICAL based method.

The demonstration of multiphoton SR in a point scanning system warrants further exploration, as point scanning is the most prominent implementation of multiphoton imaging. If the observed issues regarding artefacts from point scanning can be overcome, point scanning MUSICAL has the potential to provide super-resolution to a wide range of imaging fields, including deep tissue and *in vivo* studies. It also presents the opportunity to develop label-free super-resolution for other multiphoton imaging modalities that have only been demonstrated in a point scanning system such as SHG, CARS, and SRS.

The establishment of a 3D cell sample allowed me to exploit the advantages of lightsheet imaging. I was able to demonstrate imaging at ~65 µm depth of excitation penetration in a scattering sample. Lightsheet microscopy with two-photon excitation was used to image both mitochondria labelled with MitoTracker and unlabelled mitochondria via detection of autofluorescence. In labelled mitochondria the narrowest peak measured was 141 nm representing a 2.6x improvement over the diffraction-limited resolution. Here the diffraction limit was calculated using the centre emission wavelength (610 nm) and the NA of the detection objective as this is what affects lateral resolution in lightsheet microscopy. In unlabelled mitochondria an apparent resolution of ~100 nm was achieved, which represents a 3.4x improvement over the diffraction limit, here the peak emission of FAD (530 nm) was used to calculate the diffraction-limited resolution. The structures shown by autofluorescence indicated potential resolution of the mitochondrial membrane. However, due to the thickness of the lightsheet and potential undetected microscopic movements of the sample these features may be due to sample movement. Further characterisation of the effects of the lightsheet thickness and potential sources of signal fluctuations used by MUSICAL are vital for further progression of the lightsheet-MUSICAL method. If successfully achieved, the ability to resolve mitochondrial substructure in a label-free fashion within spheroid samples holds potential for drug screening and mode of action research. For this to become a reality the throughput of lightsheet imaging must be improved. A current key limitation is the arduous sample preparation required for lightsheet imaging.

However, new innovations in single objective (Sapoznik *et al.*, 2020), and open-top (Barner *et al.*, 2019) lightsheet systems allow imaging in traditional multi-well plate format. This is vital for high throughput screening of cell spheroids. In combination with the super-resolution methods developed in this thesis, this holds the potential for a step change in biomedical imaging research.

Both of the methods explored to achieve label-free super-resolution come with their own benefits and weaknesses. The PNJ method benefits from being independent of the contrast modality e.g. TPEF, SHG, CARS making it broadly applicable for improving the resolution of many methods and allowing for multimodal imaging experiments as demonstrated in Chapter 6. In addition, because the PNJ maintains polarisation, polarisation-based methods can be employed at a super-resolution scale. This is considered particularly interesting by the author as it has already given potential new insight into the disorder of extracellular matrix proteins. By contrast, the fluctuations-based super-resolution method explored in Chapter 7 was only demonstrated for fluorescence contrast. The source of fluctuations is not considered by MUSICAL and therefore it should be applicable to modalities that do not display inherent intensity fluctuations such as the bleaching and blinking observed in fluorescence. In theory, this means that MUSICAL could be used with SHG for example, provided fluctuations could be introduced either through nanoscopic movements of the SHG source or by introducing fluctuations by varying the intensity of the illumination. However, this is only likely to become a suitable super-resolution method in non-fluorescence-based, multiphoton modalities if the issues observed regarding point scanning are resolved, or if the modality can be demonstrated using widefield detection. To date this has only been achieved using custom-built amplified lasers (Zhao *et al.*, 2019) which are even less common than multiphoton lightsheet systems. Another potential limitation of the fluctuations-based method is that quantitative information cannot be retrieved from intensities in the final image because the intensities are determined by the strength of the fluctuations and not the concentration of the emitter. As such only structural insights can be gathered for these images.

The two methods explored hold different but complimentary roles in further research. The PNJ based method is currently better suited to more fundamental microscopy research. This is primarily due to two reasons: Firstly, many of the other multiphoton methods (to which PNJs hold most promise) mentioned such as CARS and SRS are in their relative infancy and are still being applied to simpler studies. Secondly, the comparatively low throughput of the method limits biological investigations where high n numbers are preferable. By contrast, the fluctuations-based method is better suited to higher throughput investigations, as it can produce full FOV (302 µm x 302 µm) super-resolution images. In addition, considering the recent advances in open-top lightsheet microscopes mentioned above, lightsheet looks poised to take centre stage in 3D, microscopy-based screening pipelines. The restriction to fluorescence-based modalities is not a

particular limitation, as currently these represent one of the most widely used set of techniques in biomedical research. In their current levels of readiness, the PNJ based method is closer to being a widely adopted method of label-free super-resolution. However, in the longer term, the fluctuations-based method holds more potential to become a commercial system present in many research labs. However, before this can occur many of the issues highlighted in Chapter 7 must be addressed.

8.1 Impact of the COVID-19 Pandemic

The COVID-19 pandemic can not be considered to have come at an opportune time for anyone, however, with relation to this PhD project it was particularly disruptive. The author became involved in the University's response to the pandemic, an action that took time away from the PhD project. This time was not fully recovered due to a limited extension being granted, which did not properly allow for the (necessarily) cautious re-opening of research labs. As a result, the experimental plan for the closing period of the project had to be suitably adjusted and completed alongside writing this thesis. The author does not regret the decision to become involved in the COVID-19 response but would like to reflect on the alterations it made to the PhD.

Had the author not experienced disruptions because of COVID-19, the experiments in Chapter 6 would have been extended further. Secondary verification of elastin as the source of autofluorescence using immunofluorescence would have ideally been performed. In addition, the author would have taken these experiments further to investigate potential changes in the polarisation anisotropy of elastin as a result of drug treatment or disease. Furthermore, application of the method to human tissue samples would have also been desirable after performing the verification steps above. These experiments would have involved development of immunofluorescence protocols and generation and acquisition of the required samples. This was not possible with the adjusted time scale because of the pandemic. Given more time and/or the opportunity to take the research further, the author would like to further develop the sphere-array imaging method, attempting the spin coating method mentioned in section 5.3.7. This would involve the subsequent characterisation of the effects this has on resolution of the PNJ method. Optimising the sphere-array system to overcome the limited FOV of PNJ imaging will be vital for wider application of the method.

The fluctuations-based super-resolution method provided an important opportunity to continue exploring label-free super-resolution when lab access was limited. As a computational technique, image processing pipelines could be developed with limited datasets. However, as a result of the limited lab access and limited time afforded whilst performing this work, there are experiments

and further development that the author would have ideally explored. MUSICAL was developed for one-photon excited fluorescence in a TIRF scheme and the PSF used is calculated as such. In many of the experiments performed in this thesis the images were generated using either two-photon-excited fluorescence, a lightsheet imaging geometry, or both. Thus, the data generated may show artefacts because of this. Considering the results generated in Chapter 7, given time, the author would have liked to explore and develop MUSICAL to consider different PSFs. This will be necessary for lightsheet-MUSICAL to be used for further experiments and, ultimately, for commercial implementation. However, this represents a significant body of work which the author does not consider to have been achievable within the timescale of the project. It may even represent an entire PhD in itself. Another experiment that would have ideally been completed without COVID-19 disruptions is the application of MUSICAL to imaging data acquired using point scanning. Imaging on a system without scan artefacts would reveal whether MUSICAL could be used with point scanning data, this may have altered the course of subsequent experiments had this been possible. Given more time, the author would have ideally spent more time developing suitable samples for multiphoton super-resolution, particularly fluctuations-based super-resolution. The lack of ground truth measurements for many of the samples limits the conclusions that can be drawn. The results in Chapter 7 have perhaps created as many questions as they have answered, it is the hope of the author that they can be explored further due to the exciting potential they have for achieving label-free super-resolution.

8.2 Summary

In summary, label-free super-resolution was explored using two different methods, each with their own relative merits and weaknesses. The work presented in this thesis represents important and novel steps in the infant field of label-free super-resolution. These studies pave the way for further developments of the methods explored and have the potential to guide new directions in biomedical imaging.

Appendix A Fiji Macros

A.1 Fiji macro script for calculation of anisotropy

```
source = getDirectory("Choose source directory");                    //70Pol + Hor = Par

File.makeDirectory(source + "/Ch2 anisotropy");

File.makeDirectory(source + "/Ch1 anisotropy");

array = getFileList(source);                                                    //70Pol + Vert = Perp

//Array.show(array);                                                                //160Pol + Hor
= Perp

                                                                                        //160Pol
+ Vert = Par

//****************************************Channel 1 processing
section**********************************

open(source + "/" + array[0]);

run("Make Substack...", "  slices=1");//Requires a folder containing two images, this will pick the
first image as perpendicular and the second as parralel

rename("perp");                                                  // operates on the first channel

open(source + "/" + array[1]);

run("Make Substack...", "  slices=1");

rename("par");




imageCalculator("Add create 32-bit stack", "perp","perp");          //this section calculates an
isotropy image

rename("2perp");
```

```
imageCalculator("Add create 32-bit stack", "par","2perp");

rename("T");

imageCalculator("Subtract create 32-bitstack", "par","perp");

rename("D");

imageCalculator("Divide create stack", "D","T");

selectWindow("Result of D");

rename("D over T");

saveAs("Tiff", source + "/Ch1 anisotropy/" + getTitle());

close();

saveAs("Tiff", source + "/Ch1 anisotropy/" + getTitle());

close();

saveAs("Tiff", source + "/Ch1 anisotropy/" + getTitle());

run("Close All");

run("Close All");                                    // saves all files to TPF directory


//*****************************Channel 2 processing
section*******************************

open(source + "/" + array[0]);

run("Make Substack...", "  slices=2");//Requires a folder containing two images, this will pick the
first image as perpendicular and the second as parralel

rename("par");                                              // operates on the second channel

open(source + "/" + array[1]);

run("Make Substack...", "  slices=2");

rename("perp");
```

```
imageCalculator("Add create 32-bit stack", "perp","perp");                //this section calculates an isotropy image

rename("2perp");

imageCalculator("Add create 32-bit stack", "par","2perp");

rename("T");

imageCalculator("Subtract create 32-bitstack", "par","perp");

rename("D");

imageCalculator("Divide create stack", "D","T");

selectWindow("Result of D");

rename("D over T");

saveAs("Tiff", source + "/Ch2 anisotropy/" + getTitle());

close();

saveAs("Tiff", source + "/Ch2 anisotropy/" + getTitle());

close();

saveAs("Tiff", source + "/Ch2 anisotropy/" + getTitle());

run("Close All");

run("Close All");                                                // saves all files to SHG directory
```

```
//**********************************Working on TPF images-This section sets the backgound, as definded by the user, to 0 **********************************
```

```
Ch1Dir = source + "/Ch1 anisotropy/";

open(Ch1Dir + "T.tif");                          //open total intensity image


//run("Make Substack...", "  slices=1");  //Select slice 1 of the stack which is TPF

run("Enhance Contrast", "saturated=0.35");

setAutoThreshold("Default dark");

run("Threshold...");                             // set threshold to remove BG pixels

waitForUser("Set threshold");

setOption("BlackBackground", false);

run("Convert to Mask");                  // turn thresholded image into mask

run("Median...", "radius=1");                    //median filter to smooth out random pixels in areas
of signal

run("Create Selection");

run("Create Mask");                              //Turn into useable mask

saveAs("Tiff", Ch1Dir + getTitle());

open(Ch1Dir + "/" + "D over T.tif");

//run("Make Substack...", "  slices=1");

rename("aniso");

imageCalculator("Multiply create", "aniso","Mask.tif");    // multiply anisotropy image by mask to
turn BG pixels to 0 and signal to 255*aniso score

saveAs("Tiff", Ch1Dir + "Aniso_times_mask" );

run("Divide...", "value=255");                           // return aniso values to correct value

saveAs("Tiff", Ch1Dir + "Divide_by_255" );

run("Close All");
```

```
//**********************************Working on SHG images-This section sets the backgound, as definded by the user, to 0 **********************************

Ch2Dir = source + "/Ch2 anisotropy/";

open(Ch2Dir + "T.tif");                    //open total intensity image


//run("Make Substack...", "  slices=2");  //Select slice 2 of the stack which is TPF

run("Enhance Contrast", "saturated=0.35");

setAutoThreshold("Default dark");

run("Threshold...");                       // set threshold to remove BG pixels

waitForUser("Set threshold");

setOption("BlackBackground", false);

run("Convert to Mask");                 // turn thresholded image into mask

run("Median...", "radius=1");              //median filter to smooth out random pixels in areas of signal

run("Create Selection");

run("Create Mask");                        //Turn into useable mask

saveAs("Tiff", Ch2Dir + getTitle());

open(Ch2Dir + "/" + "D over T.tif");

//run("Make Substack...", "  slices=2");

rename("aniso");

imageCalculator("Multiply create", "aniso","Mask.tif");    // multiply anisotropy image by mask to turn BG pixels to 0 and signal to 255*aniso score

saveAs("Tiff", Ch2Dir + "Aniso_times_mask" );

run("Divide...", "value=255");                    // return aniso values to correct value

saveAs("Tiff", Ch2Dir + "Divide_by_255" );
```

```
run("Close All");

justDone = substring(File.getParent(Ch2Dir),(lastIndexOf(File.getParent(Ch2Dir), "FOV")));


showMessage("You just analysed " + justDone);
```

A.2 Fiji Macro for measurement of anisotropy values

```
 dir = getDirectory("Choose a Directory ");
 count = 1;
 listFiles(dir);
 print(dir);
 function listFiles(dir) {
   list = getFileList(dir);
   for (i=0; i<list.length; i++) {
     if (endsWith(list[i], "/")){
       listFiles(""+dir+list[i]);
     }
    print(dir);
    print((count++) + ": " + dir + list[i]);


     if (endsWith(list[i], "Divide_by_255.tif")) {
                print("Eheu! Grumio est in culina. Caecilius in horto sedet. Eheu!");
                print("Cacite eum in pene!");
                kkk = dir + list[i];
                mmm = dir + "Mask.tif";
                print("kkkk" + kkk);
```

```
            print("mmmm" + mmm);
        open(kkk);
        open(mmm);
        selectWindow("Mask.tif");
                    run("Create Selection");
                    roiManager("Add");
                    selectWindow("Divide_by_255.tif");
                    roiManager("Select", 0);
                    run("Measure");
                    roiManager("Delete");
                    run("Close All");
      }
   }
}
```

Appendix B Tile Scanning Script

```
function tileMode(src,evnt,varargin)


    hSI = evnt.Source.hSI;  %#ok<NASGU>

    Xmax = 2100;

    Xstep = 100;

    Ymax = 2000;

    Ystep = 200;

    switch evnt.EventName

        case {'acqModeDone'}

            if ((hSI.hMotors.motorPosition(1) > Xmax-100) && (hSI.hMotors.motorPosition(1) < Xmax))
&& ((hSI.hMotors.motorPosition(2) > Ymax-200) && (hSI.hMotors.motorPosition(2) < Ymax))

%                 hSI.hMotors.motorPosition = [0 0 0];

                disp('Tile mode done');

            else

                nextX = hSI.hMotors.motorPosition(1) + Xstep;

                nextY = hSI.hMotors.motorPosition(2) + Ystep;

                if nextX <= Xmax

                    hSI.hMotors.motorPosition(1) = nextX;

                    hSI.startGrab;

                elseif nextX > Xmax && nextY <= Ymax

                    hSI.hMotors.motorPosition(1) = 0;

                    hSI.hMotors.motorPosition(2) = nextY;

                    hSI.startGrab;
```

```
            end

        end


    otherwise

%           warning('Unexpected event ''%s'' processed by %s',eventName,mfilename);

  end

end
```

Appendix C Photomultiplier Tube Specifications

	Type No.	Spectral response	Photocathode	Window material	Current-to-voltage conversion factor *	Frequency bandwidth *
	H10722-110	230 nm to 700 nm	Super bialkali	Borosilicate glass	1 V/μA	DC to 20 kHz
	H10722-113	185 nm to 700 nm	Super bialkali	UV glass		
	H10722-210	230 nm to 700 nm	Ultra bialkali	Borosilicate glass		
PMT1	H10722-01	230 nm to 870 nm	Multialkali	Borosilicate glass		
	H10722-04	185 nm to 870 nm	Multialkali	UV glass		
PMT2	H10722-20	230 nm to 920 nm	Extended red multialkali	Borosilicate glass		

PMT	Anode radiant sensitivity at 400 nm (V/nW)	Anode radiant sensitivity at 360 nm (V/nW)
PMT1(H10722-01)	8	7
PMT2(H10722-20)	3	2

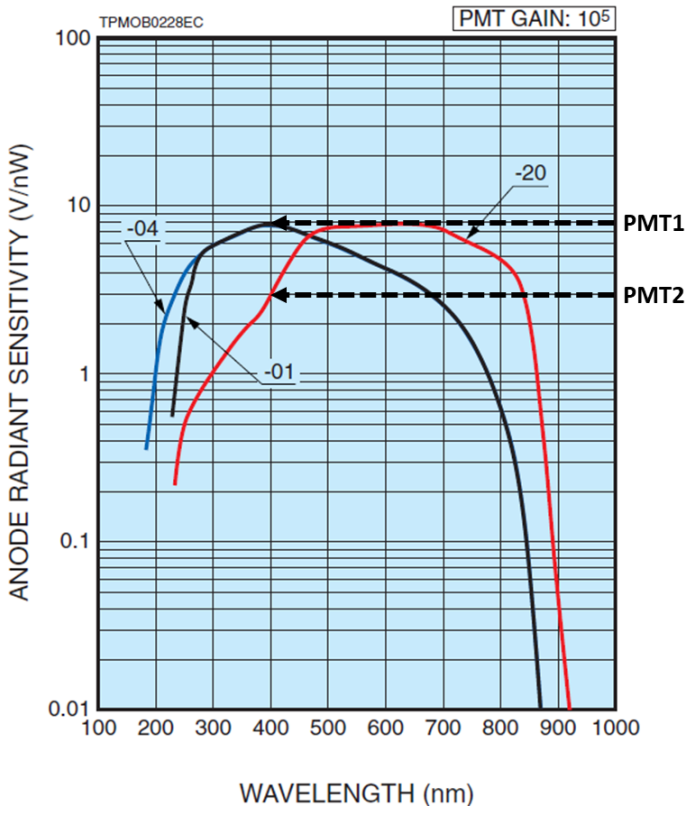

Figure 98: PMT specifications
The specifications of the PMT's used in the work in this thesis, the annotations -01/-04/-20 refer to the suffixes that identify the PMT type in the above tables.

The multiphoton imaging system described in section 3.3 was fitted with the two PMTs highlighted above. The two wavelengths tested for detecting SHG were 400 nm and 360 nm, 400 nm was ultimately chosen for data collection as stronger signals were observed. This is partially because PMT1 is ~2.7 times more sensitive than PMT2 at 400 nm and ~3.5 times more sensitive at

360 nm. The radiant sensitivity of PMT1 at 400 nm is only ~1.14 times greater at 400 nm than at 360 nm.

Appendix D Deconvolution parameters

Image Name..... /tmp/Spheroid01_R3D_D3D.dv_cor_TDS

Size (X, Y, Z)..... 1024 1024 101

Size (W, T)..... 3 1

Data Type..... 2 byte signed integer

Sequence..... Z -> T -> W

Wavelengths (nm)..... -50.00 523.00 632.00

Min, Max, Mean (w=-50.0 nm)..... 5375.00 32767.00 202.30

Min, Max, Mean (w=523.0 nm)..... 109.99 32925.76 606354.62

Min, Max, Mean (w=632.0 nm)..... 171.00 16244.00 80073.83

Rotation Angles (alpha, beta, gamma).. 0.00 0.00 0.00

Extended Header Size (bytes)..... 100352

Extended Header Type 4

Image Type..... 100

Lens ID Number..... 10211

Titles.....

IMGCORR: Norm=on Method=1

Bleach=on Zline=on

Time region selected..... 0 0 1

Wavelengths selected..... -50 523 632

Transferring field 0: CameraType c 12 EDGE / sCMOS

Transferring field 1: CameraGain f 8 1.000000

Transferring field 2: CameraBinning i 1 2

- opening OTF file...

Image Name..... /usr/local/otf/Olympus_20X_075_10205.otf

Size (X, Y, Z)..... 128 65 1

Size (W, T)..... 1 1

Data Type..... 4 byte floating-point

Sequence..... Z -> T -> W

Wavelengths (nm)..... 617.00

Min, Max, Mean (w=617.0 nm)..... 0.00 1.00 0.00

Rotation Angles (alpha, beta, gamma).. 0.00 0.00 0.00

Extended Header Size (bytes)..... 20480

Extended Header Type 0

Image Type..... 0

Lens ID Number..... 10205

Titles.....

DECON3D: 3D iterative constrained deconvolution

Method (1=add,2=ratio,3=enh add,4=enh ratio). 4

Intensity scaling factor..... 1.0000

Appendix D

Border roll-off for X and Y (pixels)..... 32

Pre-filter cut-off values (microns)..... 0.2000 0.0500

Sigma for smoothing..... 0.3050

Sigma for Wiener filter..... 0.1100

S:N value for Wiener filter..... 0.1010

Z padding..... 256

Number of iterations before smoothing..... 5

Maximum number of iterations..... 10

Memory usage (0=low, 1=med, 2=high)..... 2

Values subtracted from image..... 0.00 0.00 0.00 0.00 0.00

- allocating memory...

- generating pre-filter and smoothing function...

- Passing Wavelength -50.0

- deconvolving wavelength 523., time point # 1...

- reading data from disk...

- prefiltering...

Iteration	Standard Residual (R)	Avg Counts Residual	Normalized R
1	0.03252209	97.19	1.000
2	0.01128768	33.73	0.347

3	0.00799784	23.90	0.246
4	0.00727376	21.74	0.224
5	0.00700787	20.94	0.215
6	0.00718318	21.47	0.221
7	0.00693166	20.71	0.213
8	0.00673235	20.12	0.207
9	0.00656673	19.62	0.202
10	0.00642591	19.20	0.198

- intensity scaled by 0.33333, net scaling=0.33333

- deconvolving wavelength 632., time point # 1...

- reading data from disk...

- prefiltering...

Iteration	Residual (R)	Standard Residual	Avg Counts Normalized R
1	0.04711536	18.71	1.000
2	0.02950833	11.72	0.626
3	0.02642985	10.50	0.561
4	0.02547873	10.12	0.541
5	0.02490213	9.89	0.529
6	0.02535580	10.07	0.538

7	0.02471439	9.81	0.525
8	0.02423630	9.62	0.514
9	0.02384078	9.47	0.506
10	0.02350951	9.34	0.499

- intensity scaled by 0.50000, net scaling=0.50000

Total Deconvolution Time: 0 Hrs 1 Min 40 Sec

List of References

Aakhte, M. *et al.* (2017) 'Microsphere-assisted super-resolved Mirau digital holographic microscopy for cell identification', *Applied Optics*, 56(9), pp. D8–D13. doi: 10.1364/AO.56.0000D8.

Abbe, E. (1873) 'Beiträge zur Theorie des Mikroskops und der mikroskopischen Wahrnehmung', *Archiv für Mikroskopische Anatomie*, 9(1), pp. 413–468. doi: 10.1007/BF02956173.

Abraham, T. and Hogg, J. (2010) 'Extracellular matrix remodeling of lung alveolar walls in three dimensional space identified using second harmonic generation and multiphoton excitation fluorescence', *Journal of Structural Biology*, 171(2), pp. 189–196. doi: 10.1016/j.jsb.2010.04.006.

Acuña, S. *et al.* (2020) 'MusiJ: an ImageJ plugin for video nanoscopy', *Biomedical Optics Express*, 11(5), pp. 2548–2559. doi: 10.1364/BOE.382735.

Agarwal, K. and Macháň, R. (2016) 'Multiple signal classification algorithm for super-resolution fluorescence microscopy', *Nature Communications*, 7(13752), pp. 1–9. doi: 10.1038/ncomms13752.

Alam, S. R. *et al.* (2017) 'Investigation of Mitochondrial Metabolic Response to Doxorubicin in Prostate Cancer Cells: An NADH, FAD and Tryptophan FLIM Assay', *Scientific Reports*, 7, p. 10451. doi: 10.1038/s41598-017-10856-3.

Albert, E. N. (1972) 'Developing elastic tissue. An electron microscopic study.', *The American Journal of Pathology*, 69(1), pp. 89–102.

Alhallak, K. *et al.* (2016) 'Optical redox ratio identifies metastatic potential-dependent changes in breast cancer cell metabolism', *Biomedical Optics Express*, 7(11), pp. 4364–4374. doi: 10.1364/BOE.7.004364.

Bagshaw, C. R. and Cherny, D. (2006) 'Blinking fluorophores: What do they tell us about protein dynamics?', *Biochemical Society Transactions*, 34(5), pp. 979–982. doi: 10.1042/BST0340979.

Bancelin, S. *et al.* (2014) 'Determination of collagen fibril size via absolute measurements of second-harmonic generation signals', *Nature Communications*, 5(4920), pp. 1–8. doi: 10.1038/ncomms5920.

Barlow, A. M. *et al.* (2020) 'Super resolution measurement of collagen fibers in biological samples: Validation of a commercial solution for multiphoton microscopy', *PLOS ONE*. Edited by J. P. R. O. Orgel, 15(2), pp. 1–15. doi: 10.1371/journal.pone.0229278.

Barner, L. A. *et al.* (2019) 'Solid immersion meniscus lens (SIMlens) for open-top light-sheet microscopy', *Optics Letters*, 44(18), pp. 4451–4454. doi: 10.1364/OL.44.004451.

Ben-Aryeh, Y. (2012) 'Superresolution observed from evanescent waves transmitted through nano-corrugated metallic films', *Applied Physics B: Lasers and Optics*, 109(1), pp. 165–170. doi: 10.1007/s00340-012-5193-4.

Berry, M. V and Popescu, S. (2006) 'Evolution of quantum superoscillations and optical superresolution without evanescent waves', *Journal of Physics A: Mathematical and General*, 39(22), pp. 6965–6977. doi: 10.1088/0305-4470/39/22/011.

Best, G. *et al.* (2011) 'Structured illumination microscopy of autofluorescent aggregations in human tissue', *Micron*, 42(4), pp. 330–335. doi: 10.1016/j.micron.2010.06.016.

Betzig, E. *et al.* (2006) 'Imaging Intracellular Fluorescent Proteins at Nanometer Resolution', *Science*, 313(5793), pp. 1642–1645. doi: 10.1126/science.1127344.

Blomfield, J. and Farrar, J. F. (1969) 'The fluorescent properties of maturing arterial elastin', *Cardiovascular Research*, 3(2), pp. 161–170. doi: 10.1093/cvr/3.2.161.

Bock, F. J. and Tait, S. W. G. (2020) 'Mitochondria as multifaceted regulators of cell death', *Nature Reviews Molecular Cell Biology*, 21(2), pp. 85–100. doi: 10.1038/s41580-019-0173-8.

Born, M. *et al.* (1999) *Principles of Optics*. 7th edn. Cambridge University Press. doi: 10.1017/CBO9781139644181.

Bouchard, M. B. *et al.* (2015) 'Swept confocally-aligned planar excitation (SCAPE) microscopy for high-speed volumetric imaging of behaving organisms', *Nature Photonics*, 9(2), pp. 113–119. doi: 10.1038/nphoton.2014.323.

Boyd, R. W. (2008) *Nonlinear Optics*. 3rd edn. Academic Press, Inc.

Brdiczka, D. G., Zorov, D. B. and Sheu, S. S. (2006) 'Mitochondrial contact sites: Their role in energy metabolism and apoptosis', *Biochimica et Biophysica Acta - Molecular Basis of Disease*, 1762(2), pp. 148–163. doi: 10.1016/j.bbadis.2005.09.007.

Bredfeldt, J. S. *et al.* (2014) 'Computational segmentation of collagen fibers from second-harmonic generation images of breast cancer', *Journal of Biomedical Optics*, 19(1), p. 016007. doi: 10.1117/1.JBO.19.1.016007.

Burger, W. and Burge, M. J. (2009) *Principles of Digital Image Processing*. 1st edn. Edited by I. Mackie. Springer.

Buser, K. S. *et al.* (1982) 'Effect of cold environment on skeletal muscle mitochondria in growing rats', *Cell and Tissue Research*, 225(2), pp. 427–436. doi: 10.1007/BF00214693.

Calle, E. A. *et al.* (2014) 'The use of optical clearing and multiphoton microscopy for investigation of three-dimensional tissue-engineered constructs', *Tissue Engineering - Part C: Methods*, 20(7), pp. 570–577. doi: 10.1089/ten.tec.2013.0538.

Campagnola, P. (2011) 'Second Harmonic Generation Imaging Microscopy: Applications to Diseases Diagnostics', *Analytical Chemistry*, 83(9), pp. 3224–3231. doi: 10.1021/ac1032325.

Campagnola, P. J. and Dong, C. Y. (2011) 'Second harmonic generation microscopy: Principles and applications to disease diagnosis', *Laser and Photonics Reviews*, 5(1), pp. 13–26. doi: 10.1002/lpor.200910024.

Campagnola, P. J. and Loew, L. M. (2003) 'Second-harmonic imaging microscopy for visualizing biomolecular arrays in cells, tissues and organisms', *Nature Biotechnology*, 21(11), pp. 1356–1360. doi: 10.1038/nbt894.

Campbell, K. R. *et al.* (2018) 'Polarization-resolved second harmonic generation imaging of human ovarian cancer', *Journal of Biomedical Optics*, 23(06), p. 066501. doi: 10.1117/1.JBO.23.6.066501.

Campbell, R. M. and Tummino, P. J. (2014) 'Cancer epigenetics drug discovery and development: The challenge of hitting the mark', *Journal of Clinical Investigation*, 124(1), pp. 64–69. doi: 10.1172/JCI71605.

Campello, S. *et al.* (2006) 'Orchestration of lymphocyte chemotaxis by mitochondrial dynamics', *Journal of Experimental Medicine*, 203(13), pp. 2879–2886. doi: 10.1084/jem.20061877.

Cao, L. *et al.* (2015) 'Dependence of focal position on the microscale spherical lens imaging', *Optics Communications*, 353, pp. 184–188. doi: 10.1016/j.optcom.2015.05.022.

Cao, R., Wallrabe, H. K. and Periasamy, A. (2020) 'Multiphoton FLIM imaging of NAD(P)H and FAD with one excitation wavelength', *Journal of Biomedical Optics*, 25(01), p. 1. doi: 10.1117/1.JBO.25.1.014510.

Chance, B. (1954) 'Spectrophotometry of intracellular respiratory pigments', *Science*, 120(3124), pp. 767–775. doi: 10.1126/science.120.3124.767.

Chance, B. *et al.* (1979) 'Oxidation-reduction ratio studies of mitochondria in freeze-trapped samples. NADH and flavoprotein fluorescence signals.', *Journal of Biological Chemistry*, 254(11), pp. 4764–4771.

Chang, J.-C. (2010) 'Regulatory role of mitochondria in oxidative stress and atherosclerosis', *World Journal of Cardiology*, 2(6), pp. 150–159. doi: 10.4330/wjc.v2.i6.150.

Chen, J. *et al.* (2013) 'Super-resolution differential interference contrast microscopy by structured illumination', *Optics Express*, 21(1), p. 112. doi: 10.1364/OE.21.000112.

Chen, L.-W. *et al.* (2018) 'Remote-mode microsphere nano-imaging: new boundaries for optical microscopes', *Opto-Electronic Advances*, 1(1), pp. 17000101–17000107. doi: 10.29026/oea.2018.170001.

Chen, R. *et al.* (2019) 'Photonic nanojet beam shaping by illumination polarization engineering', *Optics Communications*, 456(August), p. 124593. doi: 10.1016/j.optcom.2019.124593.

Chen, T. *et al.* (2018) 'Scanning Liquid-Immersed Microsphere Optical Superresolution Imaging Based on Microrobotics Manipulation', *IEEE Transactions on Nanotechnology*, 17(4), pp. 860–864. doi: 10.1109/TNANO.2018.2811861.

Chen, X. *et al.* (2012) 'Second harmonic generation microscopy for quantitative analysis of collagen fibrillar structure', *Nature Protocols*, 7(4), pp. 654–669. doi: 10.1038/nprot.2012.009.

Chen, X. *et al.* (2016) 'Two-photon light-sheet nanoscopy by fluorescence fluctuation correlation analysis', *Nanoscale*, 8(19), pp. 9982–9987. doi: 10.1039/c6nr00324a.

Chen, Z., Taflove, A. and Backman, V. (2004) 'Photonic nanojet enhancement of backscattering of light by nanoparticles: a potential novel visible-light ultramicroscopy technique', *Optics Express*, 12(7), p. 1214. doi: 10.1364/OPEX.12.001214.

Chozinski, T. J., Gagnon, L. A. and Vaughan, J. C. (2014) 'Twinkle , twinkle little star : Photoswitchable fluorophores for super-resolution imaging', *FEBS Letters*, 588(19), pp. 3603–3612. doi: 10.1016/j.febslet.2014.06.043.

Cicchi, R. *et al.* (2008) 'Nonlinear laser imaging of skin lesions', *Journal of Biophotonics*, 1(1), pp. 62–73. doi: 10.1002/jbio.200710003.

Cocciolone, A. J. *et al.* (2018) 'Elastin, arterial mechanics, and cardiovascular disease', *American Journal of Physiology-Heart and Circulatory Physiology*, 315(2), pp. H189–H205. doi: 10.1152/ajpheart.00087.2018.

Cole, R. W., Jinadasa, T. and Brown, C. M. (2011) 'Measuring and interpreting point spread functions to determine confocal microscope resolution and ensure quality control', *Nature Protocols*, 6(12), pp. 1929–1941. doi: 10.1038/nprot.2011.407.

Correll, R. N. *et al.* (2017) 'Mitsugumin 29 regulates t-tubule architecture in the failing heart', *Scientific Reports*, 7, p. 5328. doi: 10.1038/s41598-017-05284-2.

Costa, E. C. *et al.* (2016) '3D tumor spheroids: an overview on the tools and techniques used for their analysis', *Biotechnology Advances*, 34(8), pp. 1427–1441. doi: 10.1016/j.biotechadv.2016.11.002.

Cox, S. *et al.* (2012) 'Bayesian localization microscopy reveals nanoscale podosome dynamics', *Nature Methods*, 9(2), pp. 195–200. doi: 10.1038/nmeth.1812.

Craig, A. S. *et al.* (1989) 'An estimate of the mean length of collagen fibrils in rat tail-tendon as a function of age', *Connective Tissue Research*, 19(1), pp. 51–62. doi: 10.3109/03008208909016814.

Culley, S. *et al.* (2018) 'Quantitative mapping and minimization of super-resolution optical imaging artifacts', *Nature Methods*, 15(4), pp. 263–266. doi: 10.1038/nmeth.4605.

Czekalla, C. *et al.* (2017) 'Impact of Body Site, Age, and Gender on the Collagen/Elastin Index by Noninvasive in vivo Vertical Two-Photon Microscopy', *Skin Pharmacology and Physiology*, 30(5), pp. 260–267. doi: 10.1159/000477854.

Czirok, A. *et al.* (2006) 'Elastic fiber macro-assembly is a hierarchical, cell motion-mediated process', *Journal of Cellular Physiology*, 207(1), pp. 97–106. doi: 10.1002/jcp.20573.

Dan, D., Yao, B. and Lei, M. (2014) 'Structured illumination microscopy for super-resolution and optical sectioning', *Chinese Science Bulletin*, 59(12), pp. 1291–1307. doi: 10.1007/s11434-014-0181-1.

Darafsheh, A. *et al.* (2012) 'Optical super-resolution by high-index liquid-immersed microspheres', *Applied Physics Letters*, 101(14), pp. 1411281–1411288. doi: 10.1063/1.4757600.

Darafsheh, A. *et al.* (2014) 'Advantages of microsphere-assisted super-resolution imaging technique over solid immersion lens and confocal microscopies', *Applied Physics Letters*, 104(6). doi: 10.1063/1.4864760.

Darafsheh, A., Guardiola, C., Nihalani, D., *et al.* (2015) 'Biological super-resolution imaging by using novel microsphere-embedded coverslips', in *Proceedings of SPIE Nanoscale Imaging, Sensing, and Actuation for Biomedical Applications XII,* pp. 933701–933705. doi: 10.1117/12.2078019.

Darafsheh, A., Guardiola, C., Palovcak, A., *et al.* (2015) 'Optical super-resolution imaging by high-index microspheres embedded in elastomers', *Optics Letters*, 40(1), pp. 5–7. doi:

10.1364/OL.40.000005.

Débarre, D. *et al.* (2006) 'Imaging lipid bodies in cells and tissues using third-harmonic generation microscopy', *Nature Methods*, 3(1), pp. 47–53. doi: 10.1038/nmeth813.

Dehez, H., Piché, M. and De Koninck, Y. (2013) 'Resolution and contrast enhancement in laser scanning microscopy using dark beam imaging', *Optics Express*, 21(13), pp. 15912–15925. doi: 10.1364/OE.21.015912.

Demmerle, J. *et al.* (2015) 'Assessing resolution in super-resolution imaging', *Methods*, 88, pp. 3–10. doi: 10.1016/j.ymeth.2015.07.001.

Deniset-Besseau, A. *et al.* (2009) 'Measurement of the Second-Order Hyperpolarizability of the Collagen Triple Helix and Determination of Its Physical Origin', *Journal of Physics Chemical B*, 113(40), pp. 13437–13445. doi: 10.1021/jp9046837.

Dertinger, T. *et al.* (2009) 'Fast, background-free, 3D super-resolution optical fluctuation imaging (SOFI)', *Proceedings of the National Academy of Sciences*, 106(52), pp. 22287–22292. doi: 10.1073/pnas.0907866106.

Devilez, A. *et al.* (2009) 'Three-dimensional subwavelength confinement of light with dielectric microspheres', *Optics Express*, 17(4), pp. 2089–2094. doi: 10.1364/OE.17.002089.

Devilez, A., Bonod, N. and Stout, B. (2010) 'Near field dielectric microlenses', in Wyrowski, F. et al. (eds) *Proceedings of SPIE,, Optical Modelling and Design*, p. 771708. doi: 10.1117/12.855019.

Deyl, Z. *et al.* (1980) 'Studies on the chemical nature of elastin fluorescence', *Biochimica et Biophysica Acta*, 625(2), pp. 248–254. doi: 10.1016/0005-2795(80)90288-3.

Diaspro, A. (ed.) (2002) *Confocal and Two-Photon Microscopy Foundations, Applications, and Advances*. Wiley.

Diekmann, R. *et al.* (2017) 'Chip-based wide field-of-view nanoscopy', *Nature Photonics*, 11(5), pp. 322–328. doi: 10.1038/nphoton.2017.55.

Dittrich, P. S. and Schwille, P. (2001) 'Photobleaching and stabilization of fluorophores used for single-molecule analysis with one- and two-photon excitation', *Applied Physics B: Lasers and Optics*, 73(8), pp. 829–837. doi: 10.1007/s003400100737.

Dixit, R. and Cyr, R. (2003) 'Cell damage and reactive oxygen species production induced by fluorescence microscopy: effect on mitosis and guidelines for non-invasive fluorescence microscopy', *The Plant Journal*, 36(2), pp. 280–290. doi: 10.1046/j.1365-313X.2003.01868.x.

Dombeck, D. a *et al.* (2003) 'Uniform polarity microtubule assemblies imaged in native brain tissue by second-harmonic generation microscopy', *Proceedings of the National Academy of Sciences*, 100(12), pp. 7081–7086. doi: 10.1073/pnas.0731953100.

Dong, B. *et al.* (2016) 'Superresolution intrinsic fluorescence imaging of chromatin utilizing native, unmodified nucleic acids for contrast', *Proceedings of the National Academy of Sciences*, 113(35), pp. 9716–9721. doi: 10.1073/pnas.1602202113.

Donnert, G. *et al.* (2006) 'Macromolecular-scale resolution in biological fluorescence microscopy', *Proceedings of the National Academy of Sciences*, 103(31), pp. 11440–11445. doi: 10.1073/pnas.0604965103.

Duocastella, M. *et al.* (2017) 'Combination of scanning probe technology with photonic nanojets', *Scientific Reports*, 7, p. 3474. doi: 10.1038/s41598-017-03726-5.

Eckes, B., Nischt, R. and Krieg, T. (2010) 'Cell-matrix interactions in dermal repair and scarring', *Fibrogenesis & Tissue Repair*, 3(4), pp. 1–11. doi: 10.1186/1755-1536-3-4.

Eggeling, C. *et al.* (2009) 'Direct observation of the nanoscale dynamics of membrane lipids in a living cell', *Nature*, 457(7233), pp. 1159–1162. doi: 10.1038/nature07596.

Enomoto, N. *et al.* (2013) 'Amount of elastic fibers predicts prognosis of idiopathic pulmonary fibrosis', *Respiratory Medicine*, 107(10), pp. 1608–1616. doi: 10.1016/j.rmed.2013.08.008.

Eshein, A. *et al.* (2018) 'Sub-10-nm imaging of nucleic acids using spectroscopic intrinsic-contrast photon-localization optical nanoscopy (SICLON)', *Optics Letters*, 43(23), pp. 5817–5820. doi: 10.1364/ol.43.005817.

Eyden, B. and Tzaphlidou, M. (2001) 'Structural variations of collagen in normal and pathological tissues: Role of electron microscopy', *Micron*, 32(3), pp. 287–300. doi: 10.1016/S0968-4328(00)00045-7.

Eyre, D. R., Paz, M. A. and Gallop, P. M. (1984) 'Cross-linking in collagen and elastin', *Annual Review of Biochemistry*, 53, pp. 717–748. doi: 10.1146/annurev.biochem.53.1.717.

Falk, M. J. (2010) 'Neurodevelopmental Manifestations of Mitochondrial Disease', *Journal of Developmental Behavour Pediatrics*, 31(7), pp. 610–621. doi: 10.1097/DBP.0b013e3181ef42c1.Neurodevelopmental.

Fish, K. N. (2009) 'Total Internal Reflection Fluorescence (TIRF) Microscopy', *Current Protocols in Cytometry*, 50(1), pp. 273–275. doi: 10.1002/0471142956.cy1218s50.

Fowler, W. E. and Aebi, U. (1983) 'A consistent picture of the actin filament related to the orientation of the actin molecule.', *Journal of Cell Biology*, 97(1), pp. 264–269. doi: 10.1083/jcb.97.1.264.

Frantz, C., Stewart, K. M. and Weaver, V. M. (2010) 'The extracellular matrix at a glance', *Journal of Cell Science*, 123(24), pp. 4195–4200. doi: 10.1242/jcs.023820.

Frederick, R. L. and Shaw, J. M. (2007) 'Moving Mitochondria: Establishing Distribution of an Essential Organelle', *Traffic*, 8(12), pp. 1668–1675. doi: 10.1111/j.1600-0854.2007.00644.x.

Freudiger, C. W. *et al.* (2012) 'Multicolored stain-free histopathology with coherent Raman imaging', *Laboratory Investigation*, 92(10), pp. 1492–1502. doi: 10.1038/labinvest.2012.109.

Freund, I., Deutsch, M. and Sprecher, A. (1986) 'Connective tissue polarity. Optical second-harmonic microscopy, crossed-beam summation, and small-angle scattering in rat-tail tendon', *Biophysical Journal*, 50(4), pp. 693–712. doi: 10.1016/S0006-3495(86)83510-X.

Friess, W. (1998) 'Collagen - Biomaterial for drug delivery', *European Journal of Pharmaceutics and Biopharmaceutics*, 45(2), pp. 113–136. doi: 10.1016/S0939-6411(98)00017-4.

Fu, J. and Zhang, C. (2019) 'Super-resolution microscopy: successful applications in centrosome study and beyond', *Biophysics Reports*, 5(5–6), pp. 235–243. doi: 10.1007/s41048-019-00101-x.

Gauderon, R., Lukins, P. B. and Sheppard, C. J. R. (1998) 'Three-dimensional second-harmonic generation imaging with femtosecond laser pulses', *Optics Letters*, 23(15), p. 1209. doi: 10.1364/ol.23.001209.

Gelse, K., Pöschl, E. and Aigner, T. (2003) 'Collagens - Structure, function, and biosynthesis', *Advanced Drug Delivery Reviews*, 55(12), pp. 1531–1546. doi: 10.1016/j.addr.2003.08.002.

Genthial, R. *et al.* (2017) 'Label-free imaging of bone multiscale porosity and interfaces using third-harmonic generation microscopy', *Scientific Reports*, 7, p. 3419. doi: 10.1038/s41598-017-03548-5.

Georgakoudi, I. and Quinn, K. P. (2012) 'Optical imaging using endogenous contrast to assess metabolic state', *Annual Review of Biomedical Engineering*, 14, pp. 351–367. doi: 10.1146/annurev-bioeng-071811-150108.

Girkin, J. M. and Carvalho, M. T. (2018) 'The light-sheet microscopy revolution', *Journal of Optics (United Kingdom)*, 20(5). doi: 10.1088/2040-8986/aab58a.

Gong, L. *et al.* (2019) 'Saturated Stimulated-Raman-Scattering Microscopy for Far-Field

Superresolution Vibrational Imaging', *Physical Review Applied*, 11(3), p. 034041(12). doi: 10.1103/PhysRevApplied.11.034041.

Göppert-Mayer, M. (1931) 'Über Elementarakte mit zwei Quantensprüngen', *Annalen der Physik*, 401(3), pp. 273–294. doi: 10.1002/andp.19314010303.

Gould, T. J. *et al.* (2008) 'Nanoscale imaging of molecular positions and anisotropies', *Nature Methods*, 5(12), pp. 1027–1030. doi: 10.1038/nmeth.1271.

Green, E. M. *et al.* (2014) 'The structure and micromechanics of elastic tissue', *Interface Focus*, 4(2), p. 20130058. doi: 10.1098/rsfs.2013.0058.

Green, N. H. *et al.* (2017) 'A new mode of contrast in biological second harmonic generation microscopy', *Scientific Reports*, 7, p. 13331. doi: 10.1038/s41598-017-13752-y.

Gregor, I. *et al.* (2017) 'Rapid nonlinear image scanning microscopy', *Nature Methods*, 14(11), pp. 1087–1089. doi: 10.1038/nmeth.4467.

Gu, G. *et al.* (2017) 'Overstepping the upper refractive index limit to form ultra-narrow photonic nanojets', *Scientific Reports*, 7, p. 5635. doi: 10.1038/s41598-017-05781-4.

Gusachenko, I. *et al.* (2012) 'Polarization-Resolved Second-Harmonic Generation in Tendon upon Mechanical Stretching', *Biophysical Journal*, 102(9), pp. 2220–2229. doi: 10.1016/j.bpj.2012.03.068.

Gustafsson, M. G. L. (2000) 'Surpassing the lateral resolution limit by a factor of two using structured illumination microscopy', *Journal of Microscopy*, 198(2), pp. 82–87. doi: 10.1046/j.1365-2818.2000.00710.x.

Gustafsson, M. G. L. (2005) 'Nonlinear structured-illumination microscopy: wide-field fluorescence imaging with theoretically unlimited resolution.', *Proceedings of the National Academy of Sciences*, 102(37), pp. 13081–13086. doi: 10.1073/pnas.0406877102.

Gustafsson, M. G. L. *et al.* (2008) 'Three-dimensional resolution doubling in wide-field fluorescence microscopy by structured illumination.', *Biophysical journal*, 94(12), pp. 4957–4970. doi: 10.1529/biophysj.107.120345.

Gustafsson, N. *et al.* (2016) 'Fast live-cell conventional fluorophore nanoscopy with ImageJ through super-resolution radial fluctuations', *Nature Communications*, 7(12471), pp. 1–9. doi: 10.1038/ncomms12471.

Haeberlé, O. and Simon, B. (2009) 'Saturated structured confocal microscopy with theoretically

unlimited resolution', *Optics Communications*, 282(18), pp. 3657–3664. doi: 10.1016/j.optcom.2009.06.025.

Hafi, N. *et al.* (2014) 'Fluorescence nanoscopy by polarization modulation and polarization angle narrowing', *Nature Methods*, 11(5), pp. 579–584. doi: 10.1038/nmeth.2919.

Han, M., Giese, G. and Bille, J. F. (2005) 'Second harmonic generation imaging of collagen fibrils in cornea and sclera', *Optics Express*, 13(15), pp. 5791–5797. doi: 10.1364/opex.13.005791.

Han, X. *et al.* (2008) 'Second harmonic properties of tumor collagen: determining the structural relationship between reactive stroma and healthy stroma', *Optics Express*, 16(3), pp. 1846–59. doi: 10.1364/OE.16.001846.

Hanrahan, N. *et al.* (2020) 'Label-free and multimodal second harmonic generation light sheet microscopy', *bioRxiv*. doi: 10.1101/2020.09.07.284703.

Hao, X. *et al.* (2013) 'Far-field super-resolution imaging using near-field illumination by micro-fiber', *Applied Physics Letters*, 102(1). doi: 10.1063/1.4773572.

Heaster, T. M. *et al.* (2020) 'Autofluorescence Imaging of 3D Tumor–Macrophage Microscale Cultures Resolves Spatial and Temporal Dynamics of Macrophage Metabolism', *Cancer Research*, 80(23), pp. 5408–5423. doi: 10.1158/0008-5472.CAN-20-0831.

Hecht, E. (2001) *Optics*. 4th edn. Edited by A. Black. Addison Wesley.

Heikal, A. A. (2010) 'Intracellular coenzymes as natural biomarkers for metabolic activites and mitochondrial anomalies', *Biomarkers in Medicine*, 4(2), pp. 241–263. doi: 10.2217/bmm.10.1.Intracellular.

Hell, S. W. *et al.* (2015) 'The 2015 super-resolution microscopy roadmap', *Journal of Physics D: Applied Physics*, 48(443001), pp. 1–35. doi: 10.1088/0022-3727/48/44/443001.

Hell, S. W. and Wichmann, J. (1994) 'Breaking the diffraction resolution limit by stimulated emission: stimulated-emission-depletion fluorescence microscopy', *Optics Letters*, 19(11), p. 780. doi: 10.1364/OL.19.000780.

Helle, Ø. I. *et al.* (2020) 'Structured illumination microscopy using a photonic chip', *Nature Photonics*, 14(7), pp. 431–438. doi: 10.1038/s41566-020-0620-2.

Hoang, T. X. *et al.* (2015) 'Focusing and imaging in microsphere-based microscopy', *Optics Express*, 23(9), pp. 12337–12353. doi: 10.1364/OE.23.012337.

Hofmann, M. *et al.* (2005) 'Breaking the diffraction barrier in fluorescence microscopy at low light intensities by using reversibly photoswitchable proteins', *Proceedings of the National Academy of Sciences*, 102(49), pp. 17565–17569. doi: 10.1073/pnas.0506010102.

Hompland, T. *et al.* (2008) 'Second-harmonic generation in collagen as a potential cancer diagnostic parameter', *Journal of Biomedical Optics*, 13(5), pp. 0540501–05405011. doi: 10.1117/1.2983664.

Hosny, N. A. *et al.* (2020) 'Planar Airy beam light-sheet for two-photon microscopy', *Biomedical Optics Express*, 11(7), p. 3927. doi: 10.1364/boe.395547.

Houé, M. and Townsend, P. D. (1995) 'An introduction to methods of periodic poling for second-harmonic generation', *Journal of Physics D: Applied Physics*, 28(9), pp. 1747–1763. doi: 10.1088/0022-3727/28/9/001.

Houston, W. V. (1927) 'A compound interferometer for fine structure work', *Physical Review*, 29(3), pp. 478–484. doi: 10.1103/PhysRev.29.478.

Hu, W. *et al.* (2012) 'Characterization of collagen fibers by means of texture analysis of second harmonic generation images using orientation-dependent gray level co-occurrence matrix method', *Journal of Biomedical Optics*, 17(2), pp. 0260071–0260078. doi: 10.1117/1.JBO.17.2.026007.

Hu, Y. S. *et al.* (2014) 'Single-Molecule Super-Resolution Light-Sheet Microscopy', *ChemPhysChem*, 15(4), pp. 577–586. doi: 10.1002/cphc.201300732.

Huang, F. *et al.* (2013) 'Video-rate nanoscopy using sCMOS camera-specific single-molecule localization algorithms', *Nature Methods*, 10(7), pp. 653–658. doi: 10.1038/nmeth.2488.

Huang, J. *et al.* (2020) 'Characteristics of photonic jets generated by a dielectric sphere illuminated by a Gaussian beam', *Applied Optics*, 59(21), p. 6390. doi: 10.1364/ao.393424.

Huang, X. *et al.* (2018) 'Fast, long-term, super-resolution imaging with Hessian structured illumination microscopy', *Nature Biotechnology*, 36(5), pp. 451–459. doi: 10.1038/nbt.4115.

Hulmes, D. J. S. and Miller, A. (1981) 'Molecular packing in collagen', *Nature*, 293, pp. 239–240.

Huszka, G. and Gijs, M. A. M. (2018) 'Turning a normal microscope into a super-resolution instrument using a scanning microlens array', *Scientific Reports*, 8, p. 601. doi: 10.1038/s41598-017-19039-6.

Huttunen, M. J. *et al.* (2017) 'Label-free super-resolution with coherent nonlinear structured-

illumination microscopy', *Journal of Optics*, 19(085504), pp. 1–9. doi: 10.1088/2040-8986/aa792d.

James, D. S. *et al.* (2019) 'Probing ECM remodeling in idiopathic pulmonary fibrosis via second harmonic generation microscopy analysis of macro/supramolecular collagen structure', *Journal of Biomedical Optics*, 25(01), p. 014505. doi: 10.1117/1.JBO.25.1.014505.

Jamieson, L. E., Harrison, D. J. and Campbell, C. J. (2015) 'Chemical analysis of multicellular tumour spheroids', *Analyst*, 140(12), pp. 3910–3920. doi: 10.1039/c5an00524h.

Järveläinen, H. *et al.* (2009) 'Extracellular matrix molecules: Potential targets in pharmacotherapy', *Pharmacological Reviews*, 61(2), pp. 198–223. doi: 10.1124/pr.109.001289.

Jastrzebska, M. *et al.* (2017) 'New insight into the shortening of the collagen fibril D-period in human cornea', *Journal of Biomolecular Structure and Dynamics*, 35(3), pp. 551–563. doi: 10.1080/07391102.2016.1153520.

Jemielita, M. *et al.* (2013) 'Comparing phototoxicity during the development of a zebrafish craniofacial bone using confocal and light sheet fluorescence microscopy techniques', *Journal of Biophotonics*, 6(11–12), pp. 920–928. doi: 10.1002/jbio.201200144.

Johnson, P. *et al.* (2020) 'Super-resolved polarisation-enhanced second harmonic generation for direct imaging of nanoscale changes in collagen architecture', *bioRxiv*. doi: 10.1101/2020.02.07.934000.

Jones, M. G. *et al.* (2018) 'Nanoscale dysregulation of collagen structure-function disrupts mechano-homeostasis and mediates pulmonary fibrosis', *eLife*, 7, pp. 1–24. doi: 10.7554/eLife.36354.

Joseph, J. *et al.* (2020) 'Improving the space-bandwidth product of structured illumination microscopy using a transillumination configuration', *Journal of Physics D: Applied Physics*, 53(4), pp. 0440061–04400610. doi: 10.1088/1361-6463/ab4e68.

K.Konig *et al.* (2005) 'Multiphoton autofluorescence imaging of intratissue elastic fibers', *Biomaterials*, 26(5), pp. 495–500. doi: 10.1016/j.biomaterials.

Kadar, A. (1977) 'Scanning Electron Microscopy of Purified Elastin with and Without Enzymatic Digestion', *Advances in Experimental Medicine and Biology*, 79, pp. 71–96. doi: 10.1007/978-1-4684-9093-0_8.

Kadler, K. E. *et al.* (1996) 'Collagen fibril formation', *Journal of Biochemistry*, 316, pp. 1–11. doi: 10.1042/bj3160001.

Kadler, K. E. *et al.* (2007) 'Collagens at a glance', *Journal of Cell Science*, 120(12), pp. 1955–1958. doi: 10.1242/jcs.03453.

Kaiser, W. and Garrett, C. G. . (1961) 'Two-Photon Excitation in CaF2:Eu2+', *Physical Review Letters*, 7(6), pp. 229–232. doi: 10.1103/physrevlett.7.229.

Kazlouskaya, V. *et al.* (2013) 'The utility of elastic Verhoeff-Van Gieson staining in dermatopathology', *Journal of Cutaneous Pathology*, 40(2), pp. 211–225. doi: 10.1111/cup.12036.

Keller, P. J. *et al.* (2008) 'Reconstruction of zebrafish early embryonic development by scanned light sheet microscopy', *Science*, 322(5904), pp. 1065–1069. doi: 10.1126/science.1162493.

Kim, B. M. *et al.* (2000) 'Collagen structure and nonlinear susceptibility: Effects of heat, glycation, and enzymatic cleavage on second harmonic signal intensity', *Lasers in Surgery and Medicine*, 27(4), pp. 329–335. doi: 10.1002/1096-9101(2000)27:4<329::AID-LSM5>3.0.CO;2-C.

Kim, M. *et al.* (2015) 'Superresolution imaging with optical fluctuation using speckle patterns illumination', *Scientific Reports*, 5, p. 16525. doi: 10.1038/srep16525.

Kim, W.-C. *et al.* (2017) 'Investigation on achieving super-resolution by solid immersion lens based STED microscopy', *Optics Express*, 25(14), pp. 16629–16642. doi: 10.1364/oe.25.016629.

Koenders, M. M. J. F. *et al.* (2009) 'Microscale mechanical properties of single elastic fibers: The role of fibrillin-microfibrils', *Biomaterials*, 30(13), pp. 2425–2432. doi: 10.1016/j.biomaterials.2009.01.038.

Kolega, J. (2004) 'Phototoxicity and photoinactivation of blebbistatin in UV and visible light', *Biochemical and Biophysical Research Communications*, 320(3), pp. 1020–1025. doi: 10.1016/j.bbrc.2004.06.045.

Korobova, F. and Svitkina, T. (2010) 'Molecular Architecture of Synaptic Actin Cytoskeleton in Hippocampal Neurons Reveals a Mechanism of Dendritic Spine Morphogenesis', *Molecular Biology of the Cell*, 21(22), pp. 165–176. doi: 10.1091/mbc.E09.

Kottmann, R. M. *et al.* (2015) 'Second harmonic generation microscopy reveals altered collagen microstructure in usual interstitial pneumonia versus healthy lung', *Respiratory Research*, 16(61), pp. 1–13. doi: 10.1186/s12931-015-0220-8.

Kozawa, Y., Matsunaga, D. and Sato, S. (2018) 'Superresolution imaging via superoscillation focusing of a radially polarized beam', *Optica*, 5(2), pp. 86–92. doi: 10.1364/optica.5.000086.

Kozel, B. A. *et al.* (2006) 'Elastic fiber formation: A dynamic view of extracellular matrix assembly

using timer reporters', *Journal of Cellular Physiology*, 207(1), pp. 87–96. doi: 10.1002/jcp.20546.

Kozel, B. A. and Mecham, R. P. (2019) 'Elastic fiber ultrastructure and assembly', *Matrix Biology*, 84, pp. 31–40. doi: 10.1016/j.matbio.2019.10.002.

Kristensen, J. H. *et al.* (2014) 'The role of extracellular matrix quality in pulmonary fibrosis', *Respiration*, 88(6), pp. 487–499. doi: 10.1159/000368163.

Krivitsky, L. A. *et al.* (2013) 'Locomotion of microspheres for super-resolution imaging', *Scientific Reports*, 3, p. 3501. doi: 10.1038/srep03501.

Kular, J. K., Basu, S. and Sharma, R. I. (2014) 'The extracellular matrix: Structure, composition, age-related differences, tools for analysis and applications for tissue engineering', *Journal of Tissue Engineering*, 5, pp. 1–17. doi: 10.1177/2041731414557112.

Kulkarni, T. *et al.* (2016) 'Matrix remodeling in pulmonary fibrosis and emphysema', *American Journal of Respiratory Cell and Molecular Biology*, 54(6), pp. 751–760. doi: 10.1165/rcmb.2015-0166PS.

Kumar, R. *et al.* (2015) 'Polarization second harmonic generation microscopy provides quantitative enhanced molecular specificity for tissue diagnostics', *Journal of Biophotonics*, 8(9), pp. 730–739. doi: 10.1002/jbio.201400086.

LaComb, R. *et al.* (2008) 'Phase matching considerations in second harmonic generation from tissues: Effects on emission directionality, conversion efficiency and observed morphology', *Optics Communications*, 281(7), pp. 1823–1832. doi: 10.1016/j.optcom.2007.10.040.

LaComb, R., Nadiarnykh, O. and Campagnola, P. J. (2008) 'Quantitative second harmonic generation imaging of the diseased state osteogenesis imperfecta: experiment and simulation.', *Biophysical Journal*, 94(11), pp. 4504–4514. doi: 10.1529/biophysj.107.114405.

Lai, H. S. S. *et al.* (2016) 'Super-Resolution Real Imaging in Microsphere-Assisted Microscopy', *PLOS ONE*, 11(10), pp. 1–17. doi: 10.1371/journal.pone.0165194.

Lakowicz, J. R. (1999) *Principles of Fluorescence Spectroscopy*. 2nd edn. Edited by J. R. Lakowicz. Springer US. doi: 10.1007/978-1-4757-3061-6.

Latour, G. *et al.* (2012) 'In vivo structural imaging of the cornea by polarization-resolved second harmonic microscopy', *Biomedical Optics Express*, 3(1), pp. 1–15. doi: 10.1364/boe.3.000001.

Lecler, S. *et al.* (2007) 'Photonic jet driven non-linear optics: example of two-photon fluorescence enhancement by dielectric microspheres', *Optics Express*, 15(8), pp. 4935–4942. doi:

10.1364/OE.15.004935.

Lee, S., Li, L., Wang, Z., *et al.* (2013) 'Immersed transparent microsphere magnifying sub-diffraction-limited objects', *Applied Optics*, 52(30), pp. 7265–7270. doi: 10.1364/AO.52.007265.

Lee, S., Li, L., Ben-Aryeh, Y., *et al.* (2013) 'Overcoming the diffraction limit induced by microsphere optical nanoscopy', *Journal of Optics*, 15(125710), pp. 1–7. doi: 10.1088/2040-8978/15/12/125710.

Lee, S. and Li, L. (2015) 'Rapid super-resolution imaging of sub-surface nanostructures beyond diffraction limit by high refractive index microsphere optical nanoscopy', *Optics Communications*, 334, pp. 253–257. doi: 10.1016/j.optcom.2014.08.048.

Lemos, M. *et al.* (1997) 'Organization of collagen and elastic fibers studied in stretch preparations of whole mounts of human visceral pleura', *Annals of Anatomy*, 179(5), pp. 447–452. doi: 10.1016/S0940-9602(97)80048-9.

Lenselink, E. A. (2015) 'Role of fibronectin in normal wound healing', *International Wound Journal*, 12(3), pp. 313–316. doi: 10.1111/iwj.12109.

Ley, B., Collard, H. R. and King, T. E. (2011) 'Concise Clinical Review Clinical Course and Prediction of Survival in Idiopathic Pulmonary Fibrosis', *American Journal of Respiratory and Critical Care Medicine*, 183(3), pp. 431–440. doi: 10.1164/rccm.201006-0894CI.

Li, L. *et al.* (2013) 'Label-free super-resolution imaging of adenoviruses by submerged microsphere optical nanoscopy', *Light: Science & Applications*, 2(e104), pp. 1–9. doi: 10.1038/lsa.2013.60.

Lienhart, W. D., Gudipati, V. and MacHeroux, P. (2013) 'The human flavoproteome', *Archives of Biochemistry and Biophysics*, 535(2), pp. 150–162. doi: 10.1016/j.abb.2013.02.015.

Lim, H. *et al.* (2014) 'Label-free imaging of Schwann cell myelination by third harmonic generation microscopy', *Proceedings of the National Academy of Sciences*, 111(50), pp. 18025–18030. doi: 10.1073/pnas.1417820111.

Van De Linde, S. *et al.* (2011) 'Direct stochastic optical reconstruction microscopy with standard fluorescent probes', *Nature Protocols*, 6(7), pp. 991–1009. doi: 10.1038/nprot.2011.336.

Ling, J. *et al.* (2018) 'Experimental study on microsphere assisted nanoscope in non-contact mode', *Optics and Lasers in Engineering*, 106, pp. 56–60. doi: 10.1016/j.optlaseng.2018.02.010.

Liu, C. Y. *et al.* (2018) 'Engineering photonic nanojet by a graded-index micro-cuboid', *Physica E: Low-Dimensional Systems and Nanostructures*, 98, pp. 105–110. doi:

10.1016/j.physe.2017.12.020.

Liu, C. Y. and Wang, Y. H. (2014) 'Real-space observation of photonic nanojet in dielectric microspheres', *Physica E: Low-Dimensional Systems and Nanostructures*, 61, pp. 141–147. doi: 10.1016/j.physe.2014.03.019.

Liu, J. *et al.* (2014) 'Second harmonic super-resolution microscopy for quantification of mRNA at single copy sensitivity', *ACS Nano*, 8(12), pp. 12418–12427. doi: 10.1021/nn505096t.

Long, B. R., Robinson, D. C. and Zhong, H. (2014) 'Subdiffractive microscopy: techniques, applications, and challenges', *Wiley Interdisciplinary Reviews: Systems Biology and Medicine*, 6(2), pp. 151–168. doi: 10.1002/wsbm.1259.

Löschberger, A. *et al.* (2014) 'Correlative super-resolution fluorescence and electron microscopy of the nuclear pore complex with molecular resolution', *Journal of Cell Science*, 127(20), pp. 4351–4355. doi: 10.1242/jcs.156620.

De Luca, G. M. R. *et al.* (2013) 'Re-scan confocal microscopy: scanning twice for better resolution', *Biomedical Optics Express*, 4(11), pp. 2644–2656. doi: 10.1364/boe.4.002644.

Luk'yanchuk, B. S. *et al.* (2017) 'Refractive index less than two: photonic nanojets yesterday, today and tomorrow [Invited]', *Optical Materials Express*, 7(6), pp. 1820–1847. doi: 10.1364/OME.7.001820.

Lutz, V. *et al.* (2012) 'Impact of collagen crosslinking on the second harmonic generation signal and the fluorescence lifetime of collagen autofluorescence', *Skin Research and Technology*, 18(2), pp. 168–179. doi: 10.1111/j.1600-0846.2011.00549.x.

M'Saad, O. and Bewersdorf, J. (2020) 'Light microscopy of proteins in their ultrastructural context', *Nature Communications*, 11(1), pp. 1–15. doi: 10.1038/s41467-020-17523-8.

Maconi, G. *et al.* (2018) 'Wide field of view 3D label-free super-resolution imaging', in *Proceedings of SPIE, Photonic Instrumentation Engineering V*. SPIE, pp. 10539121–10539128. doi: 10.1117/12.2289120.

Mannella, C. A. (2008) 'Structural diversity of mitochondria: Functional implications', *Annals of the New York Academy of Sciences*, 1147, pp. 171–179. doi: 10.1196/annals.1427.020.

Mansfield, S. M. and Kino, G. S. (1990) 'Solid immersion microscope', *Applied Physics Letters*, 57(24), pp. 2615–2616. doi: 10.1063/1.103828.

Marsh, R. J. *et al.* (2018) 'Artifact-free high-density localization microscopy analysis', *Nature*

Methods, 15, pp. 689–692. doi: 10.1038/s41592-018-0072-5.

Martin, T. P., Norris, G. and Mcconnell, G. (2013) 'A novel approach for assessing cardiac fibrosis using label-free second harmonic generation', *International Journal of Cardiovascular Imaging*, 29, pp. 1733–1740. doi: 10.1007/s10554-013-0270-2.

Masters, B. R. and So, P. T. C. (2008) *Handbook of Biomedical Nonlinear Optical Microscopy*. 1st edn. Edited by B. R. Masters and P. T. C. So. Oxford university Press.

Matsui, T. *et al.* (2017) 'Non-labeling multiphoton excitation microscopy as a novel diagnostic tool for discriminating normal tissue and colorectal cancer lesions', *Scientific Reports*, 7, p. 6959. doi: 10.1038/s41598-017-07244-2.

Mazumder, N. *et al.* (2017) 'Polarization resolved second harmonic microscopy', *Methods*, 128, pp. 105–118. doi: 10.1016/j.ymeth.2017.06.012.

Mazumder, N. *et al.* (2019) 'Label-Free Non-linear Multimodal Optical Microscopy—Basics, Development, and Applications', *Frontiers in Physics*, 7(170), pp. 1–26. doi: 10.3389/fphy.2019.00170.

Mecham, R. P. (2018) 'Elastin in lung development and disease pathogenesis', *Matrix Biology*, 73(1), pp. 6–20. doi: 10.1016/j.matbio.2018.01.005.

Meddens, M. B. M. *et al.* (2016) 'Single objective light-sheet microscopy for high-speed whole-cell 3D super-resolution', *Biomedical Optics Express*, 7(6), p. 2219. doi: 10.1364/boe.7.002219.

Mertz, J. and Moreaux, L. (2001) 'Second-harmonic generation by focused excitation of inhomogeneously distributed scatterers', *Optics Communications*, 196, pp. 325–330. doi: 10.1016/S0030-4018(01)01403-1.

Minin, I. V., Minin, O. V. and Geints, Y. E. (2015) 'Localized em and photonic jets from non-spherical and non-symmetrical dielectric mesoscale objects: Brief review', *Annalen der Physik*, 527(7–8), pp. 491–497. doi: 10.1002/andp.201500132.

Monici, M. (2005) 'Cell and tissue autofluorescence research and diagnostic applications', *Biotechnology Annual Review*, 11, pp. 227–256. doi: 10.1016/S1387-2656(05)11007-2.

Montes, G. S. (1996) 'Structural biology of the fibres of the collagenous and elastic systems', *Cell Biology International*, 20(1), pp. 15–27. doi: 10.1006/cbir.1996.0004.

Moores, C. (2008) 'Chapter 16 Studying Microtubules by Electron Microscopy', in *Introduction to Electron Microscopy for Biologists*. Allen, Terrence D(ed) Academic Press, Inc, pp. 299–317. doi:

10.1016/S0091-679X(08)00416-0.

Mouras, R. *et al.* (2010) 'Nonlinear optical microscopy for drug delivery monitoring and cancer tissue imaging', *Journal of Raman Spectroscopy*, 41(8), pp. 848–852. doi: 10.1002/jrs.2622.

Mudry, E. *et al.* (2012) 'Structured illumination microscopy using unknown speckle patterns', *Nature Photonics*, 6(5), pp. 312–315. doi: 10.1038/nphoton.2012.83.

Muiznieks, L. D. *et al.* (2014) 'Modulated growth, stability and interactions of liquid-like coacervate assemblies of elastin', *Matrix Biology*, 36, pp. 39–50. doi: 10.1016/j.matbio.2014.03.008.

Muller, C. B. and Enderlein, J. (2010) 'Image scanning microscopy', *Physical Review Letters*, 104(19), pp. 1–4. doi: 10.1103/PhysRevLett.104.198101.

Nadiarnykh, O. *et al.* (2010) 'Alterations of the extracellular matrix in ovarian cancer studied by Second Harmonic Generation imaging microscopy.', *BMC Cancer*, 10(94), pp. 1–14. doi: 10.1186/1471-2407-10-94.

Nadiarnykh, O. and Campagnola, P. J. (2009) 'Retention of polarization signatures in SHG microscopy of scattering tissues through optical clearing', *Optics Express*, 17(7), p. 5806. doi: 10.1364/oe.17.005794.

Nahidiazar, L. *et al.* (2016) 'Optimizing imaging conditions for demanding multi-color super resolution localization microscopy', *PLoS ONE*, 11(7), pp. 1–18. doi: 10.1371/journal.pone.0158884.

New, G. (2011) *Introduction to Nonlinear Optics*. 1st edn. Edited by G. New. Cambridge: Cambridge University Press. doi: 10.1017/CBO9780511975851.

Nuriya, M. *et al.* (2006) 'Imaging membrane potential in dendritic spines.', *Proceedings of the National Academy of Sciences*, 103(3), pp. 786–90. doi: 10.1073/pnas.0510092103.

Olichon, A. *et al.* (2007) 'OPA1 alternate splicing uncouples an evolutionary conserved function in mitochondrial fusion from a vertebrate restricted function in apoptosis', *Cell Death and Differentiation*, 14(4), pp. 682–692. doi: 10.1038/sj.cdd.4402048.

Opstad, I. S. *et al.* (2020) 'Fluorescence fluctuations-based super- resolution microscopy techniques : an experimental comparative study', *arXiv*.

Park, Y. K., Depeursinge, C. and Popescu, G. (2018) 'Quantitative phase imaging in biomedicine', *Nature Photonics*, 12(10), pp. 578–589. doi: 10.1038/s41566-018-0253-x.

Parker, M. W. *et al.* (2014) 'Fibrotic extracellular matrix activates a profibrotic positive feedback loop', *The Journal of Clinical Investigation*, 124(4), pp. 1622–1635. doi: 10.1172/JCI71386DS1.

Parry, D. A. D., Barnes, G. R. G. and Craig, A. S. (1978) 'A comparison of the size distribution of collagen fibrils in connective tissues as a function of age and a possible relation between fibril size distribution and mechanical properties', *Proceedings of the Royal Society of London - Biological Sciences*, 203(1152), pp. 305–321. doi: 10.1098/rspb.1978.0107.

Patel, H. S., Kushwaha, P. K. and Swami, M. K. (2018a) 'Generation of highly confined photonic nanojet using crescent-shape refractive index profile in microsphere', *Optics Communications*, 415(December 2017), pp. 140–145. doi: 10.1016/j.optcom.2018.01.050.

Patel, H. S., Kushwaha, P. K. and Swami, M. K. (2018b) 'Photonic nanojet assisted enhancement of Raman signal: Effect of refractive index contrast', *Journal of Applied Physics*, 123(2), p. 023102. doi: 10.1063/1.4994944.

Pavone, F. S. and Campagnola, P. J. (2014) *Second Harmonic Generation Imaging*. 1st edn. Edited by F. S. Pavone and P. J. Campagnola. CRC Press.

Pawley, J. B. (2006) *Handbook of Biological Confocal Microscopy*. 3rd edn. Edited by J. B. Pawley. Springer.

Pena, A.-M. *et al.* (2007) 'Three-Dimensional Investigation and Scoring of Extracellular Matrix Remodeling During Lung Fibrosis Using Multiphoton Microscopy', *Microscopy Research and Technique*, 70, pp. 162–170. doi: 10.1002/jemt.

Pena, A.-M. *et al.* (2010) 'Multiphoton microscopy of engineered dermal substitutes: assessment of 3-D collagen matrix remodeling induced by fibroblast contraction', *Journal of Biomedical Optics*, 15(5), pp. 0560181–0560187. doi: 10.1117/1.3503411.

Peng, Q. *et al.* (2015) 'Improving liver fibrosis diagnosis based on forward and backward second harmonic generation signals', *Applied Physics Letters*, 106, pp. 0837011–0837015. doi: 10.1063/1.4913907.

Pernas, L. and Scorrano, L. (2016) 'Mito-Morphosis: Mitochondrial Fusion, Fission, and Cristae Remodeling as Key Mediators of Cellular Function', *Annual Review of Physiology*, 78, pp. 505–531. doi: 10.1146/annurev-physiol-021115-105011.

Plotnikov, S. V *et al.* (2006) 'Characterization of the myosin-based source for second-harmonic generation from muscle sarcomeres.', *Biophysical Journal*, 90(2), pp. 693–703. doi: 10.1529/biophysj.105.071555.

Preibisch, S., Saalfeld, S. and Tomancak, P. (2009) 'Globally optimal stitching of tiled 3D microscopic image acquisitions', *Bioinformatics*, 25(11), pp. 1463–1465. doi: 10.1093/bioinformatics/btp184.

Ranjit, S. *et al.* (2015) 'Imaging Fibrosis and Separating Collagens using Second Harmonic Generation and Phasor Approach to Fluorescence Lifetime Imaging', *Scientific Reports*, 5, p. 13378. doi: 10.1038/srep13378.

Rayleigh, L. (1874) 'On the Manufactue and Theory of Diffraction-gratings.', *Philosophical Magazine*, 47(310).

Rayleigh, L. (1903) 'On the Theory of Optical Images, with special reference to the Microscope.', *Journal of Microscopy*, 23(4), pp. 474–482.

Reddy, P. H. (2009) 'Role of mitochondria in neurodegenerative diseases: mitochondria as a therapeutic target in Alzheimer's disease.', *CNS spectrums*, 14(8 Suppl 7), pp. 8–18. doi: 10.1017/s1092852900024901.

Rehman, A. U. *et al.* (2017) 'Fluorescence quenching of free and bound NADH in HeLa cells determined by hyperspectral imaging and unmixing of cell autofluorescence', *Biomedical Optics Express*, 8(3), p. 1488. doi: 10.1364/BOE.8.001488.

Reichert, A. S. and Neupert, W. (2002) 'Contact sites between the outer and inner membrane of mitochondria—role in protein transport', *Biochimica et Biophysica Acta (BBA) - Molecular Cell Research*, 1592(1), pp. 41–49. doi: 10.1016/S0167-4889(02)00263-X.

Remacha, E. *et al.* (2020) 'How to define and optimize axial resolution in light-sheet microscopy: a simulation-based approach', *Biomedical Optics Express*, 11(1), p. 8. doi: 10.1364/boe.11.000008.

Ricard-Blum, S. (2011) 'The Collagen Family', *Cold Spring Harbor Perspectives in Biology*, 3(1), pp. 1–19. doi: 10.1101/cshperspect.a004978.

Richeldi, L., Collard, H. R. and Jones, M. G. (2017) 'Idiopathic pulmonary fibrosis', *The Lancet*, 389(10082), pp. 1941–1952. doi: 10.1016/S0140-6736(17)30866-8.

Robertson, A. W. and Warner, J. H. (2013) 'Atomic resolution imaging of graphene by transmission electron microscopy', *Nanoscale*, 5, pp. 4079–4093. doi: 10.1039/c3nr00934c.

Robins, S. P. (2007) 'Biochemistry and functional significance of collagen cross-linking', *Cardiovascular Bioscience*, 35(5), pp. 849–852.

Rodrigues, R. M. *et al.* (2011) 'Autofluorescence microscopy: A non-destructive tool to monitor

mitochondrial toxicity', *Toxicology Letters*, 206(3), pp. 281–288. doi: 10.1016/j.toxlet.2011.06.025.

Roger, A. J., Muñoz-Gómez, S. A. and Kamikawa, R. (2017) 'The Origin and Diversification of Mitochondria', *Current Biology*, 27(21), pp. R1177–R1192. doi: 10.1016/j.cub.2017.09.015.

Rogers, E. T. F. *et al.* (2012) 'A super-oscillatory lens optical microscope for subwavelength imaging.', *Nature materials*, 11(5), pp. 432–5. doi: 10.1038/nmat3280.

Rogers, E. T. F. *et al.* (2013) 'Super-oscillatory optical needle', *Applied Physics Letters*, 102(3), pp. 1–4. doi: 10.1063/1.4774385.

Rogers, E. T. F. *et al.* (2020) 'Far-field unlabeled super-resolution imaging with superoscillatory illumination', *APL Photonics*, 5(066107), pp. 1–10. doi: 10.1063/1.5144918.

Rogers, E. T. F. and Zheludev, N. I. (2013) 'Optical super-oscillations : sub-wavelength light focusing and super-resolution imaging', *Journal of Optics*, 15(094008), pp. 1–23. doi: 10.1088/2040-8978/15/9/094008.

Romijn, E. I., Finnøy, A. and Lilledahl, M. B. (2018) 'Analyzing the feasibility of discriminating between collagen type I and II using polarization resolved second harmonic generation', *Journal of Biophotonics*, 12(1), p. e201800090. doi: 10.1002/jbio.201800090.

Roth, S. *et al.* (2013) 'Optical photon reassignment microscopy (OPRA)', *Optical Nanoscopy*, 2(5), pp. 1–6. doi: 10.1186/2192-2853-2-5.

Roth, S. and Freund, I. (1981) 'Optical second-harmonic scattering in rat-tail tendon', *Biopolymers*, 20(6), pp. 1271–1290. doi: 10.1002/bip.1981.360200613.

Rozario, T. and DeSimone, D. W. (2010) 'The extracellular matrix in development and morphogenesis: A dynamic view', *Developmental Biology*, 341(1), pp. 126–140. doi: 10.1016/j.ydbio.2009.10.026.

Rumi, M. and Perry, J. W. (2010) 'Two-photon absorption: an overview of measurements and principles', *Advances in Optics and Photonics*, 2, pp. 451–518. doi: 10.1364/aop.2.000451.

Rust, M. J., Bates, M. and Zhuang, X. W. (2006) 'Sub-diffraction-limit imaging by stochastic optical reconstruction microscopy (STORM)', *Nature Methods*, 3(10), pp. 793–795. doi: 10.1038/Nmeth929.

Sahl, S. J., Hell, S. W. and Jakobs, S. (2017) 'Fluorescence nanoscopy in cell biology', *Nature Reviews Molecular Cell Biology*, 18(11), pp. 685–701. doi: 10.1038/nrm.2017.71.

Sakaue, T. *et al.* (2018) 'Analysis of collagen fiber orientation in biological tissues using polarization-resolved second-harmonic-generation microscopy', in *Proceedings of SPIE Biomedical Imaging and Sensing Conference*. doi: 10.1117/12.2319273.

Sapoznik, E. *et al.* (2020) 'A versatile Oblique Plane Microscope for large-scale and high-resolution imaging of subcellular dynamics', *eLife*, 9(e57681), pp. 1–39. doi: 10.7554/eLife.57681.

Schaefer, L. and Schaefer, R. M. (2010) 'Proteoglycans: From structural compounds to signaling molecules', *Cell and Tissue Research*, 339(1), pp. 237–246. doi: 10.1007/s00441-009-0821-y.

Schaefer, P. M. *et al.* (2019) 'NADH Autofluorescence—A Marker on its Way to Boost Bioenergetic Research', *Cytometry Part A*, 95(1), pp. 34–46. doi: 10.1002/cyto.a.23597.

Schindelin, J. *et al.* (2012) 'Fiji: An open-source platform for biological-image analysis', *Nature Methods*, 9(7), pp. 676–682. doi: 10.1038/nmeth.2019.

Schins, J. M. *et al.* (2002) 'Determination of material properties by use of third-harmonic generation microscopy', *Journal of the Optical Society of America B*, 19(7), p. 1627. doi: 10.1364/JOSAB.19.001627.

Schneckenburger, H. *et al.* (2012) 'Light exposure and cell viability in fluorescence microscopy', *Journal of Microscopy*, 245(3), pp. 311–318. doi: 10.1111/j.1365-2818.2011.03576.x.

Schräder, C. U. *et al.* (2018) 'Elastin is heterogeneously cross-linked', *Journal of Biological Chemistry*, 293(39), pp. 15107–15119. doi: 10.1074/jbc.RA118.004322.

Schulz, O. *et al.* (2013) 'Resolution doubling in fluorescence microscopy with confocal spinning-disk image scanning microscopy', *Proceedings of the National Academy of Sciences*, 110(52), pp. 21000–21005. doi: 10.1073/pnas.1315858110.

Shah, A. T. *et al.* (2014) 'Optical metabolic imaging of treatment response in human head and neck squamous cell carcinoma', *PLoS ONE*, 9(3), p. e90746. doi: 10.1371/journal.pone.0090746.

Shao, L. *et al.* (2011) 'Super-resolution 3D microscopy of live whole cells using structured illumination.', *Nature Methods*, 8(12), pp. 1044–1046. doi: 10.1038/nmeth.1734.

Shen, Y. R. (1989) 'Optical Second Harmonic Generation at Interfaces', *Annual Review of Physical Chemistry*, 40, pp. 327–350. doi: 1989.40:327-350.

Sheppard, C. J. R. (1988) 'Super-resolution in confocal imaging', *Optik (Stuttgart)*, 80(2), pp. 53–54.

Sheppard, C. J. R. and Wilson, T. (1978) 'Image formation in scanning microscopes with partially coherent source and detector', *Optica Acta*, 25(4), pp. 315–325. doi: 10.1080/713819784.

Shim, S. H. *et al.* (2012) 'Super-resolution fluorescence imaging of organelles in live cells with photoswitchable membrane probes', *Proceedings of the National Academy of Sciences*, 109(35), pp. 13978–13983. doi: 10.1073/pnas.1201882109.

Sparrow, C. M. (1916) 'On spectroscopic resolving power', *The Astrophysical Journal*, 44, p. 76.

Starborg, T. *et al.* (2013) 'Using transmission electron microscopy and 3View to determine collagen fibril size and three-dimensional organization.', *Nature Protocols*, 8(7), pp. 1433–48. doi: 10.1038/nprot.2013.086.

Van Steenbergen, V. *et al.* (2019) 'Molecular understanding of label-free second harmonic imaging of microtubules', *Nature Communications*, 10(3530), pp. 1–14. doi: 10.1038/s41467-019-11463-8.

Stefan, S. M. and Wiese, M. (2019) 'Small-molecule inhibitors of multidrug resistance-associated protein 1 and related processes: A historic approach and recent advances', *Medicinal Research Reviews*, 39(1), pp. 176–264. doi: 10.1002/med.21510.

Stephan, T. *et al.* (2019) 'Live-cell STED nanoscopy of mitochondrial cristae', *Scientific Reports*, 9, p. 12419. doi: 10.1038/s41598-019-48838-2.

Strasser, S. *et al.* (2007) 'Structural investigations on native collagen type I fibrils using AFM', *Biochemical and Biophysical Research Communications*, 354(1), pp. 27–32. doi: 10.1016/j.bbrc.2006.12.114.

Strupler, M. *et al.* (2007) 'Second harmonic imaging and scoring of collagen in fibrotic tissues', *Optics Express*, 15(7), pp. 4054–4065.

Su, P. J. *et al.* (2011) 'Determination of collagen nanostructure from second-order susceptibility tensor analysis', *Biophysical Journal*, 100(8), pp. 2053–2062. doi: 10.1016/j.bpj.2011.02.015.

Sun, N. *et al.* (2016) 'Potential Indexing of the Invasiveness of Breast Cancer Cells by Mitochondrial Redox Ratios', in Luo, Q et al. (eds) *Oxygen Transport to Tissue XXXVIII. Advances in Experimental Medicine and Biology*, pp. 121–127. doi: 10.1007/978-3-319-38810-6_16.

Sundaram, V. M. and Wen, S. (2014) 'Analysis of deep sub-micron resolution in microsphere based imaging', *Applied Physics Letters*, 105(20), pp. 204102(1–4). doi: 10.1063/1.4902247.

Tehrani, K. F. *et al.* (2018) 'Resolution enhancement of 2-photon microscopy using high-refractive index microspheres', in *Proceedings of SPIE Multiphoton Microscopy in the Biomedical Sciences*

XVIII. SPIE, pp. 1049833(1–7). doi: 10.1117/12.2290613.

'The Diagnosis, Assessment and Treatment of Diffuse Parenchymal Lung Disease in Adults' (1999) *Thorax*, 54(Supplement 1), pp. S1–S28. doi: 10.1136/thx.54.suppl_1.S1.

The Nobel Prize in Chemistry (2014) *Nobel Prize.org*. Available at: https://www.nobelprize.org/prizes/chemistry/2014/summary/ (Accessed: 20 August 2020).

Theer, P. and Denk, W. (2006) 'On the fundamental imaging-depth limit in two-photon microscopy', *Journal of the Optical Society of America A*, 23(12), pp. 3139–3149. doi: 10.1364/josaa.23.003139.

Theer, P., Dragneva, D. and Knop, M. (2016) 'πSPIM: high NA high resolution isotropic light-sheet imaging in cell culture dishes', *Scientific Reports*, 6(1), p. 32880. doi: 10.1038/srep32880.

Theodossiou, T. A. *et al.* (2006) 'Second harmonic generation confocal microscopy of collagen type I from rat tendon cryosections', *Biophysical Journal*, 91(12), pp. 4665–4677. doi: 10.1529/biophysj.106.093740.

Thomas, G. *et al.* (2014) 'Advances and challenges in label-free nonlinear optical imaging using two-photon excitation fluorescence and second harmonic generation for cancer research', *Journal of Photochemistry and Photobiology B: Biology*, 141, pp. 128–138. doi: 10.1016/j.jphotobiol.2014.08.025.

Tiaho, F., Recher, G. and Rouède, D. (2007) 'Estimation of helical angles of myosin and collagen by second harmonic generation imaging microscopy', *Optics Express*, 15(19), pp. 12286–12295. doi: 10.1364/OE.15.012286.

Tian, N., Fu, L. and Gu, M. (2015) 'Resolution and contrast enhancement of subtractive second harmonic generation microscopy with a circularly polarized vortex beam', *Scientific Reports*, 5, p. 13580. doi: 10.1038/srep13580.

Tilbury *et al.* (2014) 'Second harmonic generation microscopy analysis of extracellular matrix changes in human idiopathic pulmonary fibrosis', *Journal of Biomedical Optics*, 19(8), pp. 086014(1–8). doi: 10.1117/1.JBO.19.8.086014.

Tilbury, K. *et al.* (2014) 'Differentiation of col I and Col III isoforms in stromal models of ovarian cancer by analysis of second harmonic generation polarization and emission directionality', *Biophysical Journal*, 106(2), pp. 354–365. doi: 10.1016/j.bpj.2013.10.044.

Tilbury, K. and Campagnola, P. J. (2015) 'Applications of Second-Harmonic Generation Imaging

Microscopy in Ovarian and Breast Cancer', *Perspectives in Medicinal Chemistry*, 7, pp. 21–32. doi: 10.4137/PMC.S13214.Received.

Tipping, W. J. *et al.* (2016) 'Stimulated Raman scattering microscopy: an emerging tool for drug discovery.', *Chemical Society Reviews*, 45(8), pp. 2075–2089. doi: 10.1039/c5cs00693g.

Travis, W. D. *et al.* (2002) 'American Thoracic Society/European Respiratory Society International Multidisciplinary Consensus Classification of the Idiopathic Interstitial Pneumonias', *American Journal of Respiratory and Critical Care Medicine*, 165(2), pp. 277–304. doi: 10.1164/ajrccm.165.2.ats01.

Truong, T. V. *et al.* (2011) 'Deep and fast live imaging with two-photon scanned light-sheet microscopy', *Nature Methods*, 8(9), pp. 757–762. doi: 10.1038/nmeth.1652.

Tuer, A. E. *et al.* (2011) 'Nonlinear optical properties of type I collagen fibers studied by polarization dependent second harmonic generation microscopy', *Journal of Physical Chemistry B*, 115(44), pp. 12759–12769. doi: 10.1021/jp206308k.

Tzaphlidou, M., Chapman, J. A. and Meek, K. M. (1982) 'A study of positive staining for electron microscopy using collagen as a model system-I. Staining by phosphotungstate and tungstate ions', *Micron*, 13(2), pp. 119–131. doi: 10.1016/0047-7206(82)90079-6.

Upputuri, P. K. *et al.* (2014) 'Super-resolution coherent anti-Stokes Raman scattering microscopy with photonic nanojets', *Optics Express*, 22(11), pp. 12890–12899. doi: 10.1364/OE.22.0128890.

Upputuri, P. K. and Pramanik, M. (2017) 'Microsphere-aided optical microscopy and its applications for super-resolution imaging', *Optics Communications*, 404, pp. 32–41. doi: 10.1016/j.optcom.2017.05.049.

Urban, B. E. *et al.* (2015) 'Super-resolution two-photon microscopy via scanning patterned illumination', *Physical Review E*, 91, pp. 042703(1–6). doi: 10.1103/PhysRevE.91.042703.

Urban, B. E. *et al.* (2018) 'Patterned-illumination second harmonic generation microscopy of collagen fibrils in rat scleras', *Optics Letters*, 43(21), pp. 5190–5193. doi: 10.1364/OL.43.005190.

Valentin Nagerl, U. *et al.* (2008) 'Live-cell imaging of dendritic spines by STED microscopy', *Proceedings of the National Academy of Sciences*, 105(48), pp. 18982–18987. doi: 10.1073/pnas.0810028105.

Vaux, D. L. (2011) 'Apoptogenic factors released from mitochondria', *Biochimica et Biophysica Acta (BBA) - Molecular Cell Research*, 1813(4), pp. 546–550. doi: 10.1016/j.bbamcr.2010.08.002.

Verkman, A. S. (2002) ‘Solute and macromolecule diffusion in cellular aqueous compartments’, *Trends in Biochemical Sciences*, 27(1), pp. 27–33. doi: 10.1016/S0968-0004(01)02003-5.

Vettenburg, T. *et al.* (2014) ‘Light-sheet microscopy using an Airy beam’, *Nature Methods*, 11(5), pp. 541–544. doi: 10.1038/nmeth.2922.

Viji Babu, P. K. *et al.* (2019) ‘Nano-mechanical mapping of interdependent cell and ECM mechanics by AFM force spectroscopy’, *Scientific Reports*, 9, p. 12317. doi: 10.1038/s41598-019-48566-7.

Vishwanath, K. and Ramanujam, N. (2011) ‘Fluorescence Spectroscopy In Vivo’, in Meyers, R. A. et al. (eds) *Encyclopedia of Analytical Chemistry*. John Wiley & Sons, Ltd, pp. 1–42. doi: 10.1002/9780470027318.a0102.pub2.

Vogel, W. F. (2001) ‘Collagen-receptor signaling in health and disease’, *European Journal of Dermatology*, 11(6), pp. 506–514.

Wagenseil, J. E. and Mecham, R. P. (2007) ‘New insights into elastic fiber assembly’, *Birth Defects Research Part C: Embryo Today: Reviews*, 81(4), pp. 229–240. doi: 10.1002/bdrc.20111.

Wagner, M. *et al.* (2010) ‘Light Dose is a Limiting Factor to Maintain Cell Viability in Fluorescence Microscopy and Single Molecule Detection’, *International Journal of Molecular Sciences*, 11(3), pp. 956–966. doi: 10.3390/ijms11030956.

Wäldchen, S. *et al.* (2015) ‘Light-induced cell damage in live-cell super-resolution microscopy’, *Scientific Reports*, 5, p. 15348. doi: 10.1038/srep15348.

Walker, C., Mojares, E. and del Río Hernández, A. (2018) ‘Role of Extracellular Matrix in Development and Cancer Progression’, *International Journal of Molecular Sciences*, 19(10), p. 3028. doi: 10.3390/ijms19103028.

Wallin, M. and Strömberg, E. (1995) ‘Cold-Stable and Cold-Adapted Microtubules’, in *International Review of Cytology*. Academic Press, Inc, pp. 1–31. doi: 10.1016/S0074-7696(08)62155-5.

Walsh, A. J. *et al.* (2013) ‘Optical metabolic imaging identifies glycolytic levels, subtypes, and early-treatment response in breast cancer’, *Cancer Research*, 73(20), pp. 6164–6174. doi: 10.1158/0008-5472.CAN-13-0527.

Wang, C.-C. *et al.* (2009) ‘Differentiation of normal and cancerous lung tissues by multiphoton imaging’, *Journal of Biomedical Optics*, 14(4), p. 044034. doi: 10.1117/1.3210768.

Wang, C. *et al.* (2015) ‘Dynamic tubulation of mitochondria drives mitochondrial network formation’, *Cell Research*, 25(10), pp. 1108–1120. doi: 10.1038/cr.2015.89.

Wang, F. *et al.* (2018) 'Microsphere-assisted super-resolution imaging with enlarged numerical aperture by semi-immersion', *Applied Physics Letters*, 112(2), p. 023101. doi: 10.1063/1.5011067.

Wang, L. *et al.* (2019) 'Solid immersion microscopy images cells under cryogenic conditions with 12 nm resolution', *Communications Biology*, 2(74), pp. 1–11. doi: 10.1038/s42003-019-0317-6.

Wang, Z. *et al.* (2011) 'Optical virtual imaging at 50 nm lateral resolution with a white-light nanoscope', *Nature Communications*, 2(218), pp. 1–6. doi: 10.1038/ncomms1211.

Wei, M. *et al.* (2019) 'Volumetric chemical imaging by clearing-enhanced stimulated Raman scattering microscopy', *Proceedings of the National Academy of Sciences*, 116(14), pp. 6608–6617. doi: 10.1073/pnas.1813044116.

Weihs, F. *et al.* (2018) 'Heterogeneous localisation of membrane proteins in *Staphylococcus aureus*', *Scientific Reports*, 8(1), p. 3657. doi: 10.1038/s41598-018-21750-x.

Wen, C. K. and Cynthia Goh, M. (2006) 'Fibrous Long Spacing Type Collagen Fibrils Have a Hierarchical Internal Structure', *Proteins*, 64, pp. 227–233. doi: 10.1002/prot.20949.

Westphal, V. and Hell, S. W. (2005) 'Nanoscale resolution in the focal plane of an optical microscope', *Physical Review Letters*, 94(14), pp. 143903(1–4). doi: 10.1103/PhysRevLett.94.143903.

Williams, R. M., Zipfel, W. R. and Webb, W. W. (2005) 'Interpreting Second-Harmonic Generation Images of Collagen I Fibrils', *Biophysical Journal*, 88(2), pp. 1377–1386. doi: 10.1529/biophysj.104.047308.

Willig, Katrin I. *et al.* (2006) 'Nanoscale resolution in GFP-based microscopy.', *Nature Methods*, 3(9), pp. 721–723. doi: 10.1038/nmeth922.

Willig, Katrin I *et al.* (2006) 'STED microscopy reveals that synaptotagmin remains clustered after synaptic vesicle exocytosis.', *Nature*, 440(7086), pp. 935–939. doi: 10.1038/nature04592.

Wilson, T. (2011) 'Optical sectioning in fluorescence microscopy', *Journal of Microscopy*, 242(2), pp. 111–116. doi: 10.1111/j.1365-2818.2010.03457.x.

Winey, M. and O'Toole, E. (2014) 'Centriole structure', *Philosophical Transactions of the Royal Society B: Biological Sciences*, 369(1650), p. 20130457. doi: 10.1098/rstb.2013.0457.

Wu, Q., Ghislain, L. P. and Elings, V. B. (2000) 'Imaging with solid immersion lenses, spatial resolution, and applications', *Proceedings of the IEEE*, 88(9), pp. 1491–1498. doi: 10.1109/5.883320.

Xiang, L. *et al.* (2020) 'Single-molecule displacement mapping unveils nanoscale heterogeneities in intracellular diffusivity', *Nature Methods*, 17(5), pp. 524–530. doi: 10.1038/s41592-020-0793-0.

Xing, C. *et al.* (2017) 'Flexible Microsphere-Embedded Film for Microsphere-Enhanced Raman Spectroscopy', *ACS Applied Materials and Interfaces*, 9(38), pp. 32896–32906. doi: 10.1021/acsami.7b09884.

Xu, H. N. *et al.* (2010) 'Quantitative mitochondrial redox imaging of breast cancer metastatic potential', *Journal of Biomedical Optics*, 15(3), p. 036010. doi: 10.1117/1.3431714.

Xu, H. N. *et al.* (2016) 'Optical redox imaging indices discriminate human breast cancer from normal tissues', *Journal of Biomedical Optics*, 21(10), p. 114003. doi: 10.1117/1.jbo.21.11.114003.

Xu, H. N. *et al.* (2019) 'Optical Redox Imaging of Lonidamine Treatment Response of Melanoma Cells and Xenografts', *Molecular Imaging and Biology*, 21(3), pp. 426–435. doi: 10.1007/s11307-018-1258-z.

Yahiatene, I. *et al.* (2015) 'Entropy-Based Super-Resolution Imaging (ESI): From Disorder to Fine Detail', *ACS Photonics*, 2(8), pp. 1049–1056. doi: 10.1021/acsphotonics.5b00307.

Yan, B. *et al.* (2017) 'Superlensing microscope objective lens', *Applied Optics*, 56(11), p. 3142. doi: 10.1364/AO.56.003142.

Yan, J. *et al.* (2011) 'A pilot study of using multiphoton microscopy to diagnose gastric cancer', *Surgical Endoscopy*, 25(5), pp. 1425–1430. doi: 10.1007/s00464-010-1409-z.

Yan, Y. *et al.* (2014) 'Microsphere-coupled scanning laser confocal nanoscope for sub-diffraction-limited imaging at 25 nm lateral resolution in the visible spectrum', *ACS Nano*, 8(2), pp. 1809–1816. doi: 10.1021/nn406201q.

Yan, Y. *et al.* (2015) 'Self-assembled dielectric microsphere array enhanced Raman scattering for large-area and ultra-long working distance confocal detection', *Optics Express*, 23(20), pp. 25854–25865. doi: 10.1364/OE.23.025854.

Yang, H. *et al.* (2014) 'Super-resolution biological microscopy using virtual imaging by a microsphere nanoscope', *Small*, 10(9), pp. 1712–1718. doi: 10.1002/smll.201302942.

Yang, H. *et al.* (2016) 'Super-Resolution Imaging of a Dielectric Microsphere Is Governed by the Waist of Its Photonic Nanojet', *Nano Letters*, 16(8), pp. 4862–4870. doi: 10.1021/acs.nanolett.6b01255.

Yang, S. *et al.* (2017) 'Influence of the photonic nanojet of microspheres on microsphere imaging',

Optics Express, 25(22), pp. 27551–27558. doi: 10.1364/OE.25.027551.

Yasui, T., Tohno, Y. and Araki, T. (2004) 'Determination of collagen fiber orientation in human tissue by use of polarization measurement of molecular second-harmonic-generation light', *Applied Optics*, 43(14), pp. 2861–2867. doi: 10.1364/AO.43.002861.

Yeh, C.-H. *et al.* (2018) 'Improving resolution of second harmonic generation microscopy via scanning structured illumination', *Biomedical Optics Express*, 9(12), pp. 6081–6090. doi: 10.1364/boe.9.006081.

York, A. G. *et al.* (2012) 'Resolution doubling in live, multicellular organisms via multifocal structured illumination microscopy', *Nature Methods*, 9(7), pp. 749–754. doi: 10.1038/nmeth.2025.

You, S., Kuang, C. and Zhang, B. (2016) 'Resolution criteria in double-slit microscopic imaging experiments', *Scientific Reports*, 6, p. 33764. doi: 10.1038/srep33764.

Youle, R. J. and Van Der Bliek, A. M. (2012) 'Good for Discussion: Mitochondrial Fission, Fusion, and Stress', *Science*, 337(6098), pp. 1062–1065. doi: 10.1126/science.1219855.Mitochondrial.

Zelent, B., Troxler, T. and Vanderkooi, J. M. (2007) 'Temperature dependence for fluorescence of β-NADH in glycerol/water solution and in trehalose/sucrose glass', *Journal of Fluorescence*, 17(1), pp. 37–42. doi: 10.1007/s10895-006-0146-0.

Zeng, Z. *et al.* (2015) 'Fast Super-Resolution Imaging with Ultra-High Labeling Density Achieved by Joint Tagging Super-Resolution Optical Fluctuation Imaging', *Scientific Reports*, 5, p. 8359. doi: 10.1038/srep08359.

Zhang, T. *et al.* (2019) 'Fabrication of Flexible Microlens Arrays for Parallel Super-Resolution Imaging', *Applied Surface Science*, 504, p. 144375. doi: 10.1016/j.apsusc.2019.144375.

Zhao, H. *et al.* (2019) 'Live imaging of contracting muscles with wide-field second harmonic generation microscopy using a high power laser', *Biomedical Optics Express*, 10(10), p. 5130. doi: 10.1364/BOE.10.005130.

Zhao, W. E. Z. *et al.* (2018) 'Faster super - resolution imaging with auto - correlation two - step deconvolution', *bioXirv*, 723(2012), pp. 664–670.

Zhou, S. *et al.* (2017) 'Effects of whispering gallery mode in microsphere super-resolution imaging', *Applied Physics B*, 123(9), p. 236. doi: 10.1007/s00340-017-6815-7.

Zhu, J. and Goddard, L. L. (2019) 'All-dielectric concentration of electromagnetic fields at the

nanoscale: The role of photonic nanojets', *Nanoscale Advances*, 1(12), pp. 4615–4643. doi: 10.1039/c9na00430k.

Zhuo, S. and Ni, M. (2015) 'Label-free and real-time imaging of dehydration-induced DNA conformational changes in cellular nucleus using second harmonic microscopy', *Scientific Reports*, 4, p. 7416. doi: 10.1038/srep07416.

Zipfel, W. R. *et al.* (2003) 'Live tissue intrinsic emission microscopy using multiphoton-excited native fluorescence and second harmonic generation', *Proceedings of the National Academy of Sciences*, 100(12), pp. 7075–7080. doi: 10.1073/pnas.0832308100.

Zipfel, W. R., Williams, R. M. and Webb, W. W. (2003) 'Nonlinear magic: Multiphoton microscopy in the biosciences', *Nature Biotechnology*, 21(11), pp. 1369–1377. doi: 10.1038/nbt899.

Zong, W.-X., Rabinowitz, J. D. and White, E. (2016) 'Mitochondria and Cancer', *Molecular Cell*, 61(5), pp. 667–676. doi: 10.1016/j.molcel.2016.02.011.Mitochondria.

Zong, W. *et al.* (2014) 'Two-photon three-axis digital scanned light-sheet microscopy (2P3A-DSLM)', in *CLEO: 2014*, p. AW3L.7. doi: 10.1364/CLEO_AT.2014.AW3L.7.

Zoumi, A., Yeh, A. and Tromberg, B. J. (2002) 'Imaging cells and extracellular matrix in vivo by using second-harmonic generation and two-photon excited fluorescence.', *Proceedings of the National Academy of Sciences*, 99(17), pp. 11014–9. doi: 10.1073/pnas.172368799.